Detection of Low Frequency Radio Signals from Space

Ph.D Thesis

by

Harsha Avinash Tanti
Roll No. 1901121009

Under the Supervision
of
Prof. Abhirup Datta

Department of Astronomy, Astrophysics and Space Engineering,
Indian Institute of Technology Indore,
Khandwa Road, Simrol, Indore - 453552, India

Detection of Low Frequency Radio Signals from Space

A THESIS

Submitted in partial fulfillment of the requirements for the award of the degree

of

DOCTOR OF PHILOSOPHY

by

Harsha Avinash Tanti

Department of Astronomy, Astrophysics and Space Engineering,
Indian Institute of Technology Indore,
Khandwa Road, Simrol, Indore - 453552, India

INDIAN INSTITUTE OF TECHNOLOGY INDORE

I hereby certify that the work which is being presented in the thesis entitled **DETECTION OF LOW FREQUENCY RADIO SIGNALS FROM SPACE** in partial fulfillment of the requirements for the award of the degree of **DOCTOR OF PHILOSOPHY** and submitted in the **DEPARTMENT OF ASTRONOMY, ASTROPHYSICS, AND SPACE ENGINEERING**, Indian Institute of Technology Indore, is an authentic record of my own work carried out during the time period from **July, 2019** to **December, 2024** under the supervision of **Prof Abhirup Datta, Professor, Indian Institute of Technology Indore**.

The matter presented in this thesis has not been submitted by me for the award of any other degree of this or any other institute.

24/06/25

Signature of the student with date
(HARSHA AVINASH TANTI)

This is to certify that the above statement made by the candidate is correct to the best of my/our knowledge.

26/6/25

Signature of Thesis Supervisor with date
(PROF. ABHIRUP DATTA)

HARSHA AVINASH TANTI has successfully given his/her Ph.D. Oral Examination held on **June 24, 2025**.

26/6/25

Signature of Thesis Supervisor with date
(PROF. ABHIRUP DATTA)

Dedicated

to

My Family

Acknowledgements

I would like to take a moment to sincerely thank and acknowledge all those who supported and guided me throughout my PhD journey.

First and foremost, I am deeply grateful to my thesis advisor, Prof. Abhirup Datta (Abhirup Sir), who empowered me to think independently and provided timely guidance. He never gave up on me, even when I doubted myself. Abhirup Sir struck the perfect balance between encouragement and constructive criticism — lifting my confidence when I felt low, and grounding me when I was overly optimistic. He taught me the importance of balanced self-assurance. Our manuscript discussions felt like engaging with a meticulous reviewer, which significantly sharpened my critical thinking skills. His unwavering support and the freedom he gives his students to explore research independently are truly unparalleled. For all this and more, I am deeply thankful.

I am eternally grateful to Prof. S. Ananthakrishnan (SAK Sir). I first met him during my Master's program, where he taught me Antenna Theory and encouraged me to pursue research. It was SAK Sir who backed my decision to take up research as a career. When I expressed interest in interdisciplinary work for my Master's thesis, he connected me with Dr. Subrata Kumar Das (Scientist E, IITM Pune), who later became a wonderful mentor. Even after I began my PhD with Prof. Abhirup, SAK Sir continued to offer valuable insights, especially from an antenna engineering perspective, which were crucial during the development of the SAM-DoA algorithm.

I'm also thankful to my research collaborator, Dr. Sushanta Kumar Bisoi, who always stepped in with support when needed. Discussions with him opened up new perspectives in solar physics and helped me dive deeper into the interplanetary medium. His and Abhirup Sir's combined guidance was instrumental in shaping this part of my work.

I'm also very grateful to my PSPC members Dr. Saurabh Das, Dr. Manoneeta Charkraborty, and Dr. Saptarshi Ghosh for their valuable, critical, and constructive suggestions on my work during the yearly evaluation.

I would like to acknowledge my seniors — Dr. Ramij, Dr. Majid, Dr. Altaf, Dr. Aishrila, Dr. Sarvesh, and others — for their openness to discussions and for sharing their insights. I extend special thanks to my senior and friend, Dr. Deepthi, for her unwavering support throughout my PhD journey. I am particularly grateful for her critical and constructive feedback on my write-ups, as well as for sharing her knowledge of essential soft skills, including email writing and how to extract meaningful insights during challenging conversations.

I am eternally grateful to my batchmates and friends for their support throughout the PhD journey. I would like to specially thank Anshuman (Tripathi ji) who has

great presence of mind and always had an answer or solution ready. He's a reliable friend who helped me in countless ways, including without whom I wouldn't have submitted my thesis. I would always be grateful to Dr. Swarna Chatterjee for being a good friend and a fellow scholar for mirroring my energy and her support. I am also thankful for her critical reviews on my writeups. I'll always cherish the dinner gatherings at Dr. Soumen and Dr. Chandrani's, which were much-needed breaks during stressful days. Tea breaks with Dr. Soumen were not only relaxing but often sparked new ideas. I would like to extend my gratitude towards Dr. Chandrashekhar (Chandra) for his support in various occasions during any grant documentation and his valuable feedback from a layman's perspective on some of my projects. I am also thankful to and acknowledge the constructive discussion on various topics with Dr. Hemapriya and Dr. Arghyadeep. Additionally, I thank all my batchmates for their support and for taking the time to review my thesis.

In the course of my PhD journey, I have been fortunate to work with exceptionally dedicated juniors whose collaboration proved invaluable. I would like to sincerely acknowledge Kundan, Tiasha, and Sheshank for their significant contributions to various research projects, and Samit, Bhuvnesh, and Gunjan, who, though juniors, became trusted colleagues and friends over time. I would like to express my sincere gratitude to Ms. Tiasha, Mr. Kundan, and Mr. Sheshank for their valuable support and active involvement in several of my side projects during the course of my PhD. I also wish to acknowledge Mr. Samit and Mr. Bhuvnesh for their support and for engaging in insightful discussions on various research topics. I would also like to thank Ms. Gunjan, a fellow research scholar and friend, whose insights helped me appreciate the importance audience-friendly communication in research.

Behind every successful PhD is the quiet, consistent help of administrative and technical staff. I sincerely thank Mr. Swapnil, Mr. Rahul, Mrs. Riyanka, Mr. Varunesh and Mr. Abhijeet for their constant support in handling official documentation and logistics. I extend my sincere thanks to Riyanka for her consistent support during her tenure in the department and for maintaining a valued friendship even after her transfer. I would also like to express my heartfelt gratitude to Abhijeet for his technical support, camaraderie, and friendship. Our shared background from the Kendriya Vidyalaya schooling system fostered a strong mutual understanding and a common work ethic, which made collaboration both effective and enjoyable. Additionally, I extend my sincere thanks to Mr. Tapesh Parihar, Section Officer (Academic Affairs), for his administrative support on various occasions throughout my PhD journey.

Lastly, I owe eternal gratitude to my parents and family, whose emotional support sustained me through every challenge of this journey. I am equally indebted to my brother, who stood by me emotionally, helped financially, and took care of responsibilities back home so I could focus on my work. And most importantly, I

want to thank my girlfriend — for being there through thick and thin. Without her love, support, and belief in me, I wouldn't have made it through this PhD journey.

Abstract

Low-frequency radio astronomy, particularly in the spectrum below 30 MHz, provides a unique opportunity to explore astronomical phenomena such as Auroral Kilometric Radiation, Magnetic reconnection event & Geotail, Galactic emissions, Interplanetary medium dynamics, and Heliosphere. This thesis examines the scientific potential and technical challenges associated with conducting radio astronomy at frequencies below 30 MHz, an area that remains largely unexplored due to limitations imposed by Earth's ionosphere. Ground-based observations in this spectrum are severely affected by radio frequency interference (RFI) and ionospheric cutoffs, making space-based observations essential. The research presented here addresses these challenges by developing new algorithms and techniques for source localization and investigating space weather phenomena using low-frequency radio observations. A key contribution of this thesis is the development of the Snapshot Averaged matrix pencil Method (SAM), which enhances the Direction-of-Arrival (DoA) estimation for the SEAMS mission, designed to explore radio frequencies below 16 MHz. The SAM-DoA algorithm improves the accuracy of estimating the direction and polarization of electromagnetic waves, and its applicability to various antenna designs is demonstrated. Additionally, this research explores the application of machine learning in source localization, offering faster inference times than traditional methods. This enables real-time monitoring of radio sources, particularly useful for observing disturbances in the interplanetary medium caused by space weather phenomena and their interactions with Earth's magnetosphere. To study the interplanetary medium (IPM), several techniques can be employed, including in-situ observations, remote observations of emissions from the IPM, and Interplanetary Scintillation (IPS) observations. The IPS technique is unique among the remote sensing techniques as scintillations observed are modulated by the Fresnel filter allowing observation of large scale density variation and evolution. Given the lack of low-frequency observations from space to study the IPM using the IPS technique, this research utilizes IPS observations from the Institute for Space-Earth Environmental Research (ISEE) in Japan to analyze microturbulence and long-term evolution in the interplanetary medium. By combining these observations with in-situ data from the Parker Solar Probe (PSP), the thesis also investigates the behavior of density and magnetic field modulation indices in the inner heliosphere.

List of Publications

A. Published:

1. **Harsha Avinash Tanti**, Abhirup Datta, S. Ananthakrishnan, "Snapshot averaged Matrix Pencil Method (SAM) for direction of arrival estimation", Experimental Astronomy, Volume 56, Issue 1, 2023, Pages 267-292, ISSN 1572-9508, 10.1007/s10686-023-09897-6

2. **Harsha Avinash Tanti**, Abhirup Datta, Tiasha Biswas, Anshuman Tripathi, "Development of a Machine Learning based Radio source localisation algorithm for Tri-axial antenna configuration", Journal of Astronomy and Astrophysics, Volume 46, article number 5, 2025, 10.1007/s12036-024-10032-w

3. **Harsha Avinash Tanti**, Susanta Kumar Bisoi, Abhirup Datta, "Inner-heliospheric signatures of steadily declining solar magnetic fields and their possible implications", The Astrophysical Journal, Volume 979, Number 2, Page 198, January 2025,10.3847/1538-4357/ada38a

B. Under Review:

1. **Harsha Avinash Tanti**, Susanta Kumar Bisoi, and Abhirup Datta, "Relative density fluctuation of the solar wind with the help of interplanetary scintillation and PSP density measurements", Submitted, The Astrophysical Journal Letters

C. Conference Publications:

1. **H. A. Tanti** and A. Datta, "Validation of Direction of Arrival with Orthogonal Tri-Dipole Antenna for SEAMS," 2021 IEEE Indian Conference on Antennas and Propagation (InCAP), 2021, pp. 312-315, doi: 10.1109/InCAP52216.2021.9726500.

2. **H. A. Tanti**, K. Sahu, A. Datta and A. K. Pradhan, "Tri-axial Patch antenna array configuration for Direction of Arrival (DoA) application," 2023 8th International Conference on Computers and Devices for Communication (CODEC), Kolkata, India, 2023, pp. 1-2, doi: 10.1109/CODEC60112.2023.10465763.

3. **H. A. Tanti**, A. K. Pradhan and A. Datta, "A Study of Wire Bi-Conical Antenna for Wide-Band Application in Radio Astronomy," 2024 IEEE Wireless Antenna and Microwave Symposium (WAMS), Visakhapatnam, India, 2024, pp. 1-4, doi: 10.1109/WAMS59642.2024.10527955.

4. K. S. Shekhar, **H. A. Tanti** and A. Datta, "Deep Learning Based Real-Time Lunar Terrain Detection for Autonomous Landing Approach," 2023 8th International Conference on Computers and Devices for Communication (CODEC), Kolkata, India, 2023, pp. 1-2, doi: 10.1109/CODEC60112.2023.10466224.

5. T. Biwas, A. Datta, **H. A. Tanti** and S. K. Pal, "Concept study of UV coverage of Radio interferometry in space using small satellites," 2023 8th International Conference on Computers and Devices for Communication (CODEC), Kolkata, India, 2023, pp. 1-2, doi: 10.1109/CODEC60112.2023.10466038.

6. K. S. Shekhar, **H. A. Tanti**, A. Datta and K. Aggarwal, "Monitoring Infrastructure Faults with YOLOv5, Assisting Safety Inspectors," 2023 International Conference on Integration of Computational Intelligent System (ICICIS), Pune, India, 2023, pp. 1-5, doi: 10.1109/ICICIS56802.2023.10430270.

N.B: Entries A1-A3, B1, and C1-C3 are parts of my thesis.

Table of Contents

List of Figures

List of Tables

Chapter 1

Introduction

1.1 Background and motivation of the thesis

Low-frequency radio astronomy, particularly in the spectrum below 16 MHz, holds excellent scientific promise but poses significant technical challenges. This range encompasses critical phenomena, such as the redshifted 21 cm line from the early universe (spanning from 0.38 to 400 million years after the Big Bang), Auroral Kilometric Radiation (AKR), Earth's magnetosphere and tail, galactic and extragalactic radio emissions, and the interplanetary medium (IPM)—the ever-flowing solar wind and high-energy events like Coronal Mass Ejections (CMEs) and Solar Flares (SFs) [10–14].

Observations at these frequencies provide valuable insights into cosmic magnetic fields and astrophysical processes, particularly in studying the IPM and high-energy solar events. One prominent method of remotely studying the IPM is through Interplanetary Scintillation (IPS). IPS refers to the intensity fluctuations caused by the diffraction and scattering of radio waves as they pass through the IPM, typically observed using compact radio sources such as distant radio stars or galaxies. Distant satellites transmitting signals can also act as point sources for these observations. The Fresnel filter function modulates the scintillations observed, $sin^2(k^2\lambda z/4\pi)$, where z represents the distance from the solar wind, λ is the observational wavelength, and k is the wave number of the irregularities. This modulation provides a filtering action that allows studying large-scale density structures and variations based on the observational wavelength [15, 16]. To examine solar wind turbulence—both micro and macro scale, including smaller and larger plasma structures—multi-wavelength observations are necessary [16]. The Fresnel filtering effect shows that the spatial scale size is proportional to the observational wavelength. For instance, observations at 327 MHz limit the density fluctuation scale size to $\leq 10^3$ km, while large-scale events like CMEs and SFs typically span from 10^4 to 10^7 km [15]. Therefore, very low-frequency observations are essential to study larger-scale events like CMEs and SFs, as the scale size directly correlates with the wavelength. However, ground-based observations face severe limitations due to the Earth's ionosphere, which becomes increasingly opaque at lower frequencies ($\leq$ 10 MHz). Below 30 MHz, signals suffer from scattering, distortion, and absorption [14]. Additionally, the ionosphere reflects and refracts radio waves, making it difficult to transmit signals and restricting the availability of radio-quiet zones crucial for precise observations.

Traditionally, interferometry has been used to combine signals from multiple antennas, enabling high-resolution observations less affected by atmospheric interference. However, ground-based interferometry faces significant limitations for extremely low-frequency (LF) observations due to ionospheric opacity and distortion. This has led to a shift toward space-based interferometry to

overcome these challenges. Key technological hurdles include suppression of radio frequency interference (RFI), achieving high time resolution, precise array element localization, antenna design, data handling, and space-qualified instrumentation [17]. Single-satellite missions have been developed to simplify the technical requirements, but they come with limitations in source localization. Effective localization of radio emissions is essential for understanding emission mechanisms and their characteristics [18]. Several space missions have historically been dedicated to exploring radio frequencies below 30 MHz. Notable examples include the Radio Astronomy Explorer (RAE-1) mission, which observed frequencies ranging from 0.4 to 6.5 MHz [19], followed by RAE-2 with a frequency range of 0.025 to 13 MHz [20]. Concurrently, the Interplanetary Monitoring Platform (IMP-6) mission recorded over 22 spectra across frequencies from 0.13 to 2.6 MHz [21]. In 2018, the Netherlands-China Low-Frequency Explorer (NCLE) was launched as part of China's Chang'E 4 Lunar mission to study the low-frequency spectrum [22]. In addition, several space missions have been designed explicitly for in-situ low-frequency measurements, such as Cassini-RPWS (Radio and Plasma Wave Science) and STEREO WAVES [23]. Ongoing initiatives, like the American-led Dark Ages Polarimeter Pathfinder (DAPPER) for the 17 to 38 MHz range [24] and the Indian-led Space Electric and Magnetic Sensor (SEAMS) for 0.3 to 16 MHz [25, 26], aim to explore this spectrum further. While single-satellite missions are often favored due to their lower complexity and cost, they come with significant drawbacks, such as limited resolution and localization capabilities. These constraints hinder detailed studies of the spatial characteristics of radio sources. Accurate source localization is critical for producing high-resolution images and understanding the spatial properties of radio emissions. Recent advancements in antenna design and direction-of-arrival (DoA) estimation techniques offer promising solutions. Missions like Cassini-RPWS and NCLE have successfully utilized goniopolarimetric techniques for source localization [6, 23, 27].

With accurate DoA (Direction-of-Arrival) estimation, scintillation observations can be significantly improved by measuring the intensity fluctuations and identifying the location of the radio source contributing to the scintillation. This capability is handy for tracking the movement and evolution of large-scale structures like Coronal Mass Ejections (CMEs) and Solar Flares (SFs) through the IPS technique, which requires low-frequency observations for effective detection. For future missions like SEAMS, developing advanced DoA algorithms will be crucial for improving IPS studies, enabling more accurate assessments of the IPM and its dynamic processes. Therefore, this thesis focuses on developing a source localization algorithm specifically for SEAMS and its application to space weather studies. Since no dedicated, very-low-frequency (< 30 MHz) observational facilities are available, the studies in this thesis are conducted using multi-station IPS telescopes operated by the Institute for Space-Earth Environmental Research (ISEE), Japan.

1.2 Objective of the thesis

This thesis investigates the observational techniques and instrumentation used in low-frequency radio studies. It also discusses the development of methods to localize radio sources from space using a single satellite system like SEAMS and examining the interplanetary medium. The following are three major aspects of the thesis:

- Understanding the basics of ground and space-based instrumentation.
- Development sensitive and accurate source localization algorithm for space missions like SEAMS.
- Studying the space weather and IPM using the IPS technique.

1.3 Thesis Arrangement

This thesis is structured into eight chapters. The first chapter of the thesis provides an overview, introduction, and motivation for the thesis. The last chapter provides the summary and future scope of the topic. A summary of each chapter is provided below:

- **Chapter 2:**

  This chapter outlines the scientific rationale that motivated the research presented in this thesis. Frequencies below 30 MHz still need to be explored. Ground-based observations in this range are limited due to interference from sky wave communication channels, radio frequency interference (RFI), and ionospheric cutoffs [14]. As a result, a space-based radio telescope is necessary for observations below 30 MHz. Observations at these frequencies open up various scientific opportunities, such as studying Auroral Kilometric Radiation (AKRs), Earth's magnetosphere and geotail, galactic and extragalactic radio spectra, the potential detection of redshifted 21 cm signals from the early universe, and the interplanetary medium (IPM) [14,28]. Among these goals, studying the IPM is crucial because it introduces distortions, scattering, and refraction that affect radio observations, particularly at low frequencies, due to the large-scale structures in the IPM. These irregularities cause phase shifts and signal fluctuations, known as scintillation effects, which are key to understanding the interference caused by the IPM. Additionally, by analyzing these scintillations, the dynamics of the interplanetary medium can be explored [15].

- **Chapter 3:**

  This chapter offers a comprehensive theoretical overview of the key concepts and advancements in radio astronomy instrumentation and observational techniques. Moreover, this chapter presents the ground-based radio instruments developed at IIT Indore, focusing on their design, functionality, and operational parameters. It provides a comprehensive overview of the development process, including the technical aspects of building these instruments for radio astronomy applications. The chapter also highlights the trade-offs in instrument design aimed at mitigating these challenges, such as antenna design optimizations, receiver sensitivity enhancements, and signal processing techniques. Despite these advancements, the inherent physical limitations of ground-based observations below 30 MHz are emphasized, pointing towards the necessity of space-based observatories or alternative approaches to overcome these barriers.

- **Chapter 4:**

  Tanti et al. 2023, *Experimental Astronomy, vol 56, 1, 267-292*

  This chapter addresses the significance and challenges of conducting space-based observations at extremely low frequencies (below 30 MHz). It further explores the issues related to radio source localization when using co-located antennas. One of the key challenges in radio astronomy is accurately estimating the direction of arrival (DoA) of electromagnetic (EM) waves from radio sources, especially when employing electrically short antennas. In this work, we present an improved algorithm that enhances direction and polarization estimations compared to existing methods. The proposed approach is a modified version of the existing Matrix Pencil Method (MPM) based DoA estimation. Typically, MPM determines the DoA of incoherent EM waves through unitary transformations and the least squares method (LSM). The Snapshot Averaged Matrix Pencil Method (SAM) modification was explicitly designed for the Space Electric and Magnetic Sensor (SEAMS) mission to explore the radio universe below 16 MHz. The SAM DoA introduces a snapshot averaging technique

to improve the estimation of incoherent frequencies, enhancing accuracy. Additionally, SAM can distinguish between different polarization states, including Right-Hand Circular Polarization (RHCP), Right-Hand Elliptical Polarization (RHEP), Left-Hand Circular Polarization (LHCP), Left-Hand Elliptical Polarization (LHEP), and Linear Polarization (LP). Along with the theoretical framework of SAM-DoA, this chapter presents the initial results of a scaled-down DoA experiment conducted at a resonant frequency of approximately 72 MHz.

- **Chapter 5:**

  Tanti et al 2024, *JoAA, Accepted for Publication*
  Tanti et al 2023, *8th CODEC Conference Proceedings*

  This chapter continues the discussion on radio source localization algorithms, focusing on the broader applicability of the developed SAM-DoA algorithm. It is observed that SAM-DoA can be adapted to various antenna types, provided the antenna configuration is triaxial. Based on this observation, a triaxial patch antenna configuration was designed to evaluate its linearity and mutual coupling, ensuring compatibility with SAM-DoA implementation. Therefore, a detailed analysis of a triaxial patch antenna array resonating at approximately 2.4 GHz has been conducted to assess its performance in the context of SAM-DoA. Using CST antenna design simulation software, an investigation is carried out to check the patch antenna's linearity and behavior under plane-wave excitation. However, while the SAM-DoA algorithm shows great promise, one limitation is its relatively slower inference time than other DoA algorithms. This slower inference time can be challenging for time-sensitive radio events, such as CMEs, SFs, and Auroral Kilometric Radiations (AKRs). Therefore, exploring faster estimation algorithms that can localize radio sources quickly and reliably in such scenarios becomes essential. We explored a novel machine learning (ML) approach to estimate DoA to address these performance constraints. It is observed that the trained ML model has a faster inference time. We developed a simplified emission and reception model by leveraging a tri-axial antenna arrangement and trained an artificial neural network (ANN) using synthetic radio signals. These synthetic radio signals are simulated based on the assumption that they can originate from any point in the sky, have an incoherent frequency range of 0.3 to 30 MHz, and exhibit signal-to-noise ratios (SNR) between 0 and 60 dB. A sizeable synthetic dataset was generated to accommodate various signal configurations and conditions, ensuring robust training for the ANN. Post-training, the ANN demonstrated exceptional performance, achieving low error rates during the training (0.02), validation (0.23%), and testing (0.21%) phases. Most notably, the ML-based approach offers significantly faster inference times (5 ms), substantially improving over traditional analytically derived DoA methods, which typically take between 100 ms and a few seconds. This speed advantage highlights the practical applicability of machine learning for real-time radio source localization, especially in scenarios with limited sensor arrays.

- **Chapter 6:**

  Tanti et al 2024, *The Astronomical Journal, Under Review*

  When observing distant radio sources in the MHz range, the interplanetary medium causes scintillation effects. These effects can be used to study the interplanetary medium remotely. Studies from the 1970s and 1980s demonstrated that interplanetary scintillation can serve as a valuable tool for investigating the magnetohydrodynamics (MHD) of the Sun and solar wind [15, 29, 30]. Building on these findings, this thesis explores how ground-based interplanetary scintillation observations can be employed to study long-term changes in the

heliosphere and solar activity. We examined solar photospheric magnetic fields across solar cycles 21 through 25, from 1975 to 2024, to investigate these dynamics. The unsigned photospheric magnetic fields at low latitudes (0°–45°), called solar toroidal fields, exhibited a clear variation of the solar cycle, with the field strength during the maximum of cycle 25 exceeding that of cycle 24. In contrast, the unsigned field strength of high-latitude solar polar fields (45°–78°) has steadily declined since the mid-1990s. Despite a brief resurgence between 2015 and 2020, the polar fields have resumed their downward trend through 2024, marking a significant 30-year decline. Parallel to these findings, we analyzed solar wind microturbulence levels in the inner heliosphere (0.2–0.8 AU) using interplanetary scintillation observations at 327 MHz. Covering the period from 1983 to 2022, the analysis shows a steady decline in microturbulence levels since the mid-1990s, corresponding with the observed decline in solar polar fields. Notably, both solar toroidal fields and solar wind magnetic fields reached a minimum during cycle 23, only to recover during the minimum of cycle 24. Further, we observed a hemispherically asymmetric solar polar field reversal during solar cycles 21 through 25. In cycle 25, while the northern hemisphere has already completed its reversal, the southern hemisphere's reversal remains incomplete. This hemispherical asymmetry and long-term declining trends in solar activity highlight significant anomalies in solar cycle dynamics that warrant further investigation, which we explore later in this chapter.

- **Chapter 7:**

  Tanti et al 2024, *In Prep.*

  This chapter highlights the critical phenomena in heliospheric physics, particularly regarding the dynamics of solar wind turbulence. Key metrics in this analysis are the density modulation index ($\epsilon_N = \Delta N/N$) and the magnetic field modulation index ($\epsilon_B = \Delta B/B$), which offer valuable insights into the evolution of solar wind turbulence. This study investigates the behavior of ϵ_N and ϵ_B in the inner heliosphere, specifically from 0.3 to 0.8 AU, by combining interplanetary scintillation (IPS) measurements with in-situ observations from the Parker Solar Probe (PSP). Here, the density modulation index ϵ_N was estimated using two distinct approaches. The first method employs ground-based IPS observations at 327 MHz, which analyze spatial scales of several hundred kilometers. Moreover, the second method uses in-situ density measurements obtained from the PSP/SWEAP experiment. Moreover, the magnetic field modulation index ϵ_B was derived from in-situ data collected by the PSP/FIELDS experiment. It is observed that both the ϵ_N and the ϵ_B exhibit minimal variation with increasing heliospheric distance. However, a notable discrepancy emerged when comparing ϵ_N estimates from ground-based IPS observations with those from in-situ PSP/SWEAP measurements.

Chapter 2

Science at Low Radio Frequencies below 30 MHz

The sub-30 MHz frequency band remains one of the least explored frontiers in observational radio astronomy. This is primarily due to the ionosphere also known as earth's upper atmosphere, which effectively blocks radio waves below 16 MHz and significantly attenuates signals up to 30 MHz. Ground-based instruments such as LOFAR (a 74-MHz system) on the Very Large Array (VLA) have pushed the boundaries of low-frequency radio astronomy, achieving high resolution and sensitivity. However, these successes are limited to frequencies above 50 MHz, where ionospheric effects can be mitigated using advanced calibration techniques. Observations below 30 MHz face significant challenges due to ionospheric distortions, particularly below 16 MHz. These limitations necessitate space-based approaches. These challenges necessitate the development of space-based observation facilities. Long-wavelength radio waves are critical for studying a wide range of phenomena within the solar system. Solar emissions dominate this spectrum, such as those produced by suprathermal electrons, interplanetary collisionless shocks, and coronal mass ejections (CMEs). Observations in the low-frequency domain provide vital insights into CME propagation, their interactions with the solar wind, and their potential to disrupt Earth's magnetosphere. Notable contributions to solar low-frequency studies have been made by missions like the STEREO spacecraft, which observed type II and type III solar radio bursts in the frequency range of 16 kHz to 16 MHz, offering valuable data on particle acceleration and solar wind structures. Observation of very low-frequency bands will also aid in studying Planetary magnetospheres. For instance, the Cassini mission's Radio and Plasma Wave Science (RPWS) experiment observed Saturn's auroral kilometric radiation (AKR), revealing critical details about the planet's magnetospheric dynamics and interactions with the solar wind. Cassini's data provided unprecedented insights into the generation mechanisms of Saturn's AKR, analogous to Earth's auroral emissions but observed at frequencies between 3 kHz and 16 MHz. Similarly, emissions from Jupiter, Uranus, and Neptune in this range will provide information about the structure and dynamics of their magnetic fields. The heliosphere is a significant source of low-frequency emissions and high-energy events like CMEs. In addition to these low-frequency emissions, the recent development of the Interplanetary scintillation technique is emerging as an important tool for understanding the large-scale dynamics of the heliosphere. Despite these advances, observations have been historically constrained by the limitations of short dipole antennas, which have angular resolutions restricted to several tens of degrees. To overcome the limitations, modern space-based missions must incorporate advanced direction-finding algorithms and interferometric imaging arrays.

Several pioneering space missions have advanced our understanding of low-frequency radio astronomy, addressing challenges such as ionospheric distortions and limited resolution. The first, Radio Astronomy Explorer 1 (RAE-1), launched in 1968, was deployed in Earth orbit and made the first measurements of the Galaxy's radio spectrum between 0.4 and 6.5 MHz [19]. These observations provided critical data on the galactic synchrotron radiation and established the feasibility of space-based low-frequency radio astronomy. The Interplanetary Monitoring Platform (IMP-6) conducted measurements of galactic radiation at 22 frequencies between 130 kHz and 2600 kHz in 1971, further expanding our understanding of the galactic spectrum[21]. The third principal mission, Radio Astronomy Explorer 2 (RAE-2), launched in 1973, was placed in lunar orbit to eliminate terrestrial radio-frequency interference. It observed radio emissions between 25 kHz and 13 MHz [20], achieving significant advances in understanding solar, planetary, and galactic radio emissions. The absence of Earth's ionospheric interference allowed RAE-2 to obtain unprecedented measurements of solar bursts, Jovian radio emissions, and interplanetary scintillation. The fourth mission, Voyager, though not dedicated exclusively to radio astronomy, contributed significantly to the field by detecting low-frequency emissions from the outer planets and the heliopause using its Plasma Wave System.

Beyond the solar system, low-frequency radio observations hold immense promise for advancing our understanding of the universe. This spectral range probes the thermal interstellar medium, supernova remnants, pulsars, galactic background emissions, and extragalactic sources like radio galaxies and quasars. Observing these sources at frequencies of a few MHz with angular resolutions approaching an arcminute could provide transformative insights into the physics of compact objects, cosmic magnetic fields, and particle acceleration mechanisms. Ancient "fossil" electron populations, remnants of past cosmic events, are also significant emitters in this frequency range. These populations offer a unique window into the history of cosmic magnetic fields and the evolution of large-scale structures in the universe. Several scientific studies can be performed in this frequency range. Section 2.1 briefly discusses about such studies.

2.1 Science Cases in Low Frequency

This section briefly overviews the scientific studies that can be conducted in the sub-30 MHz frequency band.

2.1.1 Heliosphere and Interplanetary media

The heliosphere is a vast bubble-like region in space influenced by the solar wind, which stems continuously from the Sun. This region extends beyond Pluto's orbit and serves as a protective barrier for the solar system against interstellar radiation and high-energy cosmic rays. The heliosphere is formed by the outward flow of charged particles (plasma) from the Sun, carrying its magnetic field into space and creating a dynamic environment. Structurally, the heliosphere comprises several key regions. The termination shock marks the boundary where the solar wind significantly slows due to its interaction with the interstellar medium. Beyond this lies the heliosheath, a turbulent region where the solar wind and interstellar medium mix. The outermost boundary, the heliopause, is where the pressure from the solar wind balances with that of the interstellar medium. Additionally, some models suggest the existence of a bow shock formed by the heliosphere's motion through interstellar space [31].

The interplanetary medium, in contrast, refers to the space between planets filled with charged particles, electromagnetic fields, and small solid particles. Its primary components include the

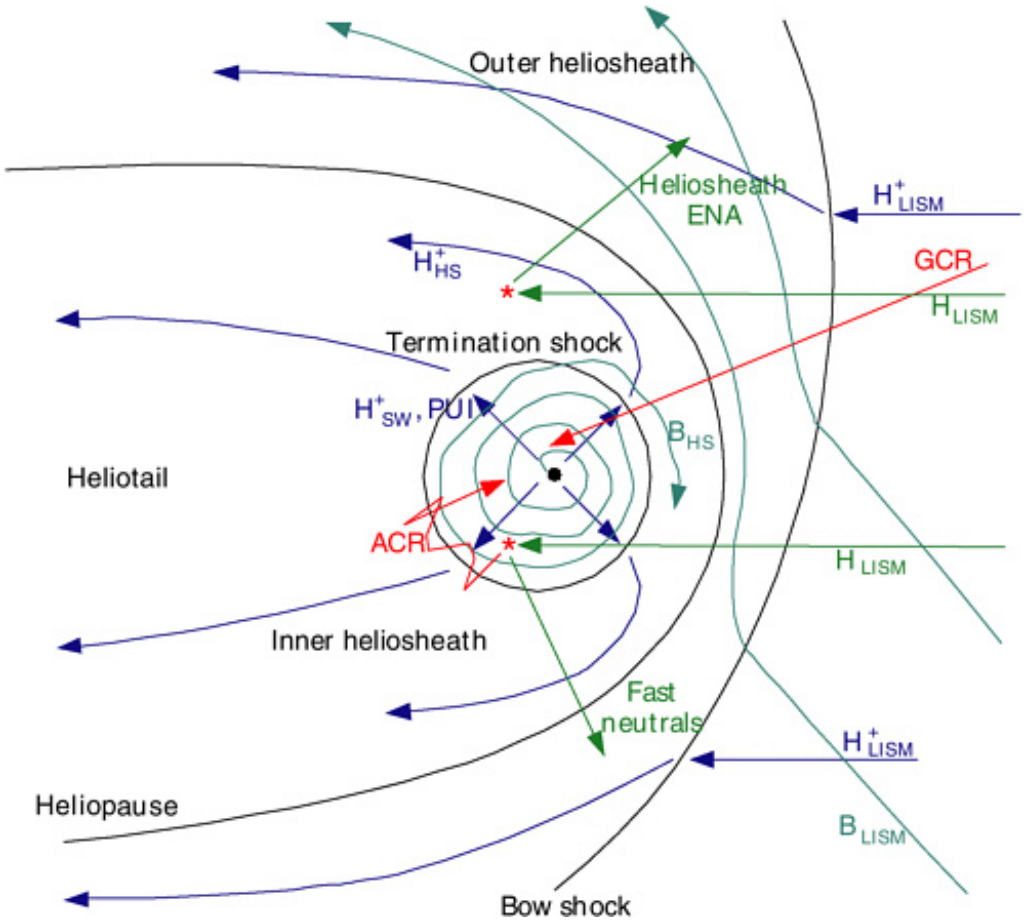

Figure 2.1: An overview of the heliosphere illustrates key regions such as the termination shock, heliopause, bow shock, and both the inner and outer heliosheath (HS). The diagram includes representative paths of plasma particles (H+), pickup ions (PU ions), and solar wind plasma (VHS). Additionally, it shows trajectories of neutral hydrogen atoms (H) originating from the interstellar medium (HISM) that undergo charge exchange (Black solid line). Galactic cosmic rays (GCRs) are also depicted. The solar magnetic field (BHS) and the interstellar magnetic field (BISM) are outlined as well. Image Credit: National Academy Open book

solar wind, the interplanetary magnetic field (IMF) carried by the solar wind, and cosmic rays. Additionally, it contains dust particles originating from asteroids, comets, and interstellar sources, along with plasma waves resulting from the interactions of charged particles with electromagnetic fields. This medium is crucial in mediating interactions between solar activity and planetary environments [32, 33]. Studying the heliosphere and interplanetary medium is essential for understanding solar-terrestrial interactions. These interactions are pivotal in shaping space weather phenomena that affect Earth's magnetosphere, ionosphere, satellites, and communication systems.

Furthermore, the heliosphere serves as a natural shield, modulating the influx of galactic cosmic rays into the solar system, with implications for planetary habitability [34,35]. Recent experiments and ongoing expeditions have significantly advanced our understanding of the heliosphere and the interplanetary medium. The Voyager, provided crucial information about the heliopause, while missions like the Parker Solar Probe and Solar Orbiter continue to explore the Sun's corona and

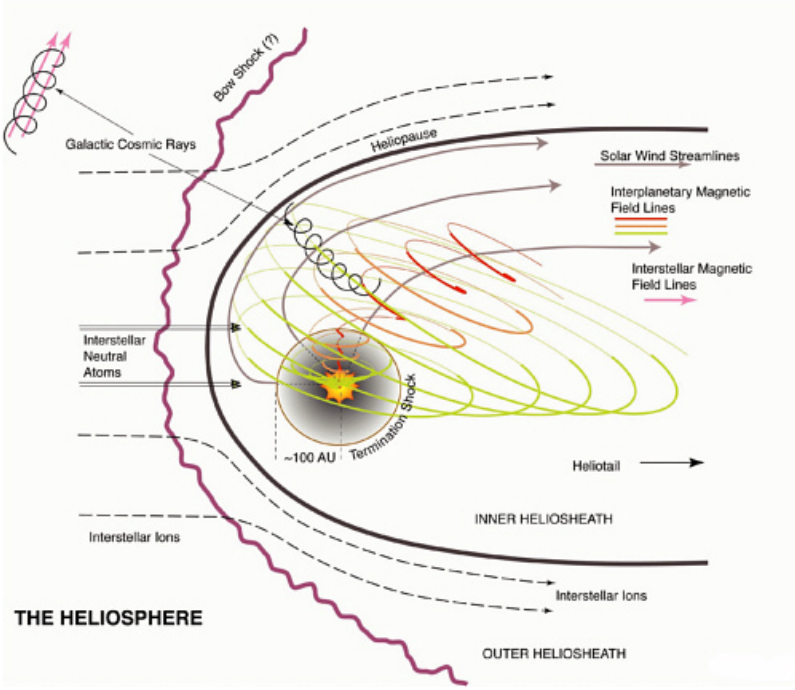

Figure 2.2: A diagram of the heliosphere shows how the solar wind, traveling at supersonic speeds, shapes the surrounding interstellar plasma as it flows around the Sun. Interstellar neutral atoms and ions move at a speed of 26 km/s relative to the Sun, while the solar wind expands outward at velocities between 400 and 800 km/s. This solar wind slows to subsonic speeds at the termination shock. Past this point, the solar wind is redirected toward the heliotail, carrying the spiral-shaped interplanetary magnetic field along with it. The heliopause acts as a boundary, separating solar-origin material and magnetic fields from those of interstellar origin. Although interstellar neutral atoms and high-energy galactic cosmic rays can enter the heliosphere, interstellar ions are deflected around it. Outside the heliopause, a bow shock may form in the interstellar medium.Image Credit:National Academy Open book

magnetic fields. These studies are crucial for uncovering the underlying processes driving the behavior of the solar wind and its interaction with the interstellar medium [36, 37].

2.1.1.1 Interplanetary Scintillation studies

Interplanetary Scintillation (IPS) is a key observational technique in low-frequency radio astronomy, particularly for studying the solar wind and its dynamics throughout the inner heliosphere. Since its discovery in the 1960s by Antony Hewish and colleagues, IPS has evolved into a fundamental tool for real-time space weather monitoring and understanding large-scale solar wind structures. This method involves measuring rapid fluctuations in the intensity of radio waves emitted by distant, compact celestial sources, such as quasars or pulsars. These fluctuations arise when radio waves traverse the turbulent and variable-density solar wind plasma, providing critical insights into the properties of this medium [38]. IPS occurs when radio waves from a compact, small-diameter background source pass through the interplanetary medium (IPM) filled with irregularities in electron density. These density irregularities, driven by solar wind turbulence, cause variations in the refractive index of the plasma, leading to interference patterns that fluctuate over time scales on the order of one second[38]. The degree and pattern of these fluctuations depend on

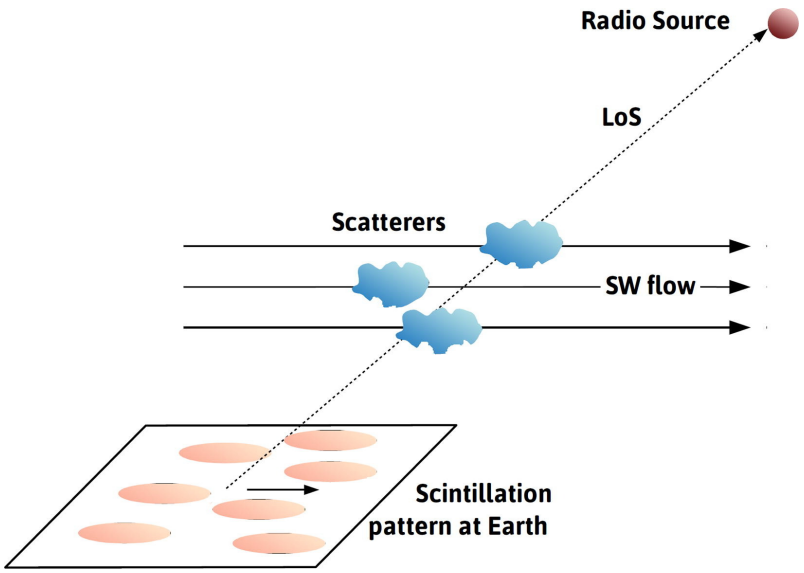

Figure 2.3: Diagram of Interplanetary Scintillation (IPS). Scatterers in the solar wind along the line of sight (LoS) to a compact radio source generate an intensity pattern on Earth's surface, which moves at the speed of the solar wind as it flows outward from the Sun. Image Credit: Jackson et al., 2022

the solar wind's speed, density, and turbulence through which the waves propagate. Because IPS is sensitive to electron density variations, it offers a way to remotely probe the solar wind speed and turbulence spectrum over vast regions of the heliosphere. Unlike direct in-situ measurements from spacecraft, which are confined to the trajectories of their orbits, IPS provides a broader, more global perspective of solar wind dynamics. When data from multiple radio telescopes at different geographic locations are combined, the spatial properties of the solar wind can be accurately mapped in three dimensions.

IPS was first detected in 1964 using the Cambridge radio array in the United Kingdom. The discovery demonstrated that the solar wind could be studied through ground-based radio astronomy by observing the scintillations of extragalactic radio sources. This breakthrough significantly advanced our ability to monitor solar wind and related space weather phenomena without needing costly and time-limited spacecraft missions. In the decades following its discovery, numerous radio telescopes worldwide have contributed to IPS observations. Early arrays like the University of California, San Diego (UCSD) system, the Miyun Synthesis Radio Telescope (MSRT) in China, and the Arecibo Observatory in Puerto Rico made significant contributions. More recently, operational systems such as the Institute for Space-Earth Environmental Research (ISEE) IPS array in Japan, the Ooty Radio Telescope (ORT) in India, and the Mexican Array Radio Telescope (MEXART) in Mexico have played critical roles in advancing IPS studies. Modern multi-station IPS facilities, such as the ISEE array consisting of the Toyokawa, Kiso, and Fuji stations, have enhanced the precision and accuracy of solar wind measurements. The ability to correlate observations from multiple stations allows scientists to resolve the spatial distribution of solar wind structures with unprecedented detail. Additionally, new facilities in China, supported by the Meridian Space Weather Monitoring Project, are expected to expand IPS capabilities further.

Space weather, driven primarily by the Sun's activity, profoundly affects Earth's magnetosphere, technological infrastructure, and human activities in space. Coronal Mass Ejections (CMEs), high-speed solar wind streams, and interplanetary disturbances can trigger geomagnetic storms,

disrupt communications, and affect power grids. Understanding and forecasting these occurrences is critical to mitigating their impacts, and it contributes significantly to space weather studies by continuously and globally monitoring solar wind speed and turbulence. Unlike spacecraft, which only provide point-based observations along their trajectories, IPS allows for tracking solar wind throughout vast portions of the heliosphere. This technique enables researchers to [15, 16, 39, 40]:

- **Monitor Solar Wind Dynamics:** IPS can detect high-speed solar wind streams, sluggish wind zones, and sporadic disruptions like CMEs. By detecting the speed and turbulence of these streams, IPS observations could help with real-time space weather forecasting
- **Track CMEs in Interplanetary Space:** IPS can detect and monitor the propagation of CME-driven shocks as they travel through the IPM toward Earth. By combining IPS data with white-light imaging and radio burst observations, scientists can triangulate the position and speed of CMEs, improving prediction models for geomagnetic storms.
- **Study Corotating Interaction Regions (CIRs):** CIRs arise when high-speed solar wind streams come into contact with the slower-moving plasma, resulting in increased density and turbulence zones. IPS is especially sensitive to these persistent formations, allowing researchers to track their evolution and potential impact on the Earth's space environment.
- **Understand Solar Wind Turbulence:** The solar wind displays a complex turbulence spectrum that affects particle transport and energy distribution in the heliosphere. IPS provides valuable data on the micro-turbulence spectrum, helping refine models of solar wind turbulence and its interaction with planetary magnetospheres.
- **Support 3D Tomographic Reconstructions:** By incorporating IPS data into computer-assisted tomography (CAT) models, researchers can reconstruct three-dimensional images of the solar wind's large-scale structures. These reconstructions are critical for understanding the global behavior of the solar wind and improving space weather prediction models.

Observations of IPS at low frequencies, particularly below 30 MHz, offer several unique advantages for space weather and solar wind studies. This frequency range corresponds to longer wavelengths, which interact more strongly with larger-scale density irregularities in the IPM. As a result, low-frequency IPS is particularly sensitive to the broader-scale structures and dynamics of the solar wind, making it an essential tool for tracking large-scale solar wind streams and CMEs [15,16,41,42].

- **Sensitivity to Large-Scale Structures:** At frequencies below 30 MHz, IPS measurements can capture density fluctuations associated with large-scale structures such as CIRs and CME-driven shocks. These observations help map these features' evolution and spatial distribution as they propagate through the heliosphere.
- **Extended Coverage of the Inner Heliosphere:** Scintillation can affect radio waves farther from the Sun as their frequency decreases. This property allows IPS observations below 30 MHz to probe regions closer to the Sun, providing insights into the early stages of solar wind expansion and CME propagation.
- **Complementing Ground-Based and Space-Based Observations:** While Earth's ionosphere restricts ground-based IPS observations to frequencies above 16 MHz, space-based platforms can observe at even lower frequencies. Combining the ground-based data and these observations provides continuous coverage across a broader frequency range, enhancing our ability to study the solar wind comprehensively.

- **Improved Accuracy in Source Localization:** At low frequencies, the diffraction patterns created by the solar wind are more significant and distinct, allowing for more accurate Direction-of-Arrival (DoA) techniques. This improved localization capability is critical for identifying and tracking specific solar wind structures and understanding their impacts on space weather.

2.2 Auroral and Planetary Magnetospheric Emissions

Auroral and planetary magnetospheric emissions play a crucial role in understanding the electromagnetic environment of planets within our solar system. These emissions, primarily in the low-frequency, originate from interactions between a planet's magnetosphere and its surrounding environment. For example, Jupiter's decametric radio emissions (DAM) are generated by cyclotron maser instability (CMI) in its polar regions, triggered by Io's volcanic activity and associated plasma torus [43]. Similarly, Saturn's kilometric radiation (SKR) is a sign of auroral processes [44], see in Figure 2.4. Observing these emissions enables the study of planetary magnetic fields, rotation rates, and magnetosphere-ionosphere coupling processes.

Even though the auroral events happen in the visible spectra, as shown in Figure 2.3, most of the emission occurs in the megahertz band. This makes space missions, such as the Voyager and Cassini spacecraft, indispensable in capturing auroral emissions [45]. Analyzing these emissions has improved our understanding of planetary magnetospheres and facilitated comparative studies of magnetospheric physics across different celestial bodies [46]. Space-based observatories promise to extend this field further by providing continuous, high-resolution data on auroral emissions—for instance, the proposed FARSIDE lunar array. [47] aims to detect faint auroral emissions from exoplanets, potentially indicating the presence of magnetic fields crucial for shielding planetary atmospheres from stellar winds. Such advancements could revolutionize our understanding of planetary habitability and the role of magnetic fields in sustaining life.

2.3 Probing the Early Universe: Dark Ages

The Dark Ages of the universe represent a critical phase in cosmic evolution, offering a pristine, undisturbed insight into fundamental cosmology. This era, occurring before the effects of astrophysical processes like star formation and supernova feedback, offers a clear window into the conditions of the early universe, similar to the Cosmic Microwave Background (CMB). However, these faint signals are redshifted into the low-frequency range and are obscured by foreground emissions and ionospheric effects, making ground-based detection extremely challenging. Space-based low-frequency observatories are currently the most viable solution for Dark Ages studies.

Ground-based experiments, such as the Low-Frequency Array (LOFAR) and the Hydrogen Epoch of Reionization Array (HERA)[48], have offered valuable insights above 30 MHz, but ionospheric distortions hinder observations below this threshold [49]. In contrast, lunar-based or spaceborne observatories can operate in a radio-quiet environment, free from terrestrial and solar interference [24]. The proposed Dark Ages Polarimeter Pathfinder (DAPPER) mission seeks to measure the spectrum of highly redshifted hydrogen emitted during Cosmic Dawn, the period of initial star formation and the Dark Ages in the universe's evolution [50]. These observations will provide crucial insights into both the Dark Ages and Cosmic Dawn, while helping to pinpoint the timing and duration of the subsequent Epoch of Reionization. Additionally, DAPPER will offer valuable

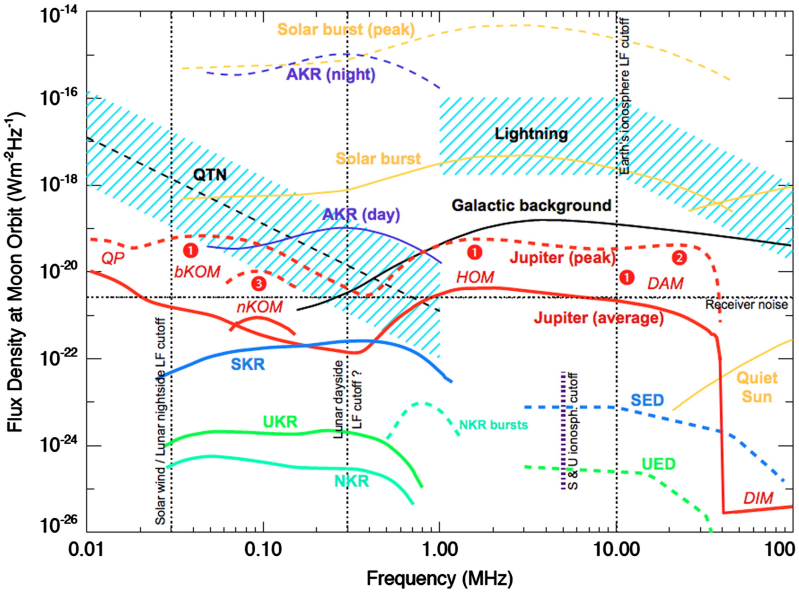

Figure 2.4: Planetary, solar, and predicted exoplanetary radio emission levels at the Moon's surface compared to the galactic background detected with a single dipole. Solid lines show average planetary spectra, and dashed lines show peak spectra. The figure includes emissions from Jupiter (HOM, DAM), Saturn (SKR), Uranus (UKR), and Neptune (NKR). The terrestrial auroral kilometric radiation (AKR) and lightning emissions are also shown, with day and night variations. The vertical dotted lines indicate LF cutoffs imposed by the solar wind, lunar dayside ionosphere, and terrestrial ionosphere. Solar bursts, quiet Sun emissions, and galactic background noise are superimposed for comparison. Image Credit: P. Zarka et al., 2012

constraints on cosmological parameters and models of dark matter annihilation [51].

Low-frequency radio astronomy is crucial in expanding our understanding of the early universe. Complementing optical and infrared observations helps connect the cosmic dark ages to the emergence of large-scale structures, offering a global picture across multiple wavelengths.

2.4 Galactic Non-Thermal Emissions

Galactic non-thermal emissions, primarily synchrotron, and inverse Compton radiation dominate the low-frequency radio spectrum of the Milky Way. Synchrotron radiation, produced by relativistic electrons spiraling in magnetic fields, provides critical insights into the structure and strength of the Galactic magnetic field [52]. Meanwhile, inverse Compton scattering reveals interactions between cosmic ray electrons and ambient photon fields [53]. Low-frequency observations of these emissions help disentangle various astrophysical processes shaping the interstellar medium (ISM). For instance, mapping synchrotron polarization at different frequencies can trace the 3D topology of Galactic magnetic fields [54]. Such studies have been bolstered by ground-based instruments like the Murchison Widefield Array (MWA), although space-based platforms offer superior resolution and sensitivity [55]. The future of Galactic non-thermal studies lies in space-based arrays capable of mapping these emissions over large sky regions. These arrays would enable detailed investigations of cosmic ray propagation and energy distribution, enhancing our understanding of star formation, supernovae, and feedback processes in galaxies [56]. Additionally, these observations are crucial for modeling and removing foreground contamination in cosmological studies [57].

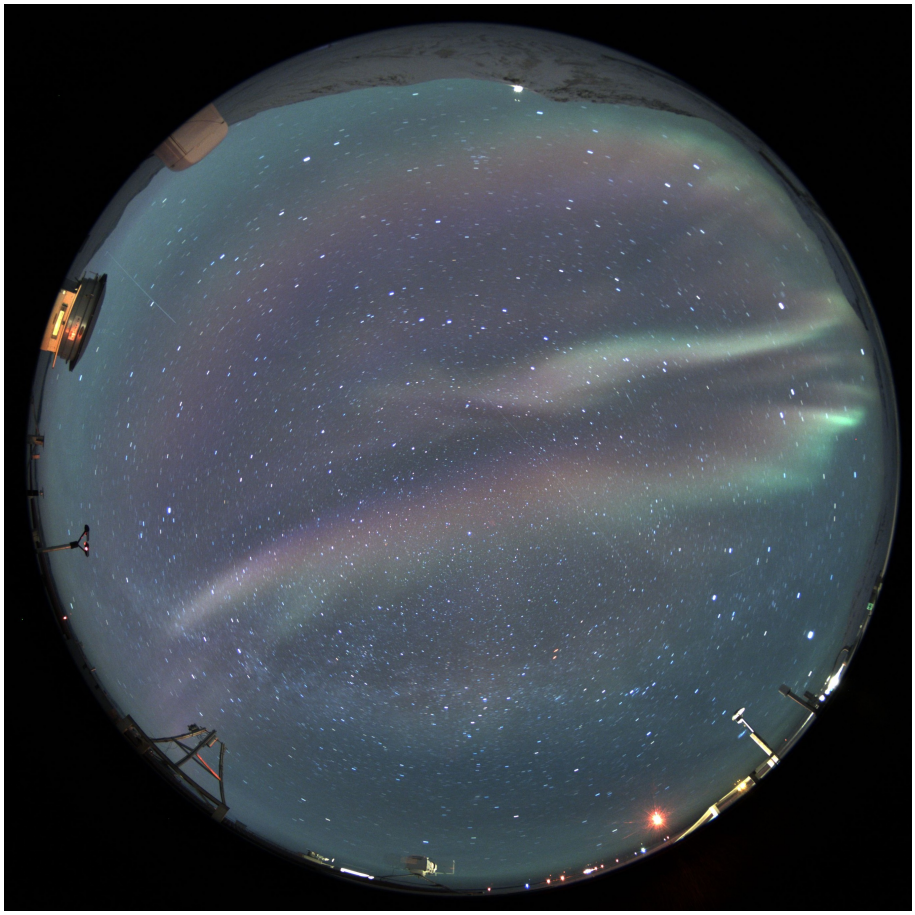

Figure 2.5: An Optical band image of an Aural event capture by an All sky camera install at the North-most Indian Scientific research station located in Gruvebadet, Ny-Alesund, Norway.

2.5 Galactic Diffuse Free-Free Absorption

Free-free absorption, arising from interactions between free electrons and ions in the ISM, manifests as a low-frequency turnover in the Galactic radio spectrum [58]. Studying this phenomenon provides direct electron density and temperature measurements, essential parameters for modeling the ISM. Recent advances in low-frequency spectroscopy have highlighted the significance of free-free absorption in constraining the physical conditions of HII regions and warm ionized media [59]. However, these studies are often limited by the inability of ground-based observatories to access the ultra-low-frequency regime where free-free effects are most pronounced [60]. Space-based observations can address this limitation, enabling comprehensive mapping of free-free absorption across the Galaxy. This would refine models of ionized gas distribution and its interplay with other ISM components [61]. Furthermore, such studies provide crucial foreground information for EoR and dark matter searches, emphasizing the interdisciplinary value of low-frequency radio astronomy.

2.6 Transient and Exotic Radio Sources

Transient radio sources, such as fast radio bursts (FRBs), pulsars, and magnetars, represent some of the most enigmatic phenomena in astrophysics. These sources often emit at low frequencies, where dispersion and scattering effects can reveal properties of the intervening medium [62]. Exotic phenomena, including potential technosignatures, also fall within this category [63]. Space-based low-frequency arrays can uniquely contribute to transient studies by enabling continuous sky monitoring in radio-quiet environments [64]. For example, detecting low-frequency counterparts of FRBs can elucidate their origins and progenitor mechanisms [65]. Similarly, monitoring pulsar emission in the low-frequency regime aids in testing theories of neutron star physics and gravitational wave detection [66]. Exploring exotic sources, such as possible artificial transmissions from extraterrestrial intelligence (ETI), also benefits from space-based platforms. These platforms enhance the sensitivity and reliability of SETI initiatives by avoiding Earth-based interference [67]. Such studies embody the broader scientific potential of low-frequency radio astronomy in addressing fundamental questions about our place in the universe.

2.7 Previous Space based Very Low-Frequency Radio Observations

Despite advancements in ground-based observation techniques and instrumentation, observation of the sub-30Mhz band is particularly challenging. Unlike higher radio frequencies, low-frequency signals are strongly influenced by Earth's ionosphere. The ionosphere's refractive and absorptive properties vary with time of day, solar activity, and geomagnetic conditions, introducing significant distortion and attenuation to incoming celestial signals. Nighttime ionospheric conditions are relatively stable, allowing improved observational capabilities, but even under these circumstances, signals below 10 MHz are often entirely reflected or absorbed, making ground-based observations impossible [68]. To overcome these challenges, astronomers have turned to space-based platforms, which bypass the ionospheric barrier and provide an unobstructed view of low-frequency emissions. Missions such as NASA's WIND/WAVES and ESA's Cluster satellites have demonstrated the feasibility of observing low-frequency emissions from planetary magnetospheres and the solar wind. More ambitious projects, like the planned Lunar surface low-frequency arrays, aim to study this regime in unprecedented detail, exploring phenomena hidden from ground-based telescopes [69].

As discussed in the sections above, observations in the sub-30 MHz frequency band are crucial for expanding our understanding of the present and early universe. To explore this frequency range, several dedicated missions have been launched, including the Radio Astronomy Explorer 1 (RAE-1), Radio Astronomy Explorer 2 (RAE-2), and the Netherlands-China Low-Frequency Explorer (NCLE) [70]. Additionally, missions such as Voyager 1 and 2, Cassini, and the Solar TErrestrial RElations Observatory (STEREO A and B) carried payloads capable of probing sub-30 MHz frequencies [70, 71].

The observations made by RAE-1 in 1968 revealed that at an altitude of 6,000 km, the Radio Frequency Interference (RFI) levels were 44 dB above the galactic background noise at 9.18 MHz. ([71] and references hereby) In contrast, data from RAE-2, which orbited the Moon at approximately 384,000 km from Earth, indicated that RFI due to terrestrial emissions was between 10 and 20 dB above the galactic background in the frequency range of 250 kHz to 13.1 MHz. Furthermore, RAE-2 observed a significant day-night variation in terrestrial interference. During Earth's daytime, RFI levels were approximately 40 dB above the background at 40 kHz and 20 dB above the background at 4 MHz. The WIND/WAVES experiment also contributed to our

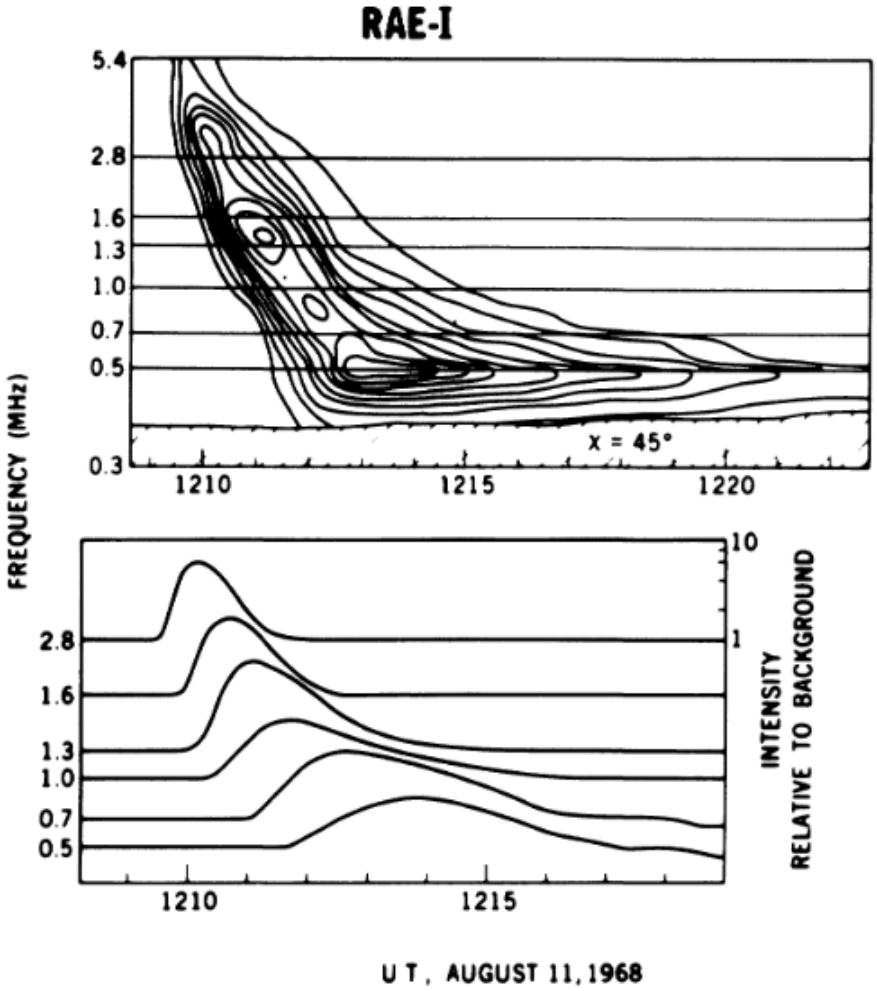

Figure 2.6: Type III burst observed by RAE-1 satellite at hectometer wavelengths [1]. (Image Credits: [1])

understanding of RFI levels. Located at the Earth-Sun L1 point (about 1.5 million kilometers from Earth), the Waves instrument recorded a maximum interference level of approximately 7 dB above the background at around 9 MHz. ([71] and references hereby) When extrapolated to lunar orbit distances—approximately four times closer to Earth than the Earth-Sun L1 point—the interference level increases by $10log_{10}(4^2) = 12$ dB, resulting in an RFI level of approximately 19 dB, which is above the background noise. If we further interpolate this noise level to an altitude of 500 km using the free-space path loss equation $20log_{10}\frac{4\pi D}{\lambda}$, the RFI at around 9 MHz increased from 171 dB in 1968 to 183 dB in 2016. This trend highlights a significant rise in RFI levels over the decades. However, after 2016, comprehensive data on terrestrial RFI levels in this frequency band have yet to be collected. Therefore, it is crucial to accurately map the current terrestrial RFI environment to enable more sensitive and precise low-frequency radio observations. ([71] and references herein)

Despite the challenges caused by Radio Frequency Interference (RFI), the RAE-1 mission successfully captured some of the earliest type III solar radio bursts (see Figure 2.6) and decametric

emissions from Jupiter [1, 72]. These groundbreaking observations demonstrated the potential of space-based instruments for low-frequency radio astronomy, overcoming the limitations imposed by Earth's ionosphere. The STEREO/WAVES experiment further expanded our understanding of type III solar bursts by observing numerous events and identifying a single power-law distribution in the number of bursts as a brightness function. The power-law index was approximately 2.1, largely independent of frequency. The Waiting Time Distribution (WTD) was consistent with a piecewise-constant Poisson process, indicating that individual type III bursts occur independently during a solar storm. This suggests that the storm dynamics are consistent with avalanche-type behavior originating from the underlying active region [73]. The Voyager 1 and 2 spacecraft were among the first to detect decametric and hectometric radiation from the outer planets, including Jupiter, Uranus, and Saturn. These observations provided critical insights into planetary magnetospheres and the interactions between planetary magnetic fields and the solar wind ([2] and references thereby). Additionally, the Cassini-RPWS (Radio and Plasma Wave Science) experiment demonstrated the effectiveness of Direction-of-Arrival (DoA) techniques for mapping Saturn's Kilometric Radiation (SKR). These measurements, illustrated in Figure 2.7, enhance our understanding of Saturn's magnetospheric dynamics [1] ([2] and references thereby).

Despite the success of previous missions, the observations in the sub-30 MHz frequency range still need to be revised to fully explore this largely uncharted spectrum [14]. This gap has motivated the proposal and development of several space-based interferometry missions designed to overcome the limitations imposed by Earth's ionosphere. Notable examples include the Farside Array for Radio Science Investigations of the Dark Ages and Exoplanets (FARSIDE) [24], which aims to conduct low-frequency observations from the far side of the Moon to study the early universe and exoplanetary environments. Another mission, the Orbiting Low-Frequency Antennas for Radio Astronomy (OLFAR), envisions deploying a fleet of nanosatellites to form a distributed interferometric array in space [14, 74]. Similarly, the Distributed Aperture Array for Radio Astronomy In Space (DARIS) aims to create an array of small satellites to enable high-resolution observations of low-frequency cosmic phenomena [74]. Other proposed missions include the Space-based Ultra-long Wavelength Radio Observatory (SURO), designed to investigate cosmic radio emissions at ultra-long wavelengths [28], and the Formation-flying sub-Ionospheric Radio Astronomy Science and Technology (FIRST) Explorer, which focuses on deploying a formation of satellites for space-based radio astronomy [74, 75]. These missions, leveraging space-based interferometry, offer the potential to provide unprecedented insights into the early universe, space weather, and planetary magnetospheres.

However, the research and development of space-based interferometers are expensive and technically complex. Deploying and maintaining multiple satellites in formation pose significant challenges compared to single-satellite missions. Consequently, a segment of the scientific community is concentrating on developing single-payload systems equipped with multiple sensors. These sensors allow for the implementation of goniopolarimetric techniques to determine the Direction of Arrival (DoA) of incoming signals [70]. This approach has led to developing missions such as the Dark Ages Polarimeter Pathfinder (DAPPER), an American-led project designed to operate in the 17 to 38 MHz frequency range [24]. DAPPER aims to probe the universe's Dark Ages, a period before the formation of the first stars, by detecting the redshifted 21 cm line of neutral hydrogen. Another significant initiative is the Space Electric and Magnetic Sensors (SEAMS) mission, led by India, which targets the 0.3 to 16 MHz frequency range [25, 26]. SEAMS seeks to study low-frequency emissions from the Sun, planetary magnetospheres, and interplanetary medium, contributing to

[1] In the figure 2.7 V refers to the stokes parameter V and α_{xw} is the elevation of Saturn above the plane formed by the orthogonal antenna x and w. Where antenna x is a dipole and antenna w is a monopole [27].

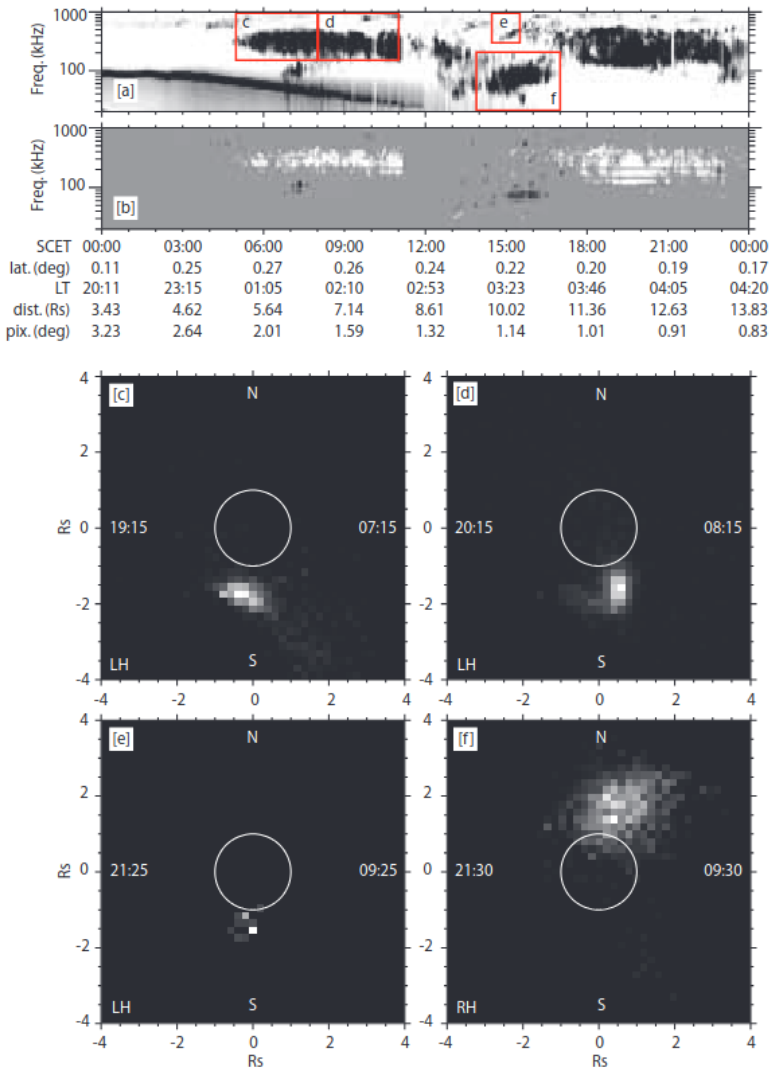

Figure 2.7: Direction-finding results for day 2005-089 [2]. Panel (a) shows the flux dynamic spectrum detected during the day within the 20–1000 kHz frequency range. Panel (b) illustrates the corresponding polarization measurements, where white indicates left-hand (LH) polarization and black indicates right-hand (RH) polarization. The details provided beneath plot (b) include the spacecraft time (SCET), latitude (lat), local time (LT), the distance to Saturn, and the angular size of each map pixel (pix). The bottom section contains four intensity maps, each representing specific selections. In panel (c), data covers the time range 05:00 to 08:00 SCET for frequencies above 150 kHz with conditions $V > 0.3$, SNR > 33 dB, and $\alpha_{xw} > 20°$. Panel (d) SCET is 08:00 to 11:00, frequency $\geq$150 kHz with the same conditions for V, SNR, and α_{xw}. Panel (e) SCET is 14:30 to 15:30 SCET for frequency $\geq$150 kHz, with $V > 0.3$, SNR > 33 dB, and $\alpha_{xw} > 20°$. Finally, panel (f) covers SCET 14:00 to 17:00 frequency $\leq$150 kHz with $V < -0.3$, SNR > 33 dB, and $\alpha_{xw} > 20°$. In each intensity map, white circles indicate Saturn's size, and each pixel measures 0.2 $R_S \times 0.2$ R_S (where R_S represents Saturn's radius). The maps display the northern and southern directions, along with the mean local time at the planet's limbs, which are marked on the edges of the maps [2]. (Image Credits: [2])

advancements in space weather forecasting and radio astronomy. These single-satellite missions with advanced DoA capabilities represent cost-effective and technically feasible precursors to full-scale interferometric arrays. They offer a promising pathway to expand our knowledge of the low-frequency universe while addressing the technical challenges of space-based interferometers.

2.8 Space Electric And Magnetic Sensors (SEAMS): An Indian initiative for Low-frequency Radio observation from Space

The Space Electric and Magnetic Sensors (SEAMS) mission is a multi-phase project designed to advance low-frequency radio astronomy in the 300 kHz to 16 MHz range. This frequency band holds significant potential for understanding various astrophysical phenomena, but Earth's ionosphere blocks observations below 16 MHz, necessitating space-based solutions. The mission aims to explore the interplanetary medium (IPM), planetary magnetospheres, and cosmological signals from the early universe. SEAMS is structured into three phases, each addressing distinct scientific objectives and technological challenges to build toward long-term space-based radio astronomy goals progressively.

Phase I of the SEAMS mission is a crucial testing phase, focusing on validating the instruments and conducting initial observations in Low Earth Orbit (LEO). The primary scientific goals of this phase are

- To map Radio Frequency Interference (RFI) and observe high-intensity and
- Local and relatively high-intensity phenomena such as Auroral Kilometric Radiation (AKRs) and Coronal Mass Ejections (CMEs).

To achieve these objectives, the payload is mounted on the fourth stage of ISRO's Polar Satellite Launch Vehicle (PSLV) and placed in a polar orbit at an altitude of 500 km. The payload consists of orthogonal active monopole antennas, a digital receiver, and an FPGA-based backend for real-time spectral analysis. The system uses commercial off-the-shelf (COTS) components to minimize costs. The data collected in Phase I will help refine the design and improve the performance of future mission phases.

Phase II represents an intermediate step in the SEAMS mission, aiming to test the feasibility of conducting space-based interferometric observations. Two to four payloads will be launched and deployed in LEO in this phase. The goal is to perform simultaneous observations using these multiple satellites to validate interferometric techniques in space. This phase shares the same scientific objectives as Phase I, including RFI mapping, AKR detection, and CME tracking. Deploying multiple payloads will enable a more detailed and accurate study of solar wind structures and space weather phenomena. The insights gained from this phase will provide substantial data to enhance the instrument design and ensure the success of the final phase.

Phase III of the SEAMS mission is the most advanced stage, focusing on conducting highly sensitive low-frequency radio observations free from terrestrial RFI. In this phase, a single payload equipped with triaxial electric sensors (linear antennas) and triaxial magnetic sensors (magnetometers and loop antennas) will be deployed in the Lunar orbit or on the far side of the Moon. The Moon's far side offers a unique, RFI-free environment ideal for low-frequency radio astronomy. The primary scientific objectives of this phase include

- The study of the Interplanetary Medium using scintillation studies and emissions studies,
- Observation and mapping of AKR emission,
- Earth's magnetosphere and its Geotail,
- Detecting the redshifted 21 cm line from neutral hydrogen during the Dark Ages and Cosmic Dawn (0.38 to 400 million years after the Big Bang) and,
- other low-frequency emissions from planetary and exoplanetary magnetospheres.

Another critical component of this phase is the development of a robust Direction-of-Arrival (DoA) estimation algorithm. Since only a single satellite will be deployed, accurate DoA techniques will be essential for localizing radio sources and conducting detailed studies of astrophysical phenomena.

2.8.1 Importance of Direction of Arrival and Low-Frequency Radio Astronomy in SEAMS and Interplanetary Scintillation studies

Low-frequency radio astronomy, significantly below 16 MHz, offers immense potential for understanding the universe while presenting unique challenges. This spectral range is crucial for studying phenomena such as the redshifted 21 cm line from the early universe, Auroral Kilometric Radiation (AKR), Earth's magnetosphere, galactic and extragalactic emissions, and the interplanetary medium (IPM), which includes solar wind dynamics and high-energy events like Coronal Mass Ejections (CMEs) and Solar Flares (SFs) [10–14]. Observations at these frequencies provide critical insights into cosmic magnetic fields, astrophysical processes, and the dynamics of solar wind turbulence, making the interplanetary scintillation (IPS) technique a valuable tool for probing the IPM.

IPS arises from intensity fluctuations caused by the diffraction and scattering of radio waves as they traverse the IPM. Compact sources like distant radio stars or satellites act as ideal probes, with observed scintillations influenced by the Fresnel filtering effect. The Fresnel filter function governs this modulation,

$$\sin^2\left(\frac{k^2\lambda z}{4\pi}\right) \tag{2.1}$$

where z is the solar wind distance, λ the wavelength, and k the wave number of irregularities. Such filtering allows for studying large-scale density variations, with multi-wavelength observations enabling investigations of both small- and large-scale plasma structures [15, 16]. For example, observations at 327 MHz resolve density fluctuations on scales $\leq 10^3$ km, whereas CMEs and SFs often span 10^4 to 10^7 km, necessitating very low-frequency observations [15].

However, ground-based low-frequency astronomy faces limitations due to ionospheric opacity and distortion, significantly below 10 MHz. The ionosphere reflects and refracts radio waves, leading to signal scattering and absorption, restricting observations to wavelengths above this threshold [14]. Space-based platforms offer solutions, with missions like RAE-1 and RAE-2 pioneering low-frequency studies. At the same time, modern initiatives like the Netherlands-China Low-Frequency Explorer (NCLE) and SEAMS aim to overcome these challenges and extend exploration into the lower frequency ranges [19, 20, 22, 25].

Source localization is pivotal for enhancing IPS observations, particularly in tracking and understanding the evolution of large-scale solar wind structures like CMEs and SFs. Direction-of-arrival

(DoA) estimation is essential in this context, offering the capability to pinpoint radio source locations and improve spatial characterization. Advanced goniopolarimetric techniques employed in missions like Cassini-RPWS and NCLE demonstrate the efficacy of DoA methods in low-frequency observations [6, 23]. Future missions such as SEAMS must prioritize DoA algorithm development to enhance IPS capabilities and provide precise diagnostics of the IPM.

This led to the development of source localization algorithms and techniques tailored for SEAMS as it is fundamental for IPS technique and mapping emissions (See Chapter 4 and 5). Given the absence of dedicated low-frequency (< 30 MHz) facilities to study the IPM thus, we utilized multi-station IPS telescopes operated by the Institute for Space-Earth Environmental Research (ISEE), Japan, to study IPM using the IPS technique (In Chapter 6 and 7).

Chapter 3

Radio Astronomy Techniques for Ground and Space Based Observations at Low-frequencies

3.1 Introduction to Radio Astronomy

Radio astronomy, a field that revolutionized our understanding of the universe, began in the 19th century with Karl Jansky's detection of radio waves from the center of the Milky Way. Working at Bell Telephone Laboratories, Jansky identified these waves while investigating interference in transatlantic communications, marking the first evidence of extraterrestrial radio signals [76]. This discovery inspired Grote Reber, an amateur astronomer who constructed the first dedicated radio telescope in 1937. Reber's systematic sky surveys in radio frequencies provided the first maps of the radio sky, revealing new celestial phenomena, such as non-thermal emissions and supernova remnants [77]. His work demonstrated the potential of radio observations and established radio astronomy as a cornerstone of astrophysical research. The mid-20th century witnessed the advent of radio interferometry, pioneered by Martin Ryle and colleagues. This innovation significantly enhanced the resolving power of radio telescopes. The development of aperture synthesis techniques allowed observations with angular resolutions comparable to optical systems [78]. Ryle's work culminated in detailed studies of radio galaxies, quasars, and the Sun's radio emissions, earning him the Nobel Prize in Physics in 1974. These advances demonstrated the transformative potential of radio astronomy in probing the non-thermal universe and set the stage for modern interferometric arrays like LOFAR and SKA [79, 80].

Radio astronomy is indispensable for exploring phenomena inaccessible to optical wavelengths. One of its primary advantages is the ability to pass through interstellar dust clouds, enabling observations of regions such as star-forming complexes, the galactic center, and distant active galactic nuclei [81]. Additionally, radio observations uniquely capture non-thermal processes like synchrotron radiation, where relativistic electrons spiral in magnetic fields, and free-free emission from ionized plasmas. These mechanisms provide critical insights into the dynamics of supernova remnants, pulsars, and galactic magnetic fields [82]. Detecting the 21 cm hydrogen line emitted by neutral hydrogen atoms is another milestone in radio astronomy. This spectral line has been instrumental in mapping the distribution of hydrogen in galaxies and studying galactic rotation curves, which provided early evidence of dark matter [83]. Furthermore, the redshifted 21 cm

line serves as a cosmic probe of the universe's large-scale structure and the epoch of re-ionization, offering a window into the universe's early stages [43].

The radio spectrum spans a vast range of frequencies, typically divided into low-frequency (<30 MHz), very high frequency (30–300 MHz), ultra-high frequency (300 MHz–3 GHz), and microwave regions (3–300 GHz) [80]. Each band corresponds to unique scientific phenomena and observational challenges. Low-frequency radio astronomy (<30 MHz) holds particular promise for exploring large-scale synchrotron radiation from cosmic rays, auroral kilometric radiation from planetary magnetospheres, and emissions from the interstellar medium. This band is also pivotal for probing the redshifted 21 cm line from the early universe, potentially unlocking secrets of the cosmic dawn [84]. However, ionospheric distortion and terrestrial radio frequency interference (RFI) present significant challenges for ground-based observations, necessitating space-based platforms such as the Lunar Crater Radio Telescope (LCRT) and heliospheric satellites for effective exploration [84].

This chapter primarily discusses radio observation techniques and the history and challenges of space-based sub-30 MHz observations. Moreover, this chapter provides some insight on the initial phase of the development of the Indian mission - Space Electric And Magnetic Sensor (SEAMS) for sub-30 MHz observation.

3.2 Radiometer

Radiometers are fundamental instruments used in radio astronomy to measure the total noise power received by an antenna within a specific frequency band. In their simplest form, radiometers consist of a combination of Low Noise Amplifiers (LNAs), Band Pass Filters (BPFs), and RF Amplifiers (high-gain amplifiers), followed by a square-law detector. Figure 3.1 shows a simplified block diagram of a radiometer. The signal is first received by an antenna and passed to the LNA to amplify the weak signal while contributing minimal noise. If the observational frequency band is noisy, the LNA design may need to be optimized for a narrower bandwidth. Alternatively, lossless filtration (filters with negligible resistive loss) can be introduced before the LNA to suppress unwanted signals. Following the initial amplification, the signal undergoes bandpass filtration to isolate the frequency band of interest. This is followed by a second stage of high-gain amplification to increase the signal power further. The amplified signal is then fed into a square-law detector[1]. Finally, the signal is integrated or averaged to obtain the total power within the specified frequency band. The resulting data is stored using a digital backend consisting of an Analog-to-Digital Converter (ADC) and a storage device for further analysis. The Radiometers are fundamental for observation of global 21cm signal and its modeling [8].

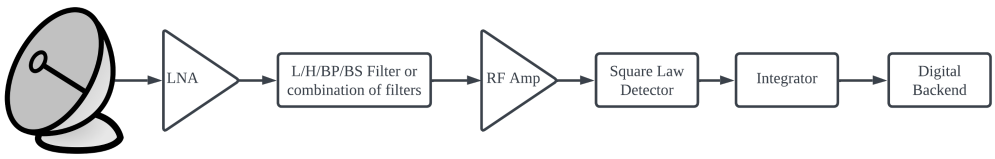

Figure 3.1: A simplified block diagram of a radiometer consists of the following components: an antenna, a Low Noise Amplifier (LNA), a filtration stage, a high-gain amplifier, a square-law detector, an integrator, and a digital backend.

[1]A component used to detect and measure the power of a radio frequency (RF) signal [8].

Figure 3.2: A simplified Block diagram of a Spectrometer consisting of components: an antenna, a Low Noise Amplifier (LNA), a filtration stage, a high-gain amplifier, and a digital backend

3.3 Spectrometer

Unlike radiometers, which measure the total power of a signal over a broad frequency range, spectrometers are designed to provide detailed information about the frequency spectrum of a signal. This distinction makes spectrometers particularly valuable in applications such as radio astronomy, enabling frequency-domain analysis. Figure 3.2 illustrates a simplified spectrometer block diagram. The main difference from a radiometer lies in the signal processing chain. While radiometers use a square-law detector and integrator to obtain the total power, spectrometers employ a digital backend that directly processes the digitized signal [8,85]. In a spectrometer, the digital backend performs a series of tasks. The signal, after being digitized by an analog-to-digital converter (ADC), passes through a series of delay blocks and a polyphase filter bank (PFB). The PFB enhances spectral resolution by dividing the input signal into multiple frequency sub-bands while minimizing spectral leakage. Following the PFB, a fast Fourier transform (FFT) is applied to convert the time-domain signal into its frequency-domain representation. The resulting spectral data is then auto-correlated to compute the power spectra of the received signal, which is a critical step for identifying and analyzing spectral features.

Both radiometers and spectrometers rely heavily on the performance characteristics of their analog-to-digital converters (ADCs), which fundamentally dictate the system's operational bandwidth, resolution, and sensitivity. The ADC's sampling rate and dynamic range are pivotal in determining the fidelity of signal acquisition, making them critical factors in the analog receiver design. The operational frequency of the ADC often sets the upper limit for direct signal digitization. When signals fall outside the operational range of the ADC, additional analog processing is required. Figure 3.1 and Figure 3.2 depict a scenario where the input signal is directly fed into the ADC within the digital backend. However, this configuration is only viable for systems observing frequencies compatible with the ADC's capabilities. For higher frequency observations, the signal must first be processed by an analog receiver chain that includes filtering, amplification, and potentially down-conversion to match the ADC's input range [8,85] (See Appendix J).

3.4 Single-Aperture Radio Telescope

Single-dish radio telescopes play a fundamental role in low-frequency radio astronomy, enabling the study of various celestial phenomena such as pulsars, galaxies, and interstellar gas clouds. These telescopes are designed to capture and process radio emissions from astronomical sources, particularly in the sub-30 MHz range, where the ionosphere constrains observations. In comparison to spectrometers, the basic configuration of a single-dish radio telescope includes an antenna connected to Low Noise Amplifiers (LNAs), Band Pass Filters (BPFs), a superheterodyne receiver, and a digital backend. However, a key difference lies in the design of the antenna itself. To en-

hance resolution and sensitivity, single-dish telescopes typically employ reflector-type antennas, which are based on the relationship λ/D, where λ is the wavelength of the observed signal and D is the diameter of the dish [86] . The larger the diameter of the dish relative to the wavelength, the higher the resolution achieved.

The essential operation of a single-dish radio telescope begins with the reflection and focusing of incoming radio waves. A parabolic dish is the primary reflector, directing the radio waves to a focal point. Some designs incorporate secondary reflectors, such as Cassegrain or Gregorian systems, to improve focus precision and reduce the size of the structure. At the focal point, a feed antenna captures the radio waves and converts them into electrical signals. These signals are then amplified using Low Noise Amplifiers (LNAs) to minimize the introduction of additional noise. The amplified signal is passed through Band Pass Filters (BPFs) to isolate the desired frequency range. After filtration, the signal undergoes further amplification using high-gain RF amplifiers. The next stage in the signal processing chain is the square-law detector, which converts the amplified radio frequency (RF) signal into a voltage proportional to the square of the signal's amplitude. This conversion is crucial for measuring the power of the incoming signal. The output of the square-law detector is then integrated or averaged to determine the total power within the frequency band of interest. Finally, the signal is digitized by an Analog-to-Digital Converter (ADC) and stored in a digital backend for subsequent analysis [8, 80, 87].

The performance of single-dish telescopes can be characterized using several key equations in radio astronomy. The brightness $B(\nu)$ of a source, which represents the power per unit area per unit frequency per unit solid angle, is given by the Planck formula:

$$B(\nu) = \frac{2h\nu^3}{c^2} \frac{1}{e^{h\nu/kT} - 1} \quad (\mathrm{W/m^2/Hz/sr}). \tag{3.1}$$

At radio frequencies, this simplifies under the Rayleigh-Jeans approximation to:

$$B(\nu) \approx \frac{2kT}{\lambda^2}, \tag{3.2}$$

where k is the Boltzmann constant, T is the temperature, and λ is the wavelength. The brightness temperature T_B, which relates to the sky brightness, is defined as:

$$T_B = \frac{\lambda^2}{2k} B(\nu). \tag{3.3}$$

Another important parameter is the antenna efficiency, described by the relationship:

$$D(\theta, \phi) = \frac{4\pi A_e}{\lambda^2}, \tag{3.4}$$

where A_e is the effective aperture of the antenna and $D(\theta, \phi)$ is the directivity. The total system noise temperature T_{sys}, which affects the sensitivity of the telescope, is given by:

$$T_{\mathrm{sys}} = T_{\mathrm{sky}} + T_{\mathrm{spill}} + T_{\mathrm{loss}} + T_{\mathrm{rec}}, \tag{3.5}$$

where T_{sky} is the sky noise temperature, T_{spill} is the spillover noise temperature, T_{loss} accounts for losses in the system, and T_{rec} is the receiver noise temperature.

The signal-to-noise ratio (SNR) for a detection can be expressed as:

$$\mathrm{SNR} = \frac{GS\sqrt{\Delta\nu\tau}}{T_{\mathrm{sys}}}, \tag{3.6}$$

where G is the system gain, S is the flux density of the source, $\Delta\nu$ is the bandwidth, and τ is the integration time.

Several significant single-dish radio telescopes have made noteworthy contributions to radio astronomy. The Arecibo Telescope in Puerto Rico, with a 300-meter spherical reflector, was instrumental in studying pulsars and the interstellar medium. Its design minimized spillover noise by incorporating ground screens. The Mauritius Radio Telescope, operating at 150 MHz, used helical antennas for wide-area sky surveys. With its cylindrical paraboloid design, the Ooty Radio Telescope (ORT) in India excelled in large-scale sky surveys, particularly at low frequencies. The Green Bank Telescope (GBT) in West Virginia, with its 100-meter steerable dish, is optimized for low-noise observations of molecular clouds and pulsars. The Parkes Observatory in Australia, known for its 64-meter dish, has played a key role in pulsar surveys and SETI research. The Effelsberg Telescope in Germany, another 100-meter dish, is renowned for studying galactic and extragalactic sources. [8, 87]

Despite their capabilities, single-dish radio telescopes face several challenges, mainly when operating at low frequencies. One of the primary challenges is ionospheric interference. Radio waves longer than a few tens of meters are absorbed or distorted by the Earth's ionosphere, making observations below 30 MHz difficult from the ground. This limitation necessitates the use of space-based platforms for low-frequency astronomy. Additionally, noise poses a significant challenge, especially at frequencies below 50 or 100 MHz, where terrestrial interference and ionospheric noise can degrade signal quality. Moreover, the design of the feed antenna also presents a challenge for single-dish telescopes. For large dishes, the feed must be carefully designed to ensure optimal aperture illumination [2]. [8, 80, 85, 88]

Another major challenge is the limited resolution of single-dish telescopes at low frequencies. The resolution of a telescope is determined by the ratio λ/D, where λ is the wavelength of the signal and D is the diameter of the dish. At wavelengths of hundreds of centimeters, achieving arcsecond or milliarcsecond resolution would require antennas with diameters extending over several kilometers, which is impractical for single-dish designs. To address this limitation, radio astronomers often use interferometric arrays, which combine signals from multiple antennas to achieve higher resolution. [8]

3.5 Radio Interferometer

As discussed in Section 3.1, one of the major limitations of single-dish telescopes is their resolving power, which is constrained by the size of the antenna. Constructing antennas on the scale of kilometers poses significant engineering challenges and is prohibitively expensive. Consequently, it is impractical to build single telescopes of such enormous size. To achieve the desired angular resolution, radio astronomers rely on a method known as aperture synthesis. Aperture synthesis employs the principles of radio interferometry, which works by combining signals from multiple antennas to simulate a much larger aperture. This concept is analogous to the double-slit experiment with quasi-monochromatic light, where interference patterns provide information about the source. Instead of drawing this analogy, radio interferometry is more commonly understood through the van Cittert-Zernike theorem. The theorem establishes a relationship between the spatial coherence

[2] Aperture illumination refers to the distribution of electromagnetic wave amplitude and phase across the antenna's surface. Proper illumination affects the telescope's beam shape, gain, sidelobe levels, and efficiency. Poor aperture illumination can lead to decreased sensitivity and increased sidelobe noise, compromising the quality of observations. [88]

function $V(r_1, r_2) =< E(r_1)E(r_2) >$ and the intensity distribution of the incoming radiation, $I(s)$. It demonstrates that the spatial correlation function $V(r_1, r_2)$ depends only on the difference $r_1 r_2$. When measurements are confined to a single plane, this correlation function can be expressed as the Fourier transform of the intensity distribution: $V(r_1, r_2) = \mathcal{F}\{I(s)\}$ [8,85]. Understanding the principles and applications of radio interferometry is essential for observational radio astronomy. To support education and research in this area, a teaching interferometer is being developed at IIT Indore to train aspiring astronomers (details are provided in Appendix J).

To further enhance resolution capabilities, techniques like Very Long Baseline Interferometry (VLBI) have been developed [8, 85]. These advancements have significantly improved the resolution, sensitivity, and overall effectiveness of radio observations. However, observations in the sub-50 MHz frequency range remain inaccessible due to ionospheric opacity below 16 MHz and terrestrial noise [70]. These limitations necessitate the establishment of space-based observational facilities to explore this frequency range effectively [24, 24, 28, 70, 71].

3.6 Space Based Observation Facility

As described in Chapter 2, observing a sub-30 MHz band requires a space-based telescope. Previously, single satellite missions such as Voyager 1 & 2, RAE 1 & 2, Interplanetary Monitoring Platform (IMP-6), Cassini-RPWS, and STEREO observed in the sub-30 MHz band [19–21, 23]. However, based on the description of radio astronomy observation techniques, it is evident that a radio interferometer in space is required to conduct high-resolution observations. Attempts have been made to create hybrid observation techniques by integrating ground and space-based telescopes, such as RadioAstron by Russia and VSOP/HALCA by Japan [89]. The ionospheric losses are lower in frequencies above 30 MHz. Thus, these hybrid observation techniques are practical at higher frequencies. This resulted in the idea of multiple missions to launch interferometers into space. Some of the notable projects are the Sun Radio Interferometer Space Experiment (SunRISE) [90], Farside Array for Radio Science Investigations of the Dark Ages and Exoplanets (FARSIDE) [24], Orbiting Low-Frequency Antennas for Radio Astronomy (OLFAR) [14,74], Distributed Aperture Array for Radio Astronomy In Space (DARIS) [74], and Space-based Ultra-long Wavelength Radio Observatory (SURO) [28], and Formation-flying sub-Ionospheric Radio astronomy Science and Technology (FIRST) Explorer [74, 75].

Space-based interferometers are ideal for exploring the sub-30 MHz band. However, deployment might be challenging due to constraints such as array element localization, array pattern, antenna design, data handling, instrumentation, RFI suppression, high time resolution and time synchronization, [17, 70], leading to the development of single satellite missions. Single satellite missions are among the most commonly funded space-based missions due to their low level of technological complexity and budget constraints [17, 91, 92]. Examples of the aforementioned missions would be Voyager 1 & 2, RAE 1 & 2, IMP-6, Cassini-RPWS, and STEREO, which had single or multiple co-located low frequency (sub 30 MHz band) spectrometer probes [19–21, 23]. Also, the antennae utilized in this experiment were linear wire antennas, which are omnidirectional, enabling observations of nearby radiative sources such as planetary and solar emissions. Yet, the Cassini-RPWS experiment demonstrated that even with the omnidirectional antenna source, localization can be conducted to map the emission and image it. [2, 23, 27]. The localization was achieved using co-located antennas in conjunction with goniopolarimetric techniques (a Direction Finding method)[3]

[3]The terms goniopolarimetry, Direction Finding (DF), and Direction of Arrival (DoA) technique will be used interchangeably. DF and DoA denote the direction of the source, while goniopolarimetry refers to a method for performing DoA/DF.

This approach provides an alternative means to investigate the sub-30 MHz frequency range until deploying a space-based interferometer becomes feasible. Such advancements inspire missions like the Netherlands Chinese Low-Frequency Explorer (NCLE) [**93**] and the forthcoming Phases of SEAMS [26, 70, 94]. Consequently, refining more sensitive Direction Finding techniques is crucial for source localization, mapping, and imaging applications.

3.6.1 Direction Finding using Co-Located Antennas

Developing direction-finding (DF) techniques is critical for enabling a single satellite mission to achieve source localization, mapping, and imaging, as previously discussed. The efficacy of DF methods is strongly influenced by antenna orientation, as these techniques utilize electromagnetic equations to determine the location of radio sources [5, 6, 18, 23, 70, 95, 96]. Methods for estimating the direction of arrival (DOA) can be categorized into subspace-based techniques (e.g., MUSIC, ESPRIT, root-MUSIC), spatial filtering approaches (e.g., Delay-and-Sum beamformer, Capon's method), and goniopolarimetric techniques (e.g., Analytical Inversion method, Pseudo Vector Estimation method, Matrix Pencil Method (MPM)) [5, 6, 23, 95–99]. Subspace-based and spatial filtering methods typically rely on antenna arrays and involve significant computational complexity. In contrast, goniopolarimetric techniques utilize the radiation properties of a limited number of co-located antennas, alongside electromagnetic theory, to estimate the source location. For sub-30 MHz applications, constructing an antenna array on a single satellite is impractical due to the required size and the associated computational and energy demands. Consequently, goniopolarimetric methods are favored for such missions, as they require fewer co-located antennas and involve comparatively lower computational complexity [96].

As discussed in Chapter 2 Section 2.7, Cassini-RPWS was among the first mission which displayed the used Analytical inversion method for direct finding and mapping the SKR emission (see Figure 2.7) [2]. The analytical inversion method for direction-finding (DF) is used to determine the Direction of Arrival (DoA) of electromagnetic waves, their flux, and polarization state using radio measurements collected by a system of electric dipole antennas [27]. The method utilizes a system of three orthogonal electric dipole antennas mounted on the spacecraft. The antennas measure the electric field components of the incoming radio waves along different axes. Each dipole antenna records the voltage induced by the electric field component of the incoming wave along its specific axis. This method is analytically derived, uses the correlation between the co-located antennas, and utilizes the inversion methods based on the least square fitting model to estimate the DoA [23, 27].

Conversely, the approach proposed by [95] employs an orthogonally co-located linear antenna. This technique utilizes a Special Unitary SU(3) matrix applied to a narrowband signal to derive the Pseudo-vector from the Spectral Density Tensor constructed using observations from the three antennas. The resulting Pseudo-vector is aligned with the propagation vector and encapsulates the polarization characteristics of the incident electromagnetic field [95] (refer to Appendix A for further details).

Although the aforementioned method offers low computational complexity and achieves accuracy at the degree level, its primary drawback lies in its limited noise immunity. The MPM-based Direction of Arrival partially addressed this issue (DoA) method proposed by [5, 6, 96], which leverages the matrix pencil method to estimate dominant frequencies within the signal bandwidth. Subsequently, the DoA is determined using the approach outlined by [95]. A comprehensive explanation of the MPM-based DoA method is provided in Appendices B and C. While the MPM-based method demonstrated improved resilience to noise, its performance declined when applied to broadband

signals or those containing multiple dominant frequencies. These limitations prompted the development of the Snapshot Averaged Matrix Pencil (SAM)-based DoA technique, detailed in Chapter 4.

3.6.2 Interplanetary Scintillation Technique

As elaborated in Chapter 2, Section 2.1.1.1, the IPS (Interplanetary Scintillation) technique has emerged as a cost-efficient approach for investigating the inner and outer heliosphere. This technique leverages the fluctuations induced by interplanetary media to study the media itself [3]. Figure 3.3 illustrates the geometry of IPS observations conducted from ground-based facilities. In this configuration, **S** and **E** represent the Sun-Earth system, while **P** denotes the intersection point of the radial solar wind with the line of sight (LOS) from Earth to a distant radio source (**R**). This intersection forms a perpendicular footprint (**A**) on the Earth's ecliptic plane. The heliocentric distance of **P** from the Sun is denoted by **r**. Dashed lines in Figure 3.3 lie within the ecliptic plane, whereas solid lines extend outside.

The angles ϵ and γ correspond to the radio source's solar elongation and heliographic latitude, respectively. As electromagnetic waves emitted by the distant radio source travel along the LOS to the Sun and Earth, they are diffracted and scattered by solar wind plasma, causing phase modulation and amplitude variations in the radio signal intensity. This phenomenon, referred to as IPS, has been extensively documented by [3, 100–104]. Ground-based telescopes detect these intensity fluctuations, particularly prominent for compact, point-like radio sources. The extent of these fluctuations is quantified by the scintillation index (m), defined as the ratio of the scintillating radio flux to the mean observed radio flux, $m = \Delta I/\langle I \rangle$. The distant radio source (**R**) may also be a signal transmitted from a satellite. Consequently, multi-satellite systems or satellites equipped with sensitive Direction of Arrival (DoA) techniques can facilitate mapping scintillation patterns across heliospheric distances.

Owing to the scarcity of sub-30 MHz data and space-based IPS observations, the 327 MHz IPS observations conducted using the ground-based facility in Japan, managed by ISEE, are employed. The ISEE IPS facility consists of four stations, located at Sugadaira (latitude/longitude: $36°31'12''N/138°19'16''E$), Toyokawa (latitude/longitude: $34°50'05''N/137°22'09''E$), Kiso (latitude/longitude: $35°47'34''N/137°37'49''E$), and Fuji (latitude/longitude: $35°25'36''N/138°36'42''E$). Prior to 1994, the ISEE IPS network consisted of three stations. In 1994, the network was expanded by adding a fourth station at Kiso, identical in design to the other three, thereby forming a four-station network. This four-station facility conducts systematic 327 MHz IPS observations of approximately 200 compact extra-galactic radio sources annually. Daily, line-of-sight (LOS) IPS observations are performed for about a dozen selected radio sources, enabling coverage over a heliocentric distance range of 0.26 to 0.82 AU, corresponding to solar elongations of 15° to 55°, throughout the year. The data from these four stations are utilized to derive solar wind velocities and scintillation indices [105, 106]. The IPS observations carried out at 327 MHz, facilitated by the action of the Fresnel filter, inherently filter out the large-scale solar wind density fluctuations caused by solar activities such as coronal mass ejections (CMEs) and solar flares, with typical scale sizes of density irregularities ranging from 10^4 to 10^7 km. This allows tracking small-scale solar wind electron density fluctuations of scale sizes $\leq 10^3$ km both within and outside the ecliptic. In addition, the IPS observations of the intensity fluctuation depend on the heliospheric distance due to the rotation and revolution of Earth, which results in multiple LOS observations of the extra-galactic radio source with different heliospheric distances. This allows to probe the solar wind in the interplanetary medium over a broader range of heliocentric distances, between 0.26 to 0.82 AU, covering the whole inner heliosphere [103, 107–109].

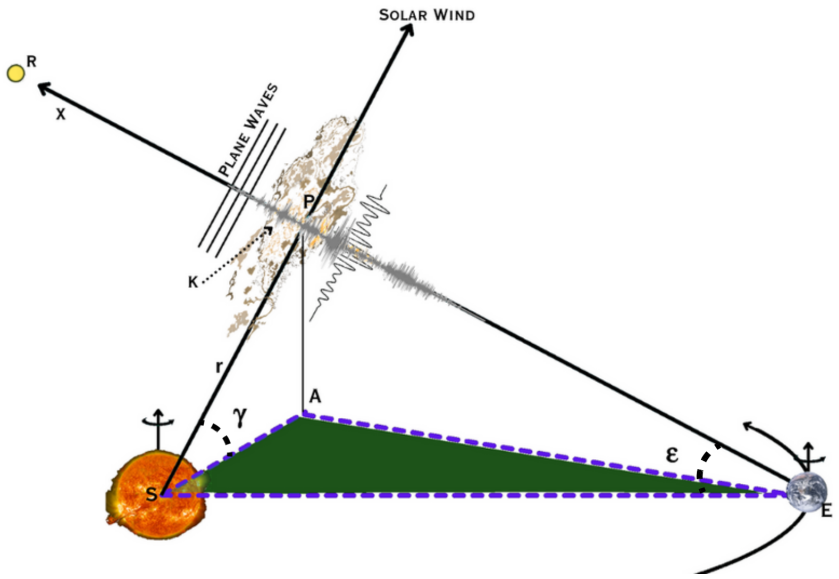

Figure 3.3: A pictorial depiction of the IPS observing geometry. The radio source, the Sun, and the Earth are indicated by points R, S, and E, respectively. The incoming plane waves along the line-of-sight (LOS) from the distant radio source R undergo phase modulation at the point of closest approach, P while passing through the solar wind, resulting in amplitude variations of the radio intensity. The footprint of the perpendicular line from the point P is indicated by a point A. All the dashed lines lie in the ecliptic plane, indicated by the triangle SAE and filled with green, while all the solid lines lie out of the ecliptic plane. The angles ϵ and γ are the solar elongation and the heliographic latitude of the radio source, while r is the heliocentric distance of the radio source.

The photospheric magnetic field extends into the interplanetary medium, forming the heliospheric magnetic field (HMF) [110, 111]. Due to the low plasma-beta condition in the solar corona, the HMF is frozen into the solar wind and carried beyond 1 AU. Consequently, long-term variations in the photospheric magnetic field influence solar wind density irregularities. IPS scintillation index measurements, which reflect solar wind density turbulence in the inner heliosphere, are suitable for examining such temporal variations. For an ideal point source, the scintillation index (m) increases with decreasing heliocentric distance (r) until reaching the turnover distance, where $m = 1$. At 327 MHz, this occurs at 0.26 AU, beyond which m decreases in the weak scattering regime, becoming dependent on r and source size. However, m should remain independent of these factors when studying temporal variations. The weak scattering regime's theoretical values of m can be modeled by assuming a power-law distribution of solar wind density irregularities [3]. Figure 3.4a illustrates m at 327 MHz for various source sizes using Marian's model, demonstrating that m depends on heliocentric distance and source size. Normalization methods described in [104] make m independent of r by adjusting for a point source at each distance, as shown by parallel lines in Figure 3.4. Similarly, source size normalization, following [112], involves scaling m values using Marian's curve fits for different source sizes, ensuring consistency across observations. Figure 3.4b demonstrates this normalization process. The upper panel compares m for source 1116-02 (blue dots) with Marian's curve for point source 1148-001 (black line). The dashed red line represents the best fit for 1116-02. After source size normalization, as shown in the lower panel, the normalized data align closely with Marian's curve for 1148-001, confirming consistency across observations. The source 1148-001 is considered an ideal point source, with an angular size of ∼12 mas from

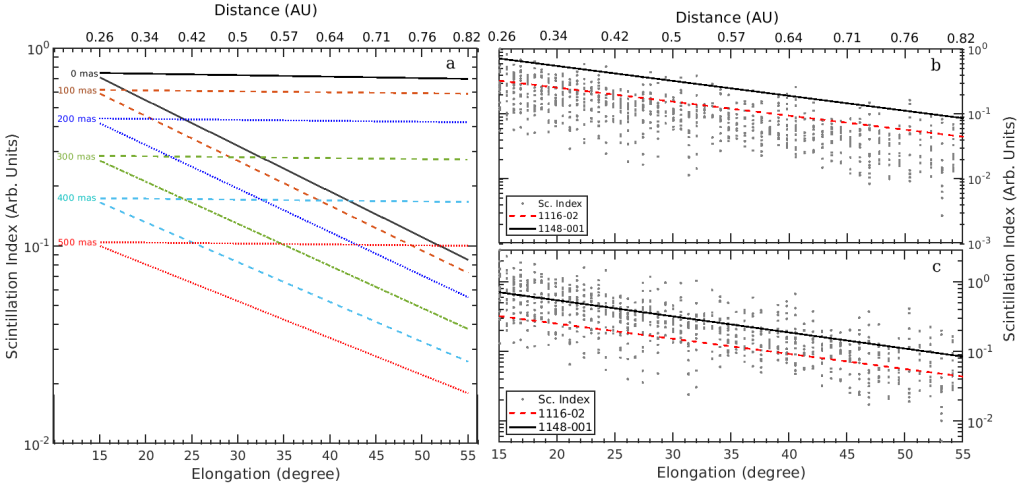

Figure 3.4: (a) The curves represent the theoretical values of variation of the Scintillation index (m) as a function of solar elongation, computed utilizing the Marians 1975 model. The grey dots in the (b & c) represent the normalized measurements of the source 1116-02 scintillation indices. The solid black curve in each panel indicates the theoretical value of the m for the source 1148-00 computed using [3]. The red dashed line in the top two panels (b & c) indicates the best fit of the Marians model for source 1116-02. The panel in the middle shows data of 1116-02 after the multiplication by a factor such that the effects of source size on the data are removed.

Ooty IPS observations [113] and 10 mas from VLBI measurements [114].

Chapter 4

Snapshot averaged Matrix Pencil Method (SAM) for direction of arrival estimation

Adapted from: ***Harsha Avinash Tanti***, *Abhirup Datta, S. Ananthakrishnan, "Snapshot averaged Matrix Pencil Method (SAM) for direction of arrival estimation", Experimental Astronomy, Volume 56, Issue 1, 2023, Pages 267-292, ISSN 1572-9508, 10.1007/s10686-023-09897-6*

4.1 Introduction

The radio frequencies ranging from 0.3 to 16 MHz is one of the unexplored realms of the electromagnetic spectrum in radio astronomy. This frequency range covers the red-shifted 21 cm line from the early Universe ($\sim$ 0.38 to 400 million years after the Big Bang) and radio emissions from the planetary and exoplanetary magnetosphere. It traces a wide range of astrophysical phenomena [10–14]. In this frequency range, ground-based astronomical observations have been infrequent due to the presence of the Earth's ionosphere and radio frequency interference (RFI). The ionosphere reflects and refracts radio waves at low frequencies. It inhibits transmissions from space below the ionospheric cut-off frequency. The cut-off frequency varies depending on the time of day and the Sun's activity, although it can go down to 10 MHz [115]. Also, finding or creating a radio-quiet zone for astronomical observations takes much work. This is due to the presence of RFIs caused by the intercontinental communication signals, which are broadcast using the ionosphere's reflective feature, which in turn makes observations at these radio frequencies complex [71].

A space or moon-based radio telescope can tackle the aforementioned challenges of such low-frequency radio observations. A few space missions have been dedicated to observations at these radio frequencies. The first space mission at these radio frequencies was Radio Astronomy Explorer (RAE-1), which made observations of the Galaxy'sspectrum from 0.4 to 6.5 MHz [19]. A successor, RAE-2, was launched to the lunar orbit for measurements in the frequency range of 0.025 to 13MHz [20]. Later, the Interplanetary Monitoring Platform (IMP-6) reported observations of galactic spectra at 22 frequencies, from 0.13 to 2.6 MHz [21]. Then, the Netherlands Chinese Low-Frequency Explorer (NCLE) was launched in 2018 as part of China's Chang'E4 Lunar mission [**93**]. This is the most recent experiment for long-wavelength observations. In addition, missions like Cassini-RPWS (Radio and Plasma Wave Science) and STEREO (Solar TErrestrial RElations Observatory)

WAVES were designed, to perform in-situ low frequency observations of Saturn's magnetosphere and Coronal mass ejections from the Sun respectively [23].

Another significant development in the past decade is the implementation of the space-based very long baseline interferometers VSOP/HALCA by Japan and RadioAstron by Russia [89]. Furthermore, there were numerous proposed concepts for space-based observations and instrumentation, such as Farside Array for Radio Science Investigations of the Dark ages and Exoplanets (FARSIDE) [24], Orbiting Low-Frequency Antennas for Radio Astronomy (OLFAR) [14,74], Distributed Aperture Array for Radio Astronomy In Space (DARIS) [74], Space-based Ultra-long wavelength Radio Observatory (SURO) [28], and Formation-flying sub-Ionospheric Radio astronomy Science and Technology (FIRST) Explorer [74,75]. Also, there are a few projects under development, such as America-led Dark Ages Polarimeter Pathfinder (DAPPER) for the frequency range 17 to 38 MHz [24] and India-led Space Electric and Magnetic Sensor (SEAMS) for the frequency range 0.3 to 16 MHz [25,26].

RFI suppression, array pattern (non-redundant baselines), high time resolution, time synchronization, array element localization, antenna design, data handling, and space-qualified instrumentation are some of the technological hurdles in deploying the space-based array [17]. This has led to the development of single satellite missions. Single satellite missions are the most often funded space-based missions due to their low technical complexity and budget constraints [17,91,92]. For very low-frequency astronomical observation, it is necessary to localize and characterize (in terms of its polarisation property) the emissions from various sources to understand the emission mechanism of the source [18]. Some of the astronomical phenomena like the Magnetic reconnection events, the Auroral kilometric radiations (AKRs), and atmospheric lightning are prominent in the very low-frequency bands and require source localization of a few degrees for in-depth study [116–118]. A space based radio telescope array can perform this using the triangulation method [119]; however, a single radio telescope will require co-located antenna configurations and gonio-polarimetric methods (DoA methods). Advances in antenna design and DoA methods/algorithms may overcome technological and economic obstacles. The widely known space projects employing gonio-polarimetric source localization methods are Cassini-RPWS, STEREO/WAVES, and NCLE [6,23,27]. DoA estimation is a technique for calculating the direction of an electromagnetic wave strongly reliant on the sensors' (antennas) orientation [120].

The antenna array methods are primarily used in developing methods for DoA estimation [121]. Multi-Signal Classification (MUSIC), Estimation of Signal Parameter via Rotational Invariance Technique (ESPRIT), Root-MUSIC, and Modified-ESPRIT are among the widely used antenna array method-based DoA estimators [97–99]. These approaches are based on the eigen-mode decomposition method wherein a co-variance matrix is generated utilizing spatial smoothing to attain an entire rank case. As a result, the DoA is well resolved while the technique is computationally complex [96]. Thus, these techniques require high computational resources, which is difficult in the case of in-situ computation. So, techniques with low computational complexity and adequate resolution are essential. Pseudo-vector-based DoA, Analytical inversion method, and MPM-based DoA are a few methods with low computational complexity. The Pseudo-vector-based DoA method estimates the EM wave direction by calculating a pseudo-vector using the spectral density tensor. This method is developed for tri-axial linear antenna configuration, wherein the antennas are arranged orthogonal to each other [95]. The analytical inversion method is developed for the STEREO/WAVES and Cassini-RPWS space missions [27]. This method is analytically derived using the correlation between the co-located antennas [27] and has low computational complexity. The analytical inversion method is developed for a specific antenna orientation and in-situ observations [23]. The Matrix Pencil Method based DoA (MPM DoA) is another method for estimating the DoA which directly operates on the obtained spectrum without estimating the

co-variance matrix depending on array configuration [4, 96]. This makes the MPM DoA method computationally light [96]. The MPM DoA technique, which needs a triaxial antenna design, finds the DoA of multiple waves falling on the antenna arrangement using a unitary transformation approach and the LSM [5, 6].

In this chapter, a Snapshot Averaged MPM (SAM) DoA algorithm is proposed, an improved version of the MPM DoA algorithm towards SEAMS mission (Section 4.2) along with the preliminary results of a proof of concept experiment performed for the DoA estimation. The SAM DoA algorithm introduces an averaging and polarisation detection method based on the boundary conditions and orientation of the antenna structure in space. This increases incoherent wave detection, simultaneously increasing the accuracy and capability to differentiate between different types of polarization. This modification allows one to study the polarisation characteristics of the emissions mechanisms at these radio frequency bands. To test the practicality of the results from the DoA algorithm, a laboratory experiment at the resonant frequency of the antenna (~ 72 MHz) has been performed. In addition, this polarisation detection capability can aid in several different remote sensing applications like synthetic aperture radar (SAR) and Vegetation monitoring [122, 123].

This chapter is organized so that Section 4.2 provides an overview of the SEAMS mission. Section 4.3 briefs about the principle of the EM wave direction and polarization detection. Section 4.3.1 and 4.4 present the DoA algorithm description along with the proposed modification and the simulation setup, respectively. Section 4.5 describes the analysis and results of the Snapshot Averaged Matrix Pencil Method (SAM) DoA algorithm, and section 4.6 demonstrates it at the resonant frequency of the antenna. Section 4.7 gives the Conclusion.

4.2 Space Electric and Magnetic Sensor(SEAMS)

SEAMS is a Radio telescope that is currently being designed to operate from 300 kHz to 16 MHz. The telescope will have three orthogonal electric and magnetic field sensors on board. The project's first phase is under development at SP Pune University, and Phase II will follow.

In the first phase, only electric field vector sensors will be used to measure RFI in low earth orbit. The system mainly consists of two orthogonal monopole antennas (electric field vector sensor, EFVS) as a proof of concept and as a precursor to Phase II, RF front end with matching network, filters, and gain stages for both arms and a two-channel data acquisition and analysis system with Telemetry-Telecommand interface. The first phase will be deployed in the Low Earth Orbit (LEO) on the 4th stage of the ISRO-PSLV rocket with the objectives of analyzing the acquired RFI from the Earth, detecting Auroral Kilometric Radiation (AKR), lightning in the atmosphere, intense solar bursts. This phase will also provide insight into the feasibility of using Commercial Off-The-Shelf (COTS) components to design LEO payloads and reduce production cost and up-gradation required for SEAMS phase 2. The SEAMS Phase-2 will have three orthogonal electric and magnetic sensors, and the payload will be placed on the far side of the Moon or in the Moon-Earth L2 to avoid the RFI from Earth.

4.3 DoA Estimation Method

Analysis of the spectral density tensor ($S = \vec{E}\vec{E}^{\dagger}$) can provide the direction and polarisation of the EM wave based on the field vector in Eq (4.1). Based on the Gell-Mann *SU(3)* matrix, the anti-symmetric part of S can be converted into a dual pseudo-vector containing information about the EM wave's direction and polarization[95].

$$\vec{E} = e_x\hat{a_x} + e_y\hat{a_y} + e_z\hat{a_z} \tag{4.1}$$

The pseudo-vector ($\vec{V}$) associated with the spectral density tensor (Eq. (4.2)) is a parallel vector to the wave vector k and represents a three dimensional analogy of Stokes parameter V (of the I, Q, U, and V) [6, 94, 95].

$$\vec{V} = -2Im[e_y e_z^* \hat{a_x} - e_x e_z^* \hat{a_y} + e_x e_y^* \hat{a_z}] \tag{4.2}$$

Thus, the DoA of the EM wave (i.e., azimuth and elevation angle) is determined in the spherical coordinate system (See Eq. (4.3)). The polarization of the EM wave can be estimated by normalizing the magnitude of $\vec{V}$ with respect to the three-dimensional analogy of the Stokes I parameter (i.e., $polarization = |\vec{V}|/I$ where $I = e_x e_x^* + e_y e_y^* + e_z e_z^*$) [5]. This results in a value between 0 to 1 where 0 signifies completely linear polarization (LP) and 1 signifies completely circular polarization (CP).

$$\vec{V} = v \cdot (sin\theta cos\phi\ \hat{a_x} + sin\theta sin\phi\ \hat{a_y} + cos\theta\ \hat{a_z}) \tag{4.3}$$

Here, θ and ϕ represent the Elevation and Azimuth angles and can be rewritten as [6]

$$\begin{aligned} \theta &= arccos(V_z/|\vec{V}|) \\ \phi &= \begin{cases} \arctan(V_y/V_x) + \pi/2, & \text{if } V_x < 0 \\ \arctan(V_y/V_x), & \text{if } V_x > 0 \end{cases} \end{aligned} \tag{4.4}$$

4.3.1 Algorithm description

A single element of a tri-dipole or a tripole receiving N incoherent EM waves is expressed as

$$s_{x'}(t) = \sum_{n=1}^{N} C_{x'}^n e^{i\theta_{x'}^n} e^{i\omega^n t} + n(t) \tag{4.5}$$

where $C_{x'}$, $\theta_{x'}$, and ω are the amplitude, phase, and frequency of the incident incoherent EM wave on the antenna along the x' axis, which is aligned at an angle to the reference axis [Sec. 4.4]. Then, the sampled signal will be represented as

$$S_{x'}[k] = \sum_{n=1}^{N} (C_{x'}^n e^{i\theta_{x'}^n} e^{i\omega^n t_0}) e^{i\omega^n k\delta} + n(t_0 + k\delta) \tag{4.6}$$

where, $S_{x'}[k]$ is a discretized signal containing N incoherent EM waves, $(t_0 + k\delta)$ represents the sampling time, $n(t_0 + k\delta)$ is noise, δ is the sampling period, and ω^n represents the angular frequency of the n^{th} incoherent wave. To compute the complex amplitude of the received EM wave and obtain the DoA using Eq. (4.2), the best estimations of N and ω^n must be found. Therefore, the developed algorithm estimates the emission frequency of the incident incoherent wave. A flow chart of the SAM DoA algorithm and its predecessor is shown in figure 4.1. The following is the description of the developed algorithm:

- The acquired signal from each antenna is averaged for n snapshots by calculating the average value of the phase difference between the antennas.

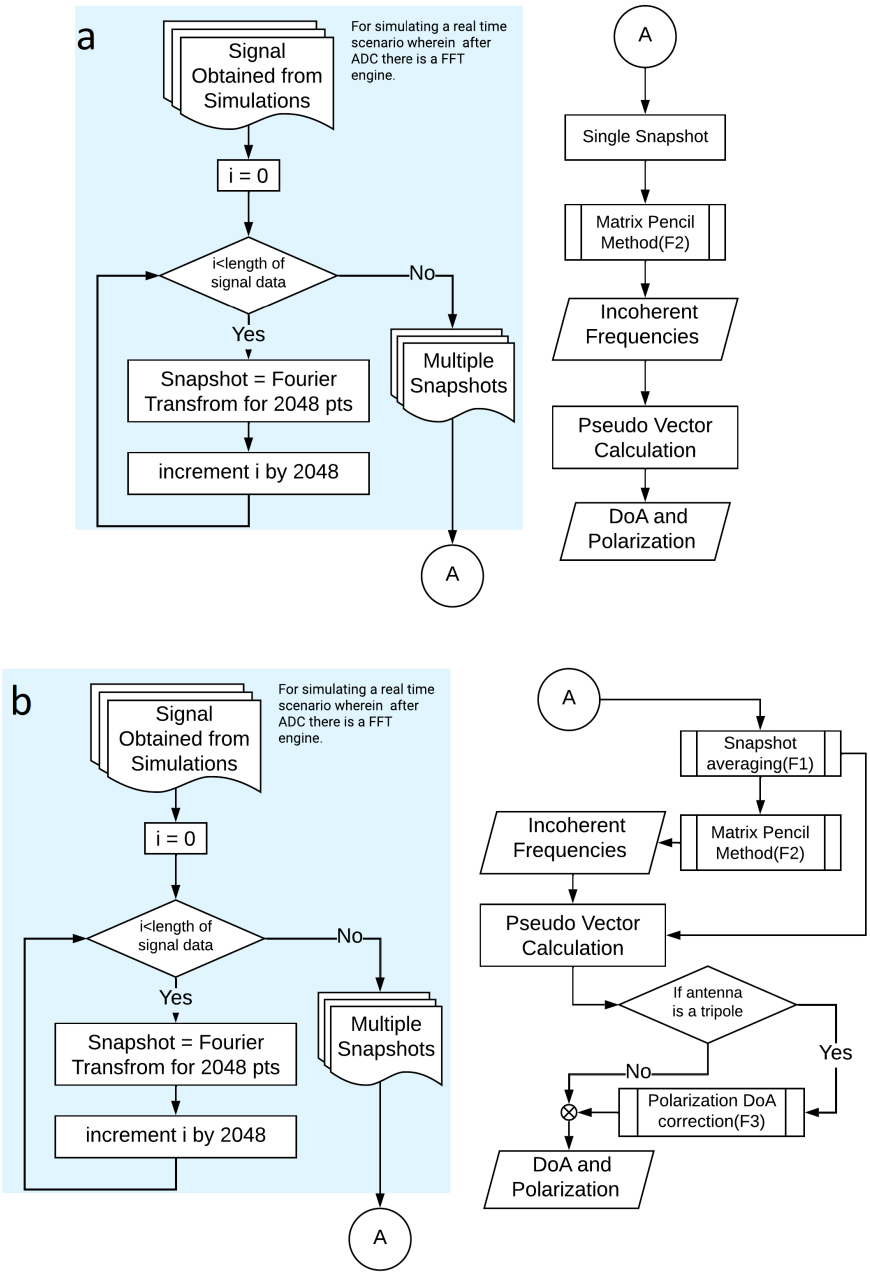

Figure 4.1: Estimation Algorithm Flowchart - (a) MPM DoA algorithm, (b) Modified-MPM DoA algorithm. Both the algorithm use Matrix pencil method (F2) [4] to estimate the number of incoherent waves and angular frequency [5, 6]. In the modified algorithm (shown in (b)) two modifications are introduced (1) Snapshot averaging algorithm (F1) and (2) Polarization, DoA correction (F3).

- after that, to reduce the computational cost, a beam forming addition [6] of snapshot aver-

aged signal is implemented.

- In order to estimate the N incoherent frequencies MPM [4–6,96] is used and is summarised in Appendix B.
- The N incoherent frequencies ω^n obtained from the MPM are then used to find the complex amplitudes for each axis using a constrained LSM. The prior phase information from the averaging method is provided to the constrained LSM. The least square method calculates the $min(|KF_i - S_i|^2)$ such that $Qp \leq F_i$ where K is a matrix of dimension $M \times M$ as the signal consists of M samples $(M = 0, 1, 2, ..., M-1)$, F_i is the complex amplitude matrix, S_i is the spectral density matrix, p is the prior phase information from averaging method, and Q is the amplitude matrix.
- Then the DoA is calculated using the pseudovector formulation $\vec{V} = -2\{A_y A_z sin(\delta_y - \delta_z)\hat{a_x} - A_x A_z sin(\delta_x - \delta_z)\hat{a_y} + A_y A_z sin(\delta_x - \delta_y)\hat{a_z}\}$ and by considering equations (4.2) and (4.4), as well as the detection of polarization ($P = |\vec{V}|/I$) and the plane wave direction constraints in our simulation setup (i.e., azimuth $[0°, 360°)$ and elevation $[0°, 90°]$). There is only one case where V_z is negative: when the incident wave has a LHCP. Since polarisation is defined as $P = |\vec{V}|/I$, the P range is limited to $[0, 1]$. As a result, the method will be limited to distinguishing between LP and CP. To increase the algorithm's polarisation detecting capacity, the polarization finding equation is updated to Eq. (4.7).

$$P = \begin{cases} |\vec{V}|/I, & \text{if } V_z > 0 \\ -|\vec{V}|/I, & \text{if } V_z < 0 \end{cases} \tag{4.7}$$

4.4 Antenna and Simulation Setup

Two types of antenna configurations were simulated for the testing of the DOA algorithm with the SEAMS mission: (1) triaxial dipoles (Tri-dipole) and (2) triaxial monopoles (Tripole). In the Tri-dipole and Tripole configurations, the dipoles and monopoles are ∼2 m and ∼1 m long, respectively. The antenna length should be adjusted according to the active matching network's sensitivity or operating frequency [124]. As illustrated in Figure 4.2, the triaxial and monopole comprise three mutually orthogonal co-located dipoles and monopoles. The dipoles or monopoles are orientated along the x', y', and z' axes, with each subtending an angle of 35.3° [1]. Equation (4.8) describes the connection between the unit vectors associated with the antenna axes (x', y', and z', from the antenna frame) and the frame axes or global axes (from the reference frame) [2].

[1] 35.3° is the angle between each monopole and the ground plane. This is derived by equating all the direction cosines of the monopoles (See Appendix E).

[2] Here the coordinate setting is such that each orthogonal monopoles subtends an angle of 35.3° with the ground plane (x-y plane). One can consider the new locations of the monopoles as the new local coordinates. The relationship between the local and the reference coordinate is given by equation 4.8.

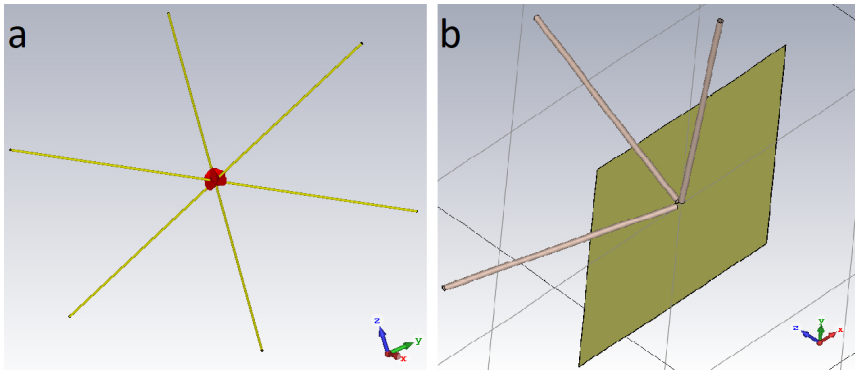

Figure 4.2: Antenna configurations - (a) Tri-Dipole - 3 orthogonal co-located dipoles and (b) Tripole - 3 orthogonal co-located monopoles

$$\begin{aligned}
\hat{a_x} &= \frac{\hat{a_{x'}}}{\sqrt{3}} - \frac{(3+\hat{\sqrt{3}})a_{y'}}{6} + \frac{(3-\hat{\sqrt{3}})a_{y'}}{6} \\
\hat{a_y} &= \frac{\hat{a_{x'}}}{\sqrt{3}} + \frac{(3-\hat{\sqrt{3}})a_{y'}}{6} - \frac{(3+\hat{\sqrt{3}})a_{y'}}{6} \\
\hat{a_z} &= \frac{\hat{a_{x'}}}{\sqrt{3}} + \frac{\hat{a_{x'}}}{\sqrt{3}} + \frac{\hat{a_{x'}}}{\sqrt{3}}
\end{aligned} \tag{4.8}$$

The field vector $\vec{E}$ (Eq. (4.1)) is characterized in the reference frame axes according to the antenna orientation, and the field vector components in the reference frame are recast in terms of the field vector components in the antenna frame using Eq. (4.8).

$$\begin{aligned}
e_x &= \frac{E_{x'}}{\sqrt{3}} - \frac{E_{y'}(3+\sqrt{3})}{6} + \frac{E_{z'}(3-\sqrt{3})}{6} \\
e_y &= \frac{E_{x'}}{\sqrt{3}} + \frac{E_{y'}(3-\sqrt{3})}{6} - \frac{E_{z'}(3+\sqrt{3})}{6} \\
e_z &= \frac{E_{x'}}{\sqrt{3}} + \frac{E_{y'}}{\sqrt{3}} + \frac{E_{z'}}{\sqrt{3}}
\end{aligned} \tag{4.9}$$

where, e_x, e_y and e_z is the field vector components in reference frame, and $E_{x'}$, $E_{y'}$, and $E_{z'}$ are the field vector components in the antenna frame [94].

In addition, the antenna configuration is designed and simulated using the CST antenna design software with a plane wave as an excitation source. This is analogous to a free-space environment with no RFIs or noise. The simulation was carried out for plane waves arriving from various directions at different frequencies in the sub 20 MHz band (300 kHz - 16 MHz) and with varying polarizations. As the SEAMS mission will be deployed on the far side of the moon, a side of the antenna will always face the moon. Even though the satellite will be on the far side of the moon, low-level RFIs and reflections from the moon's surface will cause noise in the system [14,125]. If the tripole antenna always faces the sky with its ground towards the moon, it can lessen the effect of the noise and RFI. Thus, the plane wave direction in the simulation is constrained to the azimuth - $[0°, 360°)$ and elevation - $[0°, 90°]$ since the moon is on one side of the antenna arrangement with the other side facing space.

4.5 Simulation Results and Discussion

As discussed in the above section (4.4), the antenna configuration simulation is performed for 1000 trials with RHCP and LHCP. The data set generated by the antenna simulation has a unique frequency. To simulate multiple incoherent frequencies, the noise of different Signal Noise Ratio (SNR) values (1 to 30 dB) is added to the time domain data. The performance of the DoA algorithm is evaluated using the following criteria:

1. Singular Value Ratio (SVR)[3] response with change in SNR,
2. SVR response with change in number of incoherent sources.
3. Root Mean Square Error (RMSE $= \sqrt{N^{-1}\Sigma_{i=1}^{N}(x_{estimated} - x_{actual})^2}$) of azimuth and elevation angles with change in SNR,
4. RMSE of azimuth and elevation angles with change in N, and
5. A polarization detection table.

In order to evaluate the algorithm, first, a CST simulation was carried out using a plane wave excitation, and the output voltage from the simulations was recorded. The simulation was performed at high time resolution such that the difference in the phases and amplitudes of the received signal is visible when plotting time domain data as shown in Figure 4.3(a); Figure 4.3(b) and 4.3(c) show the Amplitude and phase of the signal in the frequency domain. The simulation results shown in Figure 4.3 were obtained for RHCP plane wave with frequency 15 MHz approaching from $+z$ direction. The propagation vector of the plane wave will subtend an equal angle with all the antennas of the tripole and the tri-dipole given our antenna orientation (Section 4.4). Thus, the voltage induced on each antenna should be 120° out of phase with each other, and the same is observed from the simulation as shown in Figure 4.3(a). This phase difference is more distinct in the Figure 4.3(c) - phase of the Fourier spectrum. Furthermore, the signal received by both antenna configurations is observed to be the same.

The data obtained from the simulation are then contaminated with noise. After that, the noisy signal is used in the DoA algorithm to find the direction and polarization of the incident wave. As discussed in the section (4.3.1), N and ω^n should be estimated first using the MPM. To evaluate the efficiency of the algorithm, SVR is determined, which is the ratio of the eigenvalues obtained by decomposing Γ_R (σ_N/σ_{N+1}) [6, 126]. This singular value obtained due to the decomposition of the Γ_R will gradually decrease depending on the number of incident waves. Thus, as per the definition of SVR, the higher the value of the SVR, the better the estimation of N and ω^n [6, 126].

Figure 4.4(a) and 4.4(b) shows the effect of the change in SNR and N on the SVR response of the SAM DoA algorithm and MPM DoA algorithm. It is observed that the SVR value increases with the SNR value, which is as expected. It is also noticed from Figure 4.4(a) and 4.4(b) that the increase in the incoherent waves or frequency reduces the SVR value. This indicates that detecting an incident incoherent wave would be difficult for multiple incident waves. Furthermore,

[3]The SVR factor is the summation of the ratio between the consecutive values of the eigenvalues obtained from Singular value decomposition (SVD). This is a good measure for testing the algorithm's performance because the order of eigenvalues in the SVD is arranged from the most prominent feature in the signal to the least prominent feature. If there are a few incidents of incoherent waves, then the change observed in the consecutive eigenvalues will be abrupt or steep. If the ratio between the consecutive eigenvalues is high, it means that the signal can be detected easily.

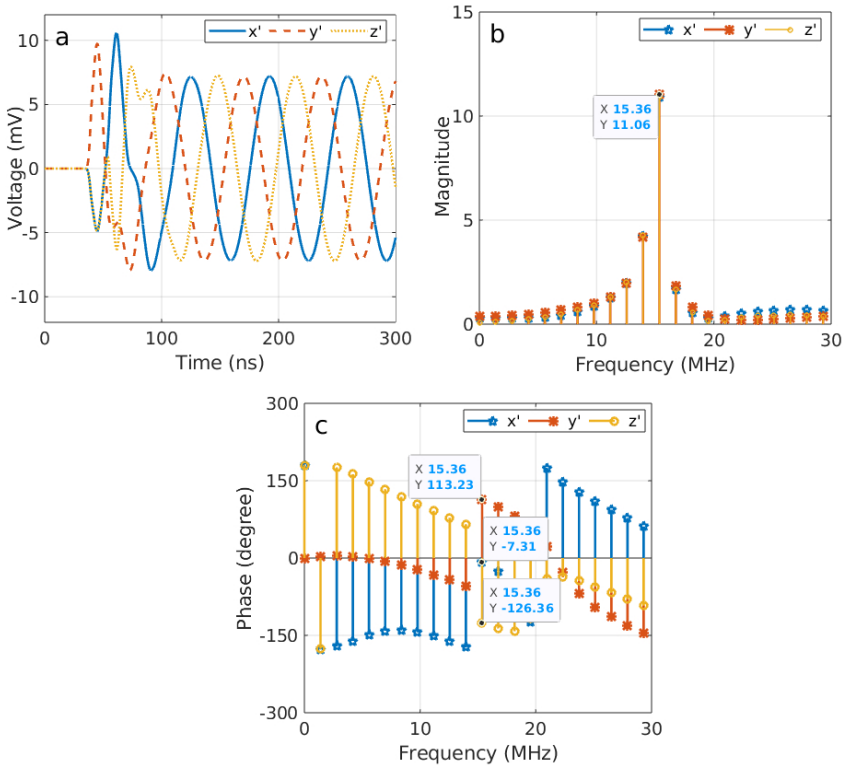

Figure 4.3: (a) Time domain Voltage readings, (b) Magnitude and (c) Phase of the Frequency spectrum of the CST simulation of antenna structure shown in Figure 4.2 for RHCP plane wave excitation of 15 MHz.

it is observed that the SAM DoA algorithm improves the SVR response with respect to changes in the SNR, along with an increase in the number of incoherent waves. From Figure 4.4(b), it is observed that increasing the number of snapshot averages improves the SVR value. Thus, the SAM DoA method provides flexibility in increasing the SVR value by averaging a large number of snapshots.

The accuracy of detecting the direction and the polarization is shown in Figure 4.4(c), 4.4(d), and Table 4.1. As discussed in the above section (4.4), the simulation is only performed for the plane wave direction in the range of azimuth 0° to 360° and elevation 0° to 90°. In this case, it was observed that the RMSE decreases when SNR increases, as expected. It is also observed that the error in the direction estimation increases with increased incoherent frequencies in the signal. However, it is to be noted that the RMSE of the SAM DoA algorithm has significantly improved for a large number of averaged snapshots. Hence, if the number of snapshots to be averaged increases, the direction detection will improve. This improvement in detection can also be observed in Figure 4.5, representing the response of SVR and RMSE with respect to an increase in the number of averaged snapshots. In the figure, the single RMSE value or the effective RMSE_{eff} for multiple incident incoherent wave is calculated by $\text{RMSE}_{eff} = \sqrt{\sum_{i=1}^{N} RMSE_i}$ where RMSE_i is an error due to individual waves. Also, the improvements mentioned can also be observed in Figure 4.6 wherein polar plot images for nine incoherent sources have azimuth along the perimeter and elevation along the concentric circles. Figure 4.6(b) shows the polar plot of the estimated DoA

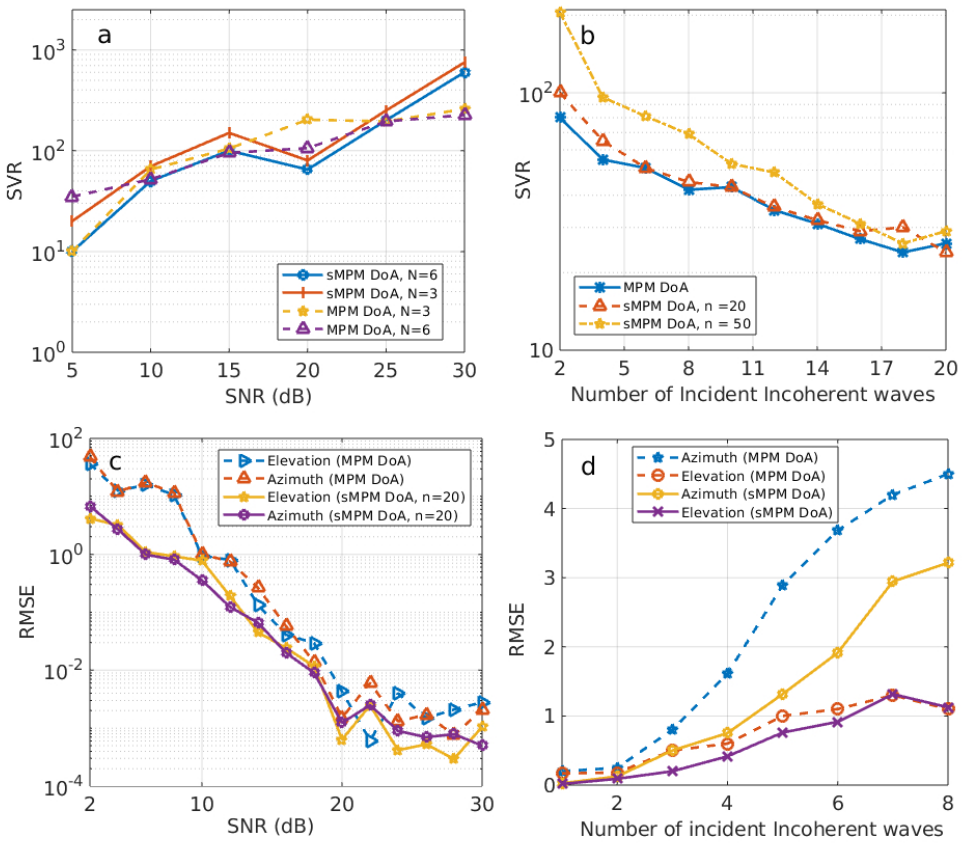

Figure 4.4: Comparing the performance of the MPM DoA and the proposed SAM DoA estimation. (a) Effect of variation of the SNR on the SVR, a measure of efficiency of the DoA algorithm when estimating N and ω^n if the number of incoherent wave incident on the antenna configuration is $N = 3$ and $N = 6$; (b) Effect of the change in the incident incoherent wave on the SVR at SNR = 15dB and $n = 20$; (c) Effect of the SNR on the detection of the direction of the Radio wave by estimating RMSE and the number of snapshots averaged in the SAM DoA estimation is $n = 20$; (d) Effect of the change in incident incoherent wave on the detection of direction of the Radio wave with $n = 20$ in the SAM DoA estimation and SNR = 15 dB.

for SAM DoA shown for SNR = 15 dB for nine incoherent frequencies from different directions with several snapshots averaged is 50. By comparing the images in Figure 4.6(a) and 4.6(b), it is noticed that the area of the estimated DoA is reduced.

Table 4.1 illustrates the improvement in the detection of the polarization due to the modified algorithm introduced by equation (4.7). From the table it is clearly observed that the SAM DoA algorithm is capable of differentiating different polarization.

Table 4.1 shows that the MPM DoA algorithm can only distinguish between Linear, Circular, and Elliptical Polarization, while the improved SAM DOA method can identify all forms of polarization. Table 4.2 compares the computational complexity of various methods such as Analytical Inversion Method [27], Pseudo-vector based method [95], and MPM DoA method [5, 6]. The computational complexity is calculated by considering the processes involved, such as Fourier transformations,

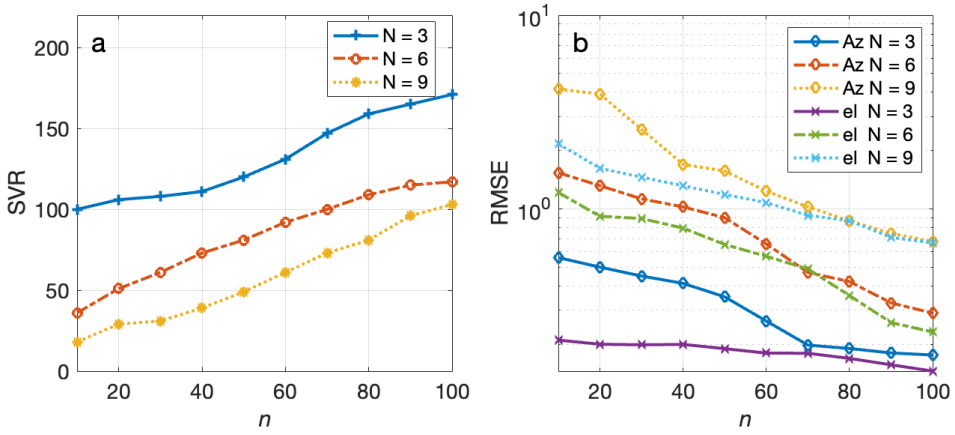

Figure 4.5: Response of SAM DoA estimation with change in number of incoherent wave (N) and number of averaged snapshot (n). (a) SVR response with change in the n; (b) RMSE response with respect to n.

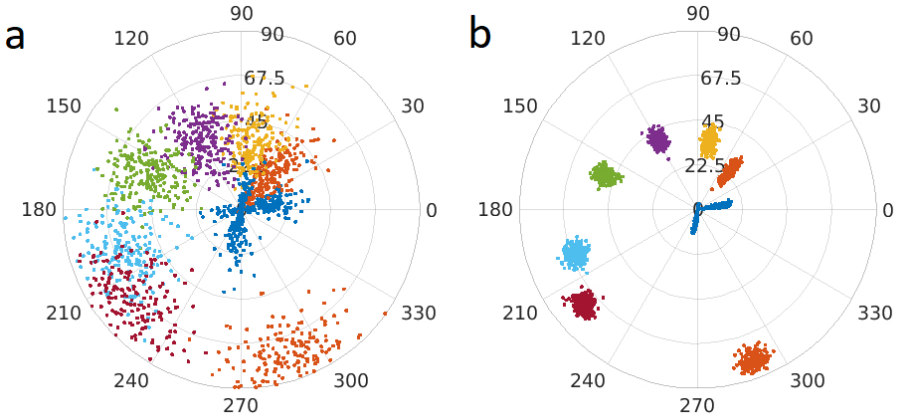

Figure 4.6: Polar representation Azimuth and elevation angles of the estimated DoA for 9 incoherent frequencies incident on the antenna simultaneously from different directions of the radio sources at SNR of 15 dB. (a) shows the DoA plot for MPM DoA method and (b) shows the plot for SAM DoA method for $n = 50$.

correlations, SVD. This is done by studying the formulation of these algorithms. Table 4.2 shows that the SAM DoA is computationally more complex, and the accuracy of estimation is the highest for this method. In addition to this, the SAM DoA algorithm provides a flexible parameter n (i.e., average points), and increasing this parameter increases the accuracy of the estimation (Figure 4.4) as well as the computational time. This parameter is a loop parameter; therefore, it will not add to the algorithm's complexity but will affect the computing time.

4.6 Setup and Result of a scaled experiment

To test the algorithm, a proof of concept scaled version of the DoA experiment was carried out at the antenna's resonant frequency (length $\geq$ 1 m). This setup consists of a prototype of the

N	SNR (in dB)	Actual Polarization of the incident waves	Detected Polarization (MPM DoA)	Detected Polarization (SAM DoA)
3	10	1 RHCP, 1 LHCP, and 1 LP	2 EP, and 1 LP	1 RHEP, 1 LHEP, and 1 LP
3	30	1 RHCP, 1 LHCP, and 1 LP	2 CP, and 1 LP	1 RHCP, 1 LHCP, and 1 LP
10	10	2 RHCP, 2 LHCP, and 2 RHEP, and 2 LHEP, and 2 LP	8 EP, and 2 LP	4 RHEP 4 LHEP, and 2 LP
10	30	2 RHCP, 2 LHCP, and 2 RHEP, and 2 LHEP, and 2 LP	3 CP, 5 EP, and 2 LP	2 RHCP, 1 LHCP, 2 RHEP, 3 LHEP, and 2 LP

Table 4.1: Polarization detection table describing the classification of the detected polarization by the MPM DoA algorithm and SAM DoA algorithm. Here N is the number of incident incoherent waves.

tripole antenna arrangement fabricated using a ∼1 m long monopoles with resonance at ∼72 MHz. The experiment is performed using a fabricated tripole antenna as receiving element (T_{RX}) and a synthetic radio source made of an aerial antenna (Nooelec monopole antenna) that transmits a monotone signal (at 72 MHz) generated by an RF generator from a known direction (Azimuth (Az) and Elevation (El)). Figure 4.7 shows the block diagram of the experimental setup. The fabricated antenna is shown in Figure 4.8. Figure 4.9 shows the arrangement of the scaled experiment. In this setup, a synthetic source is formed using a Keysight RF generator N5173B producing a monotone signal at 72 MHz with +10 dBm power, connected to the aerial antenna. The receiving system consists of a tripole antenna connected directly to a digital storage oscilloscope (DSO) via RF cable to keep the phase distortions due to inline components (like amplifiers and filters) to a minimum.

Figure 4.10 and 4.11 show the tripole antenna's reflection coefficient (S_{11}) and Radiation Impedance of each element in the configuration demonstrating its resonance at ∼72 MHz. This experiment was performed utilizing minimum circuit components since adding the circuit components would contaminate the received signal phase (see Appendix G).

The dataset of this experiment has been recorded with the sampling a frequency of 8 GHz in the DSO. The dataset is then down sampled by a factor of 4 to improve the frequency resolution (F_r) of the data. The resultant $F_s = 2$ GHz corresponds to $F_r = 0.98$ MHz for 2048 point FFT.

Figure 4.12, 4.13, and 4.14 shows the received signal in time domain and frequency domain for the

Features	Analytical Inversion Method	Pseudo vector estimation based DoA	MPM DoA Method	SAM DoA Method
Direction Estimation Error **(RMSE)** (SNR=∼15 dB)	$< 6°$	$> 10°$	$< 1°$	$< 0.5°$
Maximum Computational Complexity	$O(5N^3 log_2 N + 88N + 20N^2)$	$O(3N log_2 N + 4N^3)$	$O(3N log_2 N + (N-L)(L+1) + (M-L)^2(2L+2) + (N-L)^4)$	$O(3n^2 N log_2 N + (N-L)(L+1) + (M-L)^2(2L+2) + (N-L)^4 + N(n^2+1))$
Required Computational time	0.135s	0.104s	1.53s	1.76s
Polarization detection	Yes	Yes	Yes	Yes
Differentiation between LH and RH polarization	No	No	No	Yes
Space mission for which algorithm is Proposed	Cassini - RPWS and STEREO WAVES	-	NCLE	SEAMS
References	[27]	[95]	[5], [6], [93]	Current work

Table 4.2: Performance of SAM DoA with other proposed algorithms. Four algorithms are compared with the SAM DoA method with respect to its Estimation error, Computational complexity, Detection capability of polarization. The estimation error is reported for single source with SNR of 15 dB. The approximate value of the Maximum computational complexity is calculated by referring to the algorithm description provided in the articles mentioned in the reference row. The required computational time is calculated for clock speed - 1 ns, matrix size N=300, pencil parameter L=100, and average points n = 20. Here, the Estimation error (RMSE) is estimated for 1000 trials at SNR = 15 dB.

synthetic source located at Az/El of $\sim 197°/\sim 24°$, $210°/29°$, and $\sim 41°/\sim 51°$. It is evident from the time and frequency domain plots in figures 4.12 to 4.14 that the amplitudes and the phases received by the three elements in the antenna are different [4]. It is observed that there is an abrupt jump in the received signal phase. This phase jump may be related to the received amplitude of

[4]The URL - "https://drive.google.com/file/d/1OAucbplms8-BHGGEKt25l1jOLRERDYIo/view?usp=sharing" contains a video showing the phase shift in the received signal if the source is mobile.

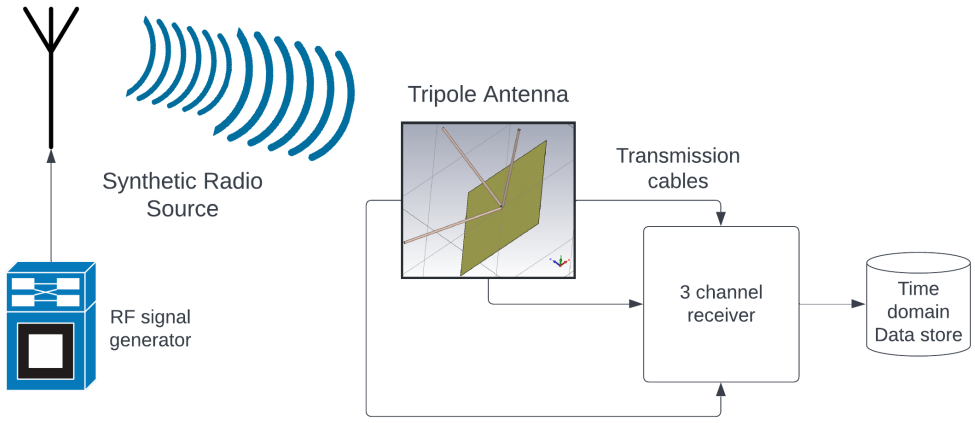

Figure 4.7: A Block diagram of the experimental setup. A high frequency oscilloscope (DSO - 100 kHz to 2 GHz) is used to record the time domain data in this setup.

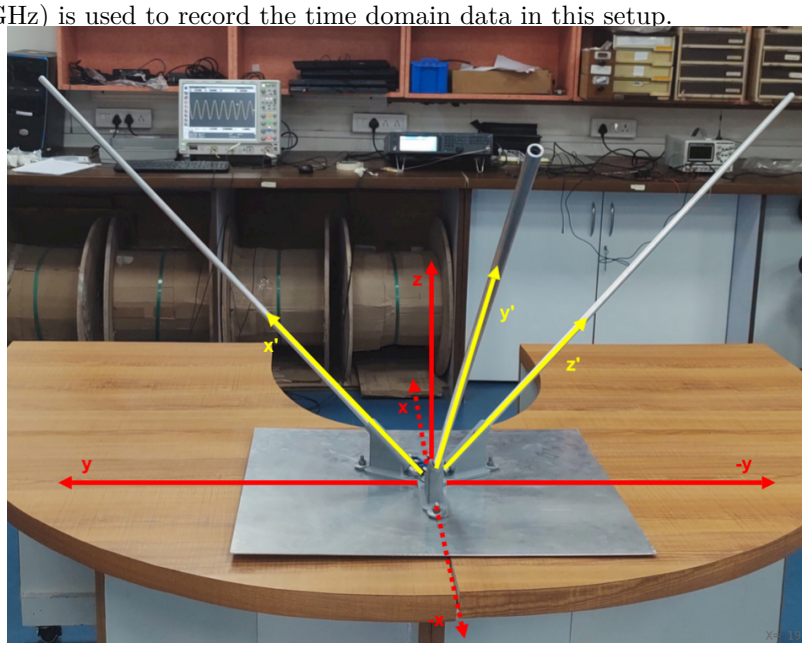

Figure 4.8: Fabricated tri-axial monopole resonant at ∼72 MHz with orthogonal antenna axis x', y', z' and reference plane axis x, y , z.

the signal. For example, in Figure 4.12(a), the x' and z' antennas have the highest and the smallest amplitude. Correspondingly, the highest and lowest step jumps as shown in Figure 4.13(b) and Figure 4.13(d), respectively. The stated phenomenon can be observed in this laboratory test's readings from all three directions. Based on the discussion in section 4.3 and 4.5, it is shown that the difference in amplitude and phases between the antennas is utilized for estimating the DoA. From figures 4.12 to 4.14, it is observed that the direction of the sources causes a change in the amplitude and phases of the received signal. In the estimate algorithm, the phase distortion caused by the antenna and the transmission cable impedance has to be considered (see Appendix G). Oscilloscope calibration with the transmission cable has been performed to account for reading errors by the oscilloscope and the phase error due to the transmission cable. This removed the

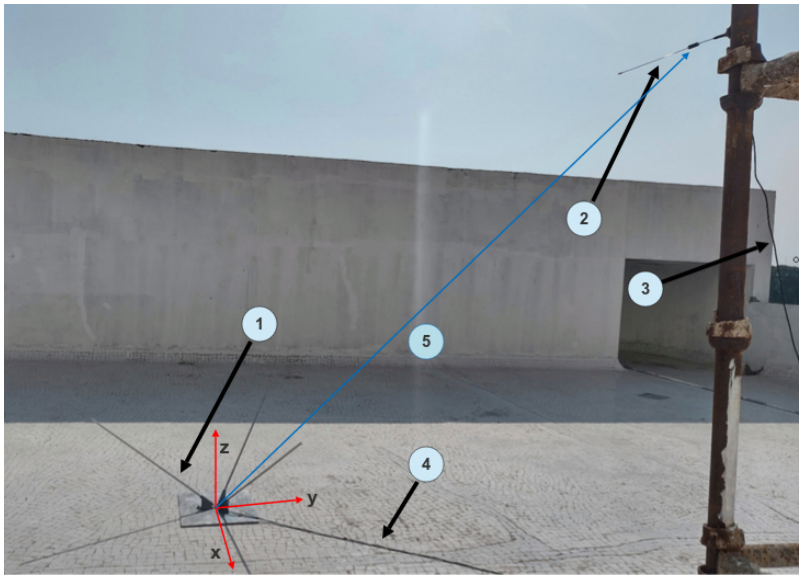

Figure 4.9: An image describing the experimental arrangement where, (1) is the Fabricated tripole antenna, the red arrows denotes the reference axis (x, y, z) and (2) is the synthetic source constitutes of a monopole and a RF generator (Keysight N5173B) set at frequency of 72 MHz and power of 10 dBm. (3) shows the RF line which connects monopole and RF generator. The data from the tripole at (1) is carried by RF line shown by (4) and is received using a DSO (Keysight Infinium DSO9254A). (5) indicates line of sight of the source which is at located at Az/El - ∼41°/∼51° from the reference axis displayed in the image.

losses due to the cable impedance as it has been calibrated along with the oscilloscope. Thus, the algorithm was modified to consider phase distortion caused by antenna impedance.

Table 4.3 shows the estimated DoA for two different sources radiating at 72 MHz with LP. The table also shows a comparative estimation between the Pseudovector estimation-based DoA method [95], MPM DoA method [4–6, 96], and SAM DoA method. In the experiment, the signal is transmitted at the resonant frequency with a power of +10 dBm having SNR of > 60 dB; it is observed that the error in the estimation is between 0 - 6° which is high for the given SNR. However, all the DoA methods could characterize the EM wave as LP. The significant estimation error might be due to several factors affecting the experiment, such as multi-path and nonplanar wavefront, due to the source being close to the receiving antenna and the laboratory's RFI environment. A detailed study is required to understand the effect of physical or environmental parameters on the DoA estimation and hardware. Similar efforts have been made to understand the arrival of waves from Saturn Kilometric Radiation by [23]. It is intended to carry out an elaborate experiment at our desired frequency band. The SEAMS antenna will be active, as discussed in section 4.4. Thus, phase contamination in the received signal by the matching network of the antenna has to be adjusted as per its frequency response (described in Appendix G).

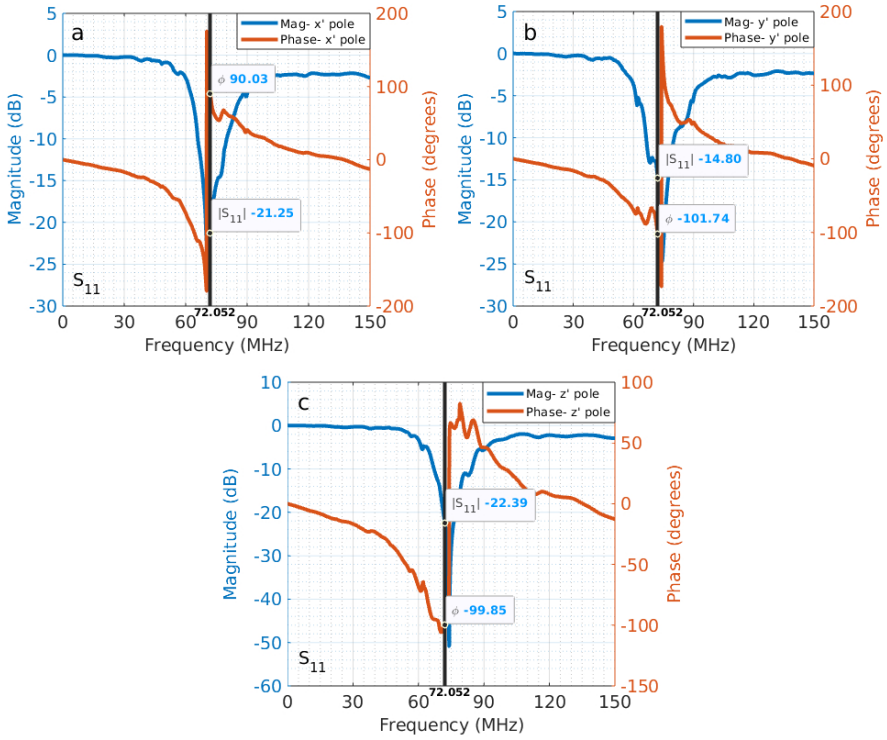

Figure 4.10: Complex Reflection coefficient measurement of all the monopole elements in the tripole antenna wherein, the black vertical marker shows the resonance frequency of 72 MHz.

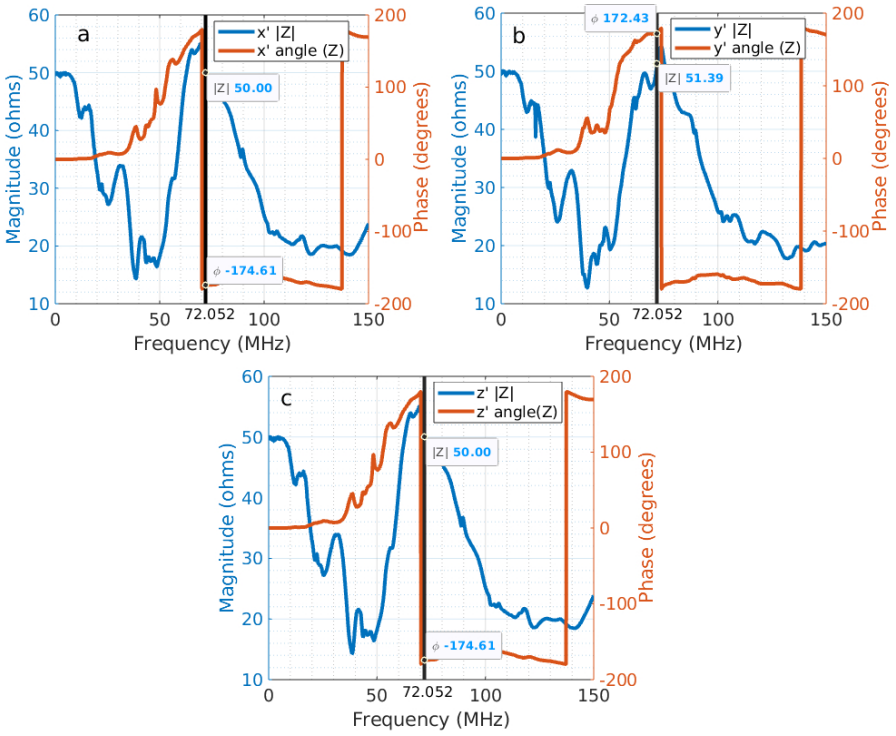

Figure 4.11: Radiation Impedance of all the elements in the tripole antenna along the local reference axis x', y', and z' as illustrated in Figure 4.8.

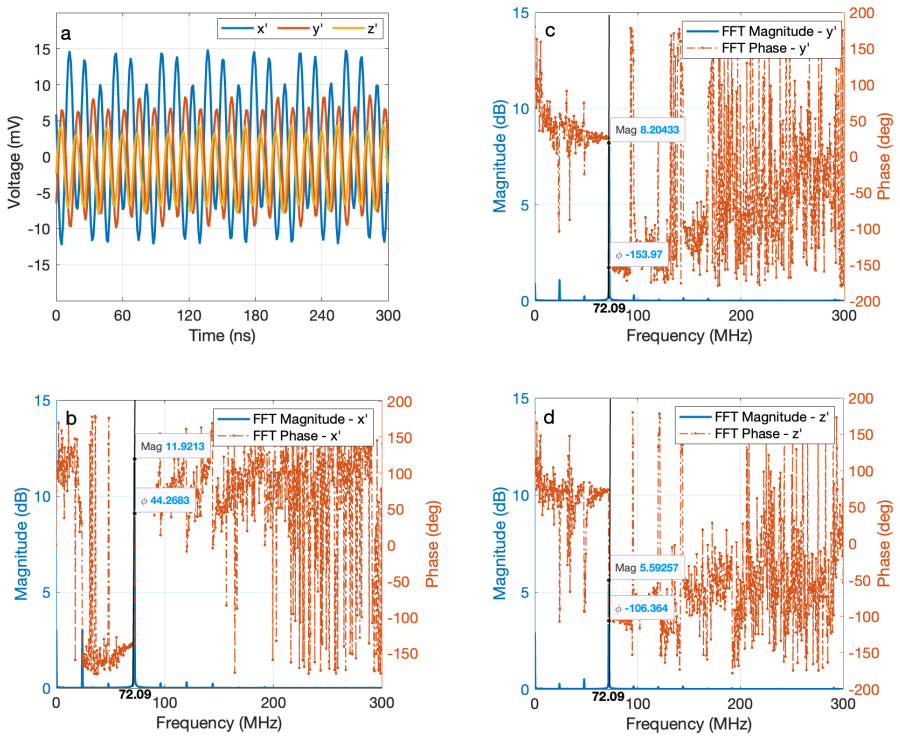

Figure 4.12: Signal received from a synthetic source of ∼72 MHz having Azimuth of ∼ 197° and elevation of ∼ 24°. Here, (a) shows high time resolution voltage values received from the source using the Tripole, (b) to (d) shows the Amplitude and phase of the received signal in frequency domain by the tripole antenna along the local reference axis x', y', and z' as illustrated in Figure 4.8.

Algorithm	Estimated Az/EL	Actual Az/El
Pseudovector estimation based DoA method [95]	212°/15°	
MPM DoA method [4–6, 96]	202°/18°	∼ 197°/∼ 24°
SAM DoA method	202°/18°	
Pseudovector estimation based DoA method [95]	207°/32°	
MPM DoA method [4–6, 96]	213°/31°	∼ 210°/∼ 29°
SAM DoA method	212°/31°	
Pseudovector estimation based DoA method [95]	43°/48°	
MPM DoA method [4–6, 96]	40°/52°	∼ 41°/∼ 51°
SAM DoA method	40°/52°	

Table 4.3: A comparison of the DoA obtained from the Experiment using different methods applicable to SEAMS antenna configuration. The test has been carried out for three different radiation directions at resonant frequency. The "Estimated Az/El" coloumn contains the estimated DoA by the algorithms and the "Actual Az/El" column shows the physically measured DoA of the source. The emitted signal was of LP and has been detected in all the algorithm as LP; the SNR for this experiment was $> 60\,\mathrm{dB}$.

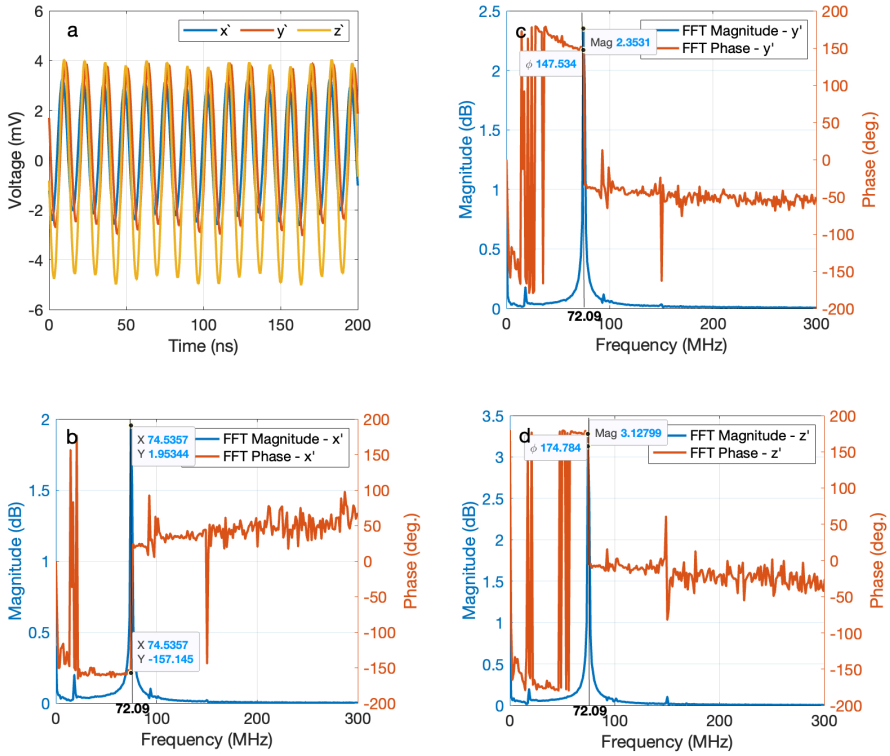

Figure 4.13: Signal received from a synthetic source of ∼72 MHz having Azimuth of ∼ 210° and elevation of ∼ 29°.

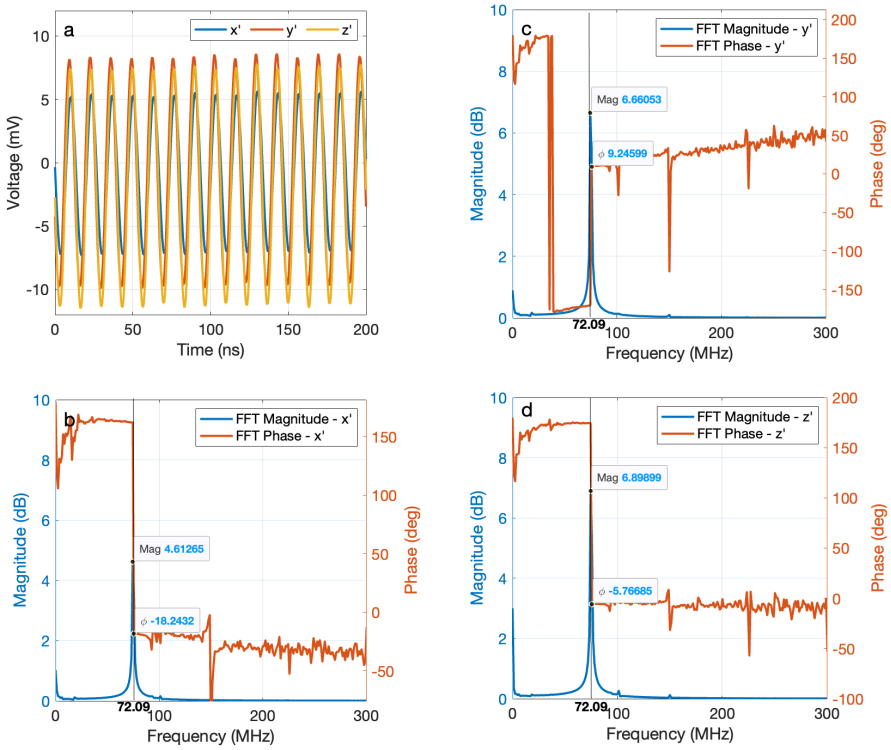

Figure 4.14: Signal received from a synthetic source of ∼72 MHz having Azimuth of $\sim 41^\circ$ and elevation of $\sim 51^\circ$.

4.7 Conclusion

An optimized MPM DoA estimation algorithm by the addition of an averaging and polarization detection method (SAM DoA) is described in this paper (see Table 4.2). The averaging algorithm estimates the mean of multiple FFT snapshots before applying the MPM to reduce noise and improves the estimation of the incoherent frequencies in the given spectra. The Polarization detection method enabled the detection of different polarisations (Table 4.1). With these improvements, the algorithm has become adaptable to respond to increased incident incoherent waves. In addition, this algorithm has multiple applications in remote sensing where the polarisation of the reflected wave is important, as in the case of agriculture, cracks in materials, etc. [122, 123].

The present analysis elaborates on the simulation with tri-dipole and tripole antenna configurations. The simulation results show that the signal received by both configurations is the same, considering the direction constraints of our simulation setup. This will be used in the SEAMS mission, which is proposed as an orbiter mission for the far side of the moon, and the antenna for such low frequencies will be active. Table 4.2 summarizes the comparison of performances for four different DoA algorithms (including SAM) relevant to SEAMS. The advantage of SAM is that performing the snapshot averaging toward the target source increases the sensitivity of detection even in the presence of other bright sources within the field of view of SEAMS.

The total computational complexity of SAM DoA has increased when compared with the other algorithms (Table 4.2). However, the computational cost remains lower than that of well-known algorithms such as MUSIC, M-MUSIC, MP-MUSIC, ESPRIT, and many more [127]. The choice of modifications in the algorithm is made such that the computational cost remains low and most of the processing can be performed by the onboard computational devices or FPGA. This is necessary due to the data transfer limitations in space [128]. SAM's low computational complexity and increased sensitivity make it more suitable for SEAMS as the onboard computing resources will be limited.

A proof of concept scaled experiment of DoA carried out in our laboratory at the resonant frequency of the antenna validated the feasibility of detection of DoA by utilizing a triaxial antenna configuration. However, extensive tests are required to test the performance of different algorithms. In the laboratory experiment, the observed phase variations before and after the received frequency (Figure 4.12 to 4.14) could be due to the noisy environment or test equipment used. In order to better understand the phase variations, the data needs to be recorded using a sensitive data logger's ADC dump and then analyzed.

Chapter 5

Exploring the Triaxial antenna configuration for DoA applications and Machine Learning approach for near realtime estimation

Adapted from: ***Harsha Avinash Tanti***, *Abhirup Datta, Tiasha Biswas, Anshuman Tripathi, "Development of a Machine Learning based Radio source localisation algorithm for Tri-axial antenna configuration", Journal of Astronomy and Astrophysics, Volume 46, article number 5, 2025, 10.1007/s12036-024-10032-w) AND*
H. A. Tanti, *K. Sahu, A. Datta and A. K. Pradhan, "Tri-axial Patch antenna array configuration for Direction of Arrival (DoA) application," 2023 8th International Conference on Computers and Devices for Communication (CODEC), Kolkata, India, 2023, pp. 1-2, doi: 10.1109/CODEC60112.2023.10465763.*

5.1 Introduction

Radio source localization, commonly referred to as Direction of Arrival (DoA) estimation, involves determining the direction of electromagnetic (EM) signal emissions from various radio sources, which is critical across domains like radio astronomy, wireless communications, and RADAR systems [27, 70]. Traditional DoA estimation presents significant challenges, primarily due to the difficulty of accurately measuring EM signal properties across antenna arrays. Nevertheless, recent advances in digital signal processing have greatly improved localization accuracy, enabling DoA estimation to be a viable solution for diverse applications [129]. In radio astronomy, DoA estimation is particularly essential as it aids in characterizing EM emissions, revealing insights into their emission mechanisms and underlying astrophysical phenomena [6, 18, 27]. This capability is imperative for observing low-frequency emissions, particularly those under 16 MHz, where the ionosphere limits terrestrial radio observations. Consequently, space- or moon-based radio telescopes, including missions such as Cassini-RPWS, STEREO, and SEAMS, have been developed as alternative solutions for low-frequency observations [74].

Radio source localization often relies on various DoA estimation algorithms, including high-resolution

techniques such as MUSIC and ESPRIT. While highly accurate, these algorithms are also computationally intensive and have longer inference times, making them challenging for real-time applications on space missions [99].

For resource-constrained missions, computationally efficient alternatives like pseudo-vector analysis, analytical inversion, and the Matrix Pencil Method (MPM) have been explored [27,95]. In this context, the Snapshot-averaged MPM-based Direction of Arrival (SAM-DoA) algorithm, designed specifically for the SEAMS mission, offers a method for high-precision DoA estimation below 16 MHz while incorporating snapshot averaging for noise reduction [70]. While SAM-DoA has shown promising results, limitations remain due to multi-path interference, terrestrial signals, and non-white noise contamination, which can impact signal fidelity and accuracy [70,94]. Additionally, the constraints of single-payload space missions—such as the limited number of co-located sensors—further complicate accurate DoA estimation due to complex signal modeling requirements and increased estimation sensitivity [46,70]. Machine learning (ML) approaches have thus emerged as a promising alternative, providing more robust DoA estimation with reduced inference times and improved accuracy, especially for scenarios with limited or non-uniform sensor arrays.

The adoption of ML in DoA estimation dates back to the 1990s, with approaches ranging from the Hopfield neural network model to modern deep convolutional neural networks (DCNN) that demonstrate comparable or superior accuracy to traditional methods [130–134]. However, many existing ML-based DoA methods are optimized for linear or planar sensor arrays, which can limit their applicability in single-payload missions where non-uniform sensor configurations are standard. This thesis addresses these challenges and explores an ML-based DoA estimation approach for tri-axial antenna configurations specifically tailored for space-based radio astronomy.

This chapter checks the applicability of the DoA estimation using other linear antennae in a triaxial configuration. It introduces a novel ML-based DoA estimation technique using artificial neural networks (ANNs) for radio source localization, aligned with the SEAMS mission's tri-axial antenna setup [70]. To validate this approach, synthetic signals are generated with varying signal-to-noise ratios (SNRs) ranging from 0 to 60 dB to model realistic signal conditions. Results show that the proposed ANN model achieves prediction accuracy of approximately 91% and significantly reduces inference time—up to 400 times faster than analytical methods—demonstrating its potential as an efficient, accurate solution for DoA estimation with limited sensor configurations. This chapter is arranged so that 5.1 talks about the triaxial configuration and its importance in DoA estimation. Section 5.2 discusses the challenges in real-time direction finding and tries to address the same using an ML algorithm.

5.2 Compatibility of Patch antenna for DoA

This section discusses the scope of applicability of linear antennae, like simple patch antennae in triaxial configuration, to estimate DoA. The linear antenna in triaxial configuration is preferred or utilized in SAM-DoA due to its following characteristics.

- Linear electrical or magnetic antenna has field lines along the direction of the electric or magnetic current [88].
- Due to this linear polarity, the coupling between is ideally nonexistent in triaxial configuration. Thus, the linear antenna along the x-axis will induce voltage due to the electric field present along the axis.

These characteristics allow us to formulate goniopolarimetric techniques such as SAM-DoA.

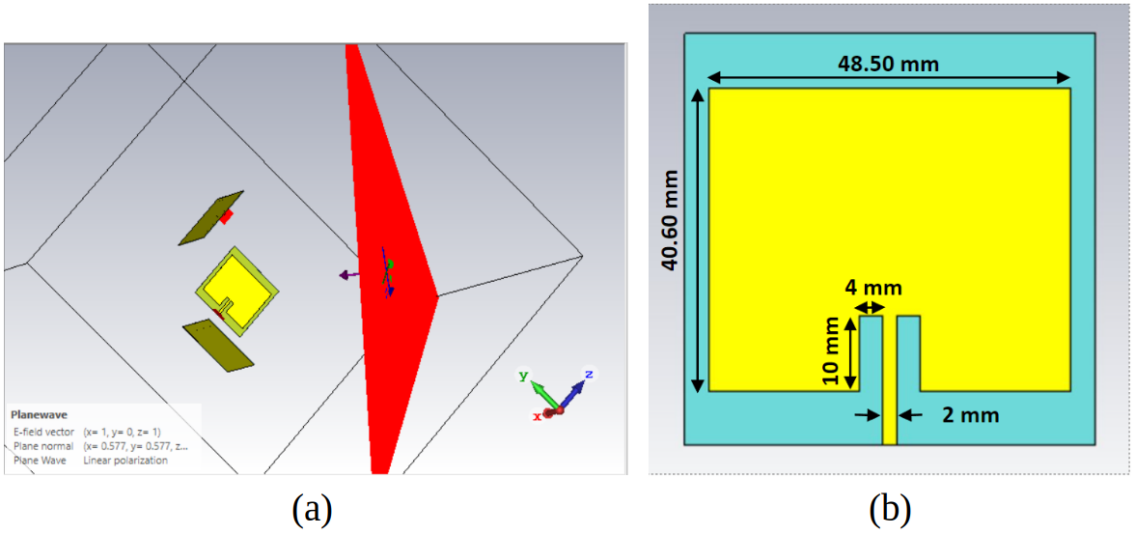

Figure 5.1: (a) Triaxial patch configuration and setup for plane wave exitation simulation (b) Schematic of the inset feed microstrip patch antenna

5.2.1 Antenna Design and Simulation

Figure 1 illustrates a patch antenna positioned along three axes, designed and simulated using CST Studio software. The antenna employs a substrate made of Rogers AD255C material with a dimension of 55 mm x 55 mm, possessing a thickness of 0.762 mm. The substrate has a relative dielectric constant of 2.33 and a loss tangent of 0.0014. The proposed antenna arrangement consists of three inset feed microstrip patch antennas. These antennas are positioned so that their radiation patterns are orthogonal and placed at the far-field ($2D^2/\lambda$). The antenna is excited using a microstrip feed line and fine-tuned through an inset feed for better impedance matching. Figure 5.1(a) shows the antenna design centered around the utilization of a plane wave signal characterized by its propagation direction along the negative z-axis (x=0.577, y=0.577, z=-0.577). The desired electric field vector (E-field) is configured to (x=1, y=0, z=1), and the polarization of the plane wave signal is linear. This design choice facilitates the realization of targeted radiation characteristics.

The reflection coefficient and transmission coefficients of the tri-axial patch antenna configuration are shown in Figure 5.2(c) and Figure 5.2(d), respectively. The antenna structure demonstrates a S_{xx} value <-20 dB and at 2.4 GHz, indicating a relatively low level of reflected energy. Figure 5.2(a) presents the three-dimensional far-field plot of a single patch antenna whose Electric field (E-field) is along the Y axis, while Figure 5.2(b) displays the polar far-field plot of the same. The antenna exhibits a peak gain of 6.84 dBi, reaching its maximum at 2.4 GHz and $\phi = 2°$. The half power points are observed at 86°.

Figure 5.3(a) and 5.3(b) presents the results obtained from the simulation of the patch antenna with an excitation port located along the Y-axis, excited by a plane wave source: one along the Y-axis (vertical polarization) and the other perpendicular to the Y-axis (horizontal polarization). In order to conduct the simulation, CST Microwave Studio was used for some time of 100 ns. By exciting the patch antenna with a plane wave polarized along the Y-axis (vertical polarization), it is seen that the antenna is effectively capturing power delivered by the plane wave. When the patch antenna was excited with a plane wave polarized perpendicular to the Y-axis (horizontal polarization), near-zero output power indicates that the antenna is non-responsive towards the horizontal polarization.

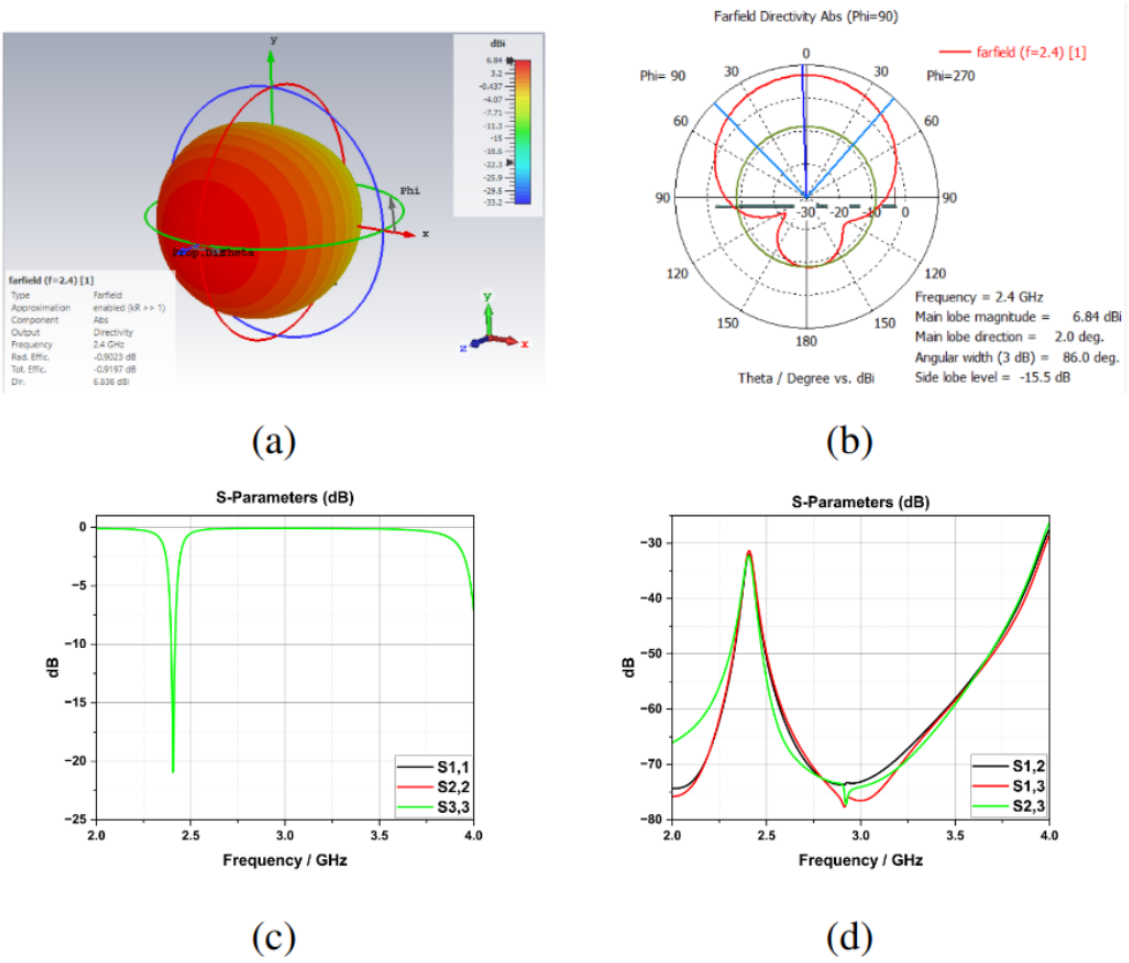

Figure 5.2: (a) Far field pattern of a single patch antenna (b) Polar Far-field plot of a single patch antenna (c) S_{aa} parameter (In legend black, red and green shows patch antennas along x, y and z axis respectively) (d) S_{ab} parameter (In legend black, red and green shows mutual coupling between patch antennas along (x,y), (x,z) and (y,z) axes).

This is concrete evidence that the patch antenna is linear along the direction of the microstrip feed line.

From the simulations carried out with the inset patch antenna (Figure 5.1(b)), it is evident that the antenna is directive and exhibits strong linearity (see Figure 5.3(a) and 5.3(b)). This makes it a suitable candidate for the SAM-DoA algorithm application purpose, wherein linear orthogonal antennas are required to find the DoA. Thus, a triaxial patch structure was designed based on this, as shown in Figure 5.1(a). The simulation of the triaxial patch showed excellent resonance at the designed frequency (Figure 5.2(c)) and very low coupling (Figure 5.2(d)), thus making it more compatible with the DoA algorithm. However, when the analysis of the same was on using a plane wave excitation with linear polarization in x-z plane (E-field vector:(1,0,1)) propagating in $\left(\frac{1}{\sqrt{3}}, \frac{1}{\sqrt{3}}, -\frac{1}{\sqrt{3}}\right)$ direction (Figure 5.3(c) and 5.3(d)) shows otherwise. As in Figure 5.3(d), we can observe that the antenna along the y-axis receives a faint signal even when there is no E-field along the y-axis as per the simulation setting. The faint signal on the y-axis antenna is due to the reflected plane waves by the orthogonal antenna ground. This error is due to the reflection or

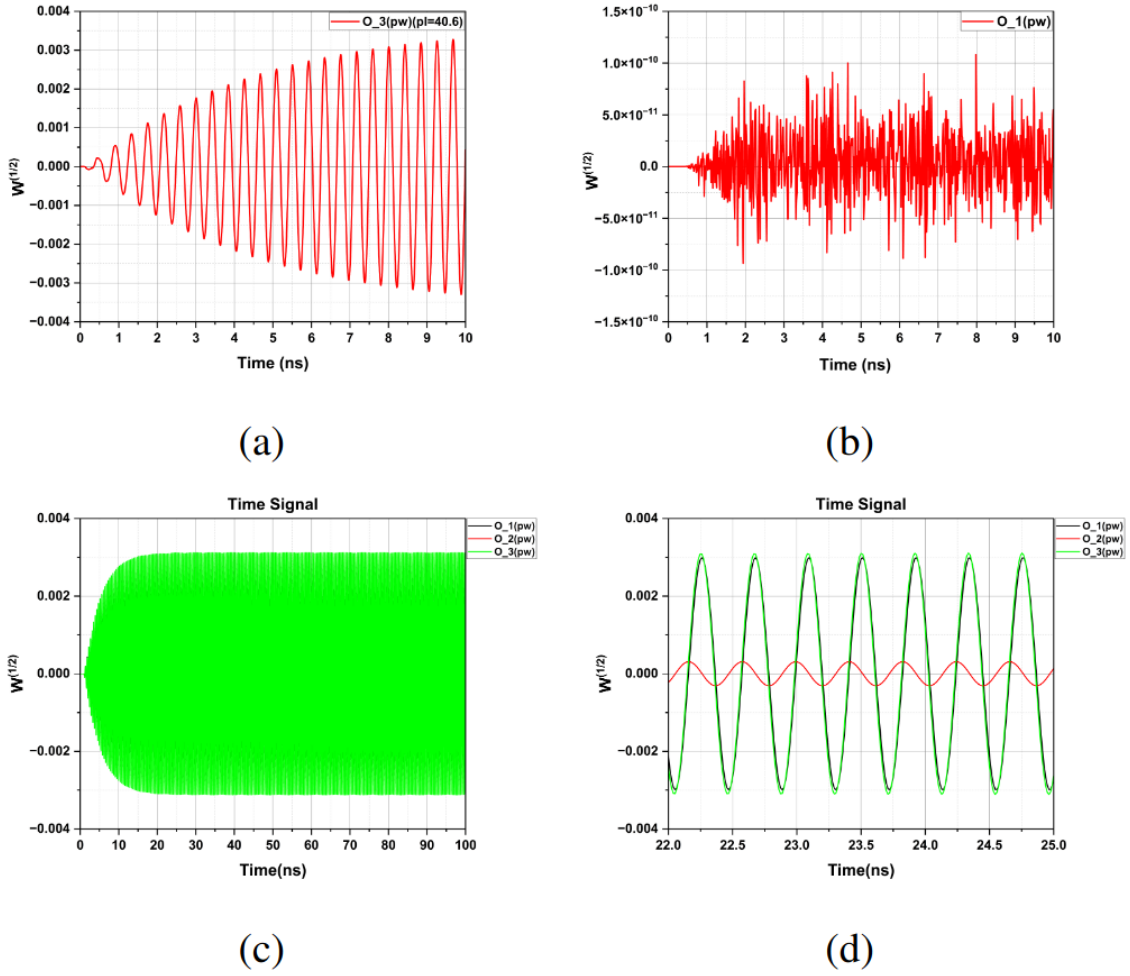

Figure 5.3: (a) Voltage values for a single patch antenna when E-field is along the antenna polarization (zoomed 0 - 10 ns) (b) Voltage for a single patch antenna when E-field is $\perp$ to the antenna polarization (zoomed 0 - 10 ns) (c) Output voltages of triaxial patch configuration, exitation - plane wave (d) Zoomed snippet of (c) (In legend black, red and green are readings for patch antennas along x, y and z axis respectively).

multipath, which is significant enough to produce errors in DoA estimation; however, innovation in the system or calibration procedure can reduce this error.

Based on the observation, the simulations of an inset patch suggest that the patch antenna shows strong linearity in the radiation, having the E-field align itself along the direction of the microstrip-feed line. Thereby making the inset patch a suitable candidate for implementing the SAM-DoA algorithm. However, the plane-wave simulation of the triaxial configurations suggests otherwise. This is because the patch antenna has a ground plane or a reflective plane behind the patch structure, causing the plane wave to reflect, thereby increasing the magnitude of the voltage observed at the antenna ports. However, suppose the losses and reflective gain in the voltages can be compensated by calibration. In that case, the triaxial inset patch antenna is a suitable candidate for implementing the SAM-DoA algorithm. Moreover, the patch antennas are primarily utilized for high-frequency operations, thus extending the applicability of the SAM-DoA in high-frequency radio astronomy.

5.2.2 Simulation Results

The results from the antenna design simulations reveal several notable observations regarding the antenna's reflection and transmission properties, far-field behavior, and the effectiveness of a triaxial patch structure for DoA applications. Reflection and Transmission Coefficients: The simulated reflection (S_{xx}) and transmission (S_{ab}) coefficients, shown in Figures 5.2(c) and 5.2(d), indicate that the designed antenna structure achieves an S_{xx} value below -20 dB at 2.4 GHz, pointing to minimal reflected energy. This suggests a well-matched antenna configuration at the desired frequency. Far-Field Characteristics in Figure 5.2(a) presents the three-dimensional far-field radiation pattern for a single patch antenna, with the electric field (E-field) aligned along the Y-axis. The polar far-field plot (Figure 5.2(b)) shows that the antenna exhibits a peak gain of 6.84 dBi, reaching its maximum at 2.4 GHz and an azimuthal angle (ϕ) of 2°. The half-power beamwidth spans 86°, indicating a suitable directivity for applications requiring linear polarization along a specific axis. Simulations with plane wave excitation along and perpendicular to the Y-axis reveal the antenna's strong linear polarization properties, with significant power capture along the Y-axis (vertical polarization) and near-zero response for horizontal polarization (Figures 5.3(a) and 5.3(b)). This demonstrates that the patch antenna responds effectively to the Y-axis aligned electric field, confirming its strong linearity and suitability for applications requiring polarized response consistency. Based on these findings, a triaxial patch antenna structure was designed to enable Direction-of-Arrival (DoA) estimation in the SAM-DoA algorithm, requiring orthogonal linear antennas. The triaxial configuration (Figure 5.1(a)) demonstrated strong resonance at the design frequency with low coupling between patch elements (Figures 5.2(c) and 5.2(d)), improving its compatibility for DoA estimation.

Moreover, despite promising performance, further simulations using a plane wave excitation along the x-z plane (E-field vector $(1, 0, 1)$) and propagating in the direction $(\frac{1}{\sqrt{3}}, \frac{1}{\sqrt{3}}, \frac{-1}{\sqrt{3}})$ revealed limitations. As shown in Figures 5.3(c) and 5.3(d), a faint signal was detected along the Y-axis patch due to reflections from the orthogonal antenna ground plane. This reflection, producing a multi-path effect, could lead to significant errors in DoA estimation. Future calibration or system design improvements may mitigate these reflection-induced errors, increasing accuracy in DoA estimation.

5.3 Development of DoA estimator using ANN

Direction finding is a challenge and topic of research using a limited number of co-located sensors. The placement of the sensor is critical based on the direction-finding algorithms designed. However, near real-time assessment of the

5.3.1 Received signal model

A substantial volume of data was generated analytically to train our machine-learning model. It includes Fourier components of electric fields, noise, azimuth, elevation, and signal frequency. The data was generated by considering a tri-axial linear antenna configuration positioned orthogonally to one another, considering the entire configuration is at the origin. In the case of a simple linear antenna such as a dipole or monopole, the voltage generated by the antenna due to the received plane wave can be approximated by $V = |\vec{E}|/h_{\text{ant}}$ where, h_{ant} is the antenna height, V is the voltage or potential difference across the antenna terminals and electric field ($\vec{E}$) of the incident wave [27,88]. Thus, considering the antennas of unit length and placed at origin along the orthogonal axes $\hat{a}_x$, $\hat{a}_y$, and $\hat{a}_z$, we can model the electrical field by each antenna due to incident

Table 5.1: Different signal Cases for ANN model training.

Cases	SNR Range (dB)
1	0 to 60
2	20 to 30
3	30 to 40

incoherent waves P, traveling towards the origin(reference axes) as,

$$E_m = \frac{1}{h_{ant}} \sum_{i=1}^{P} \vec{E_i} e^{-j(\vec{k_i} \cdot \vec{r_m} - \omega_i t)} \cdot \hat{a}_m + n(t) \tag{5.1}$$

Here, E_m represents the field due to each antenna element in the tri-axial orthogonal arrangement, $\vec{E_i}$ is the orientation of the field in three dimension which is perpendicular to the propagation vector $\vec{k_i}$, $\vec{r_m}$ is the position vector of each antenna, $\hat{a}_m$ is the unit vector along antenna polarisation that is along the axis of the antenna (where, $m \in (x, y, z)$), and $n(t)$ is the additive white noise due to the media. Then, the sampled signal is shown as,

$$X_m[u] = \sum_{i=1}^{P} \vec{E_i} e^{-j(\vec{k_i} \cdot \vec{r_m} - \omega_i t_0)} e^{j\omega u\delta} \cdot \hat{a}_m + n(t_0 + u\delta) \tag{5.2}$$

Where, the signal is sampled at $t_u = t_0 + u\delta$, δ being the sampling interval, and $0 \leq u \leq N-1$, N is the sample length. Thus, to generate the received signal for model training, data has been modeled using equation 5.1 and 5.2 and by selecting various combinations of azimuth(ϕ_{az}) and elevation(θ_{el}) given by the equations 5.3 and 5.4.

$$\phi_{az} = 2\pi - tan^{-1}(\frac{k_y}{k_x}) \tag{5.3}$$

$$\theta_{el} = \pi/2 - sin^{-1}k_z \tag{5.4}$$

Following the previous studies, it is understood that the dominant astrophysical phenomena between 0.3 to 30MHz are Auroral Kilometric Waves (AKR), solar bursts, and lighting [135]. Generally, at these frequencies, the flux density of the galactic background varies from $\sim 10^5$ Jy to $\sim 10^7$ Jy, and the dominant astrophysical phenomena are $\sim 10^1$ to $\sim 10^4$ orders higher than the galactic background [135]. So, if the receiver noise temperature is maintained below the galactic background, the galactic background will become the System Equivalent Flux Density (SEFD). [68, 136]. Thus, following the radiometric equation $SNR = T_{source}\sqrt{\Delta\nu\tau}/T_{sys}$ (where, T_{source} represents the brightness temperature of the source, T_{sys} is the system temperature, $\Delta\nu$ is the bandwidth of observation, and τ is the integration time) and the flux densities of the dominant astrophysical phenomena the SNR of comes out ~20dB at 1MHz for $\tau = 1$ ms and $\Delta\nu = 2$MHz [8,137]. Also, based on flux density spectra observations made by different instruments like Wind/WAVES in the range 0.3 to 30MHz, it can be deduced that the dominant phenomena will have SNR in the range of ~20 to 30 dB [135, 138–140]. Assuming a Lunar orbiter satellite or a satellite at L1, such as the SEAMS project under development, we consider three data synthesis and model training cases, as outlined in Table 5.1. Cases 2 and 3 have been designed to detect dominant astrophysical phenomena, while Case 1 has been designed for commercial or general use.

5.3.2 Overview of the ML model

In this paper, we have employed the ANN machine learning architecture due to its versatility to resolve numerical problems. The initial framework of a neural network consists of three main layers: an input layer, a hidden layer, and an output layer. The number of hidden layers determines the network's depth, whereas the network's width is determined by the number of neurons in those layers. An information flow is unidirectional in feed-forward networks as each neuron in one layer is connected to every neuron in the next layer, and the neurons are connected based on weights(w_{ij}) and bias(b_j) with x_j being the input data to the jth neuron. Analytically, this can also be represented as [141, 142],

$$Y_i = \sum_{j=1}^{L} w_{ij} x_j + b_j \tag{5.5}$$

The developed ANN architecture comprises nine dense layers, seven of which serve as hidden layers. The input layer comprises 16384 neurons, followed by 1024 neurons in the first hidden layer. The remaining layers consist of 512, 64, 32, and 16 neurons. In the output layer, three neurons provide three outputs that indicate the location of the source in azimuth and elevation, along with the frequency at which the emission occurs. In the developed model, the Rectified Linear Unit (ReLU) is employed as the activation function for each layer.

5.3.3 Training and Test Data set

The data set for the model's training is generated following the theory in Section 5.3.1. The entire process is depicted in the flow chart shown in Figure 5.4.

The data set is created assuming a randomly located source emitting incoherent frequencies in the range of 0.3 to 30MHz. Thus, all plausible combinations of azimuth and elevation with a degree-level accuracy are considered for random selection to emulate this. This is required in order to train the model to deduce the relation between the acquired signal and DoA angle (analytically related as shown in equation 5.3 and 5.4), which 32,400 DoA angles combination for random selection for signal emulation. Subsequently, 5×10^4 realization of signals was generated using the method discussed in Section 5.3.1 with the DoA angle randomly selected from 32,400 combinations of azimuth and elevation. Then, each realization was contaminated with the noise of 30 different SNR levels between 0 to 60 dB, making 30 copies of the same signal with different SNRs. That is, the generated plane wave was exposed to noise, thereby generating a set of signals having SNR ranging from 0 to 60 dB, as determined by the equation (5.2); data by each antenna is generated and stored for model training and testing. There were 1.5×10^6 data points to train and test data for different random frequencies and SNRs. Later, the data was stratified into three sets for training, validation, and testing. The total data is split into 9:1 parts for training and testing, and from the training data set, 10%

The methodology outlined above in Section 5.3.2 is the proposed model for DoA estimation using ML, Case 1 in Table 5.1. In addition to this, two more cases were considered, as shown in Table 5.1, wherein the same network was trained for a smaller range of SNR. Similar to Case 1, training and test data are generated for Cases 2 and 3.

5.3.4 Results and Discussions

A study of different analytical DoA algorithms found that accuracy varies with the employed DoA methods. For example, in case of signals with SNR $\sim$ 15 dB, Snapshot Averaged Matrix Pencil

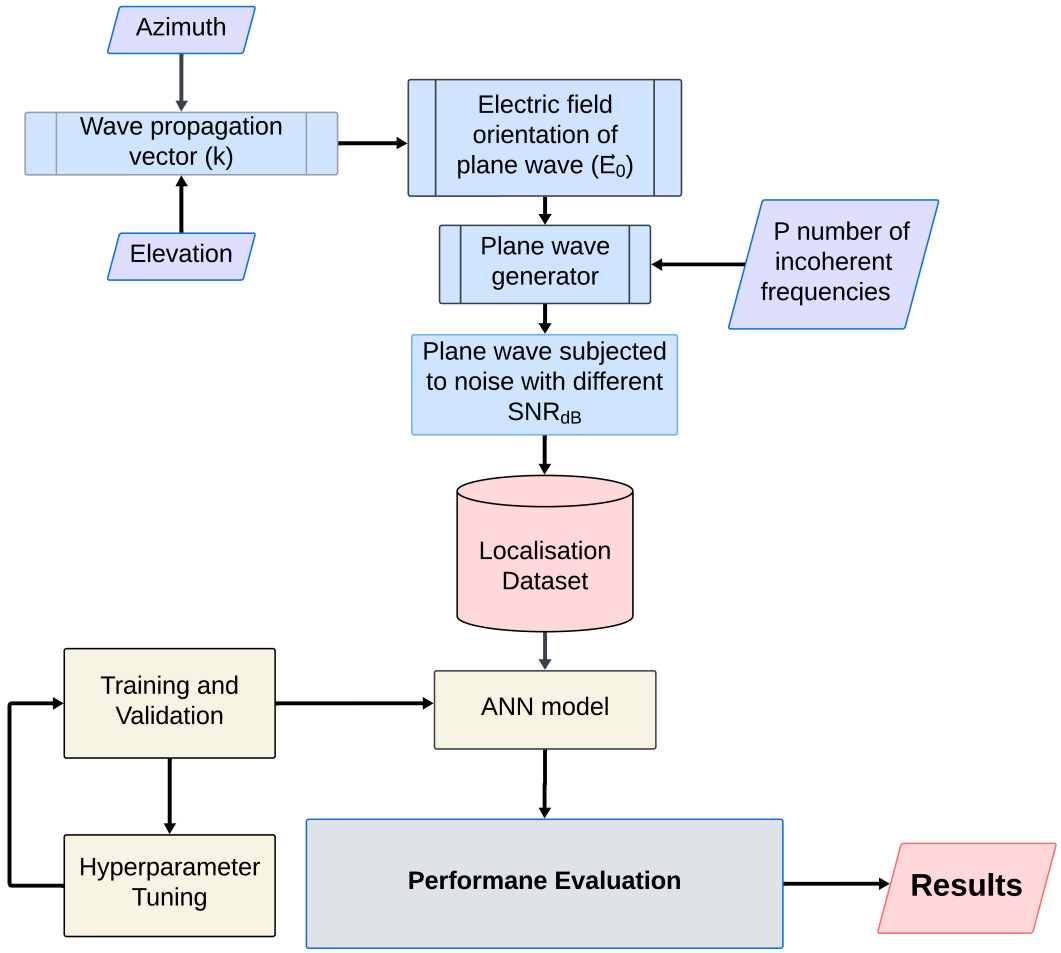

Figure 5.4: Workflow of the proposed ML model for Radio source localization.

Method (SAM) ($< 0.5°$), Matrix Pencil Method (MPM) ($< 1°$), and Pseudo-vector estimation-based DoA ($> 10°$), Analytical Inversion method ($< 6°$). Regarding the practical implementation of these algorithms, it is noted that errors arose to degrees despite the algorithms being capable of achieving precision at the second level [70]. This is due to the constraints of the instruments and the interference caused by the reflection of signals, which is challenging to represent accurately. Machine learning provides a feasible alternative by allowing computers to acquire knowledge from data without human intervention. On analysing vast data sets, one can identify patterns that enable precise predictions of radio source locations, making it a valuable tool for resolving localisation problems.

In this study, the developed ANN model has been trained for three different cases with a maximum of 1.2×10^6 data points (or signal realisations) for 100 epochs (see Section 5.3.3) with the desired output as azimuth, elevation, and signal frequency. It is important to note that the model training starts saturating after the 100th epoch. Thus, the training is halted at the 100 epoch[1], as seen in Figure 5.5. From Figure 5.5, it is evident that loss of model training and validation converges till ~ 0.02 & ~ 0.23, respectively, for Case 1. Table 5.2 shows training and validation loss achieved

[1]Appendix H elaborates on the model training and evaluation.

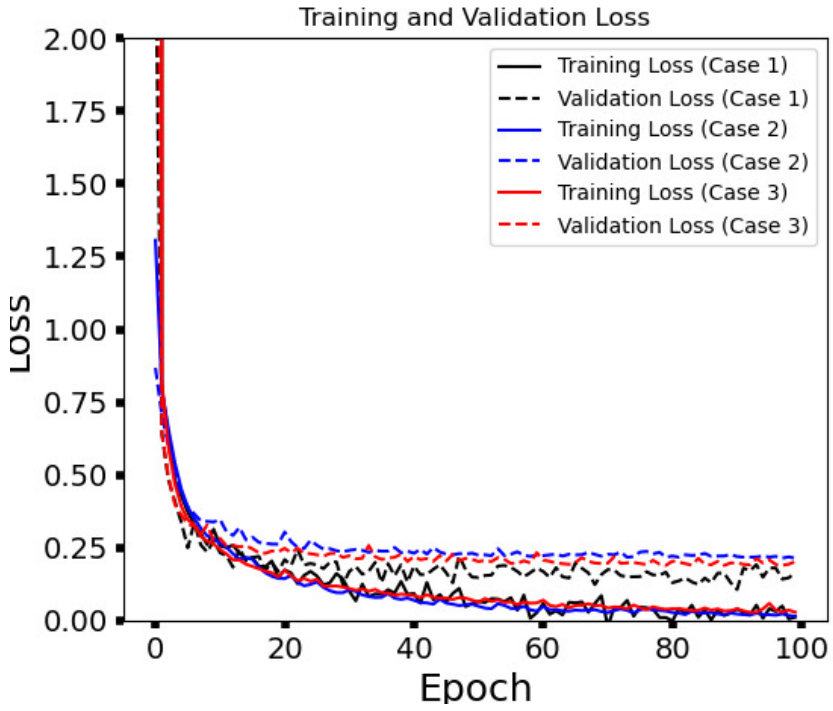

Figure 5.5: Training and Validation Loss Evolution for Different SNR Ranges: The plot displays the training and validation losses over 100 epochs for Case 1 (black, SNR range 0-60 dB), Case 2 (blue, SNR range 20-30 dB), and Case 3 (red, SNR range 30-40 dB). The curves show rapid convergence to low loss values, indicating robust model performance across varying SNR conditions.

for all three test cases, with an inference time of ~ 5 ms. Also, from Table 5.2 and Figure 5.5, the validation loss for Case 1 is consistently lower than for Case 2 and Case 3. This might be due to the presence of a higher SNR signal in the data set or due to the fact that the same network is used to train for all three cases. In the training and validation evolution, the figure displays fluctuations. These drops are mainly due to the smaller batch size in comparison to the data size, optimizer selection, or due to the introduction of random shuffling during training, where both training and validation data sets have been randomly distributed prior to each epoch (see Appendix H). The purpose of this shuffling is to ensure impartial model training.

Figure 5.6 represents a scatter plot between the true and predicted azimuth, elevation, and emission frequency values for Case 1 when the model is subjected to an untouched data set i.e., test data set.

Table 5.2: Training and Validation Loss for three different cases.

	Training Loss	Validation Loss
Case 1	~ 0.02	~ 0.23
Case 2	~ 0.02	~ 0.26
Case 3	~ 0.02	~ 0.25

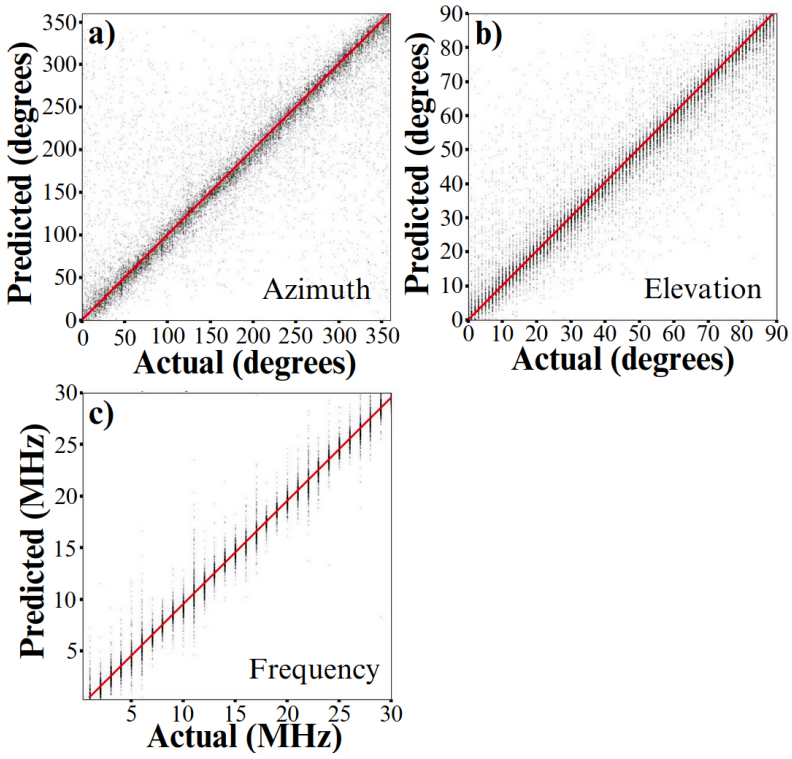

Figure 5.6: Comparison of Actual to Predicted Values for Azimuth, Elevation, and Frequency: Scatter plots illustrating the relationship between actual and predicted values for a) Azimuth in degrees (top-left panel), b) Elevation in degrees (top-right panel), and c) Frequency in MHz (bottom-left panel). The red line represents the ideal $y = x$ line. The close alignment of points to the red line across all three plots indicates the model's high accuracy in predicting these parameters. The relationship represented here is for Case 1, which remains similar for the other two cases.

It can be observed that the majority of the predictions are around the red line, indicating that the predicted results are equal to actual values. We had possible combinations of azimuth, elevation and frequency (in the range of 0.3 to 30 MHz), causing an almost uniform distribution along the red line in Figure 5.6. Moreover, the merit of any ANN model is quantified using R^2 - value [143]. It is a statistical measure of how well the regression line approximates the data. It is defined by, $R^2 = 1 - [\sum(y_i - \hat{y}_i)^2]/[\sum(y_i - \bar{y})^2]$. Here, y_i is the actual value, $\hat{y}_i$ is the predicted value, and $\bar{y}$ is the mean of the true y values. Table 5.3 presents the R^2 values of the ANN model across all three cases, utilizing the test signal with SNR within the same range as outlined in Table 5.1. It is observed that the R^2 score remains almost the same across the three different cases. Moreover, in the top left panel of Figure 5.6, an increase in scattering is observed towards the beginning and end of the Azimuth angle, displaying an error of 300 degrees and above. This is because azimuth is an angle, and if there is an error of -20 degrees at 0 degrees azimuth, it will be represented as 340 degrees.

Further, an unseen data set was segregated into different SNR values to understand the effect of SNR on the estimation (of Azimuth, Elevation and Frequency of emission). It was used to predict the incident signal's Azimuth, Elevation and Frequency. Figure 5.7 shows the variation of the estimation error in the Root Mean Squared Error (RMSE) form in the Azimuth, Elevation, and Frequency Predictions. Figure 5.7 illustrates the RMSE as a function of SNR for three different cases. Each case is shown by a different colour (Black for Case 1, Blue for Case 2, and Red

Table 5.3: Evaluating R^2 score for the trained model during prediction for different cases as shown in Table 5.1.

R^2 scores	Case 1	Case 2	Case 3
Azimuth	0.74	0.75	0.74
Elevation	0.76	0.78	0.79
Frequency	0.96	0.97	0.98

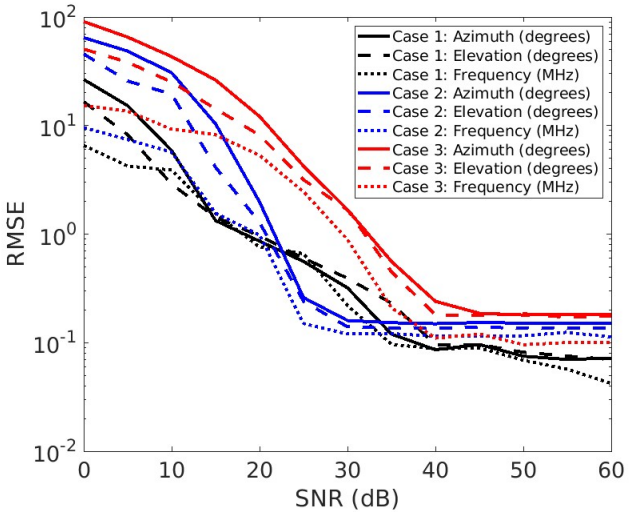

Figure 5.7: RMSE vs. SNR for Azimuth, Elevation, and Frequency Predictions: This illustrates the RMSE for three different cases as a function of SNR. Case 1 (black), Case 2 (blue), and Case 3 (red) are shown with different line styles representing Azimuth (solid), Elevation (dashed), and Frequency (dotted). The RMSE decreases with increasing SNR, indicating improved prediction accuracy at higher SNR values, with Case 1 showing the best overall performance.

for Case 3), while the estimation RMSE in Azimuth, Elevation, and Frequency is indicated by a different line style (solid for Azimuth, dashed for Elevation, and dotted for Frequency). Although Case 2 and Case 3 are trained for the limited range of SNR, the model is tested for the entire SNR range from 0 to 60 dB in order to assess the behaviour of the model across the entire range. From Figure 5.7, it is observed that for Cases 2 and 3, the prediction accuracy is very low for lower SNR. This is expected as the model was trained for smaller range of SNR; thus, its accuracy should be poor for values outside the range. Notably, for higher SNR values(that is, for SNR values greater than 30 dB and 40 dB for Case 2 and Case 3, respectively), the estimation RMSE remained nearly constant. Whereas the RMSE for Case 1 is significantly lower than the other two cases and decreases consistently till 40 dB thereafter saturating. Also, it is observed that the model achieves an estimation error of less than 1 degree for SNR greater than 15 dB.

In a study carried out in [70], it was observed that there are analytical methods with low computational complexity and low accuracy. It is also observed that to increase the accuracy of such algorithms, the complexity of the method increases exponentially (see I). Therefore, there is always a trade-off between accuracy and computational complexity. However, the ML-based techniques might provide a viable solution as they require high computational costs while training the model. In contrast, the trained model has a low computational cost as it assumes the form of multiple

Table 5.4: Inference time and Error comparison of different DoA Estimation techniques (for Az/El = 180°/45°, with 4096 number of discrete signal samples, SNR = 15 dB, and clock speed ∼2Ghz).

Type of DoA Estimator	Inference Time	Error in Az/El (degrees)
Elementary ML DoA estimator*	∼6ms	∼1
SAM-DoA (n = 20) [70]	∼409s	∼0.015
MPM-DoA [5, 6]	∼98s	∼0.0915
Analytical Inversion Method [23, 27]	∼630ms	∼5.9
Pseudo vector estimation based DoA [95]	∼560ms	∼10.2

* The comparison is for Case 1, which does not include the pre and post-scaling time. The pre and post-scaling of the data will add at most ∼10ms more to the inference time.

linear equations [141, 142]. This reduces the computational cost, thereby lowering the inference time. Table 5.4 compares the inference time of different analytical algorithms with the developed elementary ML-based DoA estimator. It is observed that the inference time of this ML-based method is at least ∼ ten times faster, including the pre and post-data scaling of the data using a general-purpose computer. Faster inference time is essential for observing and studying transients. Also, this reduction in the inference time is applicable in the field of communication and passive localisation, wherein the transmission time is just a few milliseconds, and localisation has to be performed within a short period. This inference time will vary if implemented on small form factor machines such as Raspberry Pi, Nvidia Jetson Board, or any other single-board computer (SBC). In addition, the inference time can be further reduced with the introduction of the new generation of FPGAs capable of hosting ML models.

5.4 Conclusion

The inset patch antenna simulations demonstrate strong linearity, with the E-field direction aligning well with the microstrip-feed line, making it highly suitable for the Snapshot Averaged Matrix Pencil Method (SAM-DoA) algorithm. However, simulations with a triaxial configuration reveal challenges, such as reflections from the antenna's ground plane, which cause signal interference and increase errors in DoA estimation. These multipath errors necessitate further refinement through improved calibration techniques or structural modifications to achieve reliable, high-precision DoA applications. To address these challenges and explore alternative methods, a novel ML-based DoA model has been proposed using a tri-axially oriented orthogonal linear antenna. The ML

approach employs an Artificial Neural Network (ANN) architecture, which effectively handles multi-dimensional simulated data. This model was trained with 1.2 million data points over 100 epochs, achieving training and validation losses of approximately 0.02 and 0.23, respectively. The study illustrates that an ML-based approach can provide accurate localization even with a finite and limited number of sensors.

One of the key advantages of the ML-based DoA model is its potential to significantly reduce inference time. While conventional DoA algorithms may take several seconds for estimation, the ML model achieves inference times on the order of a few milliseconds when run on a general-purpose computing machine equipped with an Intel Xeon 2nd generation processor. However, when implemented on compact devices like a Raspberry Pi or Nvidia Jetson board, the inference time increases by at least an order of magnitude. The use of new-generation FPGAs capable of hosting ML models can further decrease inference times, making the approach suitable for real-time applications such as transient detection, communication, and passive localization where rapid response times are essential. Despite the promising results, the current ML-based DoA model does not yet provide polarization information, unlike the SAM-DoA and Matrix Pencil Method (MPM)-based algorithms. Nevertheless, it represents an important step toward developing a more robust and redundant DoA model. To improve the model's accuracy and reliability, future work will focus on creating realistic signal datasets that incorporate IPS signatures and reflect actual operating conditions. Additionally, a more comprehensive signal model will be developed to enhance the robustness of the ML-based DoA algorithm.

Chapter 6

Inner-heliospheric signatures of steadily declining solar magnetic fields and their possible implications

Adapted from: ***Harsha Avinash Tanti***, *Susanta Kumar Bisoi, Abhirup Datta, "Inner-heliospheric signatures of steadily declining solar magnetic fields and their possible implications", The Astrophysical Journal, Volume 979, Number 2, Page 198, January 2025,10.3847/1538-4357/ada38a*

6.1 Introduction

The 11-year regular variation in sunspot activity, known as sunspot or solar cycle, perfectly demonstrates the cyclic evolution of the Sun's magnetic field, operated by a solar dynamo through a magnetohydrodynamic process. The process converts the poloidal fields of the Sun into the sunspot (or toroidal) fields (the Ω-effect) and then back into the poloidal fields through a Babcock-Leighton mechanism, constituting the 11-year solar cycle or 22-year solar magnetic cycle [144–149]. The recent trends in solar activity witnessed a solar cycle 23 with a cycle period of more than 12 years due to an unusually long extended solar minimum at the end of cycle 23. This delayed the beginning of the solar cycle 24, which started in March 2010 instead of December 2008 [104]. Not only was Solar Cycle 24 delayed and weaker than the earlier three solar cycles, but it was also the weakest solar cycle in the past 100 years. In our earlier studies, we attempted to study and understand these anomalies in solar cycle variability using measurements of the Sun's photospheric magnetic fields during the period 1975 – 2017 and covering solar cycles 21 – 24 [109, 150–152]. The significant finding of our studies of solar photospheric magnetic fields obtained using magnetic field measurements from the National Solar Observatory at Kitt Peak (NSO/KP), USA, was a steady decline in the (unsigned) photospheric field strength in the latitude above 45°, referred to as polar fields. Unsigned photospheric field strength decline began in the mid-1990s and continued until 2017 [150, 152]. Unlike earlier, the signed photospheric polar field strength in the latitude above 45° showed a sunspot cycle modulation with the maximum field strength at the solar cycle minimum and the minimum field strength at the solar cycle maximum when the signed polar field reversal occurs. The solar polar reversal process is usually considered hemispherically asymmetric

[153]. The study of signed polar fields using NSO/KP magnetic field measurements in solar cycle 24 revealed a peculiar solar polar reversal, with the reversal in the southern hemisphere completed 1.5 years earlier than in the northern hemisphere [154]. On the other hand, the unsigned photospheric field strength in the latitude below 45°, referred to as toroidal fields, demonstrated a clear sunspot cycle modulation. However, each solar cycle's peak toroidal field strength steadily decreased from cycles 21 to 24 [109, 150]. [155] investigated the global photospheric and coronal magnetic field strength using a synoptic magnetogram database from the NSO/KP and Global Oscillation Network Group (GONG), covering solar cycles 21 – 24 and the ascending phase of the solar cycle 25. The author reported a global decrease in solar magnetic field strength both at the photospheric and coronal levels.

To investigate the inner heliospheric solar wind signature of the steady decline in photospheric polar field strength, the solar wind microturbulence levels have been studied using interplanetary scintillation (IPS) observations at 327 MHz for the period 1983 – 2017 [104, 109, 156], obtained from the ground-based telescope of the Institute for Space-Earth Environmental Research (ISEE), Nagoya University, Japan. The IPS refers to the random intensity fluctuations observed in signals of the distant extra-galactic radio sources on Earth due to diffraction and scattering caused by the turbulent and refracting solar wind plasma when the radio signals traverse through it [3, 100, 101, 112]. The IPS observations at 327 MHz, facilitated by the action of the Fresnel filter, allow the exploration of solar wind electron density fluctuations of scale sizes $\leq 10^3$ km both within and outside the ecliptic [157–160] over heliocentric distances of 0.26 to 0.82 AU, covering the inner heliosphere. It inherently filters out contributions from large-scale density irregularities such as coronal mass ejections, making it feasible to track solar wind electron density fluctuations with scale sizes of $\leq 10^3$ km in the inner heliosphere. Similar to the steady decrease in the unsigned polar field strength, a steady decline in the scintillation level of the inner heliospheric solar wind in sync with the total photospheric fields was reported [104]. Based on this, it was suggested by [104] that the buildup to the unusually long minimum of solar cycle 23 would have started as early as in the mid-1990s and later on the same was also suggested by [151] based on their study of changes in quasi-periodic variations of solar photospheric fields, which showed a distinct hemispheric asymmetry in the periodicities of solar photospheric polar fields before and after mid-1990s.

Not only the measurements of photospheric fields and solar wind microturbulence levels had shown steady declines, but the measurements of sunspot umbral magnetic field strength had also shown a steady decline of ∼50 Gauss per year since ∼1998 [161]. Based on the steady decrease of umbral magnetic field strength, the authors claimed that the umbral field strength would be less than 1500 Gauss around solar cycle 25, and for sunspot field strength below 1500 Gauss, there would be no contrast between the sunspot regions and the photosphere. Thus, the sunspots would disappear in the solar cycle 25. The global decrease in the sunspot magnetic activity also impacted the heliospheric magnetic field (HMF) measurements at 1 AU, and a significant decline in the peak strength of HMF at each cycle from solar cycle 21 to 24 was noticed [109, 152, 162, 163]. [164] that the HMF approaches a minimum value at each solar cycle minimum, and the minimum value was found to be 4.6 nT, called the floor level of the HMF. The global decrease in solar field strength resulted in a reduced floor level of 3.5 nT for the HMF during solar cycle 23 [163], and the authors proposed a new floor value of 2.8 nT. In contrast, our study [109, 152], based on the continuing decline in solar polar field strength, proposed a floor value of 3.2 nT for the HMF. The reduced floor level was attributed to the global decline in the solar field strength during solar cycles 23 and 24 [152]. [165] proposed a floor value for the unsigned photospheric magnetic field based on the tight correlation of the F10.7cm solar radio flux and unsigned photospheric flux and the existence of a baseline flux of 67 solar flux units (sfu) for the F10.7 cm solar radio flux [166].

We have witnessed a deep solar minimum at the end of solar cycle 24, with sunspotless days of more than 200 days each in 2018, 2019, and 2020. Now, we are already into solar cycle 25 and approaching the solar cycle maximum of cycle 25, with a substantially increased sunspot activity every day. Thus, it is clear that solar cycle 25 would no longer be a solar cycle devoid of sunspots, as [161] claimed. However, it is imperative to follow up on whether the global trends in solar activity have been continuing or recovered. Also, how the weakest solar cycle 24 and the deep solar minimum at the end of solar cycle 24 impact the floor level for the HMF and other activity indicators. The global decline in recent solar activity prompted researchers to predict the amplitude of the solar cycle 25, and two main trends were proposed. The first trend predicts a strong solar cycle 25 with a peak smoothed sunspot number (SSN) between 150 and 180 [167]. In contrast, the second trend predicts a solar cycle weaker/similar to the solar cycle 24 with a peak SSN between 110 and 140 (refer to Table 1 of [152]; [168]; [169]). It is, therefore, important to study and understand the activity indicators of solar cycle magnetic activity during solar cycle 24 – 25. This study focuses on the variation of solar photospheric magnetic field and its signatures in the inner heliospheric solar wind during solar cycles 21 – 25 with an extended data set of photospheric magnetic fields and solar wind microturbulence levels, which are now available beyond 2017 until 2024.

6.2 Observation and Data Analysis

6.2.1 Solar Magnetic Fields

Measurements of solar photospheric magnetic fields from ground-based solar telescopes have been publicly available since 1975. However, high-resolution space-based measurements of solar photospheric fields have been available only since 1996 with the launch of the Solar and Heliospheric Observatory (SOHO) spacecraft. To date, direct measurements of the Sun's coronal magnetic field have not been made, and they are mostly estimated indirectly. Therefore, we focus on measurements of solar photospheric magnetic fields in this article to study the variation of solar magnetic fields during solar cycles. For the estimation of the solar magnetic fields over solar cycles 21 – 25, we used ground-based Carrington rotation (CR) synoptic magnetograms from three different databases: i) the Vacuum Telescope of the National Solar Observatory (NSO) at Kitt Peak, USA (NSO/KPVT), ii) the Vector Spectro Magnetograph (VSM) of the Synoptic Optical Long-term Investigations of the Sun (SOLIS) facility of the NSO at Kitt Peak, USA (NSO/SOLIS), and iii) the Global Oscillation Network Group (GONG). The CR synoptic maps are available in standard FITS files and are usually produced from daily observed full-disk magnetograms obtained over a CR period (27.2753 days). The synoptic maps are in the latitude and longitude format of 180 × 360 arrays. The maps usually contain photospheric magnetic field values measured in Gauss units. The magnetic maps from NSO/KPVT cover data starting from CR1625 to CR2006 corresponding to the years 1975.14 – 2003.66 and are available at https://nispdata.nso.edu/ftp/kpvt/synoptic/mag, while magnetic maps from NSO/SOLIS cover data starting from CR2007 to CR2195 corresponding to the years 2003.66 to 2017.70 and are available at https://nispdata.nso.edu/ftp/synoptic/level3/vsm/merged/carr-rot/. The synoptic maps from GONG cover data from CR2055 to CR2283 correspond to the years 2007.25 – 2024.27, and are available at https://gong.nso.edu/. Together the three databases cover a total period of 1975.14 – 2024.27, spanning over five solar cycles 21 – 25. The NSO data has a few data gaps during CR1640–CR1644, CR1854, CR1890, CR2015–CR2016, CR2040–CR2041, CR2091, CR2152–CR2155, CR2166–CR2167 and CR2192, while the GONG data has a few data gaps during CR2185–CR2187. The data gaps were filled using a cubic spline interpolation while plotting the magnetic field derived from the data sets.

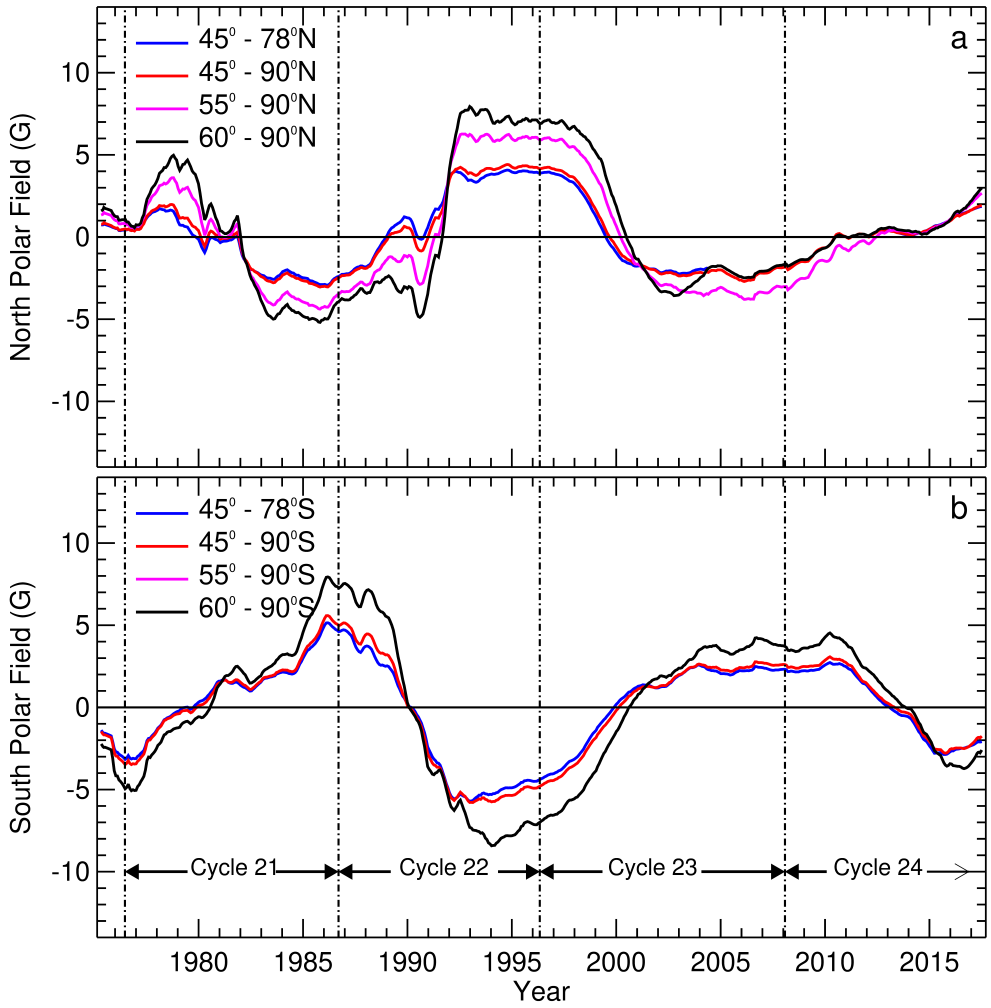

Figure 6.1: (a, b) Variation of signed solar surface polar field strengths, obtained from line-of-sight NSO magnetograms, in the latitude ranges, 45° – 78°, 45° – 90°, 55° – 90°, and 0° – 45° for the northern (panel a) and southern hemisphere (panel b), covering solar cycles 21–24.

The synoptic maps from the three databases were then used to obtain the photospheric magnetic field of the Sun at two desired latitude ranges, i) 0° – 45°, and ii) 45° – 78°. The solar photospheric magnetic fields obtained in the latitude range 0° – 45° are referred to in this study as toroidal magnetic fields (TMF), the variation of which represents the changes in the sunspot fields. Since the latitude of emergence for sunspots is restricted to 0° – 45°, we selected the latitude-range 0° – 45° for the estimation of TMF. On the other hand, the photospheric magnetic fields obtained in the latitude range 45° – 78° are referred to in this study as polar magnetic fields (PMF), the variation of which represents the changes in the polar fields of the Sun. This is to remind you that different researchers select different latitude ranges for the estimation of the PMF, such as poleward of 45° [112, 150], 55° (Wilcox Solar Observatory [WSO] polar fields and [154]), 60° [170–173], and 70° [174]. Further, it is to be noted that [154] showed that the PMF obtained from the NSO database for the latitude ranges, poleward of 45°, 55°, and 60° show similar temporal behavior. Therefore, we used the latitude range poleward of 45° to estimate PMF. Also, since one of the poles of the

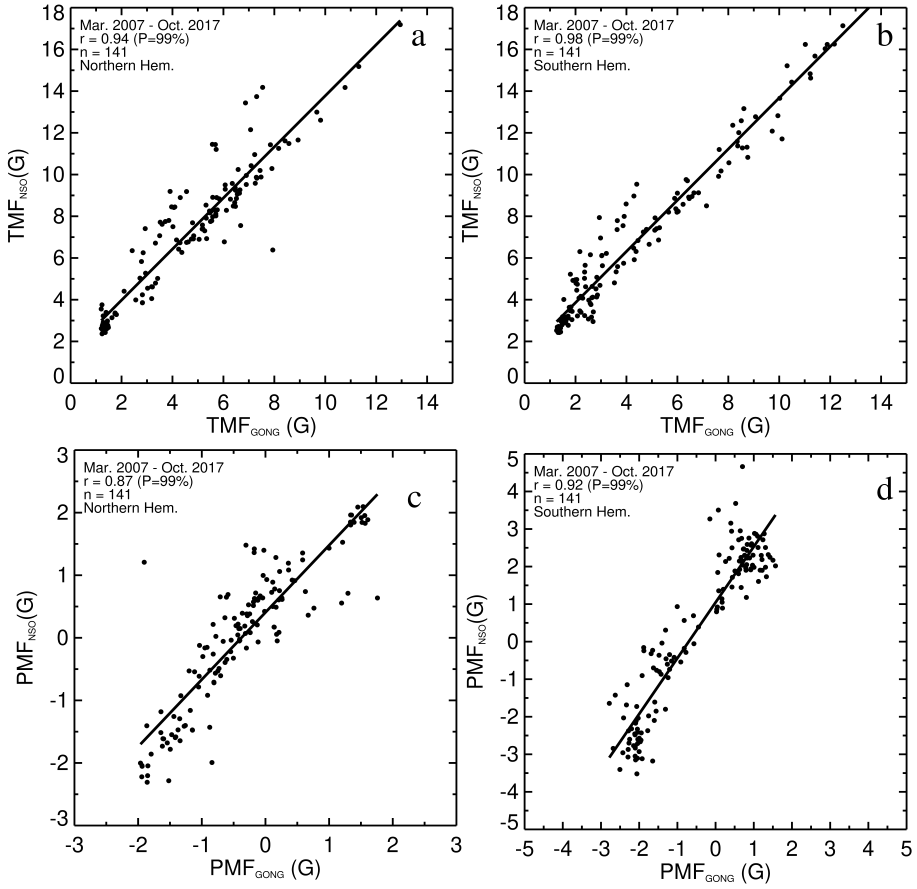

Figure 6.2: (a) NSO northern toroidal field as a function of GONG northern toroidal field. (b) NSO southern toroidal field as a function of GONG southern toroidal field. (c) NSO northern polar field as a function of GONG northern polar field. (d) NSO southern polar field as a function of GONG southern polar field. The filled black dots in all four panels are CR averaged magnetic field data points for the period Mar 2007 – Oct 2017 covering solar cycle 24, while the solid black lines fit the respective data points. The correlation coefficient value, r, for each fit, is indicated in the top left corner of each panel, along with a total number of data points = 141.

Sun is not visible due to the inclination of the Earth's orbit to the Sun's equator, we left out the pole-most regions above the latitude range 78° while estimating the PMF from the NSO database. Fig.6.1 shows the variation of surface polar fields obtained in the latitude range poleward of 45°, 55°, and 60°, for the northern (panel a) and southern (panel b) hemispheres. Also included is the variation of surface polar fields in the desired latitude range of 45° – 78°. It is evident from Fig.6.1 that the overall behavior polar fields poleward of 45°, 55°, and 60° is similar to the temporal behavior of polar fields in the latitude range of 45° – 78°. To learn the details of the computation of photospheric magnetic fields from the synoptic maps at the selected latitude ranges, one can refer to [150].

When plotted, the photospheric magnetic fields obtained from the NSO and GONG databases showed a significant difference in their strength due to the different NSO and GONG measuring instruments. Thus, the NSO magnetic fields for the northern and southern hemispheres were cross-calibrated to the GONG magnetic fields for the northern and southern hemispheres, respectively, to

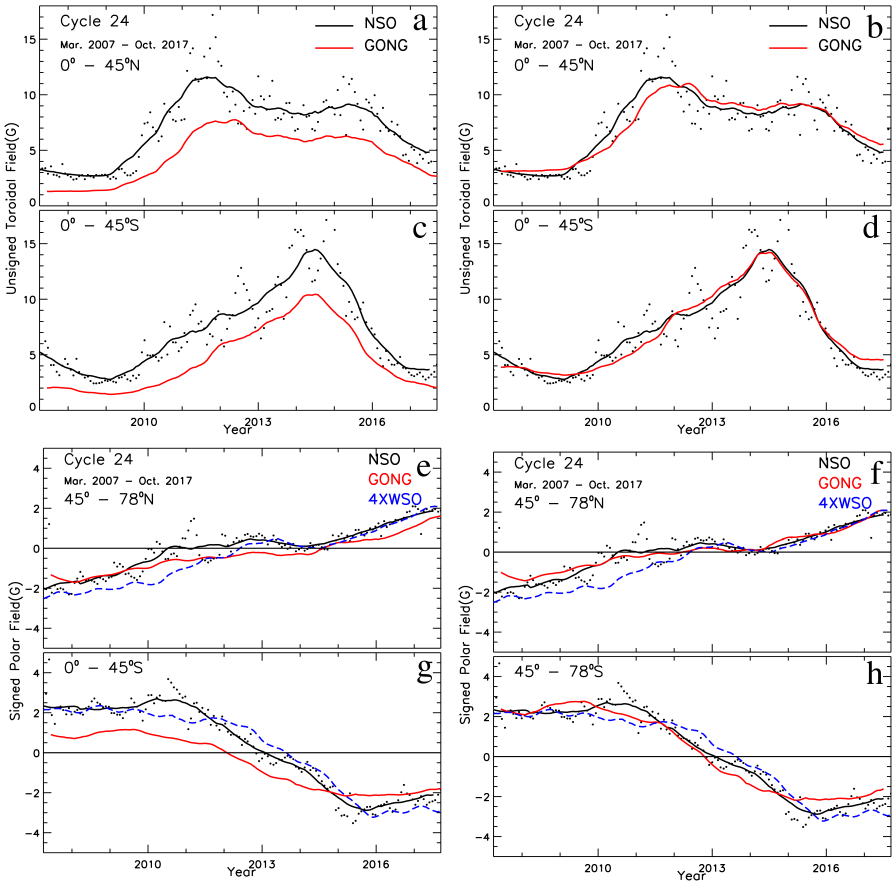

Figure 6.3: (a, c) Uncalibrated northern and southern toroidal fields for NSO (black) and GONG (red) databases. (b, d) Calibrated northern and southern toroidal fields for NSO and GONG databases. (e, g) Uncalibrated northern and southern polar fields for NSO and GONG databases. (f, h) Calibrated northern and southern polar fields for NSO and GONG databases. The filled black dots in all panels are NSO magnetic field data points for the period Mar 2007 – Oct 2017 covering solar cycle 24. The overplotted solid curve in blue in panels (e, f, g, h) is the four times WSO-smoothed solar polar fields.

find a normalization factor. The normalization factor was then multiplied by the GONG magnetic field values to prepare a continuing photospheric magnetic field data set of NSO/GONG covering 1975.14 – 2024.27, spanning over solar cycles 21–25. Figure 6.2 (a, b) shows the correlation between the northern and southern hemispheres' NSO and GONG toroidal fields. Similarly, a normalization factor between the NSO and GONG polar fields was obtained using the correlation between the NSO and GONG polar fields for both the northern and southern hemispheres, as shown in Fig.6.2(c, d). The filled black dots in each panel are CR averaged magnetic field data points for the common period May 1976 – Jan 1996, covering solar cycle 24, between NSO and GONG databases. The solid line in each panel best fits the data points. The linear fits give the relations between the NSO and GONG fields. The Pearson's correlation coefficients, r, are obtained. The significance of the correlation was tested using a Null hypothesis of t-test statistics. A p-value (P), representing the confidence level, was computed considering the r and the sample size, n. The correlations are found to be statistically significant. The r, P, and n values are indicated at the top left corners of each

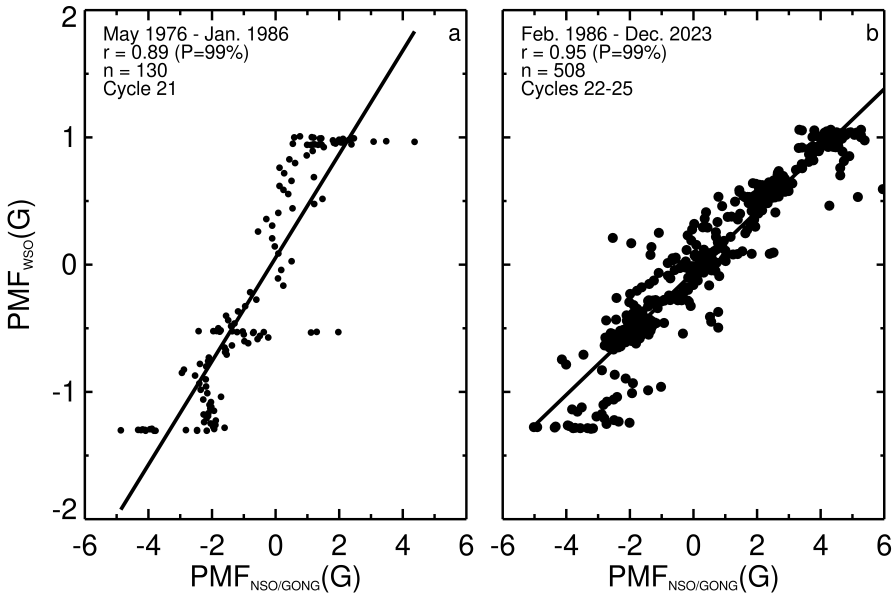

Figure 6.4: (a) Polar magnetic field from WSO (PMF_{WSO}) as a function of polar magnetic fields from NSO ($\mathrm{PMF}_{NSO/GONG}$) shown for the period May 1976 – Jan. 1986 covering solar cycle 21. (b) PMF_{WSO} as a function of $\mathrm{PMF}_{NSO/GONG}$ shown for the period Feb. 1986 – Dec. 2023, covering solar cycles 22–25. The filled black dots in both panels are data points for the above-mentioned periods, while the solid black lines fit the respective data points. The values of r = 0.89 and r = 0.95 are indicated in the top left corners of the panels, along with the total number of data points used, n = 130 and n = 508, respectively, for the above-mentioned period.

panel of Fig.6.2. Figure 6.3(a, c) plots uncalibrated northern and southern TMF for the period May 1976 – Jan 1996, covering solar cycle 24, for NSO (black) and GONG (red) databases. It is evident from panels (a, c) of Fig.6.3 that the strength of NSO and GONG toroidal fields for both the north and south are of different magnitudes. After the calibration, the GONG toroidal fields are multiplied by the normalization factor obtained from the linear relations, as shown in Fig.6.2(a, b). The calibrated northern and southern TMF was plotted for the period May 1976 – Jan 1996, covering solar cycle 24, for NSO (black) and GONG (red) databases, as shown in Fig.6.3(b, d). It is apparent from Fig.6.3(b, d) that the difference in magnitudes of the NSO and GONG toroidal fields for both the hemispheres was removed after the normalization of the GONG fields. Similarly, the differences in the magnitudes of NSO and GONG polar fields were removed, evident from Fig.6.3 (e, f, g, h). The (signed values) polar fields obtained by the Wilcox Solar Observatory (WSO) are considered more reliable in the solar community. The WSO polar fields are the line-of-sight (LOS) measurements of magnetic fields in the latitude range poleward of 55° obtained every 10 days (https://wso.stanford.edu/Polar.html) at WSO. A 1.58-year filter is commonly used to eliminate the yearly geometrical projection effects observed at the pole due to the rotation of the Earth on the measured LOS fields. Therefore, the four-time smoothed values of WSO solar polar fields were overplotted in blue in panels (e, f, g, h) of Fig.6.3 to validate the NSO polar fields. However, this is evident from panels (b, d) of Fig.6.3 that the strength of NSO/GONG and WSO polar fields are different, and since the WSO polar fields are considered more reliable, the NSO/GONG polar fields were calibrated to the WSO polar fields.

Figure 6.4 plots the correlation of NSO/GONG and WSO polar fields. It is noticed that from the temporal variation of the NSO/GONG and WSO polar fields (see Fig.6.7 (b, d)) that the field

strength between the NSO/GONG and WSO is large during cycle 21, while the field strength between the NSO/GONG and WSO is less during cycles 22-25. Therefore, the NSO/GONG polar fields for Cycle 21 were correlated with the WSO polar fields for Cycle 21 separately, as shown in Fig.6.4(a). On the other hand, the NSO/GONG polar fields for Cycles 22–25 were correlated with the WSO polar fields for Cycles 22–25, as shown in Fig.6.4(b). The filled black dots in Fig.6.4 (a, b) are CR-averaged magnetic field data points. The data points in Fig.6.4a cover the period May 1976 – Jan 1996, covering cycle 21, while the data points in Fig.6.4b cover the period Feb. 1986 – Dec. 2023, covering cycles 22-25. The linear fit of the data points in Fig.6.4(a, b) gives the relations between the NSO/GONG and WSO fields, and the respective Pearson's correlation coefficients, r, for the relations are 0.89 and 0.95, respectively, with a p-value (P) of 99%, representing the confidence level. The r, P, and n values are indicated at the top left corners of Fig.6.4a and b. Next, the linear relation obtained between the two fields was used to correct the differences observed between NSO/GONG and WSO polar fields. Further, the signed and unsigned field strength of NSO/GONG polar fields are normalized using these linear relations (see Fig.6.4 (a, b)).

6.2.2 Heliospheric Magnetic Field

We used heliospheric magnetic fields (HMF) obtained from the OMNI2 database (http://gsfc.nasa.gov/omniweb). These are daily measurements of HMF at 1 AU, covering the period Feb. 1975 – Mar. 2024 that span solar cycles 21 – 25. The CR-averaged (27.27 days) values of HMF were derived from daily values and compared with those of detrended CR-averaged TMF and PMF.

6.2.3 Smoothed Sunspot Numbers

We used daily values of smoothed sunspot numbers (SSN) obtained from the Royal Observatory of Belgium, Brussels (http://www.sidc.be/silso/datafiles). The SSN v2.0 was used here for SSN data, a recalibrated SSN data that has been in use since Jul 2015. The original version SSN v1.0 was used earlier to Jul 2015 and is maintained at the Zurich observatory. The SSN data used cover the period Feb.1975 – Mar. 2024, covering solar cycles 21 – 25. The CR-averaged values of SSN were derived from daily values to obtain the detrended SSN and compared with those of detrended CR-averaged TMF and PMF.

6.2.4 F10.7cm Solar Radio Flux

We used daily values for F10.7 cm solar radio flux, publicly available in the OMNI2 database (http://gsfc.nasa.gov/omniweb). The F10.7 cm solar radio flux is a widely used solar activity index. Each data value of F10.7 cm is a measurement of the solar disk integrated radio emission at a wavelength of 10.7 cm (or a frequency of 2.8 GHz), made over 1 hour. It has been the best monitor of the solar cycle activity because of the sensitivity of solar emissions at 10.7 cm wavelength to conditions in the upper chromosphere and at the base of the corona. The CR-averaged values of F10.7cm solar radio flux were derived from daily values to obtain the detrended SSN and compared with those of detrended CR-averaged TMF and PMF.

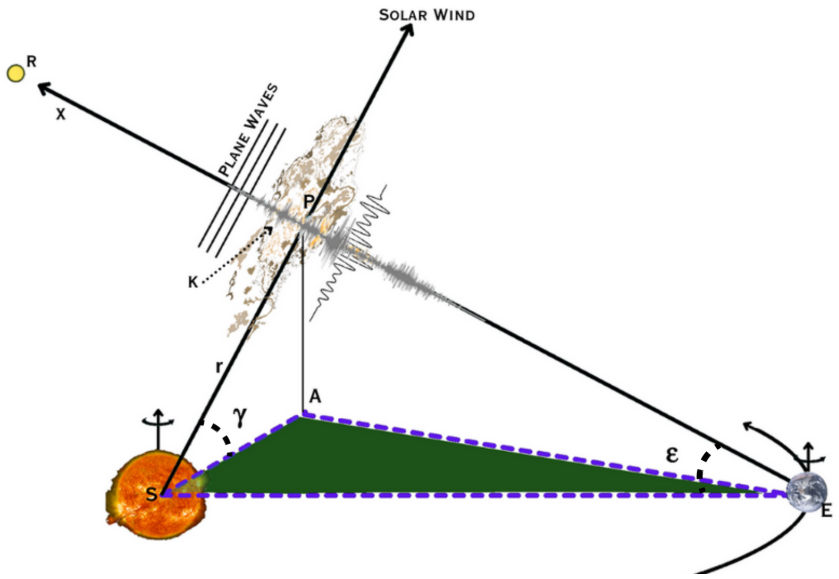

Figure 6.5: A pictorial depiction of the IPS observing geometry. The radio source, the Sun, and the Earth are indicated by points R, S, and E, respectively. The incoming plane waves along the line-of-sight (LOS) from the distant radio source R undergo phase modulation at the point of closest approach, P, while passing through the solar wind, resulting in amplitude variations of the radio intensity. The footprint of the perpendicular line from the point P is indicated by a point A. All the dashed lines lie in the ecliptic plane, indicated by the triangle SAE and filled with green, while all the solid lines lie out of the ecliptic plane. The angles ϵ and γ are the solar elongation and the heliographic latitude of the radio source, while r is the heliocentric distance of the radio source.

6.2.5 Interplanetary Scintillation

We used IPS data from the Institute of Space Earth Environment Research (ISEE), Nagoya, Japan. The IPS facility at ISEE comprises four stations. The four stations are located at Sugadaira (lat/lon–$36°31'12''N$ / $138°19'16''E$), Toyokawa (lat/lon– $34°50'05''N$ / $137°22'09''E$), Kiso (lat/lon–$35°47'34''N$ / $137°37'49''E$), and Fuji (lat/lon - $35°25'36''N$ / $138°36'42''E$). Before 1994, the ISEE IPS facility was comprised of three stations. In 1994, the three-station IPS network at ISEE was expanded by adding a fourth IPS station at Kiso, identical to the other three, resulting in a four-station IPS network. The four-station IPS facility at ISEE regularly carries out systematic IPS observations at 327 MHz of about 200 compact extra-galactic radio sources over 1 year. Every day, line-of-sight (LOS) IPS observations of about a dozen selected radio sources are carried out so that each radio source is observed over a heliocentric distance range between 0.26 and 0.82 AU, corresponding to the solar elongations between 15° and 55°, over 1 year. The IPS observations from the four stations have been utilized to determine solar wind velocities and scintillation indices [105, 106]. For this study, the daily values of the scintillation index from 1983 to 2022, spanned over solar cycles 22–25, have been utilized. The data had a one-year data gap in 1994 due to the addition of the fourth IPS station.

Figure 6.5 illustrates an IPS observing geometry, where **S** and **E** represent the Sun-Earth system, and **P** denotes the point where the radial solar wind intersects the LOS from Earth to a distant radio source **R**. The intersection creates a perpendicular footprint **A** on the Earth's ecliptic plane. The distance of point **P** from the Sun is measured in terms of the heliocentric distance **r**. The

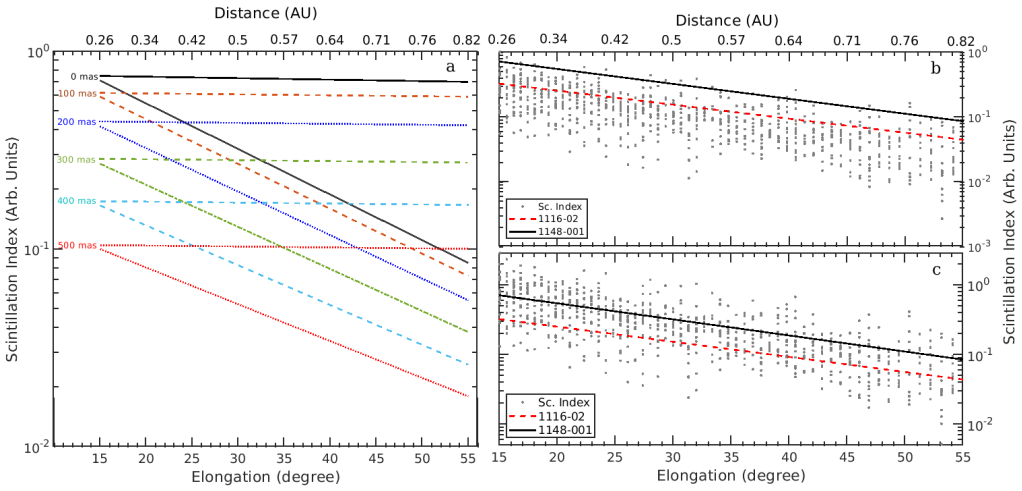

Figure 6.6: (a) The curves represent the theoretical values of variation of the Scintillation index (m) as a function of solar elongation, computed utilizing the Marians 1975 model. The grey dots in the (b & c) represent the normalized measurements of the scintillation indices of the source 1116-02. The solid black curve in each panel indicates the theoretical value of the m for the source 1148-00 computed using [3]. The red dashed line in the top two panels (b & c) indicates the best fit of the Marians model for source 1116-02. The panel in the middle shows data of 1116-02 after the multiplication by a factor such that the effects of source size on the data are removed.

dashed lines in Fig.6.5 are in the ecliptic plane, while the solid lines are out of the ecliptic plane. The angles ϵ and γ represent the radio source's solar elongation and heliographic latitude. The incoming plane electromagnetic waves from the distant radio source along the LOS to the Sun and the Earth undergo diffraction and scattering due to the intervening solar wind plasma, resulting in the phase modulation of the waves and amplitude variations in the radio signal intensity, which is known as IPS [3, 100–104]. The ground-based telescope observes the intensity fluctuations the compact point-like radio sources exhibited due to the IPS phenomenon. The fluctuations can be quantified by a parameter called scintillation index (m), which is defined as the ratio of the scintillating radio flux to the mean observed radio flux, $m = \Delta I/\langle I \rangle$. The IPS observations carried out at 327 MHz at ISEE, facilitated by the action of the Fresnel filter, inherently filter out the large-scale solar wind density fluctuations caused by solar activities such as coronal mass ejections (CMEs) and solar flares, with typical scale sizes of density irregularities ranging from 10^4 to 10^7 km. This allows tracking small-scale solar wind electron density fluctuations of scale sizes $\leq 10^3$ km both within and outside the ecliptic. In addition, the IPS observations of the intensity fluctuation depend on the heliospheric distance due to the rotation and revolution of Earth, which results in multiple LOS observations of the extra-galactic radio source with different heliospheric distances. This allows to probe the solar wind in the interplanetary medium over a broader range of heliocentric distances, between 0.26 to 0.82 AU, covering the whole inner heliosphere [103, 107–109].

The photospheric magnetic field is known to extend into the interplanetary medium, forming the heliospheric magnetic field (HMF) [110,111]. The low-plasma beta nature of the solar corona results in a frozen-in condition for the HMF that allows it to be dragged out to 1 AU and beyond by the solar wind plasma. Thus, any long-term change in the photospheric magnetic field is expected to be exhibited by the density irregularities present in the solar wind plasma. The IPS measurements of the scintillation index, which represents the changes in the solar wind density turbulence level in the inner heliosphere, are ideal for studying the signatures of long-term temporal variations of the photospheric magnetic field.

For an ideal point source, the values of the scintillation index, m, gradually increase with a decrease in the heliospheric distance "**r**" until a distance where the m becomes unity. This distance is known as turnover distance. At 327 MHz, the turnover distance is 0.26 AU. Thereafter, the values of m start to decrease again, going below unity. The regime beyond the turn-over distance is known as the weak scattering regime, where m is a function of heliocentric distance. In addition, with an increase in source size, the values of m also decrease. However, the values of m must be independent of heliocentric distance and source size when studying their temporal variations. For a steady-state solar wind, the values of "m" in a weak scattering regime can be obtained using a solar wind model by assuming a power-law distribution of solar wind density irregularities in the interplanetary medium for any given radio source size and heliocentric distance **r** [3]. Figure 6.6a shows the theoretically computed values of m at 327 MHz for different source sizes using the Marians model. It is clear from Figure 6.6a that the values of m are functions of solar elongations (or heliocentric distances). The value of m is unity at the turn-over distance of 0.26 AU for a radio source size of 0 milliarcsec (mas). It decreases below the unity as the heliocentric distance increases. Similarly, with the increase in the source size, *i.e.*, for source sizes of 100, 200, 300, 400, and 500 mas, the value of m at the turnover distance further decreases progressively below the unity. To make m as heliocentric distance independent, as described in [104], the m value must be normalized by that of a point source at each heliocentric distance. Normalizing in this manner, all the values of m can be made heliocentric distance independent, as shown for different source sizes in Fig.6.6 in color parallel lines. Similarly, to remove the effect of source size dependency of m, a normalization was carried out as in [112]. A least square minimization determined which of Marian's curves best fits a given source size. Then, the normalization was carried out by multiplying the observed values of m at each elongation for all other sources with a factor, which is equal to the difference between the best fit of Marian's curve for a given source and the best fit of Marian's curve for a point source. Figure 6.6b demonstrates the source size normalization. The upper panel of Fig.6.6b shows, by filled blue dots, a plot of m as a function of heliocentric distance for a selected source 1116-02. The solid black line is Marian's curve for a point source (1148-001). The 1148-001 is considered an ideal point source as systematic IPS observations from the Ooty Radio Telescope [113] at 327 MHz, [175] have reported a source size of ∼12 mas for 1148-001, while VLBI observations have also reported an angular size of 10 mas [114] for 1148-001. The dashed red line best fits the data for 1116-02. On the other hand, the lower panel of Fig.6.6b plots the same sources after removing the source size effect. After normalization, the solid black line, Marian's curve for the point source 1148-001, best fits the filled blue dots, the 1116-02 radio source data.

The IPS observations from ISEE, Japan, have over 200 radio sources. We prepared a uniform data set by selecting only those radio sources for which the data is available for the full period 1983 – 2022, and have at least 400 observation points. Using this selection criterion, we ended up with 27 radio sources for which the source size normalization was carried out as described in Fig.6.6b. Once the angular size dependency of m values was removed, the distance normalization was carried out as described in Fig.6.6a.

6.3 Result and Discussion

6.3.1 Solar Magnetic Fields

Figure 6.7 plots the NSO/KP and calibrated GONG magnetic fields together for Feb. 1975 – Mar. 2024, covering solar cycles 21 – 25. The panels (a, b) of Fig.6.7 plot the fields for the northern hemisphere, while the panels (c, d) of Fig.6.7 plot the fields for the southern hemisphere. The filled black dots in each panel are Carrington rotation's averaged magnetic field estimates.

The solid curve in red in each panel shows the smooth variation of magnetic field estimates. The vertical dashed lines demarcate the solar cycles 21 – 25. The panels (a, c) of Fig.6.7 show the solar cycle variation of total (absolute) photospheric toroidal field strength for the northern and southern hemispheres. The monthly averaged smoothed variation of hemispheric SSN is overplotted in the panels (a, c) of Fig.6.7 in the solid curves in blue. It is clear from Fig.6.7(a,c) that the temporal behavior of total photospheric toroidal field corresponds to the temporal variation in hemispheric SSN. A strong sunspot cycle modulation with an average period of 11 years is observable for both the northern and southern toroidal fields. It is apparent from panels (a, c) of Fig.6.7 that the toroidal field strengths of the ongoing solar cycle 25 is going to be stronger than the toroidal field strengths of the solar cycle 24 for the respective northern and southern hemispheres. Also, it is seen from (a, c) of Fig.6.7 that the toroidal field strength returns to a minimum value at each solar minimum. The minimum value of the total toroidal field in each cycle from solar cycles 20–22 is the same. This is the floor value of photospheric toroidal fields. It is similar to the existence of a floor value for the solar wind magnetic field. It can be seen that the strength of the toroidal field during the minimum of solar cycle 23 went down well below the floor value of the photospheric toroidal field, indicating a reduced floor level for the photospheric toroidal field. However, in the minimum of solar cycle 24, the strength of the toroidal field has increased again, compared to the minimum value of the photospheric toroidal field as found for solar minima of cycles 20–22.

On the other hand, the panels (b, d) of Fig.6.7 show the solar cycle variation of the photospheric polar field strengths for the northern and southern hemispheres. Unlike the photospheric toroidal fields, in the case of the photospheric polar fields, the signed value (without absolute) of the field strength was estimated. It is apparent from panels (b, d) of Fig.6.7 that the strength of photospheric polar fields shows a sunspot cycle modulation with its value being minimum at the solar cycle maximum and maximum at the solar cycle minimum. Further, the value of field strength crosses over the zero line, causing a solar polar reversal at the maximum of each solar cycle. The time of solar polar reversal for cycles 21 – 25 is indicated by short blue vertical bars. As already pointed out by earlier studies [150, 151, 154], the solar polar reversal in each cycle from cycle 21 to 24 exhibits a hemispheric asymmetry. Also, it is noteworthy that the solar polar reversal in cycle 24 is unique, with a clean and single solar polar reversal happening in the southern hemisphere around mid-2013. In contrast, the polar reversal in the northern hemisphere was started earlier in June 2012. Still, it was delayed due to the hovering of the polar fields around zero value and only being completed in 2014 [154]. After the polar reversal of cycle 24, the field strength of solar polar fields approached its maximum at the minimum of cycle 24, and it was relatively stronger when compared with the field strength of solar polar fields at the minimum of previous cycle 23. Also, it is evident from panels (b, d) of Fig.6.7 that the solar polar reversal initiated in the northern hemisphere around Aug 2023, while the solar polar reversal in the southern hemisphere will happen soon. The occurrence of solar polar reversal suggests that the solar cycle 25 is approaching or in its solar maximum phase. The four-time smoothed values of WSO solar polar fields were also overplotted in blue in panels (b, d) of Fig.6.7 to compare with the NSO/GONG polar fields. It is to be noted that the WSO polar fields are widely accepted to reflect the actual behavior of solar magnetic fields in the polar region of the Sun. From Fig.6.7, it is apparent that the overall temporal behavior of NSO/GONG polar fields matches well with the WSO polar fields during solar cycles 21 – 25. However, the NSO/GONG polar fields show a slight difference in strength during solar cycle 21, and they are of the same strength during cycle 22 – 25. Therefore, a calibration of NSO/GONG polar fields was carried out for the WSO polar fields.

Fig.6.8(a) plots, in the black filled dots, the hemispheric averaged field strength of the NSO/GONG signed polar magnetic field (signed B_p), covering a period Feb. 1975 – Mar. 2024 and spanned over solar cycles 21 – 25. The hemispheric averaged polar field strength was estimated by taking

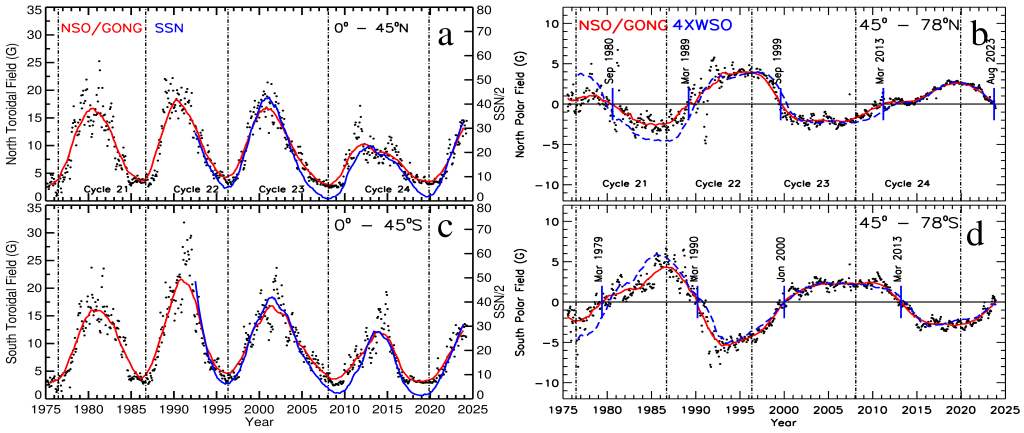

Figure 6.7: (a, c) Variation of solar surface toroidal fields in the latitude range $0° - 45°$, obtained from NSO and GONG for Feb. 1975 – Mar. 2024. covering solar cycles 21 – 25, for the northern (panel a) and southern (panel c) hemispheres. Overplotted is the smoothed monthly averaged hemispheric SSN, scaled down by a factor of 2, in solid curves in blue. (b, d) Variation of solar surface polar fields in the latitude range $45° - 78°$, obtained from NSO and GONG for Feb. 1975 – Mar. 2024, covering solar cycles 21 – 25, for the northern (panel b) and southern (panel d) hemispheres. The filled dots are Carrington rotation's (CR) averaged magnetic field estimates, while the solid curve in red represents the 13-month smoothed variation of CR averaged magnetic field estimates. The overplotted solid curve in blue panels (b, d) is the four times WSO-smoothed solar polar fields. The vertical lines in each panel demarcate the solar cycles 21 – 25. The blue vertical bars in panels (b, d) denote the period of solar polar reversal in the solar cycles 21 – 24.

an average of the solar northern and southern signed B_p, which are the surface polar magnetic fields obtained in the latitude range of 45°-78°. It is to be noted that the northern and southern signed B_p of the NSO/GONG were calibrated to the smoothed signed B_p of WSO before the estimation of the average field strength. The smoothed signed B_p of NSO/GONG is shown by a red curve, while the smoothed signed B_p of WSO is shown by a black curve. It is clear from the annual means, shown by blue open circles in Fig.6.8(a), that the overall temporal behavior of the calibrated signed B_p of NSO/GONG agrees very well with the signed B_p of WSO. A solar cycle modulation is apparent from the temporal variation of the hemispheric averaged signed B_p, with a maximum value in one solar minimum to a maximum value in another solar minimum running in between through a zero value. After a polar reversal around 2014, at the maximum of cycle 24, the hemispheric averaged field strength of the signed B_p rises to a maximum value until 2020, when the minimum of cycle 24 was begun. The averaged signed B_p strength at the solar minimum of the previous cycle acts as a precursor to the amplitude of the next solar cycle. As the average signed B_p strength at the minimum of cycle 24 is comparatively stronger than the average signed B_p strength at the minimum of cycle 23, a relatively stronger cycle 25 is expected. This is the case when we plot the smoothed SSN v2.0 data as a function of time in Fig.6.8(d) for the period Feb. 1975 – Jun. 2023, covering solar cycles 21 – 25 that shows a relatively stronger cycle 25 is in progress. After 2020, the average signed B_p strength again declines until it attains a zero value around 2024, suggesting a possible start of the polar reversal process of cycle 25.

Fig.6.8(b) plots, in the black filled dots, the hemispheric averaged field strength of the NSO/GONG unsigned polar magnetic field (unsigned B_p), covering a period Feb. 1975 – Mar. 2024 and spanned over solar cycles 21 – 25. The hemispheric averaged polar field strength, in this case, was estimated by taking an average of the solar northern and southern unsigned B_p. The unsigned B_p are the surface unsigned (total) polar magnetic fields obtained in the latitude range of $45° - 78°$. It is to

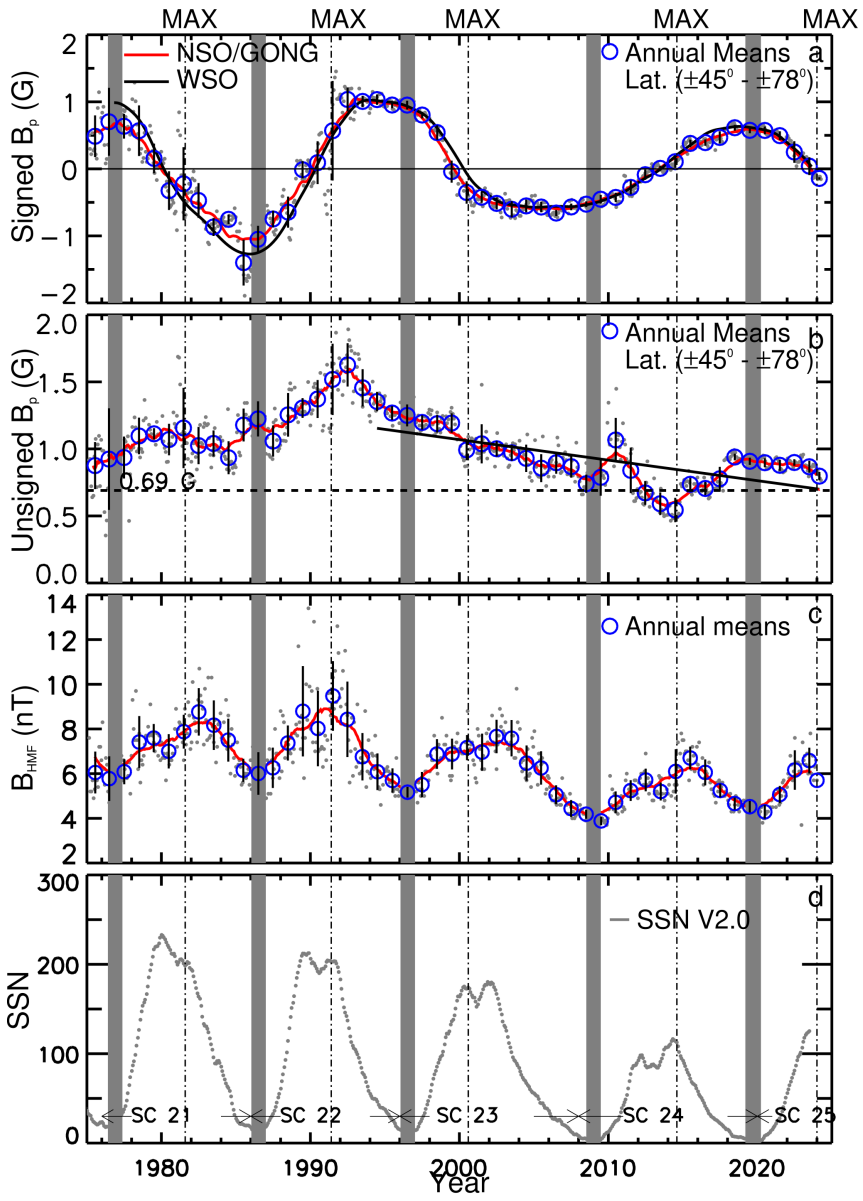

Figure 6.8: a) The signed field strength of the calibrated solar photospheric fields (Signed B_p) from NSO/GONG in the latitude range 45° – 78°, spanning the period Feb. 1975 – Mar. 2024. The smoothed NSO/GONG polar and WSO polar fields are overplotted in red and black. b) The unsigned field strength of the calibrated solar photospheric fields (Unsigned B_p) from NSO/GONG in the latitude range 45° – 78°, spanning the period Feb 1975 – Mar 2024. The black straight line fits the annual means between 1994 and 2024. The horizontal dotted line marks the value of the Unsigned B_p in Mar. 2024. c) The strength of heliospheric magnetic fields (B_{HMF}) at 1 AU, spanning the period Feb. 1975 – Dec 2023. d) The SSN spanning the period Feb. 1975 – Jun. 2023. The solid-filled black dots in panels (a, b, c) are the Carrington rotation's averaged data points, while the open circles in blue with 1 σ error bars are the annual means. The vertical grey bands demarcate 1-year intervals around the solar minima of solar cycles 20 – 24. The vertical dashed lines mark the solar maxima of solar cycles 21 – 25.

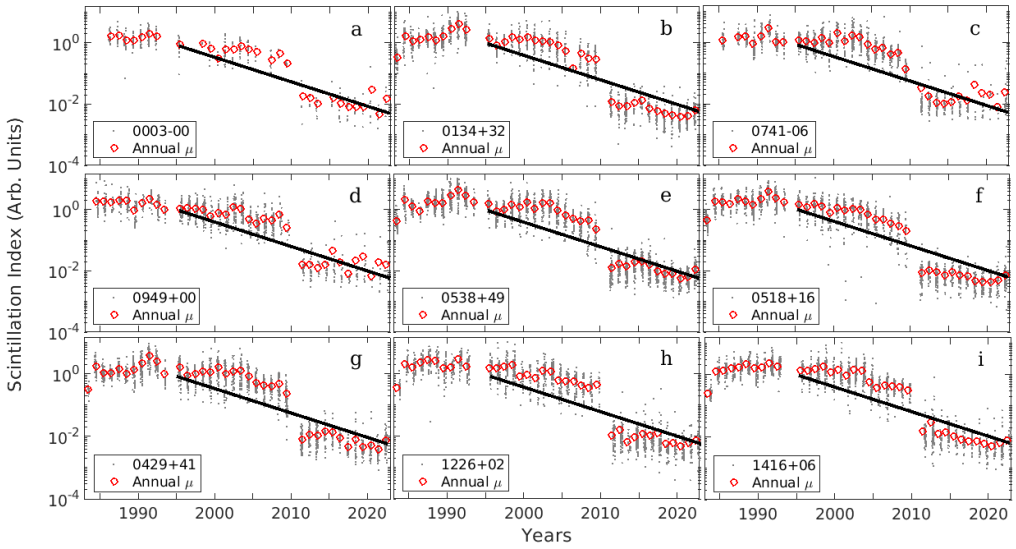

Figure 6.9: (a-i) Plots of m as a function of time during 1983 – 2022 for selected 9 sources after making m source size and heliocentric distance independent. The filled-grey dots are daily values of m after these are made independent, while the red open circles are annual means of m with 1 σ error bars. The IAU names of the radio sources are indicated at the bottom left of each panel. The solid black line is the least square fit to the observed decline in the values of m for the period 1995 – 2024.

be noted that the unsigned B_p for the northern and southern solar hemispheres were calibrated similarly to the smoothed signed B_p before the estimation of the average field strength. It is evident from Fig.6.8(b) that the strength of the unsigned B_p shows a different temporal behavior, unlike the signed B_p. A steady increase in the field strength of the unsigned B_p from the start of cycle 21 until the maximum of cycle 22 is observed from the smoothed unsigned B_p of NSO/GONG, shown by a red curve in Fig.6.8(b), and the annual means of the unsigned B_p, shown by blue open circles in Fig.6.8(b). However, a steady decline in its field strength is seen from the maximum of cycle 22 (around 1992) until the end of cycle 23 (2010). Again, at the start of cycle 24, there is an increase in the field strength of the unsigned B_p for the year 2010 – 2011. After 2011, the field strength sharply declined from 2012 to 2014, only to increase in 2015 after the solar maximum of cycle 24 until the minimum of cycle 24 (2020). Since 2020, the unsigned B_p has steadily declined again until 2024. Overall, a long-term declining trend of the unsigned B_p has begun since the mid-1990s (around 1994) and has continued until now (2024). It means that the unsigned B_p shows a steady decline in its strength for $\sim$ 30 years (nearly three solar cycles). The solid black line in Fig.6.8(b) is the least square fit to the declining trend of the unsigned B_p for all the annual means in the period 1994 – 2024. The least-square fit is statistically significant with $r = -0.70$, at a significance level of P=99%.

6.3.2 Heliospheric Magnetic Field, SSN and F10.7cm radio flux

Fig.6.8(c) plots the strength of HMF (B_{HMF}) at 1 AU for the period Feb. 1975 – Dec. 2023, covering cycles 21 – 25. The smoothed variation of B_{HMF} is plotted as shown by a red curve in Fig.6.8(c), while the annual means of B_{HMF} is plotted in blue open circles. It is evident from

Fig.6.8(c) that the strength of HMF shows a strong sunspot cycle modulation with the maximum strength during the maximum of each solar cycle. However, there is a 1-year lag between the peak time of the SSN and the B_{HMF}. Also, a global reduction in the strength of B_{HMF} during the maximum of each solar cycle is evident from Fig.6.8c from solar cycle 22 through solar cycle 23 to solar cycle 24. However, the strength of B_{HMF} in solar cycle 25 is relatively stronger than in solar cycle 24. Also, it is seen from Fig.6.8c that the HMF returns to an annual average value at each solar cycle minimum. This is known as the floor value of the solar wind magnetic field or HMF, which is the baseline heliospheric open flux from the slow solar wind flows, contributed to the surviving polar fields or the small-scale magnetic fields during the solar cycle minimum. As mentioned earlier, the floor value of HMF is found to be 4.6 nT [164], estimated based on the correlation between SSN and B_{HMF} during the solar cycles 20–22. However, as seen from Fig.6.8c, the B_{HMF} during the solar minimum of cycle 23 has decreased to ∼3.5 nT, well below the proposed floor level of 4.6 nT by [164]. On the other hand, the floor level of HMF during the solar minimum of cycle 24 has increased to a value of 4.2 nT, indicating an increase in the baseline heliospheric magnetic field during the solar minimum of cycle 24. Fig.6.8(d) plots the SSN v2.0 observations as a function of time for the period Feb. 1975 – Jun. 2023, covering solar cycles 21 – 24. As mentioned earlier, a global reduction of SSN from cycle 21 up to cycle 24 is evident from Fig.6.8d. Similarly, a global reduction of F10.7cm solar radio flux values has been observed (the plot is not shown here).

6.3.3 Interplanetary Scintillation

After making "m" independent of source size and heliocentric distance, m was plotted for all 27 sources as a function of years. Figure 6.9 (a-i) shows a plot of m as a function of years only for the selected 9 sources. The values of m for these sources cover the data period 1983 – 2022 and lie in the heliocentric distance range of 0.26 – 0.82 AU. The filled grey dots are daily measurements of m, while the red open circles are annual means of m. The IAU name of the radio source is indicated at the bottom left of each panel. It is evident from Fig.6.9 (a-i) that there has been a steady decline in values of m for all the 9 sources since around the mid-1990s. The steady decline in values of m is shown by a black solid line, which best fits the values of m for 1995 – 2022.

To show the steady decline in the m value, all the m values for all 27 sources are plotted together in Fig.6.10 again for clarity. The grey-filled dots are measurements of m, while the red open circles are annual means with 1 σ error bar. The decline in m values since 1995 is also evident from Fig.6.10. However, it is clearer that the decline in values of m is separated into two trends: one for 1995 – 2010, covering cycle 23, shown by a solid blue straight line, and the other for 2010 – 2024, covering the full solar cycle 24 and the rising phase of solar cycle 25, shown by a solid green straight line. A shift in the decline from the first to the second period is evident. This shift could well be attributed to the global reduction in the polar field strength of the unsigned B_p, which is different in solar cycles 23 and 24, as explained in Fig.6.8(b).

Fig.6.11 shows a comparison of temporal variations of (a) the unsigned B_p, (b) the values of m, (c) the detrended SSN, (d) the detrended unsigned toroidal field (B_t), (e) the detrended F10.7cm solar radio flux, and (f) the detrended B_{HMF} for the same period of 1983 – 2022, for which the values of m were used for this study. The filled grey dots are daily (panel–b) or CR-averaged values (panels–a and c–f) and the red open circles in each panel are annual means of the respective parameters. A steady long-term decline in the values of annual means of all the parameters has been evident since around the mid-1990s. A black straight line in each panel best fits the annual means for the declining period 1995 – 2022 and shows a 30-year declining trend of all the parameters that has continued for nearly three solar cycle periods. As explained earlier, the steady decline

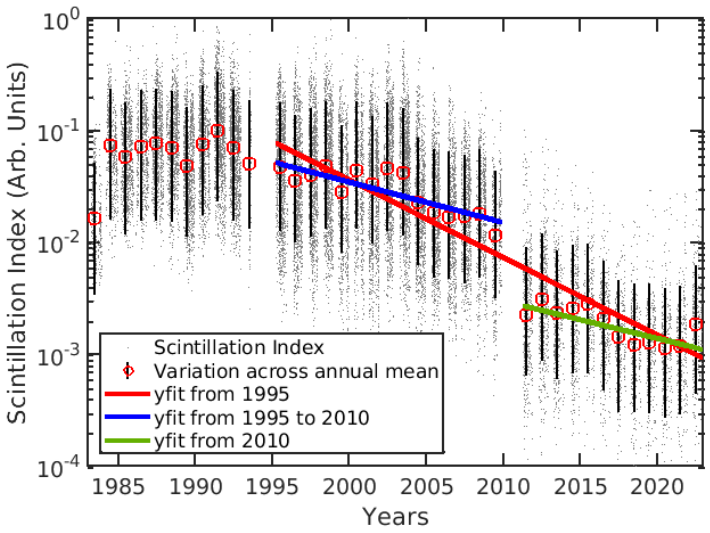

Figure 6.10: Plot of m as a function of time (1983 – 2022) for all the 27 sources after making the values of m independent of source size and heliocentric distance. The filled grey dots are daily values of m after they made independent and the red open circles are annual means of m with 1 σ error bars. The blue and green solid lines are power-law fits of the values of m for 1995 – 2010 and 2010 – 2020, respectively, while the red solid line is a power-law fit of the values of m for 1995 – 2022.

in the unsigned B_p started as early as 1994 and continued until 2014, only to increase thereafter from the year 2015 until the year 2020. However, the decline started in 2021 and has continued since then. As explained earlier, the steady decline in the values of m started in 1995 and has continued until 2022. As mentioned earlier, the two separate declining trends for the values of m could be attributed to the unusual declining trend of the unsigned B_p, which also showed a break in the continuing declining trend in the years 2010–2011. The detrended data for the SSN, unsigned B_t, F10.7cm solar radio flux, and B_{HMF} also shows a long-term declining trend, similar to the unsigned B_p and values of m, since around the mid-1990s. However, the variation of annual means additionally shows a sinusoidal variation riding on the declining trend. This indicates that the steady decline observed in the values of m in the inner heliosphere is more consistent with the declining photospheric field strength of the unsigned B_p confined to the latitude above 45°.

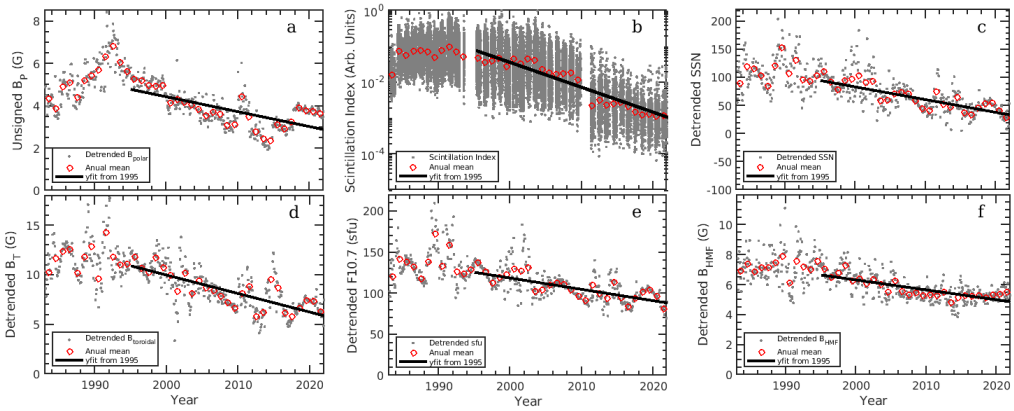

Figure 6.11: Plots for variation of (a) the unsigned B_p, (b) the scintillation index, (c) the detrended SSN, (d) the detrended unsigned B_t, (e) the detrended F10.7cm solar radio flux, and (f) the detrended B_{HMF} for the period 1983 – 2022. The filled grey dots in panels (a) and (c–f) are CR averaged values of the respective parameters, while the filled grey dots in panels (b) are daily values of the scintillation index. The red open circles in each panel are annual means. The black straight line best fits the annual means for the period 1995 – 2022.

6.4 Conclusions

6.4.1 Summary

Our present study extensively investigated solar activity parameters and indices such as SSN, solar photospheric toroidal and polar magnetic fields, solar wind microturbulence level at 327 MHz, F10.7cm solar radio flux, and HMF at 1 AU. SSN, F10.7cm solar radio flux, and HMF at 1 AU are direct measurements obtained for 1975 – 2024, spanned over solar cycles 21 – 25. The study of solar photospheric magnetic fields using ground-based synoptic magnetograms from NSO/KPVT, NSO/SOLIS, and GONG for a combined period of 1975 – 2024 and spanned over solar cycles 21 – 25 showed a contrasting trend in unsigned solar photospheric toroidal and polar fields. The unsigned solar toroidal field data showed a solar cycle modulation, whereas the unsigned solar photospheric polar fields showed a steady decline since around the mid-1990s, and the trend was continued until the maximum of solar cycle 25. The declining activity trend was found global in nature when the solar wind microturbulence level was investigated using the IPS measurements from the ISEE, Nagoya University, Japan, covering the period 1983 – 2022, which also revealed a steady decline as well in their values since around the mid-1990's. The declining trend in the solar wind microturbulence level continued until the end of the data period, *i.e.,* 2022, in synchronous with the solar photospheric polar fields.

In addition to the global declining nature of solar activity, it is observed that the floor value of the solar photospheric magnetic field was reduced during the minima of solar cycle 23. A similar reduction in the floor value of solar wind magnetic field was also observed during the minima of solar cycle 23, around 2008–2009. The floor levels during the minimum solar cycle 23 were breached and went well down the previous floor values for both the photospheric and solar wind magnetic fields. However, the floor levels were recovered in the minimum of solar cycle 24, but the floor values were still lower than observed during solar cycles 20 – 22. On the other hand, the signed polar field strength showed no such declining trend but rather a solar cycle modulation in its field strength. However, it was found that the signed polar field strength was stronger in the minimum of cycle 24 than in the minimum of cycle 23. Although all the solar activity parameters except the

unsigned polar fields and solar wind microturbulence levels also showed a declining trend when we plotted their corresponding detrended data.

In addition, a hemispherically asymmetric polar reversal was evident for the signed polar field during solar cycles 21–25. Particularly, the polar reversal in solar cycle 24 was unique, with a single clean reversal in the southern hemisphere completed 1.5 years earlier than in the northern hemisphere, whereas the polar reversal process in the north solar hemisphere started earlier but was completed later because of a sustained period of near-zero polar field conditions for around 1.5 years. On the other hand, the polar reversal in the ongoing solar cycle 25 was completed in the northern hemisphere around August 2023. However, the polar reversal in the southern hemisphere is still in process and is yet to complete

6.4.2 Discussions

The signatures of the long-term behavior of photospheric fields are expected to be reflected in the solar wind magnetic field, as they are extensions of photospheric polar fields providing most of the heliospheric open flux during the solar minimum [110]. The solar wind magnetic field is then frozen in the solar coronal outflow, carried out by the solar wind flow into the inner heliosphere [111]. The scintillation index, as derived from IPS observations, measures the level of solar wind turbulence resulting from the relative electron density fluctuations and large-scale magnetic field fluctuations found in the solar wind [102]. Also, there exist a causal relation between the stronger photospheric magnetic fields over the polar region and the solar wind turbulence [104]. Hence, the steady decline observed in the values of the scintillation index in the inner heliosphere can be the inner heliospheric signature of the long-term decline behavior of photospheric polar fields. A similar global decrease in photospheric, coronal, and radial solar wind magnetic field strength during solar cycles 21 – 25 was reported in [155].

A floor level for the photospheric magnetic field was recently proposed by [165], based on the combined magnetic field estimates from the Magnetic Doppler Image (MDI) on board Solar and Heliospheric Observatory and the Helioseismic and Magnetic Imager (HMI) onboard Solar Dynamics Observatory (SDO) and the existence of a baseline F10.7cm solar radio flux. Also, the reduction in the floor level of the solar wind during the minimum of cycle 23 prompted [163] to suggest a revised floor level of 2.8 nT for HMF. It is to be noted that the [176] reported that the floor level for HMF was well below around 1.5 nT during the Maunder minimum period. The reduction in the floor level of the solar photospheric field and solar wind magnetic field during the solar minimum of cycle 23 agrees with the global decreasing trend observed for the solar polar fields and solar wind turbulence level that started in 1995 and continued until 2009. The observed increase in photospheric polar fields and solar wind turbulence level after 2010 is why the floor level of the HMF has increased from 2.8 nT back to 4.2 nT during the minimum of solar cycle 24.

A study of hemispherically asymmetric polar reversal in the ongoing solar cycle 25 [155] has reported that the reversal process in solar polar fields (poleward of $\pm 60^{\circ}$) has been completed for both the poles. Also, the authors reported the occurrence of a more symmetric polar reversal as compared to the previous solar cycle 24. This indicates that symmetric or regular solar activity can be expected in solar cycle 25, unlike the earlier solar cycles 23 and 24, which showed unusual solar activities. The amplitude of the upcoming solar cycle is strongly correlated [177] with the solar polar field and the heliospheric field at the solar minimum [164]. The relatively stronger solar polar field and HMF strength at the end of solar cycle 24 as compared to the previous solar cycle 23 suggest that the amplitude of solar cycle 25 would be comparatively stronger than the amplitude of solar cycle 24. Even with a stronger solar cycle 25, the continuing global trend in

solar magnetic and solar wind activities can't rule out the claim [109] that we are heading into a grand minimum beyond solar cycle 25.

Chapter 7

Relative density fluctuation of the solar wind with the help of interplanetary scintillation and PSP density measurements

Adapted from: ***Harsha Avinash Tanti***, *Susanta Kumar Bisoi, and Abhirup Datta, Relative density fluctuation of the solar wind with the help of interplanetary scintillation and PSP density measurements, Submitted, The Astrophysical Journal Letters*

7.1 Introduction

The solar wind is a natural laboratory for studying magnetohydrodynamic turbulence (MHD), offering insights into the evolution and dissipation of turbulent energy across spatial scales [178–183]. As the solar wind moves away from the Sun, its properties change, providing an opportunity to observe how MHD turbulence develops and dissipates across different spatial scales [184]. Closer to the Sun, at around 0.14 AU ($\sim 30R_{\odot}$), the solar wind is in its early expansion phase, where turbulent structures are strongly influenced by solar surface processes and intense interactions between magnetic fields and plasma [184–186]. As the solar wind extends to 1 AU ($\sim 215R_{\odot}$), it becomes more developed, and the turbulence may shift from nonlinear interactions to larger-scale structures [40, 184, 187, 188].

Early studies have documented turbulent density fluctuations in the solar wind within this range of distances from the Sun. These fluctuations reveal how the electron density spectrum changes over large distances, which is key to understanding the dynamics of solar wind turbulence [40, 183, 187–193]. Density variations in the solar wind are often considered accurate indicators of solar wind velocity. Additionally, in MHD turbulence models, it is observed that the fluctuations are primarily driven by the magnetic field and plasma velocity, with the influence of density fluctuations being minimal or completely negligible [194–197]. Moreover, observations of turbulent density fluctuations often show a scaling pattern in wavenumber space that aligns with the Kolmogorov theory. This is valid in the absence of magnetic field for incompressible fluid. Thus, theories of MHD turbulence and the implications of compressibility (due to turbulent density fluctuations)

are a topic of considerable discussion [3, 15, 198–200]. Therefore, by studying the density fluctuation in the solar wind can reveal the contribution of compressibility in the turbulent solar wind. Specifically, investigating the radial evolution of the density modulation index is crucial because it serves as a significant indicator in comprehending turbulent dissipation and the resulting local heating of the solar wind [201]. This density fluctuation index ($\epsilon_N = \Delta N/N$) is defined as the ratio of turbulent density fluctuation (ΔN) to the background density (N) [15, 197]. The ϵ_N is one of the important parameter for estimating amplitude of the density turbulence spectrum (C_N^2) [202]. This understanding is crucial for interpreting the angular broadening of radio sources due to solar wind turbulence [203, 204], and for explaining the relatively low brightness temperatures of the solar corona at wavelengths in meters to decameters range [202]. Moreover, ϵ_N additionally serves an important role in regulating the heliospheric propagation of energetic electrons generated by solar flares and other explosive solar surface phenomena [205].

Recent studies using in-situ observations, such as those from PSP, reveal turbulent behaviour of the solar wind in the inner heliosphere. Turbulence, especially on smaller scales, is observed to be influenced by various ion instabilities, contributing to both heating and dissipation of energy in the solar wind [206]. Observations from PSP have also shown that non-Maxwellian electron distributions, ion-scale turbulence, and magnetic field fluctuations play critical roles in the evolution of solar wind turbulence closer to the Sun [207, 208]. Also, hybrid simulations of solar wind-like turbulence have highlighted the importance of compressible modes, which can lead to local heating and energy dissipation in regions of enhanced turbulence [209]. Furthermore, interplanetary scintillation (IPS) data have provided key insights into solar wind disturbances, particularly during periods of increased solar activity [30]. The combination of IPS and in-situ measurements offers a powerful method for studying the radial evolution of both density and magnetic field fluctuations, especially in the context of large-scale solar wind disturbances such as coronal mass ejections (CMEs) [210, 211].

In this study, we leverage both IPS measurements and PSP observations to explore the radial evolution of the density modulation index (ϵ_N) and the magnetic field modulation index (ϵ_B) between 0.3 AU and 0.8 AU. For the first time, we systematically compare ϵ_N estimates derived from two different methodologies: scintillation measurements from the Institute for Space-Earth Environmental Research (ISEE) multi-station IPS observatory in Japan, and in-situ measurements from PSP. This analysis covers the period from October 2018 to January 2022, providing a detailed investigation of the evolution of solar wind turbulence over the range of heliospheric distances.

7.2 Interplanetary Scintillation (IPS)

Interplanetary Scintillation (IPS) refers to the fluctuation of electromagnetic signals from distant radio sources caused by solar wind in the interplanetary medium. IPS is used to remotely study solar wind propagation within the solar system. Figure 7.1 illustrates how plane waves from a radio source (R) are disturbed by the solar wind as they travel toward Earth (E). This interaction is modeled using phase screen theory, which treats the solar wind as a thin plasma slab that induces phase variations in the waves [39, 212]. The effect of solar wind on these waves is strongest near the Sun and is inversely proportional to the fourth power of the Earth-source distance [15, 212, 213]. At 327 MHz, IPS observations can detect solar wind electron density fluctuations on scales of about 1000 km, covering a wide range of heliospheric distances [214–217]. Large-scale density variations, like those caused by coronal mass ejections (CMEs), range from 10^4 to 10^7 km, while the Fresnel filter primarily highlights small-scale fluctuations around 10^3 km, where Earth lies within the Fresnel zone. The phase variation ϕ_{rms}, which is critical to IPS analysis, depends

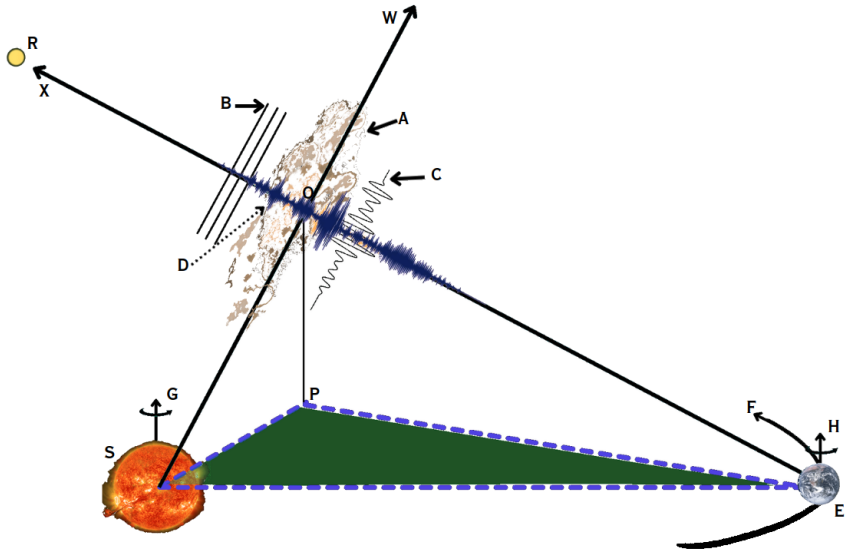

Figure 7.1: Pictorial depiction of IPS phenomenon. Here, S is the Sun and E is the Earth, A is the outwards flowing solar wind in SW direction and R is a distant point source (Radio source). XOP indicates line of sight (LOS) of the observation of R from E passing through A intersecting SW at O. B is a pictorial representation of plane wave emitted from the R which undergoes phase variations and is then translated to amplitude variation at the fraunhofer region indicated by D and C and ΔSPE is a triangle on the epileptic plane. H and G indicates the rotational axis of E and S respectively. F indicates the revolution path of the earth.

on several factors including observational wavelength λ, plasma screen thickness L, and plasma density turbulence ΔN [15]:

$$\phi_{rms} = (2\pi)^{\frac{1}{4}} \lambda r_e (aL)^{\frac{1}{2}} [< \Delta N^2 >]^{\frac{1}{2}} \tag{7.1}$$

This phase variation is related to the scintillation index m by [15]:

$$m = \sqrt{2}\phi_{rms} \tag{7.2}$$

7.3 Data Analysis

In this Letter, to estimate the density modulation index ($\epsilon_N = \Delta N/N$), three different methods are analysed and compared. Wherein, level 2 data products obtained from the Solar Probe Cup (SPC) instrument, part of the Solar Wind Electrons Alphas and Protons (SWEAP) experiment on board the Parker Solar Probe (PSP) [218–220] is used. Along with the scintillation measurements provided by the Institute for Space-Earth Environmental Research (ISEE) [221–223] and Solar wind density measurements obtained from the OMNI2 database (http://gsfc.nasa.gov/omniweb). In the first method the ϵ_N is estimated using the method depicted in [15]. Wherein, the density fluctuation (ΔN) is initially determined utilizing scintillation values, followed by the estimation of ϵ_N through the ratio of ΔN to the mean density (N) at the specific heliospheric distance. In the method by [15], the mean density (N) is estimated by extrapolating the density measurements carried out at 1AU using [7] method. Whereas in the second method, following the approach by [15], the mean density (N) is substituted with measurements obtained from the PSP. In contrast,

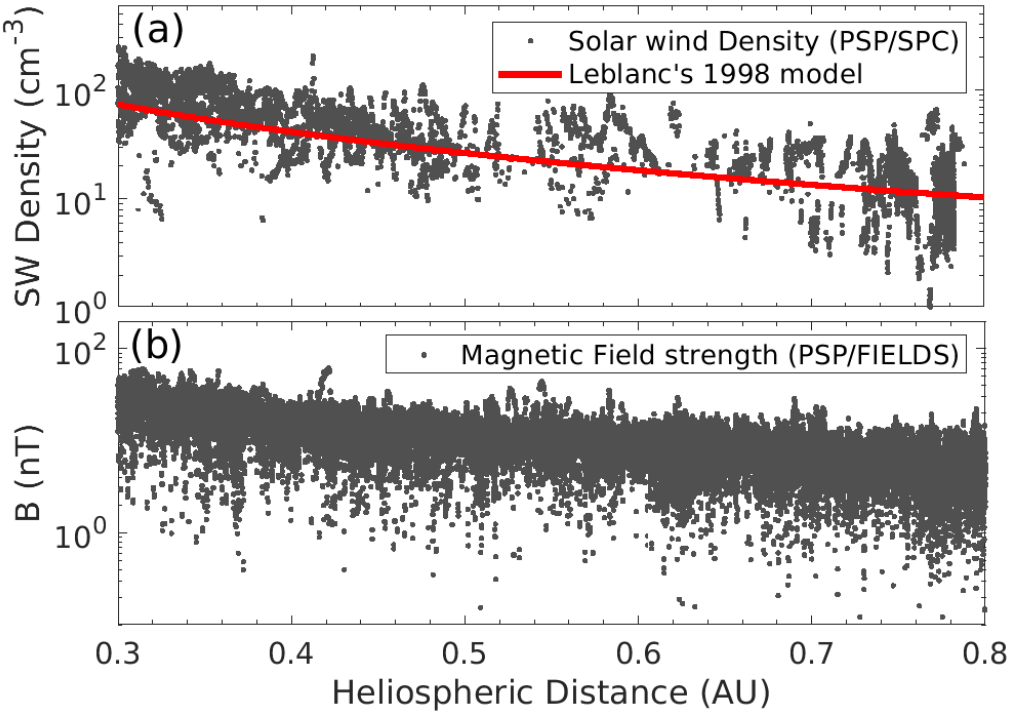

Figure 7.2: Solar wind density data was collected with the PSP/SPC and PSP/FIELDS instruments. The top panel (a) depicts the radial evolution of solar wind density via in-situ observations using the PSP/SPC instrument, indicated by gray dots, alongside the solid red line representing the [7] model. The bottom panel (b) demonstrates the radial evolution of the heliospheric magnetic field based on in-situ measurements taken with the PSP/FIELDS instrument.

the third method follows [197] and employs PSP measurements to determine ϵ_N, where ΔN is calculated by deducting the mean density from the observed density values. Moreover, to investigate the relationship between the magnetic field and density fluctuation, the magnetic field modulation index ($\epsilon_B = \Delta B/B$) is also estimated using observation from the PSP/FIELDS experiment. Further, the analysis covers the period from October 2018 to January 2022, ensuring data overlap within the heliospheric distance in the range of 0.3 to 0.8 AU.

Figure 7.2(a) shows the radial evolution of the solar wind and the magnetic field strength obtained from the PSP/SPC and PSP/FIELDS isntruments. Also, it is evident that the density of the plasma cloud is linearly decreasing in logarithmic scale with increasing radial distance. Further the Figure 7.2(a) shows that the density evolution is consistent with [7] extrapolation model for solar wind plasma density. This model suggests that the solar wind density (N) follows an inverse power law relationship with heliospheric distance (R), expressed as $N \propto R^{-p}$. In logarithmic scales, this translates to a straight line with a constant negative slope ($-p$). If Figure 7.2(a) shows the plasma density declining with a constant slope on a logarithmic scale with increasing radial distance, it aligns with [7, 208]. The constant slope would correspond to the power law exponent ($-p \approx 1.96$) and signifies a consistent rate of decline in plasma density as we move farther from the Sun [208]. Moreover, from Figure 7.2(b) it can be observed that the radial evolution of the heliospheric magnetic field is proportional the to the solar wind density. Suggesting that the magnetic field lines moving along with the density, as if they frozen-in [184, 191].

7.4 Results & Discussion

The radial evolution of the ϵ_N is crucial for understanding not only the dissipation of the turbulence but also the local heating within the solar wind [15, 197, 201]. However, the propagation of energetic electrons produced by solar flares and other energetic phenomena on the Sun's surface could be significantly influenced by the radial evolution of ϵ_N, since variations in turbulence and magnetic field structures along their path can alter their trajectories, energy distribution, and eventual interaction with the interplanetary medium [15,197,205,224]. Understanding this relationship is essential for accurately modeling particle transport and predicting space weather effects caused by solar activity. As discussed in Section 7.3, estimating ϵ_N requires both the density fluctuation (ΔN) and the background density (N). Wherein, ΔN can be derived from multistation interplanetary scintillation (IPS) observations, such as those conducted by the Institute for Space and Astronautical Science (ISEE) in Japan [15]. However, it is well established that IPS measurements depend on the radial distance from the Sun to the Line-of-Sight (LOS) of the source, as noted in earlier studies [15, 39, 213, 225]. In addition, a comprehensive analysis by [15] revealed that the magnitude of the IPS values is also influenced by the angular size of the source.

In contrast to IPS, which probes density variations along the LOS, in-situ measurements from spacecraft such as the Parker Solar Probe (PSP) provide direct measurements of the solar wind plasma. Observations and numerical Magnetohydrodynamic (MHD) simulations suggest that both the density fluctuation (ΔN) and the background density (N) exhibit an exponential decrease with radial distance from the Sun [181]. This behavior of N is likely reflected in the bottom panel of Figure 7.2 bottom panel, which displays solar wind density data obtained by the PSP's Solar Wind Plasma Composition (SPC) instrument. Wherein, it is evident that the density of the plasma cloud is linearly decreasing in logarithmic scale with increasing radial distance. [226] suggests that in a perfectly steady solar wind with a constant outward velocity then the magnetic flux density inversely with the square of the heliospheric distance. Furthermore, from the in-situ density measurements, as shown in Figure 7.2 bottom panel, it is evident that there is a linear decrease in a logarithmic scale suggesting a power-law relationship. This pattern might be attributed to variations in the solar wind speed or the presence of solar wind streams with differing magnetic field strengths [227].

Prior to the Parker Solar Probe (PSP) mission, estimating the background density (N) one of the crucial element for ϵ_N relied upon extrapolations derived from in-situ density measurements conducted at 1 AU [7, 15]. These extrapolations predominantly utilized the model proposed by [7], which assumed a specific power-law decline in solar wind density with radial distance. The launch of PSP in August 2018 enabled us to perform in-situ measurements to investigate the solar wind in close proximity to the Sun. Through these in-situ measurements obtained by PSP's Solar Wind Plasma Composition (SPC) instrument provides a more direct and reliable means of determining the background density (N) at heliospheric distances between 0.3 to 0.8 AU (see Figure 7.2, bottom panel). Thereby, providing an opportunity to verify the ϵ_N estimation using the extrapolation method. Figure 7.3 top panel shows the ϵ_N estimated using extrapolation method whereas the bottom panel shows the ϵ_N estimated using the in-situ readings by PSP. Intriguingly, despite the inherent limitations of extrapolations, it is noteworthy that the central tendency of the ϵ_N values derived from PSP data aligns closely with those obtained from the [7] model.

Using the IPS measurements provides estimates for the ϵ_N however, ϵ_N can also be directly calculated using the number density data by the PSP as discussed in Section 7.3. The top panel of Figure 7.4 shows the variation of ϵ_N as a function of heliospheric distances calculated using in-situ measurements by PSP. Whereas, the bottom panel shows the radial evolution of ϵ_B, which is the ratio of the magnetic field variation to the median radial magnetic field measure at that

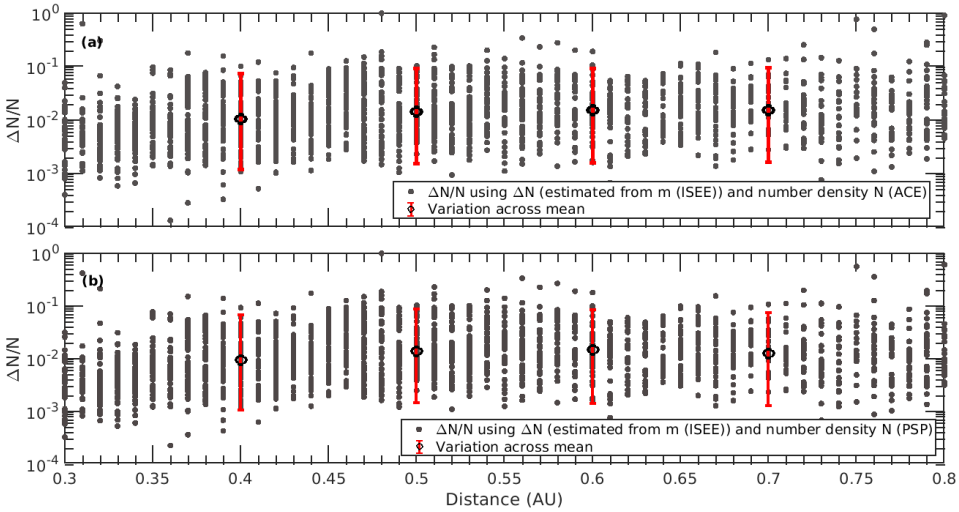

Figure 7.3: The image on the top panel shows the variation of the density modulation index (ϵ_N=$\Delta N/N$) with respect to heliospheric distance wherein the background density is estimated using the extrapolation method (see Section 7.3). Whereas, the image on the bottom panel shows the ϵ_N variation calculated using in-situ observation obtained from the PSP.

particular heliospheric distance. It is observed from Figures 7.3 and 7.4 that the mean variation of the ϵ_N and ϵ_B remains constant over the heliospheric distance. Furthermore, it is observed that the mean ϵ_N estimated using the scintillation reading differs from the mean ϵ_N estimated using in-situ observations by PSP by $\sim 10^{-1}$ order (refer to Figures 7.3(a) and 7.4(a)). Upon examining ϵ_N with in-situ observations, it is evident that the mean ϵ_N remains steady across the heliospheric distance from 0.3 to 0.8 AU, with values ranging between 0.15 and 0.21. A similar trend is noticed when ϵ_N is determined using scintillation observation; however, the mean values fall within the range of 0.01 to 0.016. Therefore, there is an observed difference ranging from 10 to 15 times between in-situ and remotely estimated ϵ_N. The study by [15] demonstrated through analysis of ϵ_N estimated using scintillation data that the density modulation index is constant regardless of heliospheric distance, consistent with findings by [228]. Present analysis with in-situ observations also indicates that both ϵ_N and ϵ_B are independent of heliospheric distance. It is established that Earth-based scintillations are influenced by the Fresnel filter function. Due to this function, IPS observations at 327 MHz allow for the probing of solar wind electron density fluctuations of scales $\geq$1000 km [214–216] and across various heliospheric distances in the inner heliosphere [189]. Since the length scales examined by the IPS technique fall within the inertial range, it is plausible to infer that the magnetic field remains frozen in, thus allowing density fluctuations to serve as a proxy for magnetic field fluctuations [15, 191]. The proportional trend of the modulation indices ϵ_N and ϵ_B in Figure 7.4 further implies that the magnetic field is frozen in.

7.5 Conclusion

The present study has investigated the radial evolution of the density modulation index (ϵ_N) and magnetic field modulation index (ϵ_B) in the inner heliosphere. The analysis, conducted using comprehensive IPS measurements and in-situ observations from PSP, reveals a discrepancy of approximately 10-15 times between the ϵ_N estimates derived from remote sensing and in-situ

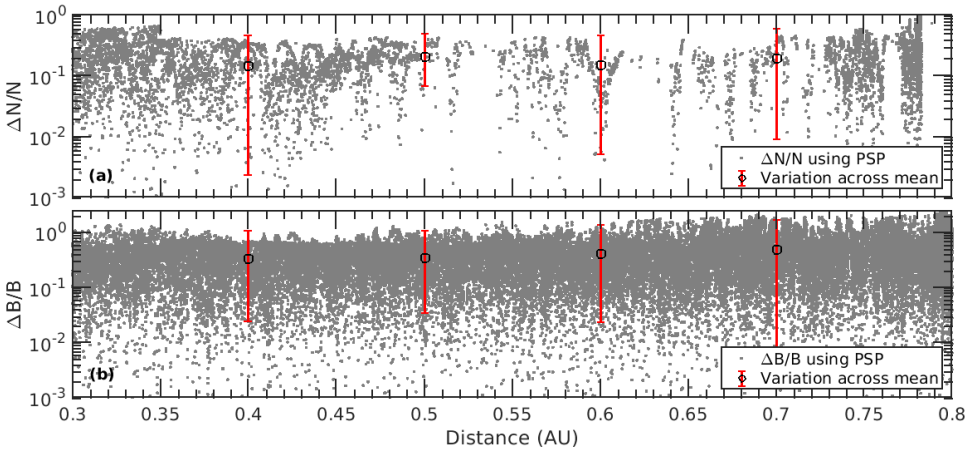

Figure 7.4: The top panel in the image shows the variation of density modulation index (ϵ_N) as a function of heliospheric distances and the image in the bottom panel shows the evolution of the magnetic field modulation index (ϵ_B) in-situ measurements from PSP.

methods. This discrepancy can be attributed to the distinct scales probed by these techniques: IPS measurements capture larger-scale fluctuations ($\geq$1000 km), while in-situ measurements capture smaller-scale variations. Furthermore, the study demonstrates that both ϵ_N and ϵ_B exhibit minimal variation with heliospheric distance, suggesting a consistent level of turbulence within the investigated range. This observation supports the notion of a frozen-in magnetic field, where the magnetic field is tightly coupled to the plasma, leading to proportional fluctuations in density and magnetic field.

Chapter 8

Summary and Future scope

8.1 Summary

This thesis presents a comprehensive investigation into low-frequency radio astronomy, mainly focusing on the frequency range below 30 MHz, where observations are limited due to ionospheric opacity and terrestrial radio frequency interference (RFI). The research is structured into eight chapters and explores key areas such as ground-based and space-based instrumentation, direction-of-arrival (DoA) algorithm development, machine-learning applications, and heliospheric studies. The findings of this work significantly contribute to the broader understanding of low-frequency radio astronomy, addressing both scientific opportunities and technical challenges associated with this field.

The motivation for this research stems from the immense scientific potential of low-frequency observations. The spectrum below 16 MHz enables us to explore the interplanetary medium (IPM) with its dynamic solar wind and high-energy events like Coronal Mass Ejections (CMEs) and Solar Flares (SFs), the redshifted 21 cm line from the early universe, Auroral Kilometric Radiation (AKRs), Earth's magnetosphere and geotail, galactic and extragalactic emissions. Observing these phenomena provides valuable insights into astrophysical processes and space weather dynamics. However, ground-based observations face severe limitations due to ionospheric effects distorting and blocking signals below 30 MHz. To overcome these challenges, space-based observation techniques are necessary. The thesis highlights the historical and contemporary space missions dedicated to low-frequency radio astronomy, including Radio Astronomy Explorer (RAE-1 and RAE-2), Interplanetary Monitoring Platform (IMP-6), and more recent missions like the Netherlands-China Low-Frequency Explorer (NCLE), Cassini-RPWS, and STEREO WAVES. These missions demonstrated the potential of space-based platforms to bypass ionospheric interference and RFI, enabling more precise observations of solar bursts, planetary emissions, and galactic radio sources. Despite these efforts, the data collected still needs to be improved, prompting the need for new missions and advanced techniques for low-frequency radio astronomy.

A significant aspect of this thesis is the development of an advanced source localization algorithm for the Space Electric and Magnetic Sensor (SEAMS) mission, designed to operate in the 0.3 to 16 MHz frequency range. Accurate source localization is crucial for understanding radio emissions' spatial characteristics and improving Interplanetary Scintillation (IPS) studies. IPS is a key technique for studying the IPM by observing the intensity fluctuations of radio waves caused by

diffraction and scattering through solar wind turbulence. The Snapshot Averaged Matrix Pencil Method (SAM-DoA) algorithm introduced in this thesis offers improved DoA estimation validated through scaled experiments. This algorithm's adaptability and speed are further enhanced using machine learning (ML) techniques, specifically through an artificial neural network (ANN) approach, which delivers superior inference times and real-time localization accuracy. The thesis also investigates heliospheric phenomena by combining ground-based IPS measurements with in-situ data from the Parker Solar Probe. These studies reveal important trends and anomalies in solar wind microturbulence, solar cycle dynamics, and hemispherical asymmetries in solar polar field reversals. The results show minimal variation in modulation indices but point to discrepancies that need further exploration. These findings help improve our understanding of the heliosphere's dynamic processes and contribute to developing better space weather prediction models. Given the technical challenges associated with space-based interferometry, such as high costs and operational complexity, the thesis explores the feasibility of single-payload missions equipped with multiple sensors. These sensors can implement goniopolarimetric techniques to estimate the direction of incoming signals. Missions like the Dark Ages Polarimeter Pathfinder (DAPPER) and SEAMS are highlighted as promising initiatives to explore low-frequency radio astronomy soon.

8.2 Future Scope

The findings presented in this thesis establish a solid foundation for advancing low-frequency radio astronomy, particularly for observations below 30 MHz. Several promising avenues for future research and development arise from this work, focusing on enhancing the accuracy, robustness, and practicality of direction-of-arrival (DoA) algorithms and leveraging machine learning (ML) techniques to improve the study of space weather and interplanetary phenomena. A critical next step is the extensive practical experimentation to validate the performance of the Snapshot Averaged Matrix Pencil Method (SAM-DoA) and the ML-based DoA algorithms developed in this thesis. Conducting experiments in controlled environments and real-world scenarios, such as using data from multi-station IPS telescopes and upcoming space missions like SEAMS, will help refine these algorithms. These tests will provide insights into the accuracy, efficiency, and algorithm adaptability under several conditions as well as noise levels.

Another important aspect is designing a signal model comprising IPS signatures. By including IPS's distinctive features, such as variation in intensity resulting from solar wind turbulence, into the signal model, we might develop a more robust DoA algorithm. This new model will boost the accuracy of detecting radio sources contributing to IPS while providing more insight into solar wind dynamics and structure. Integrating beamforming methods is viable for improving the SAM-DoA algorithm's precision. Beamforming allows the algorithm to focus on specified directions while reducing noise from undesired sources, resulting in better radio signal localization. The improvement proves particularly useful for space-based investigations, where precise source localization is essential for researching solar and heliospheric processes. Exploring different machine learning architectures and Physics-Informed Neural Networks (PINNs) provides more chances to improve DoA estimation. By incorporating physical constraints and an understanding of the underlying processes into neural network models, PINNs can produce exact and comprehensible results. Testing various ML designs, such as Convolutional Neural Networks (CNNs) and Recurrent Neural Networks (RNNs), may improve the adaptability and performance of the DoA algorithms.

In addition to algorithm development, conducting long-term and short-term studies to investigate the relationship between IPS data and in-situ observables is essential. Data from missions like Ulysses, the Parker Solar Probe (PSP), and Aditya-L1 can be compared with IPS measurements to identify correlations between scintillation patterns and direct measurements of solar wind prop-

erties. By understanding these relationships, we can create predictive models for studying solar wind remotely, improving our ability to monitor and forecast space weather events. Developing these predictive models will allow us to study solar wind dynamics more effectively from a distance, reducing the need for continuous in-situ measurements. This approach can provide a broader and more continuous view of the heliosphere, aiding in the prediction of Coronal Mass Ejections (CMEs), Solar Flares (SFs), and other space weather phenomena that impact Earth's technological infrastructure. Furthermore, machine learning-based approaches can be explored for parameter extraction from IPS readings. ML techniques can automate the extraction of key parameters such as solar wind speed, density, and turbulence levels from IPS data, improving the efficiency and accuracy of space weather analysis. This capability will be particularly useful for real-time monitoring and forecasting of space weather events, enhancing our preparedness for potential disruptions caused by solar activity.

Appendix A

Direction of Arrival using Pseudo-Vector estimation

A.1 Introduction

Direction-of-Arrival (DoA) estimation is a crucial technique for determining the direction from which electromagnetic waves propagate to an observer. This process becomes particularly challenging when the source direction is unknown, as conventional methods rely on phase and polarization properties. Typically, wave polarization in the transverse propagation plane is described using Stokes parameters, derived from the two-dimensional coherency tensor. However, when the full three-dimensional field components must be considered, a more generalized approach using a three-dimensional coherency tensor or spectral tensor is required [95]. Advanced DoA estimation methods leverage these extended models to analyze wave polarization comprehensively. Techniques such as the expansion of the spectral tensor in higher-dimensional Hermitian matrices enable characterization of wave properties in three or more dimensions. For instance, SU(3) generators, analogous to Pauli spin matrices in lower dimensions, provide a robust framework for deriving spectral parameters like intensity and circular polarization. These advanced tools are particularly valuable in fields like space-based radio astronomy, where coherent detection of all electric or magnetic field components is necessary [95]. In this Appendix a pseudo vector estimation method is discussed which became the basic theory behind development of SAM-DoA.

A.1.1 Pseudo-Vector estimation

This section describes a goniopolarimetric technique for three orthogonal dipoles, which uses the electrodynamics equation to estimate the DoA. Consider three dipoles along each axis (x, y, and z). Then, the voltage received by the dipole is represented by

$$V_x = hE_x, \quad V_y = hE_y, \quad V_z = hE_z \tag{A.1}$$

where, V_x, V_y and V_z is the voltages from dipole on x, y and z of height h. E_x, E_y and E_z represents the electric field in the (x, y, z) direction. Now, in the Fourier domain, the field vectors can be represented as shown in equation A.2].

$$\vec{E}(\vec{r},\omega) = \begin{pmatrix} E_x(\vec{r},\omega) \\ E_y(\vec{r},\omega) \\ E_z(\vec{r},\omega) \end{pmatrix} = \begin{pmatrix} E_1(\vec{r},\omega)e^{i\delta_1(\vec{r},\omega)} \\ E_2(\vec{r},\omega)e^{i\delta_2(\vec{r},\omega)} \\ E_3(\vec{r},\omega)e^{i\delta_3(\vec{r},\omega)} \end{pmatrix} \tag{A.2}$$

Now, one can form a spectral density tensor using equation A.2 by multiplying the field vector by its Hermitian conjugation. However, the signal needs to be band-limited to obtain a spectral density tensor. Thus, by considering the operator $\hat{B} = \int_{\omega-\Delta\omega/2}^{\omega+\Delta\omega/2} d\omega$ the signal can be band-limited

to a small window of $\Delta\omega$. Therefore, we have

$$\begin{aligned} F_S(r,\omega) = \vec{E}\vec{E}^{\dagger} &= \begin{pmatrix} E_xE_x^* & E_xE_y^* & E_xE_z^* \\ E_yE_x^* & E_yE_y^* & E_yE_z^* \\ E_zE_x^* & E_zE_y^* & E_zE_z^* \end{pmatrix} \\ &= \begin{pmatrix} E_1^2e^{i(\delta_1-\delta_1)} & E_1E_2e^{i(\delta_1-\delta_2)} & E_1E_3e^{i(\delta_1-\delta_3)} \\ E_2E_1e^{i(\delta_2-\delta_1)} & E_2^2e^{i(\delta_2-\delta_2)} & E_2E_3e^{i(\delta_2-\delta_3)} \\ E_3E_1e^{i(\delta_3-\delta_1)} & E_3E_2e^{i(\delta_3-\delta_2)} & E_3^2e^{i(\delta_3-\delta_3)} \end{pmatrix} \end{aligned} \tag{A.3}$$

* denotes the complex conjugate and δ_1, δ_2 and δ_3 phases of the wave-front incident on the dipoles.

$$F_S(r,\omega) = \begin{pmatrix} E_1^2 & E_1E_2e^{i(\delta_1-\delta_2)} & E_1E_3e^{i(\delta_1-\delta_3)} \\ E_2E_1e^{i(\delta_2-\delta_1)} & E_2^2 & E_2E_3e^{i(\delta_2-\delta_3)} \\ E_3E_1e^{i(\delta_3-\delta_1)} & E_3E_2e^{i(\delta_3-\delta_2)} & E_3^2 \end{pmatrix} \tag{A.4}$$

Now, if we consider the wave is propagating along the z direction, then the field component along the z direction will become zero as the EM wave is transverse; thus, the equation A.2 will reduce to

$$\vec{E}(\vec{r},\omega) = \begin{pmatrix} E_x(\vec{r},\omega) \\ E_y(\vec{r},\omega) \\ 0 \end{pmatrix} = \begin{pmatrix} E_1(\vec{r},\omega)e^{i\delta_1(\vec{r},\omega)} \\ E_2(\vec{r},\omega)e^{i\delta_2(\vec{r},\omega)} \\ 0 \end{pmatrix}$$

In assumption taken into consideration, the field vector does not have any z component as shown by the equation above; thus, spectral density (refer equation A.4) of the field will reduce to 2D tensor,

$$F_S^{2D}(r,\omega) = \begin{pmatrix} E_x^2 & E_xE_ye^{i(\delta_1-\delta_2)} \\ E_yE_xe^{i(\delta_2-\delta_1)} & E_y^2 \end{pmatrix} \tag{A.5}$$

As per the Stokes parameter in the electromagnetic field theory[88], we know that,

$$\begin{aligned} I &= E_x^2 + E_y^2 \\ Q &= E_x^2 - E_y^2 \\ U &= 2E_xE_ycos(\delta_1-\delta_2) \\ V &= 2E_xE_ysin(\delta_1-\delta_2) \end{aligned} \tag{A.6}$$

where I is the total intensity of the field, Q is the preponderance of Linear Horizontal Polarisation (LHP) of the field over Linear Vertical Polarisation (LVP) of the field, U is the domination of Linear $+45$ degree Polarization of the field over the Linear -45 degree Polarization of the field, and the V describes the dominance of the Right Circular Polarisation (RCP) of the field over the Left Circular Polarisation (LCP) of the field. Now, by analysing the equation A.6 and the Euler's formula $e^{i\theta} = cos\theta + isin\theta$ and $e^{-i\theta} = cos\theta - isin\theta$. The following equation can be derived.

$$\begin{aligned} E_x^2 &= \frac{1}{2}(I+Q) \\ E_y^2 &= \frac{1}{2}(I-Q) \\ E_xE_ye^{i(\delta_1-\delta_2)} &= \frac{1}{2}(U+iV) \\ E_xE_ye^{i(\delta_2-\delta_1)} &= \frac{1}{2}(U-iV) \end{aligned} \tag{A.7}$$

Thus equation A.5 can be rewritten as

$$F_S^{2D} = \frac{1}{2}\begin{pmatrix} I+Q & U+iV \\ U-iV & I-Q \end{pmatrix} \tag{A.8}$$

It is important to note that the trace of the spectral density matrix, as shown in equations A.5 and A.8, represents the total intensity of the electromagnetic wave. If the equation A.8 is split

based on the Stokes parameter, the following relation can be derived.

$$F_S^{2D} = \frac{1}{2}\left[\begin{pmatrix} I & 0 \\ 0 & I \end{pmatrix} + \begin{pmatrix} 0 & U \\ U & 0 \end{pmatrix} + \begin{pmatrix} 0 & iV \\ -iV & 0 \end{pmatrix} + \begin{pmatrix} Q & 0 \\ 0 & -Q \end{pmatrix}\right] \tag{A.9}$$

Now using the Special unitary type 2 matrix i.e, SU(2) also known as Pauli's spin matrix that is [95],

$$\sigma_0 = \begin{pmatrix} 1 & 0 \\ 0 & 1 \end{pmatrix} \qquad \sigma_1 = \begin{pmatrix} 0 & 1 \\ 1 & 0 \end{pmatrix}$$
$$\sigma_2 = \begin{pmatrix} 0 & -i \\ i & 0 \end{pmatrix} \qquad \sigma_3 = \begin{pmatrix} 1 & 0 \\ 0 & -1 \end{pmatrix}$$

The equation A.9 can be rewritten as

$$F_S^{2D}(r,\omega) = \frac{1}{2}(I\sigma_0 + Q\sigma_3 + U\sigma_1 + V\sigma_2) \tag{A.10}$$

Depicting the two-dimensional spectral density tensor in terms of Stokes parameters. In the Stokes parameter, the parameter V gives the measure of the degree of circular polarization in the EM signal(equation A.6) [88]. By considering the previous statement along with equations A.5, A.6, and A.8, it observed that the anti-symmetric part of the spectral density matrix gives the information about the degree of circular polarization. Thus, following the SU matrix analogy to extrapolate the Stokes parameter in 3 dimensions, SU type 3, known as the Gell-Mann matrix, can describe the spectral density. The Gell-Mann matrix is defined as,

$$I_3 = \begin{pmatrix} 1 & 0 & 0 \\ 0 & 1 & 0 \\ 0 & 0 & 1 \end{pmatrix} \quad \lambda_1 = \begin{pmatrix} 0 & 1 & 0 \\ 1 & 0 & 0 \\ 0 & 0 & 0 \end{pmatrix} \quad \lambda_2 = \begin{pmatrix} 0 & -i & 0 \\ i & 0 & 0 \\ 0 & 0 & 0 \end{pmatrix}$$
$$\lambda_3 = \begin{pmatrix} 1 & 0 & 0 \\ 0 & -1 & 0 \\ 0 & 0 & 0 \end{pmatrix} \quad \lambda_4 = \begin{pmatrix} 0 & 0 & 1 \\ 0 & 0 & 0 \\ 1 & 0 & 0 \end{pmatrix} \quad \lambda_5 = \begin{pmatrix} 0 & 0 & -i \\ 0 & 0 & 0 \\ i & 0 & 0 \end{pmatrix} \tag{A.11}$$
$$\lambda_6 = \begin{pmatrix} 0 & 0 & 0 \\ 0 & 0 & 1 \\ 0 & 1 & 0 \end{pmatrix} \quad \lambda_7 = \begin{pmatrix} 0 & 0 & 0 \\ 0 & 0 & -i \\ 0 & i & 0 \end{pmatrix} \quad \lambda_8 = \frac{1}{\sqrt{3}}\begin{pmatrix} 1 & 0 & 0 \\ 0 & 1 & 0 \\ 0 & 0 & -2 \end{pmatrix}$$

Following the analogy of the 2D stokes parameter (equation A.10) the

$$F_{3D}^{'} = \frac{I_3\Lambda_o}{3} + \sum_{j=1}^{8}\Lambda_j g_j \tag{A.12}$$

where, $g_j = \frac{1}{2}\lambda_j$, I_3 is the identity matrix of 3×3 dimensions, and Λ_k is the 3D equivalent of the stokes parameter ($k \in [0,9)$). Then the equation A.12 can be rewritten as,

$$F_{3D} = \begin{pmatrix} \frac{\Lambda_0}{3} + \frac{\Lambda_3}{2} + \frac{\Lambda_8}{2\sqrt{3}} & \frac{\Lambda_1}{2} - i\frac{\Lambda_2}{2} & \frac{\Lambda_4}{2} - i\frac{\Lambda_5}{2} \\ \frac{\Lambda_1}{2} + i\frac{\Lambda_2}{2} & \frac{\Lambda_0}{3} - \frac{\Lambda_3}{2} + \frac{\Lambda_8}{2\sqrt{3}} & \frac{\Lambda_6}{2} - i\frac{\Lambda_7}{2} \\ \frac{\Lambda_4}{2} + i\frac{\Lambda_5}{2} & \frac{\Lambda_6}{2} + i\frac{\Lambda_7}{2} & \frac{\Lambda_0}{3} - \frac{\Lambda_8}{\sqrt{3}} \end{pmatrix} \tag{A.13}$$

Now, by comparing equation A.13 and A.3 results in following relations,

$$E_xE_x^* = \frac{\Lambda_0}{3} + \frac{\Lambda_3}{2} + \frac{\Lambda_8}{2\sqrt{3}} \qquad E_yE_x^* = \frac{\Lambda_1}{2} + i\frac{\Lambda_2}{2} \qquad E_zE_x^* = \frac{\Lambda_4}{2} + i\frac{\Lambda_5}{2}$$
$$E_xE_y^* = \frac{\Lambda_1}{2} - i\frac{\Lambda_2}{2} \qquad E_yE_y^* = \frac{\Lambda_0}{3} - \frac{\Lambda_3}{2} + \frac{\Lambda_8}{2\sqrt{3}} \qquad E_zE_y^* = \frac{\Lambda_6}{2} + i\frac{\Lambda_7}{2} \tag{A.14}$$
$$E_xE_z^* = \frac{\Lambda_4}{2} - i\frac{\Lambda_5}{2} \qquad E_yE_z^* = \frac{\Lambda_6}{2} - i\frac{\Lambda_7}{2} \qquad E_zE_z^* = \frac{\Lambda_0}{3} - \frac{\Lambda_8}{\sqrt{3}}$$

Since the trace of the spectral density matrix gives the total intensity of the spectra. Therefore,

$$\Lambda_0 = E_x E_x^* + E_y E_y^* + E_z E_z^* \tag{A.15}$$

or,

$$\Lambda_0 = E_1^2 + E_2^2 + E_3^2 \tag{A.16}$$

To validate this assumption, the 3D analogy of the Stokes parameter must also hold in 2D. In other words, F_{3D} should reduce to F_{2D} when the wave propagates along the z-axis. Therefore, by assuming the field along the z-axis to be zero (that is, $E_z = E_z^* = 0$) the equation A.14 reduces to,

$$F_{3D}^{'} = \begin{pmatrix} \frac{\Lambda_0}{3} + \frac{\Lambda_3}{2} + \frac{\Lambda_8}{2\sqrt{3}} & \frac{\Lambda_1}{2} - i\frac{\Lambda_2}{2} & 0 \\ \frac{\Lambda_1}{2} + i\frac{\Lambda_2}{2} & \frac{\Lambda_0}{3} - \frac{\Lambda_3}{2} + \frac{\Lambda_8}{2\sqrt{3}} & 0 \\ 0 & 0 & 0 \end{pmatrix} \tag{A.17}$$

By performing element wise comparison of equation A.14 and A.17,

$$\begin{aligned} \frac{\Lambda_4}{2} - i\frac{\Lambda_5}{2} = 0, \quad & \frac{\Lambda_6}{2} - i\frac{\Lambda_7}{2} = 0, \quad & \frac{\Lambda_0}{3} - \frac{\Lambda_8}{\sqrt{3}} = 0, \\ \frac{\Lambda_4}{2} + i\frac{\Lambda_5}{2} = 0, \quad & \frac{\Lambda_6}{2} + i\frac{\Lambda_7}{2} = 0, \quad & \Lambda_0 = \frac{\Lambda_0}{\sqrt{3}} \\ \Lambda_4 = \Lambda_5 = 0, \quad & \Lambda_6 = \Lambda_7 = 0, \quad & \end{aligned}$$

Thus, $F_{3D}^{'}$ becomes

$$\begin{aligned} F_{3D}^{'} &= \begin{pmatrix} \frac{\Lambda_0}{3} + \frac{\Lambda_3}{2} + \frac{\Lambda_8}{2\sqrt{3}} & \frac{\Lambda_1}{2} - i\frac{\Lambda_2}{2} & 0 \\ \frac{\Lambda_1}{2} + i\frac{\Lambda_2}{2} & \frac{\Lambda_0}{3} - \frac{\Lambda_3}{2} + \frac{\Lambda_8}{2\sqrt{3}} & 0 \\ 0 & 0 & 0 \end{pmatrix} = \begin{pmatrix} \frac{\Lambda_0}{2} + \frac{\Lambda_3}{2} & \frac{\Lambda_1}{2} - i\frac{\Lambda_2}{2} & 0 \\ \frac{\Lambda_1}{2} + i\frac{\Lambda_2}{2} & \frac{\Lambda_0}{2} - \frac{\Lambda_3}{2} & 0 \\ 0 & 0 & 0 \end{pmatrix} \\ &\approx \begin{pmatrix} \frac{\Lambda_0}{2} + \frac{\Lambda_3}{2} & \frac{\Lambda_1}{2} - i\frac{\Lambda_2}{2} \\ \frac{\Lambda_1}{2} + i\frac{\Lambda_2}{2} & \frac{\Lambda_0}{2} - \frac{\Lambda_3}{2} \end{pmatrix} \end{aligned} \tag{A.18}$$

if now, $\Lambda_0 = I$, $\Lambda_1 = U$, $\Lambda_2 = V$ & $\Lambda_3 = Q$ the $F_{3D}^{'}$ converges to equation A.8 thereby validating the assumption of 3D equivalent stokes parameter. From equation A.13, it is evident that the spectral density matrix in terms of 3D equivalent Stokes' parameter can be divided into real and imaginary matrices.

$$F_{3D}^{'} = \begin{pmatrix} \frac{\Lambda_0}{3} + \frac{\Lambda_3}{2} + \frac{\Lambda_8}{2\sqrt{3}} & \frac{\Lambda_1}{2} & \frac{\Lambda_4}{2} \\ \frac{\Lambda_1}{2} & \frac{\Lambda_0}{3} - \frac{\Lambda_3}{2} + \frac{\Lambda_8}{2\sqrt{3}} & \frac{\Lambda_6}{2} \\ \frac{\Lambda_4}{2} & \frac{\Lambda_6}{2} & \frac{\Lambda_0}{3} - \frac{\Lambda_8}{2\sqrt{3}} \end{pmatrix} + j \begin{pmatrix} 0 & -\frac{\Lambda_2}{2} & -\frac{\Lambda_5}{2} \\ \frac{\Lambda_2}{2} & 0 & -\frac{\Lambda_7}{2} \\ \frac{\Lambda_5}{2} & \frac{\Lambda_7}{2} & 0 \end{pmatrix} \tag{A.19}$$

Now, the anti-symmetric part of a rank two tensor is associated with a Dual tensor (refer Appendix C) by this we get:

$$V_i = \sum_{j,k=1}^{3} \epsilon_{ijk} \Im[(\vec{E}_{3D}^{'})_{jk}] \tag{A.20}$$

Here, $i \in \mathbb{N}$ and $1 \leq i \leq 3$. Moreover, the standard form of any anti-symmetric 3D tensor or matrix is given by,

$$T = \begin{pmatrix} 0 & T_{12} & -T_{13} \\ -T_{21} & 0 & T_{23} \\ T_{31} & -T_{32} & 0 \end{pmatrix} \tag{A.21}$$

By comparing $\Im[(F_{3D}^{'})]$ with equation A.21 that is, standard anti-symmetric tensor, the following relation can be drawn,

$$\Lambda_2 = -\Lambda_2, \qquad \Lambda_5 = \Lambda_5, \qquad \Lambda_7 = -\Lambda_7 \tag{A.22}$$

Therefore, by using the Dual tensor or the Pseudo vector relation given by equation A.20, we have,

$$V_1 = \Lambda_7, \qquad V_2 = -\Lambda_5, \qquad V_3 = \Lambda_2 \tag{A.23}$$

That is, $\vec{V} = (\Lambda_7, -\Lambda_5, \Lambda_2)$ and by comparing the imaginary parts of equation A.23 to (A.3) the pseudo-vector $\vec{V}$ containing the directional information of the field can be derived as,

$$\Lambda_7 = -2\Im\{E_y E_z^*\}\Lambda_5 = -2\Im\{E_x E_z^*\}\Lambda_2 = -2\Im\{E_x E_y^*\} \tag{A.24}$$

that is,

$$\vec{V} = (-2\Im\{E_y E_z^*\}, 2\Im\{E_x E_z^*\}, -2\Im\{E_x E_y^*\}) \tag{A.25}$$

Now, if we consider the time-dependent field vector $\vec{E}(\vec{r}, t)$ traces the polarization ellipse. Then the complex vector $\vec{E}(\vec{r}, w)$ and its complex conjugate $\vec{E}^*(\vec{r}, w)$ will form a polarization plane in space. This plane is the same as the polarization ellipse because the vector V, defined by a dual tensor, will be orthogonal to the plane of polarization. Thus,

$$\begin{aligned}\vec{V}.\vec{E} = &-E_1E_2E_3(e^{i(\delta_1+\delta_2-\delta_3)} - e^{i(\delta_1-\delta_2+\delta_3)} + E_1E_2E_3(e^{i(\delta_1+\delta_2-\delta_3)} - e^{i(-\delta_1+\delta_2+\delta_3)} \\ &- E_1E_2E_3(e^{i(\delta_1-\delta_2+\delta_3)} - e^{i(-\delta_1+\delta_2+\delta_3)} \\ = &\vec{V}.\vec{E}^* = 0\end{aligned}$$

Therefore, it can be shown that a vector normal to the plane of polarization is parallel to $i\vec{E} \times \vec{E}^*$ and the magnitude of this vector is $2/\pi$ times the area of the polarization ellipse. Thus, $i\vec{E} \times \vec{E}^*$ = V = (Λ_7,$-\Lambda_5$,Λ_2) this can be obtained by as follows, $\vec{E} = (E_x, E_y, E_z)$, $E^* = (E_x^* E_y^* E_z^*)$. Then,

$$i\vec{E} \times \vec{E}^* = \begin{pmatrix} \hat{i} & \hat{j} & \hat{k} \\ iE_x & iE_y & iE_z \\ E_x^* & E_y^* & E_z^* \end{pmatrix} = \hat{i}(iE_yE_z^* - iE_zE_y^*) - \hat{j}(iE_xE_z^* - iE_zE_x^*) + \hat{k}(iE_xE_y^* - iE_yE_x^*)$$

this comes out to be $j\vec{E} \times \vec{E}^* = \hat{i}(-2Im(E_yE_z^*)) - \hat{j}(-2Im(E_xE_z^*)) + \hat{k}(-2Im(E_xE_y^*))$ (see Appendix B). Using equation A.24, $j\vec{E} \times \vec{E}^* = \hat{i}\Lambda_7 - \hat{j}\Lambda_5 + \hat{k}\Lambda_2$ = V = (Λ_7,$-\Lambda_5$,Λ_2)

$$V = \begin{pmatrix} \Lambda_7 \\ -\Lambda_5 \\ \Lambda_2 \end{pmatrix} = \text{Vector specifying Direction of Arrival} \tag{A.26}$$

A.2 Example

Consider plane waves having 1 degree of freedom δ(relative phase) between 2 plane waves. Let one vector lay along x and the other along y intersecting each other at the origin. Assuming right-handed circular polarisation, the following will hold,

$$E_1 = \begin{bmatrix} 0 \\ -1 \\ -i \end{bmatrix} \quad \& \; E_2 = \begin{bmatrix} e^{i\delta} \\ 0 \\ -ie^{i\delta} \end{bmatrix} = \begin{bmatrix} cos\delta + jsin\delta \\ 0 \\ sin\delta - jcos\delta \end{bmatrix}$$

Now, by electrostatics, we know that fields are additive in nature; thus, at the intersection, we will get,

$$E = E_1 + E_2 = \begin{bmatrix} cos\delta + jsin\delta \\ -1 \\ sin\delta - j(cos\delta + 1) \end{bmatrix}$$

Thus, the spectral density tensor would be,

$$F_{3D} = EE^H = \begin{bmatrix} cos\delta + jsin\delta \\ -1 \\ sin\delta - j(cos\delta + 1) \end{bmatrix} \begin{bmatrix} (cos\delta + jsin\delta) - 1(sin\delta - j(cos\delta + 1)) \end{bmatrix}$$

$$F_{3D} = \begin{bmatrix} 1 & (-cos\delta - isin\delta) & -sin\delta + j(1 + cos\delta) \\ (-cos\delta + jsin\delta) & 1 & (-sin\delta - j(1 + cos\delta)) \\ (-sin\delta - i(1 + cos\delta)) & (-sin\delta + i(1 + cos\delta)) & 2(1 + cos\delta) \end{bmatrix}$$

We know that,

$$V = \begin{bmatrix} \lambda_7 \\ -\lambda_5 \\ \lambda_2 \end{bmatrix} = -2 \begin{bmatrix} Im(F_y(F_z)^*) \\ -Im(F_x(F_z)^*) \\ Im(F_x(F_y)^*) \end{bmatrix} = -2 \begin{bmatrix} -(1 + cos\delta) \\ -(1 + cos\delta) \\ -sin\delta \end{bmatrix}$$

$$V = 2 \begin{bmatrix} (1 + cos\delta) \\ (1 + cos\delta) \\ sin\delta \end{bmatrix}$$

Appendix B

Matrix Pencil Method and DoA

B.1 Introduction

The Matrix Pencil method obtains the best estimates since it interacts directly with the data instead of generating a co-variance matrix, reducing computer complexity [96]. Eq. (4.6) generates a Hankel matrix to estimate N and ω^n.

$$\Lambda = \begin{bmatrix} S(0) & S(1) & \cdots & S(L) \\ S(1) & S(2) & \cdots & S(L+1) \\ \vdots & \vdots & \ddots & \vdots \\ S(M-L-1) & S(M-L) & \cdots & S(M-1) \end{bmatrix}_{(M-L)\times(L+1)}$$

where, L is selected between $(M/3, M/2]$ for optimum performance and is known as the pencil parameter [4]; M is the total sample length. The real matrix(Λ_R) is computed using a Unitary matrix transformation [4]($\Lambda_R = U^{\dagger}[\Lambda \mid \Pi_{M-L}\Lambda^*\Pi_{L+1}]U$; where, † represents hermitian conjugate and U is the unitary matrix [5]) and the complex number matrix Λ. Later, an estimate of the singular values of Λ_R is generated using SVD formulation. Matrix A_s consisting of N largest singular vectors of Λ_R is estimated by performing a thresholding operation on the normalized Eigenvalue, i.e., σ_i/σ_{max}. N generalized singular values are then calculated using an unitary transformation $(-[Re(U^{\dagger}J_1U)A_s]^{-1} \cdot Im(U^{\dagger}J_1U)A_s)$ which are, $\psi_1, \psi_2, \cdots, \psi_N$. Also, N incoherent frequencies are calculated by $\omega^n = 2arctan(\psi_n)/\delta$ for $n = 1, 2, \cdots, N$ [5, 6, 94].

B.2 MP method based DoA

Consider a tri-monopole antenna consisting of 3- orthogonal monopoles. Considering xy-plane as the ground plane, the antenna should not lie along x & y. also, if the angle of elevation is different with respect to xy & each antenna, then RP will not be identical, which may cause an error(but for an infinitely small dipole, it doesn't matter). So, due to this, each antenna is elevated by 35.3°(See Appendix E) as shown below.

To study the polarization of incident waves, the electric field on the P_1,P_2 & P_3 can be described by three components E_1, E_2 & E_3. So, $\vec{E}(t)$ can be described as,

$$\vec{E}(t) = (A_1^m e^{j\theta_1^m} A_2^m e^{j\theta_2^m} A_3^m e^{j\theta_3^m}) e^{j\omega t} \tag{B.1}$$

where,$A_1, A_2, A_3, \theta_1^m, \theta_2^m, \theta_3^m$represents amplitude and corresponding phases in 3D. We can map the electric field to the reference axis using the following relation:

$$E_x = E_1(\frac{\sqrt{6}}{3}) - E_2(\frac{\sqrt{6}}{6}) - E_3(\frac{\sqrt{6}}{6}) \tag{B.2}$$

$$E_y = E_2(\frac{\sqrt{2}}{2}) - E_3(\frac{\sqrt{2}}{2}) \tag{B.3}$$

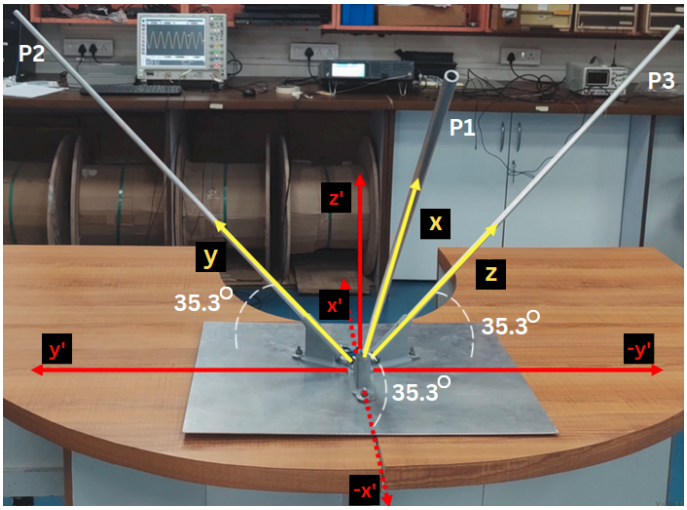

Figure B.1: Tri-axial antenna configuration.

$$E_z = E_1(\frac{\sqrt{3}}{3}) + E_2(\frac{\sqrt{3}}{3}) + E_3(\frac{\sqrt{3}}{3}) \tag{B.4}$$

Alternatively, we can directly consider P_1, P_2, P_3 as our reference axis without doing any conversion like above, and this approach will be most suited for space applications as in space, there are no references as we have a ground/earth. Considering,

$$E_1 = E_x = A_1^m e^{j\theta_1^m \hat{x}} \tag{B.5}$$
$$E_2 = E_y = A_2^m e^{j\theta_2^m \hat{y}} \tag{B.6}$$
$$E_3 = E_z = A_3^m e^{j\theta_3^m \hat{z}} \tag{B.7}$$

Using equation, $\vec{V} = -2\Im(E_y E_z^* \hat{x} + E_z E_x^* \hat{y} + E_x E_y^* \hat{z})$. Here, if we normalised the $\vec{V}$ with respect to the total intensity of the received signal $I = |E_x|^2 + |E_y|^2 + |E_z|^2$ we have,

$$\frac{\vec{V}}{I} = \frac{\vec{v}}{I}(sin\theta cos\phi\hat{x} + sin\theta sin\phi\hat{y} + cos\theta\hat{z}) \tag{B.8}$$

where, $\vec{v} = 2\sqrt{(Im(E_y E_z^*))^2 + (Im(E_z E_x^*))^2 + (Im(E_x E_y^*))^2}$. Now, let $v = \frac{\vec{V}}{I}$ & by using the spherical coordinate system, the following relations can be drawn,

$$\theta = cos^{-1}(\frac{V_z}{\sqrt{V_x^2 + V_y^2 + V_z^2}}) \tag{B.9}$$

$$\phi = \begin{cases} tan^{-1}(\frac{V_y}{V_x}), & if V_x > 0 \\ tan^{-1}(\frac{V_y}{V_x}) + \frac{\pi}{2}, & if V_x < 0 \end{cases} \tag{B.10}$$

where,

$$V_x = -2Im(E_y E_z^*) \tag{B.11}$$
$$V_y = -2Im(E_z E_x^*) \tag{B.12}$$
$$V_z = -2Im(E_x E_y^*) \tag{B.13}$$

and θ, & ϕ will describe the direction of arrival in terms of zenith & azimuth angle in a spherical coordinate system. As it is easy to understand the direction in terms of zenith & azimuth rather than dealing with a Cartesian vector. Now, if we consider that M coherent waves are incident on the tri-monopoles, then the superimposed wave for one monopole can be modeled as,

$$x(t) = \sum_{m=1}^{M} A_1^m e^{i\theta_m} e^{i\omega_m t} + n(t) \tag{B.14}$$

where, $n(t)$ is noise. Now, if we sample the above equation in N samples having $k \in [0, N-1]$ & where $t_n = t_o + k\delta$ & δ is the sample interval then the above equation can be written as

$$X[k] = \sum_{m=1}^{M} (A_1^m e^{i\theta_m} e^{i\omega_m t}) e^{i\omega_m k\delta} + n(t_o + k\delta) \tag{B.15}$$

Now, the Matrix Pencil Method is used to estimate M & ω^m. The MP method utilizes a set of unitary matrix transformations and SVD(singular value decomposition) to minimize noise and give a normalized & real value of M, which is then used to determine all the frequencies. The first step to realizing all this is to window the incoming signal and create a Hankel matrix, i.e., a matrix where the right upper triangular values are equal to the lower one as described below (see Section B.3 explaining Hankel matrix),

$$y = \begin{bmatrix} x(0) & x(1) & \dots & x(L) \\ x(1) & x(2) & \dots & x(L+1) \\ \vdots & \vdots & \ddots & \vdots \\ x(N-L-1) & x(N-L) & \dots & x(N-1) \end{bmatrix}_{(N-L)\times(L+1)} \tag{B.16}$$

As we know, $X[k]$ is complex; thus, the formed Hankel matrix will also be complex. Processing a complex matrix consumes much time; thus, using a unitary transform, a matrix Y is converted to a pure real matrix using the following equation.

$$X_{real} = U^{\dagger}[Y\Pi_{N-L}Y^{*}\Pi_{L+1}]U \tag{B.17}$$

See Appendix D for a detailed explanation of unitary transformation. Here, Y is a centro-Hermitian as equation B.15 denotes the DFT of the discrete real signal as practically the signal coming via antenna will be real then the amplitude the $-i\omega$ & $i\omega$ will be the complex conjugate of each other. There are two methods to find the principal frequency present in the signal. proposed the original method citeSarkar1995, and the improvement was performed to reduce the computation it was done by [5]. However, the following is required before understanding the methods for finding frequencies. Let us consider,

$$J_1 = \begin{bmatrix} 1 & 0 & \dots & 0 & 0 \\ 0 & 1 & \dots & 0 & 0 \\ \dots & & & & \\ \dots & & & & \\ \dots & & & & \\ 0 & 0 & \dots & 1 & 0 \end{bmatrix}_{(N-L-1)\times(N-L)}$$

$$J_2 = \begin{bmatrix} 0 & 1 & 0 & \dots & 0 & 0 \\ 0 & 0 & 1 & \dots & 0 & 0 \\ \dots & & & & & \\ \dots & & & & & \\ \dots & & & & & \\ 0 & 0 & 0 & \dots & 1 & 0 \end{bmatrix}_{(N-L-1)\times(N-L)}$$

To find the frequency, we can create an eigenvalue problem as follows.

$Y_a - \lambda Y_b = 0$

where, $Y_a = J_2 Y$ & $Y_b = J_1 Y$ This will shift the Y by one row to achieve equality so that we can make it an eigenvalue problem.

Thus, we get

$$J_2 Y = \lambda J_1 Y \tag{B.18}$$

performing unitary transform on equation B.18 we get,

$$U_{N-L-1}^{\dagger} J_2 Y U_{L+1} = U_{N-L-1}^{\dagger} \lambda J_1 Y U_{L+1} \tag{B.19}$$

Since, $U_{N-L} U_{N-L}^{\dagger} = I_{N-L}$ thus we get

$$U_{N-L-1}^{\dagger} J_2 U_{N-L} U_{N-L}^{\dagger} Y U_{L+1} = U_{N-L-1}^{\dagger} \lambda J_1 U_{N-L} U_{N-L}^{\dagger} Y U_{L+1} \tag{B.20}$$

Since, $U_{N-L}^{\dagger} Y U_{L+1} = X_R$ see Appendix D or,

$$U_{N-L-1}^{\dagger} J_2 U_{N-L} X_R = U_{N-L-1}^{\dagger} \lambda J_1 U_{N-L} X_R \tag{B.21}$$

It is known that $\Pi\Pi = I$ thus we have

$$\begin{aligned} & U_{N-L-1}^{\dagger} \Pi_{N-L-1} \Pi_{N-L-1} J_2 \Pi_{N-L} \Pi_{N-L} U_{N-L} X_R \\ &= U_{N-L-1}^{\dagger} \Pi_{N-L-1} J_1 \Pi_{N-L} X_R \\ &= U^T J_1 U^* X_R \\ &= (U^{\dagger} J_1 U)^* X_R \end{aligned} \tag{B.22}$$

As $U_p^{\dagger} \Pi_p = U_p^T$, $\Pi_p U_p = U_p^*$ & $\Pi_p J_2 \Pi_{p+1} = J_1$. Thus, the equation reduces to

$$(U^{\dagger} J_1 U)^* X_R = \lambda U^{\dagger} J_1 U X_R \tag{B.23}$$

or,

$$\begin{aligned} Re(U^{\dagger} J_1 U) X_R = -j Im(U^{\dagger} J_1 U) X_R \\ = Re(\lambda) + j I_m(\lambda) \times \{ Re(U^{\dagger} J_1 U) X_R + j Im(U^{\dagger} J_1 U) X_R \} \end{aligned} \tag{B.24}$$

Now, the shift of one row was created; thus, the difference or Eigenvalue will be,

$$\lambda = e^{j \omega_m \delta} \tag{B.25}$$

where,δ is sampling time. Thus,

$$\begin{aligned} Re(\lambda) = Re(e^{j \omega_m \delta}) = cos(\omega_m \delta) \\ Im(\lambda) = Im(e^{j \omega_m \delta}) = sin(\omega_m \delta) \end{aligned}$$

Let $k = U^{\dagger} J_1 U$, thus equation B.24 reduces to,

$$\begin{aligned} & Re(k) X_R - j Im(k) X_R = e^{j w_m t_o} Re(k) X_R + j Im(k) X_R \\ \Rightarrow & X_R \sqrt{(Re(k))^2 + (Im(k))^2} e^{-j tan^{-1}(\frac{Im(k) X_R}{Re(k) X_R})} = e^{j w_m \delta} X_R \sqrt{(Re(k))^2 + (Im(k))^2} e^{j tan^{-1}(\frac{Im(k) X_R}{Re(k) X_R})} \\ & \Rightarrow e^{-j 2 tan^{-1}(\frac{Im(k) X_R}{Re(k) X_R})} = e^{j w_m \delta} \\ & \Rightarrow -2 tan^{-1}(\frac{Im(k) X_R}{Re(k) X_R}) = w_m \delta \\ & \Rightarrow \frac{Im(k)}{Re(k)} = tan(\frac{-w_m \delta}{2}) \\ & \Rightarrow Im(k) X_R = -tan(\frac{-w_m \delta}{2}) Re(k) X_R \\ & \Rightarrow Im(U^{\dagger} J_1 U) X_R = -tan(\frac{-w_m \delta}{2}) Re(U^{\dagger} J_1 U) X_R \end{aligned} \tag{B.26}$$

Now, as proposed by [4] after obtaining Hankel matrix Y, to estimate the frequencies present in the concerned band or FFT point present in Y, we need to perform $\delta V D A = U \sum V^{\dagger}$, this is useful to reduce some of the noise effects. Thus,

$$Y = W \Sigma V^{\dagger} \tag{B.27}$$

In equation B.27 W & V are the unitary matrices whose columns are eigenvectors of $YY^{\dagger}$, and Σ are the eigenvalues of Y or singular values in Y. In Σ, the singular values are located on the main diagonal. The choice parameter or the number of prominent/incoherent waves M in equation B.14 is estimated by normalizing the singular values $\sigma_0, \sigma_1, ..., \sigma_{N-1}$ $\epsilon \Sigma$ to the maximum value of the

singular value, i.e.,

$$\frac{\sigma_l}{\sigma_{max}} = 10^{-p} \tag{B.28}$$

where p is the number of significant decimal digits in the data; for example, if the data is accurate up to 3 decimal points, then p=3. The values below this will be singular values of noise. In this estimation procedure, Y is considered a complex variable, and the level of contamination from noise and processing duration is significant. To manage this, it is advantageous to apply a unitary transform, converting it into a real variable, as demonstrated in the equation. So, equation B.17 can be rewritten as,

$$X_R = W\Sigma V^{\dagger} \tag{B.29}$$

where, W & V are the orthogonal eigenvectors of X_R and Σ is the eigen/singular values of X_R. By utilizing equation B.28, M is estimated. Then, let $W = [u_1, u_2, u_3, ..., u_M....]$. After that, the matrix is made by considering the M largest value of eigenvector W. Then, by modifying equation B.26 we have,

$$-tan(\frac{w_m\delta}{2})Re(U^{\dagger}J_1U)As = Im(U^{\dagger}J_1U)As$$
$$\Rightarrow -tan(\frac{w_m\delta}{2}) = [Re(U^{\dagger}J_1U)As]^{-1}Im(U^{\dagger}J_1U)As = T$$

Thus, $-tan(\frac{w_m\delta}{2})$ is the eigenvalue of $T = [\gamma_1, \gamma_2, ..., \gamma_M]$

$$w_m = \frac{2tan^{-1}\gamma_M}{\delta} \tag{B.30}$$

where, $m = 1, 2, ..M$. After estimating the principle frequencies using the equation B.14, a k-point DFT of x(t) can be estimated, thereby providing us with N DFT points, i.e., X[0], X[1],..X[N-1]. This can form a matrix shown below in equation B.31 by separating the $e^{jw_m\delta k}$ term out of the series.

$$\begin{bmatrix} X[0] \\ X[1] \\ . \\ . \\ . \\ . \\ X[N] \end{bmatrix} = \begin{bmatrix} 1 & 1 & ....1 \\ e^{jW_1\delta} & e^{jW_2\delta}....e^{jW_m\delta} & \\ . & . & .... \\ . & . & .... \\ . & . & .... \\ . & . & .... \\ e^{jW_1(N-1)\delta} & e^{jW_2(N-1)\delta}....e^{jW_m(N-1)\delta} & \end{bmatrix} \begin{bmatrix} {A_1}^1 e^{jw_1t_0}e^{j\theta_1} \\ {A_1}^2 e^{jw_2t_0}e^{j\theta_2} \\ . \\ . \\ . \\ . \\ {A_1}^m e^{jw_mt_0}e^{j\theta_m} \end{bmatrix} \tag{B.31}$$

$$\Rightarrow X[k] = [e^{jw_mk\delta}]_{(N-1)\times M}[A]_{m\times 1}$$

Here, matrix [A] is contaminated by noise; thus, to eliminate this, we use the least square method to fit [A] linearly by using,

$$na + b\sum x_i = \sum y_i$$

and

$$a\sum_{i=1}^{n} x_i + b\sum_{i=1}^{n} {x_i}^2 = \sum_{i=1}^{n} x_iy_i$$

Here, n is the number of observations i.e., N, so we can find the values of a & b by setting

$$[x_i] = [w] \& [y_i] = [A]$$

after finding the constants a & b we can fit the value linearly to avoid deviation due to noise by using,

$$\hat{y_i} = a + bx_i$$

where, $b = \frac{convol(x,y)}{{\sigma_x}^2}$ and $a = \bar{y} - b\bar{x}$. After that, we arrive at a less noisy $[A]_{m\times 1}$ for a single monopole or, say, a monopole along one of the axes. This is to be done for all three of the axes. Thereafter, we can map equation B.11, B.12, and B.13 to estimate the Pseudo Vector.

$$\begin{aligned} V_x &= -2ImA_y{}^m e^{jw_m t_o} e^{j\theta_y{}^m} (A_z{}^m e^{jw_m t_o} e^{j\theta_z{}^m})^* \\ V_y &= -2ImA_z{}^m e^{jw_m t_o} e^{j\theta_z{}^m} (A_x{}^m e^{jw_m t_o} e^{j\theta_x{}^m})^* \\ V_z &= -2ImA_x{}^m e^{jw_m t_o} e^{j\theta_x{}^m} (A_y{}^m e^{jw_m t_o} e^{j\theta_y{}^m})^* \end{aligned} \tag{B.32}$$

Now, by using equation B.9 and B.10, DoA can be estimated. Furthermore, we could take singular values of all three dimensions to improve the estimation of choice parameter M, as shown.

$$b_i = \sqrt{(\sigma_i{}^1)^2 + (\sigma_i{}^2)^2 + (\sigma_i{}^3)^2} \tag{B.33}$$

where , i = 1,2,3,...

and then final τ_{max} and normalize ζ with respect to b_{max} to get an estimate of M by choosing the accuracy p as shown,

$$\frac{b_i}{\tau_{max}} >= 10^{-p} \tag{B.34}$$

Another method is proposed to produce the computational process by adding known phases to X[L] from each antenna. For each pattern, an excitation pattern is calculated and looked up.

B.3 Example

The following are some examples of the Hankel matrix.

$$\begin{bmatrix} 0 & 2 & 4 \\ 2 & 0 & 9 \\ 4 & 9 & 0 \end{bmatrix}$$

$$h = \begin{bmatrix} 1 & 2 & 3 & 4 \\ 2 & 3 & 4 & 5 \\ 3 & 4 & 5 & 6 \end{bmatrix}$$

Here, for the above example, say we have the following dataset or matrix, d = {1,2,3,4,5,6}. The Hankel matrix can be formed using the following formula $h(i,j) = d(i+j-1)$ or, $h_{ij} = d_{i+j-1}$ where i & j are the locations in the Hankel matrix. So, to form a Hankel matrix of $N \times M$, then the amount of data needed, i.e., M+N = 1. Let us say we have N data points, and then we can make a Hankel matrix with the following dimensions.

$$(N-x)(x+1) \text{ as } N - x + x + 1 - 1 = N$$

Appendix C

Pseudo vector

It is a quantity that transforms like a vector under a proper rotation, but in 3D, it gains an additional sign flip, i.e., an improper rotation such as a reflection. For example, $\vec{r} = \vec{p} \times \vec{q}$ where, $\vec{p}$ & $\vec{q}$ are position vector, and $\vec{r}$ is the resultant vector. Like any other vector, it will also point in a specific direction. However, the $\vec{\nabla} \times \vec{r}$ will state there is a rotational parameter present & it represents a surface vector. For example, magnetic field, torque, angular momentum, etc.

C.1 Anti-symmetric Tensor

It is a tensor that is in the form of a skew-symmetric matrix, i.e., $a_{ij} = -a_{ji}$

C.2 Dual Tensor

When a tensor is **Anti-symmetric as well as pseudo vector**, it is called a dual tensor. The standard representation of dual tensor(T) of rank 2 in 3D space is given by,

$$T = \begin{bmatrix} 0 & T_{12} & -T_{13} \\ -T_{21} & 0 & T_{23} \\ T_{31} & -T_{32} & 0 \end{bmatrix}$$

Thus, the tensor has only three independent components if use form a contraction between the tensor and Levi-Civita symbol ϵ_{ijk} (i.e., if we define a new vector which is defined as the summation of Levi-Civita symbol multiplied by each tensor element) we get,

$$V_i = \sum_{jk} \epsilon_{ijk} T_{ijk}$$

where,

$$\epsilon_{ijk} = \begin{cases} 0 & \text{for } i = j = k \text{ or } i = j \text{ or } j = k \text{ or } k = i \\ 1 & \text{for } (i,j,k) = (3,1,2) \text{ or } (1,2,3) \text{ or } (2,3,1) \\ -1 & \text{for } (i,j,k) = (3,2,1) \text{ or } (1,3,2) \text{ or } (2,1,3) \end{cases}$$

Thus, $V_1 = T_{23} + (-1)(-T_{32}) = 2T_{23}$, $V_2 = 2T_{31}$ & $V_3 = 2T_{12}$

Appendix D

Complex Vector Property

D.1 Statement

Complex vectors in electromagnetics have a one-to-one correspondence between complex vectors and time-harmonic vectors, which allows us flexibility in working with complex vectors instead of handling time-dependent sinusoidally varying real signals. Say we have a time-varying harmonic vector

$$A(t) = A_1 cos(\omega t) + A_2 sin(\omega t)$$

and a = complex vector, $a = a_r + ja_i$ then the mappings are as follows.

$a \Rightarrow A(t)$: $A(t) = ae^{j\omega t} = a_r cos(\omega t) - a_i sin(\omega t)$, and

$A(t) \Rightarrow a$: $a = A(0) - jA(\frac{\pi}{2\omega})\ \forall\ a_r = \Re(a)\ \&\ a_i = \Im(a)$

Now, if $\vec{A}$ & $\vec{B}$ are two vectors & if they are $\perp$ to each other then, $\vec{A} \cdot \vec{B} = 0$ and if they are $\parallel$ to each other then $\vec{A} \times \vec{B} = 0$. Now, If a vector $\vec{K}$ is $\perp$ to $\vec{A}$ then, $\vec{K} \cdot \vec{A} = \vec{K} \cdot \vec{A}^* = 0$. So, for a plane defined by $i\vec{A} \times \vec{A}^*$, the $\vec{K}$ should be $\parallel$ to this plane.

D.2 Proof

Let us consider $p = a + ib$ & $q = c + id$. Now, by performing pq^* & p^*q we have,

$$pq^* = (a + ib)(c - id) = (ac + bd) + i(bc - ad) \tag{D.1}$$

$$p^*q = (a - ib)(c + id) = (ac + bd) - i(bc - ad) \tag{D.2}$$

Thus,

$$pq^* - p^*q = 2i(bc - ad) = 2Im(pq^*) \tag{D.3}$$

Now, we know that

$$|i\vec{A} \times \vec{A}^*|^2 = \sum_{1 \le i \le j \le 3} (a_i b_j - a_j b_i)^2 \qquad \text{[By Lagrange's Identity]}$$

$$= \sum_{1 \le i \le j \le 3} (iA_i A_j^* - iA_j A_i^*)^2$$

$$= \sum_{1 \le i \le j \le 3} (i\{A_i(A_j^*) - A_j(A_i^*)\})^2$$

Now, by using equation D.3 we have,

$$|i\vec{A} \times \vec{A}^*|^2 = \sum_{1 \le i \le j \le 3} (-2\Im(A_i(A_j)^*)) \tag{D.4}$$

Therefore,

$$i\vec{A} \times \vec{A}^* = \hat{i}(-2\Im(A_2 A_3^*)) - \hat{j}(-2\Im(A_1 A_3^*)) + \hat{k}(-2\Im(A_1 A_2^*)) \tag{D.5}$$

Appendix E

Tri-axial antenna orientation calculation

Now, let us consider the following

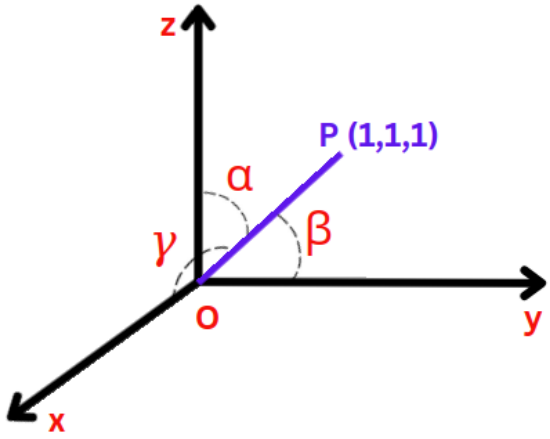

Figure E.1: Image Illustrating a line passing through (1,1,1).

Now, if $\vec{OP}$ passes through the center, then $\alpha = \beta = \gamma$, i.e., the projection of $\vec{OP}$ on z,x, and y axes will be equal.

$$\therefore \vec{OP} = \hat{i} + \hat{j} + \hat{k}$$
$$\therefore cos\alpha = cos\beta = cos\gamma = \frac{1}{\sqrt{3}}$$
$$\therefore \alpha = \beta = \gamma = 54.7°(approx.)$$

Consider a scenario involving a plane intersecting the z-axis and vector $\vec{OP}$ and another plane intersecting the x-axis and vector $\vec{OP}$. The angle formed between these two planes is defined by:

$$\theta = \cos^{-1}\left(\frac{(\text{normal of } OP_z \text{ plane}) \cdot (\text{normal of } OP_x \text{ plane})}{|\text{norm of } OP_z||\text{norm of } OP_x|}\right)$$

Here, the normal to $\vec{OP}$ and the z-axis is given by $\vec{z} \times \vec{OP} = \hat{i} - \hat{j}$, while the normal to $\vec{OP}$ and the x-axis is $\vec{x} \times \vec{OP} = \hat{j} - \hat{k}$. Thus, $\theta = \cos^{-1}\left(\frac{-1}{2}\right) = \frac{\pi}{2} + 60° = 120°$. Therefore, to align the monopoles relative to the x-y plane, an angle of $90° musttiltea ch - \alpha = 90° - \beta = 90° - \gamma = 35.3°$, ensuring that the plane defined with the z-axis and the monopoles is spaced 120° apart from each other.

Appendix F

Unitary Transformations

This section is based on the paper [96] in the reference list, and it only describes the mathematics in detail, not its physical significance.

F.1 Unitary matrix

A $N \times N$ matrix is called unitary, if and only if $B^{-1} = B^{\dagger}$ where † denotes a Hermitian conjugate, i.e., a transpose of the complex conjugate of a matrix.

Thus,

$$\begin{gathered} B^{\dagger}B = I \\ or, B^{-1} = B^{\dagger} \\ \longrightarrow {b^{\dagger}}_i b_j = \delta_{ij} \end{gathered}$$

where, ${b_i}^{\dagger} \& b_j$ are elements of $B^{\dagger} \& B$ respectively, and δ_{ij} elements of the identity matrix, I.

F.2 Centro-Hermitian matrix

Say, if there is a matrix $A \in \mathbb{C}^{P \times Q}$ where, P & Q are the dimensions of A and A belong to the set of complex numbers, $\mathbb{C}$. Then the matrix A will be called Centro-Hermitian if and only if,

$$A = \prod_{P} A^{*} \prod_{Q} \tag{F.1}$$

where,A^{*} is conjugate of A, $\prod_P$ & $\prod_Q$ are exchange matrix defined as

$$\prod_{P} = \begin{bmatrix} 0 & 0 & \dots & 0 & 0 & 1 \\ 0 & \dots & 0 & 1 & 0 & 0 \\ 0 & \dots & 1 & 0 & 0 & 0 \\ \vdots & \vdots & \vdots & \vdots & \vdots & \vdots \\ 1 & \dots & 0 & 0 & 0 & 0 \end{bmatrix}_{P \times P}$$

and,

$$\prod_{Q} = \begin{bmatrix} 0 & 0 & \dots & 0 & 0 & 1 \\ 0 & \dots & 0 & 1 & 0 & 0 \\ 0 & \dots & 1 & 0 & 0 & 0 \\ \vdots & \vdots & \vdots & \vdots & \vdots & \vdots \\ 1 & \dots & 0 & 0 & 0 & 0 \end{bmatrix}_{Q \times Q}$$

Now, let $X = [x(0)x(1)x(2)...x(N-1)]^T$. If X is Centro-Hermitian then,

$$\prod_N X^* = X \tag{F.2}$$

Here, $X^* = [x^*(0)x^*(1)....x^*(N-1)]^T$ and $\prod_N = \begin{pmatrix} 0 & \cdots & 0 & 1 \\ 0 & \cdots & 1 & 0 \\ \vdots & \ddots & \vdots & \vdots \\ 1 & \cdots & 0 & 0 \end{pmatrix}_{N\times N}$

Thus, $\prod_N X^* = \begin{pmatrix} 0 & \cdots & 0 & 1 \\ 0 & \cdots & 1 & 0 \\ \vdots & \ddots & \vdots & \vdots \\ 1 & \cdots & 0 & 0 \end{pmatrix}_{N\times N} \begin{pmatrix} x^*(0) \\ x^*(1) \\ \vdots \\ x^*(N-1) \end{pmatrix}_{N\times 1} = \begin{pmatrix} x^*(N-1) \\ x^*(N-2) \\ \vdots \\ x^*(0) \end{pmatrix}_{N\times 1}$ Thus, from equation F.2, we have, $\begin{pmatrix} x^*(N-1) \\ x^*(N-2) \\ \vdots \\ x^*(0) \end{pmatrix} = \begin{pmatrix} x(0) \\ x(1) \\ \vdots \\ x(N-1) \end{pmatrix}$ or, $x^*(N-i) = x(i-1)$ where, i = 1,2, ...N. Let us assume we have an N data set, $X = x(0)x(1)\cdots\cdots x(N-1)$. Now, preparing a matrix Y out of X such that,

$$Y = \begin{pmatrix} x(0) & x(1) & \cdots & x(L) \\ x(1) & x(2) & \cdots & x(L+1) \\ \vdots & \vdots & \ddots & \vdots \\ x(N-L-1) & x(N-L) & \cdots & x(N-1) \end{pmatrix}_{(N-L)\times(L+1)}$$

Then,

$$Y^* = \begin{pmatrix} x^*(0) & x^*(1) & \cdots & x^*(L) \\ x^*(1) & x^*(2) & \cdots & x^*(L+1) \\ \vdots & \vdots & \ddots & \vdots \\ x^*(N-L-1) & x^*(N-L) & \cdots & x^*(N-1) \end{pmatrix}_{(N-L)\times(L+1)}$$

Now, performing

$$\prod_{N-L} Y^* \prod_{L+1} = \begin{pmatrix} 0 & \cdots & 0 & 1 \\ 0 & \cdots & 1 & 0 \\ \vdots & \ddots & \vdots & \vdots \\ 1 & \cdots & 0 & 0 \end{pmatrix}_{N\times N} Y^* \prod_{L+1}$$

$$= \begin{pmatrix} x^*(N-L-1) & x^*(N-L-2) & \cdots & x^*(N-1) \\ x^*(N-L-2) & x^*(N-L-3) & \cdots & x^*(N-2) \\ \vdots & \vdots & \ddots & \vdots \\ x^*(0) & x^*(1) & \cdots & x^*(L) \end{pmatrix} \prod_{L+1}$$

$$= \begin{pmatrix} x^*(N-1) & x^*(N-2) & \cdots & x^*(N-L-1) \\ x^*(N-2) & x^*(N-3) & \cdots & x^*(N-L-2) \\ \vdots & \vdots & \ddots & \vdots \\ x^*(L) & \cdots & x^*(1) & x^*(0) \end{pmatrix}_{(N-L)\times(L+1)}$$

As we established earlier,

$$x^*(N-i) = x(i-1)$$

where, $i \in [0, N]$. Thus,

$$\prod_{N-L} y^* \prod_{L+1} = Y \tag{F.3}$$

If we concatenate Y with $\prod_{(N-L)} Y^* \prod_{(L+1)}$, i.e., $Y|\prod_{(N-L)} Y^* \prod_{(L+1)}$, then the resultant matrix is also Centro-Hermitian which is proved below.

Let, T = $[Y|\prod_{(N-L)} Y^* \prod_{(L+1)}]_{(N-L)\times(2L+2)}$

Then, if T is Centro Hermitian, then,

$$\prod_{(N-L)} T^* \prod_{(2L+2)} = T$$

Now,

$$\begin{aligned} T^* &= [Y| \prod_{(N-L)} Y^* \prod_{(L+1)}]^* \\ &= [Y^*| \prod_{(N-L)}{}^* (Y^*)^* \prod_{(L+1)}{}^*] \end{aligned}$$

as, $\prod_{N-L}{}^* = \prod_{N-L}$ and $\prod_{L+1}{}^* = \prod_{L+1}$ where, $\prod$ is real matrix. Then, $T^* = [Y^*|\prod_{(N-L)} Y \prod_{(L+1)}]$. Now, to find $\prod_{N-L} T^* \prod_{2L+2}$ utilising the property $A[B|C] = [AB|AC]$ we have,

$$\prod_{N-L} T^* \prod_{2L+2} = [\prod_{N-L} Y^*| \prod_{N-L} \prod_{N-L} Y \prod_{L+1}] \prod_{2L+2}$$

Since, $\prod_X \prod_X = I$ and $IA = A$. Moreover, $[A|B]\prod_{2N} = [B\prod_N |A\prod_N]$ as the exchange matrix $\prod$ reverses the order of the matrix,

$$\begin{aligned} \prod_{N-L} T^* \prod_{2L+2} &= \left[\prod_{N-L} Y^* \mid IY \prod_{L+1} \right] \prod_{2L+2} \\ &= \left[IY \prod_{L+1} \prod_{L+1} \mid \prod_{N-L} Y^* \prod_{L+1} \right] \prod_{2L+2} \\ &= \left[IYI \mid \prod_{N-L} Y^* \prod_{L+1} \right] \\ &= \left[Y \mid \prod_{N-L} Y^* \prod_{L+1} \right] = T \end{aligned}$$

Hence, it is proven that the matrix T is Centro-Hermitian.

F.3 Unitary Transform

For a centro Hermitian matrix A of $P \times Q$ dimension. The unitary transform of A will result in a Real matrix, and it is given by

$$A_R = U^*{}_P A U_Q \tag{F.4}$$

Here, the unitary operator matrix U is defined as, $U = \frac{1}{\sqrt{2}} \begin{bmatrix} I & iI \\ \prod & -i\prod \end{bmatrix}_{N\times N}$, if the N = even. Here, I is an Identity matrix of dimension $\frac{N}{2} \times \frac{N}{2}$, $\prod$ is the Exchange matrix of dimension $\frac{N}{2} \times \frac{N}{2}$.

When N is odd, the the U is defined as $U = \frac{1}{\sqrt{2}} \begin{bmatrix} I & o & iI \\ o & \sqrt{2} & o \\ \prod & o & -i\prod \end{bmatrix}_{N\times N}$, where, I is the Identity matrix of dimension $\frac{N-1}{2} \times \frac{N-1}{2}$, $\prod$ is the Exchange matrix of dimension $\frac{N-1}{2} \times \frac{N-1}{2}$, o is the Zero matrix of dimension $1 \times \frac{N-1}{2}$ or $\frac{N-1}{2} \times 1$ depending on the location.

Now let us examine the following,

$$A_R = {U^\dagger}_P A U_Q$$

if A_R is real then ${A^*}_R = A_R$,

$$\therefore ({U^\dagger}_P A U_Q)^* = {U^\dagger}_P A U_Q$$

Considering LHS,

$$({U^\dagger}_P A U_Q)^* = {U^T}_P A^* {U_Q}^* = {U^T}_P I_P A^* I_Q {U_Q}^*$$

as, $K^\dagger = K^{*T} = K^{T*}$ and $K^{\dagger *} = K^{T**} = K^T$ Now, I_P can be written as $\prod_P \prod_P$. Similarly, I_Q as $\prod_Q \prod_Q$

as,

$$\prod \prod = I$$

or,

$$({U^\dagger}_P A U_Q)^* = U_P^T \prod_P \prod_P A^* \prod_Q \prod_Q U_Q^*$$

Since, A is a centro-Hermitian then, $\prod_P A^* \prod_Q = A$ or,

$$({U^\dagger}_P A U_Q)^* = {U_P}^T \prod_P A \prod_Q U^*$$

Now using, $\prod U^* = U$ & $U^T \prod = U$ (see Section F.3.1), we get,

$$({U^\dagger}_P A U_Q)^* = ({U^T}_P)^* A U_Q \tag{F.5}$$

$$({U^\dagger}_P A U_Q)^* = {U^\dagger}_P A U_Q \tag{F.6}$$

Since, ${A_R}^* = A_R$. Thus, the unitary transform on A provides a real matrix.

F.3.1 Properties of U

The unitary operator matrix has two main properties: (a) $\prod U^* = U$, and (b) $U^T \prod = U^*$. Say, $U = \frac{1}{\sqrt{2}} \begin{bmatrix} 1 & 0 & 0 & i & 0 \\ 0 & 1 & 0 & 0 & i \\ 0 & 0 & \sqrt{2} & 0 & 0 \\ 0 & 1 & 0 & 0 & -i \\ 1 & 0 & 0 & -i & 0 \end{bmatrix}$ then, $U^* = \frac{1}{\sqrt{2}} \begin{bmatrix} 1 & 0 & 0 & -i & 0 \\ 0 & 1 & 0 & 0 & -i \\ 0 & 0 & \sqrt{2} & 0 & 0 \\ 0 & 1 & 0 & 0 & i \\ 1 & 0 & 0 & i & 0 \end{bmatrix}$,

and $U^T = \frac{1}{\sqrt{2}} \begin{bmatrix} 1 & 0 & 0 & 0 & 1 \\ 0 & 1 & 0 & 1 & 0 \\ 0 & 0 & \sqrt{2} & 0 & 0 \\ i & 0 & 0 & 0 & -i \\ 0 & i & 0 & -i & 0 \end{bmatrix}$

Then,

$$\prod U^* = \frac{1}{\sqrt{2}} \begin{bmatrix} 0 & 0 & 0 & 0 & 1 \\ 0 & 0 & 0 & 1 & 0 \\ 0 & 0 & 1 & 0 & 0 \\ 0 & 1 & 0 & 0 & 0 \\ 1 & 0 & 0 & 0 & 0 \end{bmatrix} \begin{bmatrix} 1 & 0 & 0 & -i & 0 \\ 0 & 1 & 0 & 0 & -i \\ 0 & 0 & \sqrt{2} & 0 & 0 \\ 0 & 1 & 0 & 0 & i \\ 1 & 0 & 0 & i & 0 \end{bmatrix}$$

$$= \frac{1}{\sqrt{2}} \begin{bmatrix} 1 & 0 & 0 & i & 0 \\ 0 & 1 & 0 & 0 & i \\ 0 & 0 & \sqrt{2} & 0 & 0 \\ 0 & 1 & 0 & 0 & -i \\ 1 & 0 & 0 & -i & 0 \end{bmatrix}$$

$$= U$$

$\therefore \prod U^* = U$

Now, examining $U^T \prod$,

$$U^T \prod = \frac{1}{\sqrt{2}} \begin{bmatrix} 1 & 0 & 0 & 0 & 1 \\ 0 & 1 & 0 & 1 & 0 \\ 0 & 0 & \sqrt{2} & 0 & 0 \\ i & 0 & 0 & 0 & -i \\ 0 & i & 0 & -i & 0 \end{bmatrix} \begin{bmatrix} 0 & 0 & 0 & 0 & 1 \\ 0 & 0 & 0 & 1 & 0 \\ 0 & 0 & 1 & 0 & 0 \\ 0 & 1 & 0 & 0 & 0 \\ 1 & 0 & 0 & 0 & 0 \end{bmatrix}$$

$$= \frac{1}{\sqrt{2}} \begin{bmatrix} 1 & 0 & 0 & -i & 0 \\ 0 & 1 & 0 & 0 & -i \\ 0 & 0 & \sqrt{2} & 0 & 0 \\ 0 & 1 & 0 & 0 & i \\ 1 & 0 & 0 & i & 0 \end{bmatrix}$$

$$= U^*$$

Hence, $U^T \prod = U^*$.

Appendix G

Phase Contamination by electronic components

In circuit theory, any receiving antenna can be viewed as an independent voltage source with a source impedance called antenna impedance or radiation resistance [88]. Figure G.1 is the circuit equivalent diagram of a receiving antenna with a load resistance of 50 Ω.

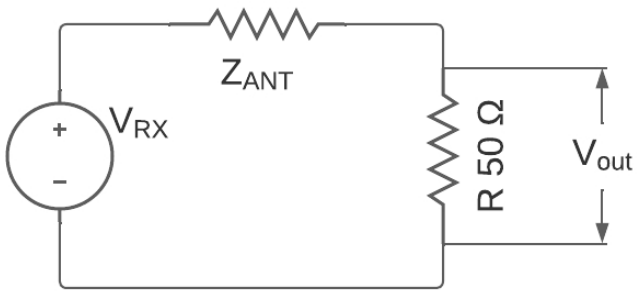

Figure G.1: Receiving antenna circuit equivalent. V_{RX} is the voltage received by the antenna, Z_{ANT} is the intrinsic impedance or radiation resistance of the antenna, R is the load resistance of 50 Ω, and V_{out} voltage across the load.

Since the voltage received (V_{RX}) by the antenna is due to the electric field of EM wave, then, $V_{RX} = h_{eff}\vec{E}$ where h_{eff} is the effective height of the antenna and $\vec{E}$ is the electric field present in the EM wave. Using the plane wave consideration, the electric field component can be written as $\vec{E} = E_0 e^{j(\vec{k}\cdot\vec{r}-\omega t)}$ here, $\omega = 2\pi f$. Thus, the voltage received can be written as follows:

$$V_{RX} = h_{eff}E_0 e^{j\vec{k}\cdot\vec{r}}e^{-j\omega t} = Ae^{-j\omega t} \tag{G.1}$$

Using equation G.1 and circuit in Figure G.1 the received signal V_{out} can be written as

$$V_{out} = \frac{V_{RX} \times 50}{50 + Z_{ANT}} \tag{G.2}$$

As impedance comprises of resistive (R) and reactive component thus antenna impedance can be written as $Z_{ANT} = R_{ANT} + jX_{ANT}$. Considering the antenna impedance and equation G.2, one can observe analytically how phase is being modified due to the impedance in equation G.3.

$$V_{out} = \frac{50A}{\sqrt{R_{ANT}^2 + 50^2}} e^{-j[wt + tan^{-1}(X_{ANT}/(R_{ANT}+50))]} \tag{G.3}$$

In case of the addition of several circuit components either in series or in parallel, the antenna impedance Z_{ANT} in equation G.3 has to be replaced by the effective impedance of the circuit, also known as the Thevenin's equivalent.

Appendix H

Model Training and Evaluation

Adapted from the Appendix of: ***Harsha Avinash Tanti***, *Tiasha Biswas, Abhirup Datta, Anshuman Tripathi, "Development of a Machine Learning based Radio source localization algorithm for Tri-axial antenna configuration," Journal of Astronomy and Astrophysics, Accepted for Publication, (Preprint Version: arXiv:2409.20209)*

Training an artificial neural network (ANN) model entails segmenting the data set into input parameters and corresponding outputs. The data set must be split into two portions to train the model efficiently: the training set and the test set. The training set is divided into two subsets: one for training the model and another for validating it, ensuring model convergence at each epoch during training. The test set remains untouched until after training, serving to evaluate the model's performance. Several hyperparameters impact the model training process, including epochs, batch size, and optimizer choice [229]. An epoch is a single pass through the entire training data set within one machine learning model training cycle. During each epoch, the model adjusts its weights and biases based on the error or loss calculated from processing every sample in the data set. Batch size refers to the number of training instances processed in one iteration during model training [230, 231]. So, in one cycle, i.e., epoch, several such iteration is performed till the entire training data set is processed. Large data sets are divided into smaller batches to reduce computational costs. Due to hardware limitations, smaller batches are often used, enabling more frequent parameter updates, which can help with convergence. However, smaller batches may introduce noise into gradient estimates, potentially reducing overfitting by allowing the model to explore the loss surface more effectively [229–231].

An optimizer modifies model weights in machine learning to reduce the loss function during training. The most common optimizers are SGD (utilizes a data subset (batch) for weight updates), Adam (an adaptive optimizer that merges AdaGrad and RMSProp), and RMSProp (modulates the learning rate based on recent gradients) [229]. Selection of the right optimizer is fundamental as it affects training speed, stability, and the final accuracy. For instance, Adam efficiently manages noisy gradients and achieves quicker convergence, whereas SGD may struggle with noisy or sparse gradients [229]. This research tested various combinations of batch sizes and optimizers to find the optimal neural network. Given the large data set, we opted for a batch size 16384, considering our computational constraints. Ultimately, the Adam optimizer was chosen for its efficacy in handling noisy gradients and achieving quicker convergence. Additionally, the model is assessed or trained during training based on the convergence of the training and validation loss curves. Training loss indicates the model's performance on the training data and is computed during the training process, guiding parameter updates via methods like gradient descent to minimize it [230, 231]. Validation loss, on the other hand, measures the model's performance on a distinct data set called the validation set. Part of the data is reserved as the validation set and

is periodically assessed (e.g., after each epoch) to calculate the validation loss. This metric helps evaluate the model's generalization to unseen data and monitors performance to detect overfitting. An increase in validation loss while training loss decreases signals overfitting [143, 230–232].

Appendix I

Computation Speed of SAM-DoA

Adapted from the Appendix of: ***Harsha Avinash Tanti***, *Tiasha Biswas, Abhirup Datta, Anshuman Tripathi, "Development of a Machine Learning based Radio source localization algorithm for Tri-axial antenna configuration", Journal of Astronomy and Astrophysics, Accepted for Publication, (Preprint Version: arXiv:2409.20209)*

In [70], an algorithm SAM-DoA is proposed wherein the snapshot averaging method is used to improve the SNR of the signal. This addition improved the detection capability in terms of precision of the DoA estimation; however, this came with a cost of increased computational complexity and inference time.

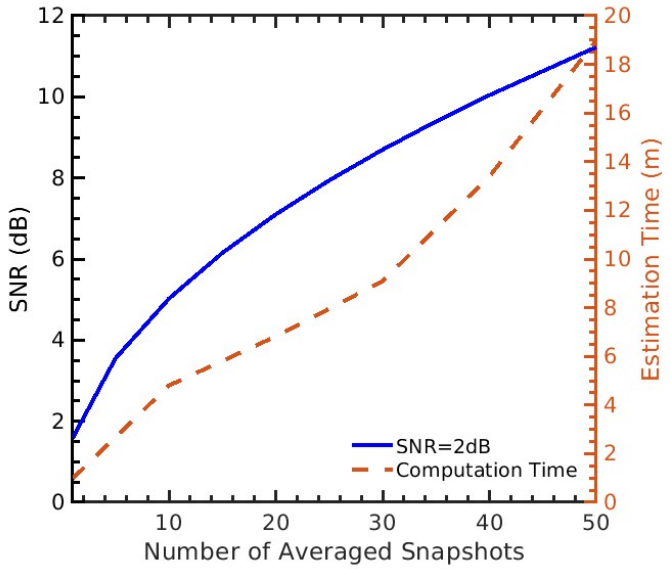

Figure I.1: Increase in SNR and Inference time of SAM-DoA algorithm to the number of averaged snapshots.

Figure I.1 shows how the SNR (solid blue line) and inference/estimation time (orange dotted line) depend on the number of snapshots averaged. The computational complexity and time of SAM-DoA depend upon the Sample length, the pencil parameter of the matrix pencil method, and the time required to average over snapshots. The timing calculations of SAM-DoA in [70] were performed for a sample length of 300; however, for practical cases, the sample length is between

1024 and 8192 in multiples of 2. For the SEAMS case, the sample length will be 2048 or 4096 based on the Phase I observations. In this case, the SAM-DoA will become much slower as for the 4098 sample length, the computation time is in minutes at a clock speed of 2GHz (number of snapshots averaged = 1). If SAM-DoA is to be implemented onboard, wherein the clock speed will be in MHz, the computation time might reach from a few minutes to hours based on the average length. Thus, even though the SAM-DoA provides high accuracy compared to the other algorithms, its exponential scaling in inference time to the number of snapshots averaged is a challenge.

Appendix J

IIT Indore Radio Interferometer (IIRI)

J.1 Introduction

The construction of very large single-dish radio telescopes (dia$\geq 500m$) is constrained by practical limitations, primarily arising from the combined effects of gravitational deformations and wind forces. Moreover, significantly longer wavelengths of radio waves (ranging from hundreds to millions of times the length of optical wavelengths) exacerbate diffraction effects. Consequently, the angular resolution of single-dish radio telescopes is generally restricted to several arcminutes, in stark contrast to the sub-arcsecond resolution achieved by ground-based optical telescopes or the 50 milliarcsecond resolution of the Hubble Space Telescope operating near its diffraction limit.

The development of radio interferometry, made possible by remarkable advancements in electronics and signal processing, transformed our ability to explore the universe. In 1947, McCready, Pawsey, and Payne-Scott unveiled a revolutionary concept: the response of an interferometer to an extended radio source could be understood as sampling specific points of the Fourier transform of the source's brightness distribution. This insight sparked a wave of excitement and innovation within the radio astronomy community, particularly at leading institutions in Sydney, Cambridge, and Manchester. Astronomers began building arrays with multiple baselines to sample the Fourier transform of extended sources across various spatial frequencies as these techniques gained traction. This approach opened a new era in radio astronomy, allowing researchers to piece together intricate details of cosmic structures with unprecedented precision.

The 1970s and 1980s had been a revolutionary period for radio astronomy, marked by the importance of aperture synthesis arrays that transformed how we observe the universe. Groundbreaking facilities like the Westerbork Synthesis Radio Telescope (WSRT) in the Netherlands, the Australia Telescope Compact Array (ATCA), the Very Large Array (VLA) in the United States, and the MERLIN array in the United Kingdom pushed the boundaries of imaging capabilities. These arrays and global Very Long Baseline Interferometry (VLBI) networks harnessed the Earth's rotation to achieve extraordinary imaging performance, unveiling intricate details of the cosmos. In recent years, interferometry has expanded into new frontiers of frequency. Cutting-edge arrays like the Low-Frequency Array (LOFAR) in Europe, the Giant Metrewave Radio Telescope (GMRT) in India, and the Atacama Large Millimeter/submillimeter Array (ALMA) in Chile have opened up a low, meter, and submillimeter wavelength regimes, offering fresh insights into the universe. Furthermore, the Square Kilometre Array (SKA), under construction in Australia and South Africa, is set to create a new benchmark in radio astronomy, combining unprecedented sensitivity with remarkable angular resolution to explore the cosmos like never before.

Interferometric arrays synthesize observations from multiple smaller antennas, achieving the resolving power, which in turn is much larger than that of a single-dish telescope. Unlike single-dish systems, which measure only the intensity of incoming signals and lose phase information, interferometry prioritizes the phase differences between signals received by multiple antennas. This technique requires accuracy in timing, frequency synchronization, and precision of geometric calibration of the array to ensure the quality of the imaging. Coupled with the demands of a complex data processing pipeline, interferometry is more sophisticated and technically challenging than single-dish observations.

A basic interferometer consists of two antennas separated by a baseline of length b, observing the same celestial source. As the electromagnetic waves from the source reach the antennas, a geometric delay arises due to the finite speed of light ($c \approx 3 \times 10^5$ km/s). This delay manifests as a phase difference in the received signals, encoding spatial information about the source. Achieving high angular resolution, such as a beam size of approximately 1 arcsecond (2×10^{-5} radians) at 1420 MHz, would require an impractically large single-dish telescope, approximately 10 km in diameter. Instead, modern radio arrays utilize distributed antennas, where the resolution is dictated by the maximum baseline length between antennas rather than the size of individual dishes. This approach circumvents the engineering challenges of constructing massive single dishes and enhances observational flexibility and capability.

Understanding the operation of interferometric systems requires a comprehensive grasp of signal flow and instrumentation. Radio astronomers must be well-versed in data acquisition principles, radio frequency instrumentation, and their limitations to process and analyze data effectively. To train the next generation of radio instrumentation engineers and astronomers, a dedicated instructional facility has been established at IIT Indore, known as the IIT Indore Radio Interferometer (IIRI). This appendix details the development of the IIRI, particularly the electronics designed for signal acquisition, along with initial observational results.

J.2 Key components of an Interferometer - An Instrumentation perspective

Figure J.1 illustrates the general block diagram of a two-element interferometer. In this configuration, signals from two antennas are multiplied and time-averaged, known as correlation or cross-correlation. A specialized instrument performs this operation called a correlator [85, 233]. At the heart of interferometry lies the Van Cittert-Zernike theorem, which establishes that the correlated value, referred to as visibility, represents the two-dimensional Fourier transform of the sky's brightness distribution [85, 233]. Consequently, the correlator is a critical component of any radio interferometer. There are two primary types of correlators employed in astronomical observations:

1. **XF Correlator:** In an XF correlator, cross-correlation is performed before applying the Fourier transform (see Figure J.2 for a typical block diagram). The process begins with digitizing the incoming signals using an Analog-to-Digital Converter (ADC), followed by an integral delay block to synchronize the signals. One antenna's signal is then processed through a sequence of delay lines, multipliers, and accumulators to perform cross-correlation. Once the signals are correlated, they are quantized and subsequently Fourier-transformed. Essentially, the XF correlator follows a "correlate-first, Fourier-transform-later" approach.
2. **FX Correlator:** In an FX correlator, the Fourier transform of the incoming signals is performed before correlation, as per the Wiener-Khinchin theorem [85, 233] (refer to Figure J.3 for a block diagram of FX correlator). The workflow begins similarly, with signal digitization via an ADC and synchronization through an integral delay block. The signals then undergo

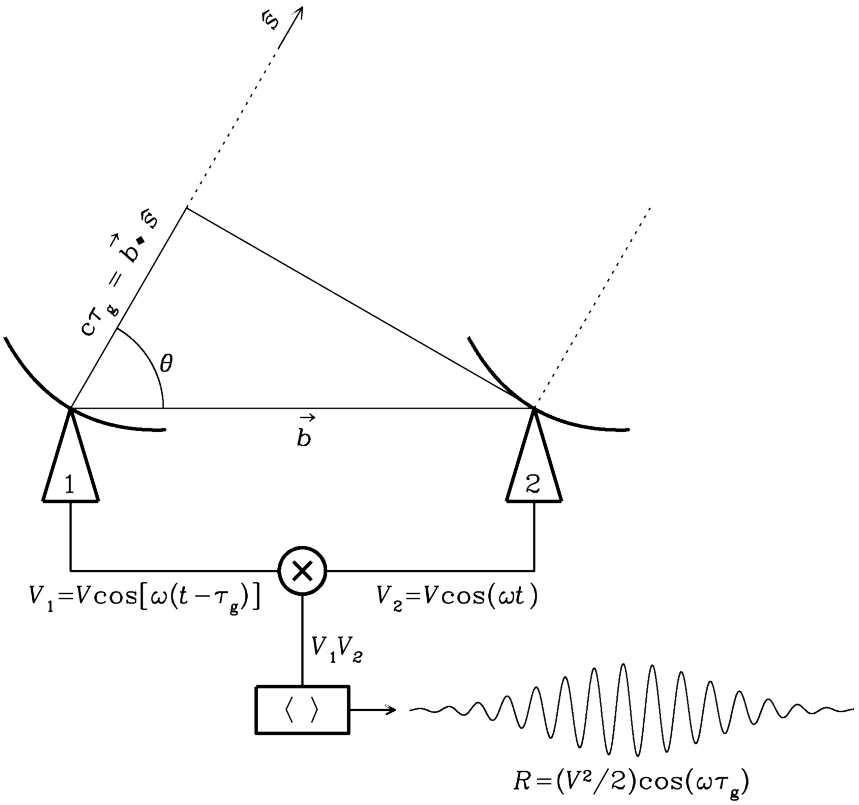

Figure J.1: A general block diagram of two element Radio Interferometer.

fringe stopping, achieved by multiplying them with a signal generated by a Numerically Controlled Oscillator (NCO) to account for the apparent motion of the source. Following this, the signals are Fourier-transformed, subjected to complex multiplication (correlation), accumulated, and finally stored. The FX correlator adopts a "Fourier-transform-first, correlate-later" methodology.

FX correlators are widely used among the two primary correlation strategies due to their lower complexity, reduced hardware requirements, and greater configurability. This approach, which applies the Fourier transform before signal processing, underpins modern technologies like digital beamformers. To implement an FX correlator, signals from the antenna must first be digitized. This crucial step is performed by an Analog-to-Digital Converter (ADC), which converts the continuous, real-time signals received by the antenna into digital signals. General-purpose or application-specific computing systems then process these digital signals to compute their Fourier transform. As a result, the ADC emerges as a pivotal component, exerting a profound influence on the design and performance of the entire receiver system.

The specification of the ADC is a critical factor in correlator and receiver design, as it dictates the requirements for both the analog front-end and back-end electronics. Parameters such as operational frequency, resolution, and voltage range directly impact the design of the associated analog components. Typically, ADCs operate at lower frequencies, up to a few gigahertz, as electronics designed for higher frequencies pose significant challenges and costs. In radio astronomy, the operational frequency is often within hundreds of megahertz, making low-frequency ADCs ideal for signal digitization. To bring the signal within the ADC's operational range, a superheterodyne

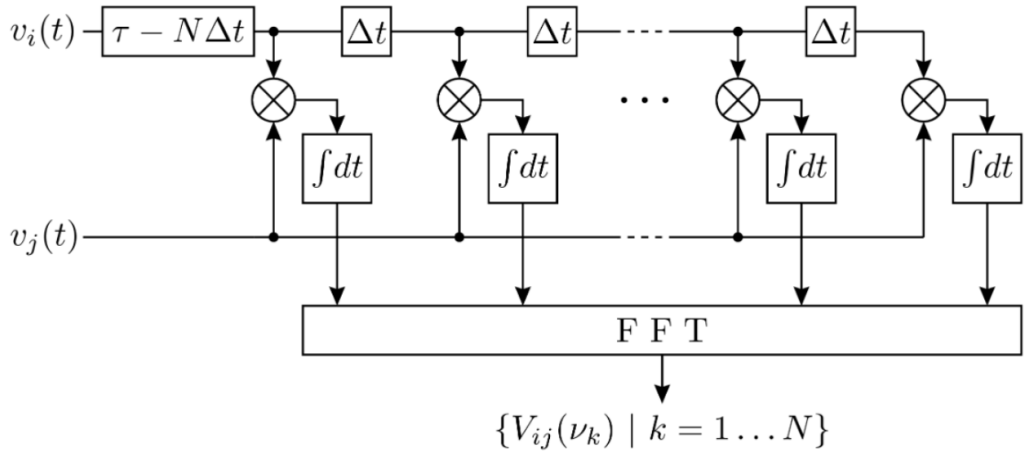

Figure J.2: Block diagram of XF correlator. (Image Credits: Jayce Dowell and Greg Taylor)

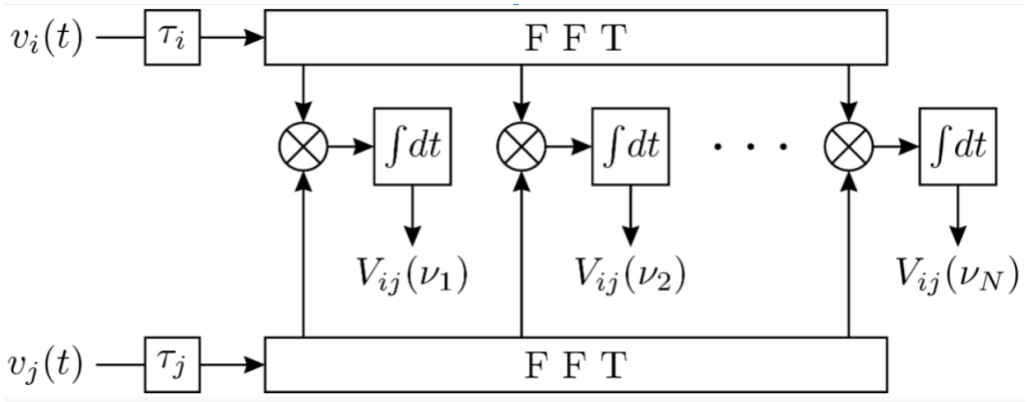

Figure J.3: Block diagram of FX correlator. (Image Credits: Jayce Dowell and Greg Taylor)

receiver is commonly used in the analog back-end to downconvert the signal frequency, ensuring accurate digitization. In addition to ADC specifications, several other factors must be considered when designing a receiver system. A primary consideration is the operating frequency, particularly for radio-frequency (RF) instrumentation dealing with signals above 30 MHz. At these frequencies, the wavelength matches the size of metal tracks, requiring careful design to reduce radiative, inductive, and capacitive losses. Transmission lines and proper shielding are used to minimize these losses.

Moreover, factors like Noise figure (NF) and noise temperature (T_N) are equally crucial parameters in receiver design, as they directly influence the sensitivity and performance of the system. The noise figure quantifies how much noise the receiver adds compared to an ideal, noise-free system. In contrast, the noise temperature represents this noise in terms of an equivalent temperature. Lower noise figures and temperatures are essential to ensure high sensitivity, especially in radio astronomy, where weak celestial signals must be detected against background noise. Careful selection of low-noise amplifiers (LNAs) and optimization of the receiver chain are necessary to maintain the instrument's sensitivity. Thus, when designing and testing RF instruments, atleast the following considerations need to be taken care of:

- Ensure proper shielding to protect against external noise and electromagnetic pulses (EMP).

Table J.1: IIRI Antenna Specifications

Specifications	Values
Number of Antennas	4
Antenna Type	Parabolic Reflector
Antenna Diameter	4.5m
Antenna Feed	VE4MA
Longest Baseline	73 m
Operational Frequency	1.37 - 1.47 GHz
Field of View	$\sim 2.7^{\circ}$
Angular resolution	$\sim 10'$
Movement accuracy	$\Delta\phi = 90''$ and $\Delta\theta = 90''$

- When connecting two amplifiers in series, include a passive element between them to reduce the risk of oscillations.
- Design the receiver chain to minimize the noise figure and maintain a low system noise temperature, using high-performance LNAs and robust component selection.

J.3 Development of IIRI - System Design

The IIRI consists of four 4.5 m fully steerable parabolic dish antennas operating in the L band, having the specifications tabulated in Table J.1. Considering the previous section, the ADC and digital backend selection were prioritized. The CASPER ROACH2 board was selected due to its ease of configuration and controllability without compromising sensitivity. The ROACH is an acronym for Reconfigurable Open Architecture Computing Hardware. ROACH-2 successor to ROACH 1 and uses the new Xilinx Virtex-6 series of FPGAs [1]. A block diagram of ROACH 2 is shown J.4. It maintains all the aspects that made ROACH 1 a success, but there is a significant increase in overall performance in processing power, Input-Output throughput, and memory bandwidth. The ROACH board includes twin Z-DOK ADC cards, based around 8 Texas Instruments ADS5272 ADC chips, each digitizing 8 signals at 12 bits resolution and up to 65MSa/s. The ADCs can be clocked by an on-board 50MHz oscillator or an external clock source of up to 2 GHz[2].

As the IIRI is an educational facility, care has been taken to make the design basic and straightforward. Therefore, a simple design, as shown by the block diagram in Figure J.5, has been implemented for the interferometer facility. Following Figure J.5, there are four major instrument blocks - 1) Antenna, 2) Front-End, 3) Analog Back-End (Super Heterodyne Receiver), and 4) Digital Back-End (ROACH2 - FX Correlator). Figure J.6 shows a more detailed signal flow diagram, which is the same for all the antennas.

[1] https://casper.berkeley.edu/wiki/ROACH-2_Revision_2
[2] https://casper.berkeley.edu/wiki/X64_adc

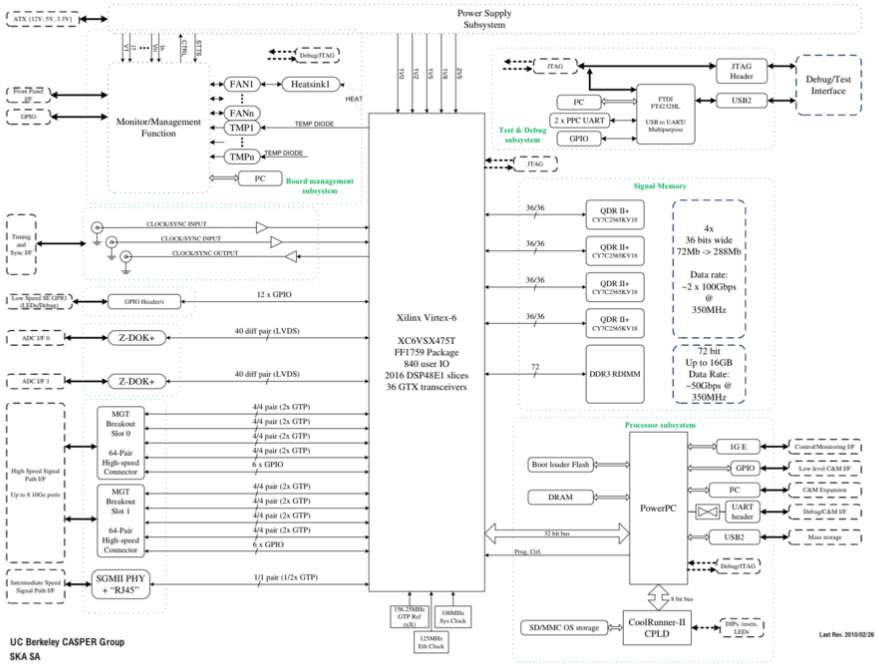

Figure J.4: Block diagram of ROACH-2. (Image credits: CASPER community)

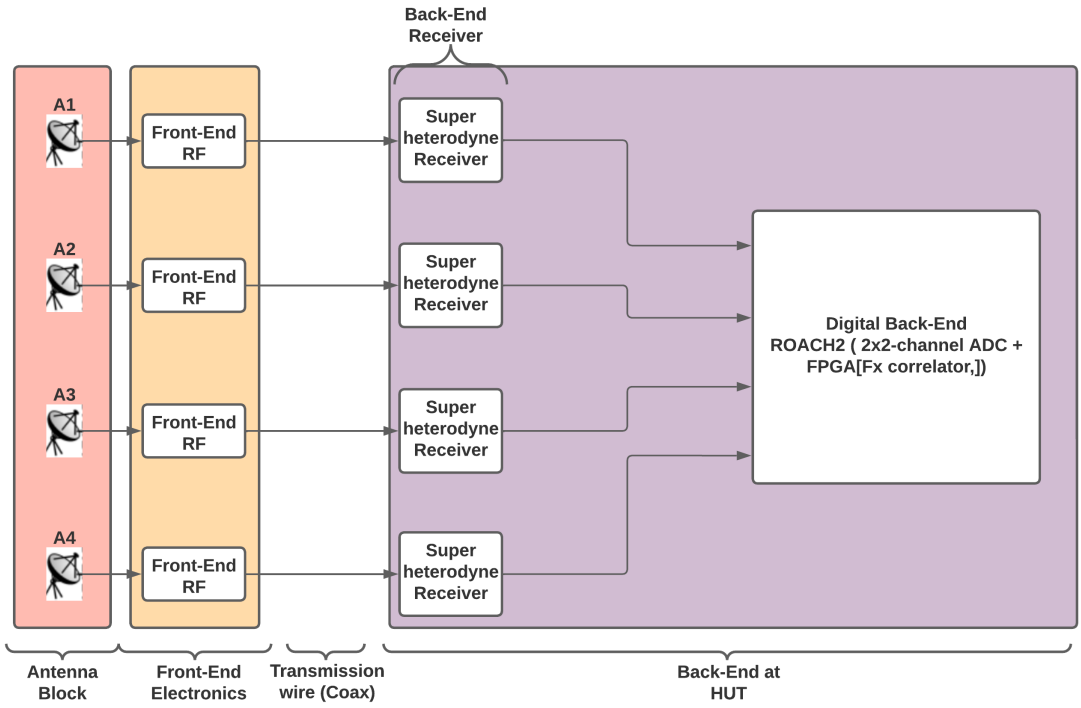

Figure J.5: A simplified block diagram of IIRI.

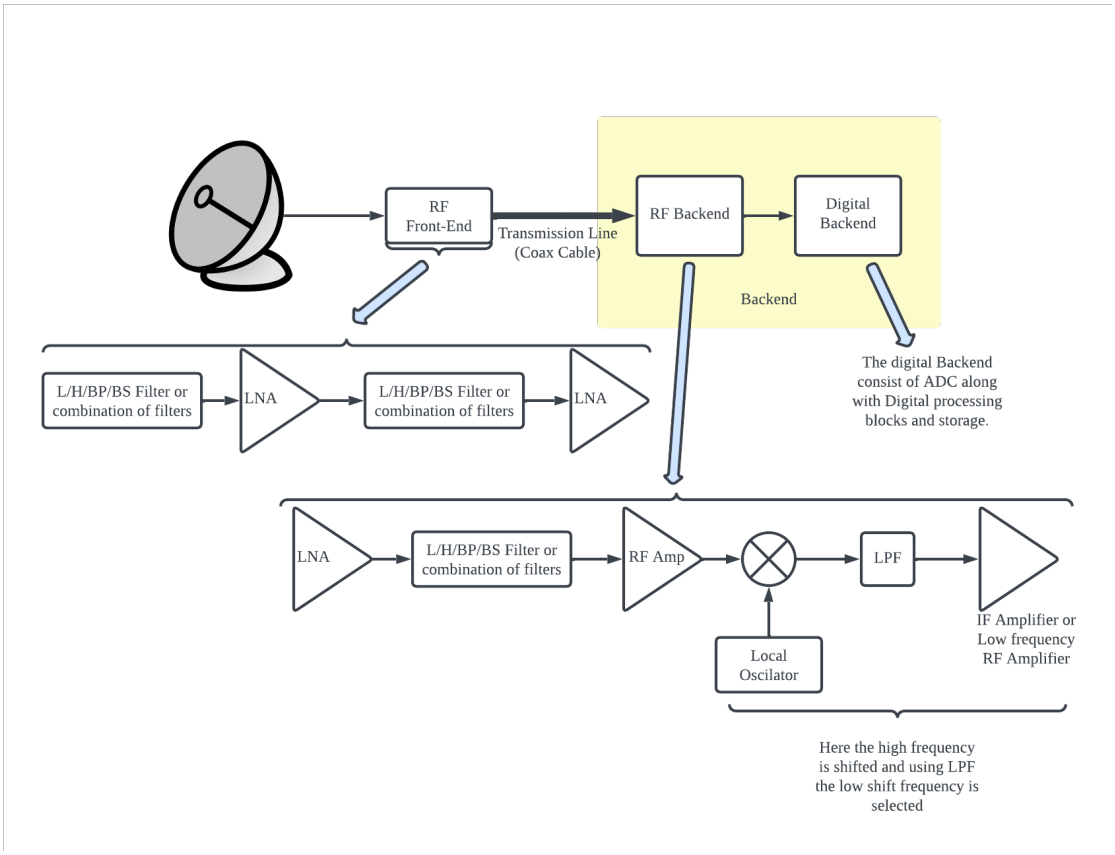

Figure J.6: Block diagram illustrating the signal flow from single antenna to the digital receiver, as implemented for all four antennas of the IIT Indore Radio Interferometer (IIRI).

J.3.1 Antenna

As discussed earlier, the IIRI consists of four steerable 4.5 m parabolic dish antennas. A parabolic dish antenna consists of a parabolic reflector that focuses incoming electromagnetic waves onto a focal point, where a feed antenna is placed to capture the signal, where feed is generally the radiating element. This configuration allows parabolic dish antennas to effectively collect and amplify weak signals, making them useful for astronomical observations. Typically, the diameter of the dish is much larger than the wavelength of the signal it operates on, ensuring precise focusing and minimal diffraction effects [80]. These dish antennas can be broadly classified into four types based on the feeding mechanism (see Figure J.7). These types of dish antennas are

1. **Axial Feed antenna:** In an Axial Feed antenna, also known as a prime focus antenna, the feed of the antenna is placed at the focal point of the parabolic reflector [234]. The axial feed system is one of the most widely used for larger parabolic reflector antennas as it is straightforward and is commonly used in radio astronomy. The major disadvantage is that the feed structure blocks a portion of the incoming signal, reducing aperture efficiency. This is true for the large antennas utilized for sensitive astronomical measurements, wherein the antenna feeds are large due to the radiating element, the front-end electronics, and the temperature maintenance unit.

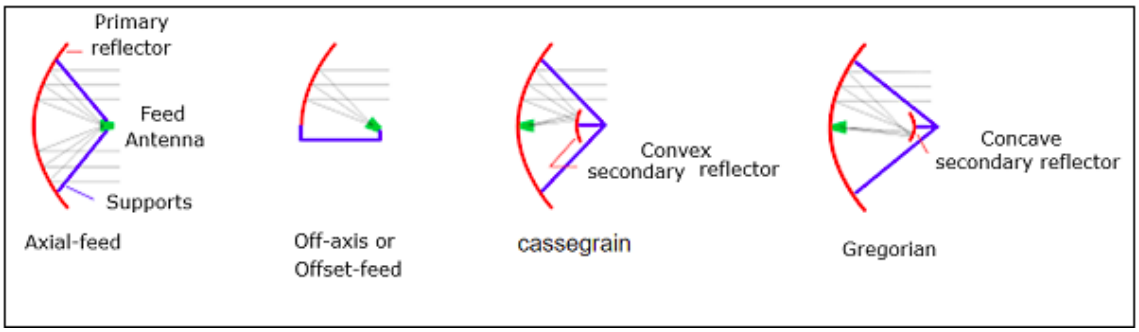

Figure J.7: Image illustrating different types based on the feeding mechanism [8, 9]. (Image Credits: du Preez et al 2016)

2. **Off-axis or Offset feed antenna:** In the offset feed system, the feed is positioned off the central axis of the parabolic reflector. This design uses an asymmetrical parabolic segment, with the feed and focal point on one side of the reflector surface. By doing so, the feed structure does not obstruct the main beam, leading to improved antenna performance. This design enhances antenna efficiency and minimizes signal loss [88]. It is commonly used in applications such as satellite TV antennas, particularly smaller-sized ones, where preventing obstruction by the feed structure and low-noise block amplifier is crucial.

3. **Cassegrain Antenna:** The Cassegrain feed system is a widely used design for parabolic reflector antennas, characterized by a secondary reflecting surface between the primary parabolic reflector and the radiating feed element. This configuration shortens the effective length of the antenna system, as the secondary reflector redirects the signal's focus [235]. This compact design can be advantageous for systems requiring reduced physical dimensions. The concept originates from the Cassegrain telescope, developed in 1672 by Laurent Cassegrain and adapted for antennas to enhance efficiency and design practicality. Typical efficiency levels for antennas using the Cassegrain feed system range between 65% and 70%.

4. **Gregorian Antenna:** The Gregorian feed system is similar to the Cassegrain design but features a concave (ellipsoidal) secondary reflector. This configuration allows for enhanced aperture efficiency, typically exceeding 70%, by providing better illumination of the entire reflector surface. This design is particularly suitable for applications that demand precise beam shaping and high efficiency. As a result, it is commonly employed in high-performance communication systems where these attributes are critical.

The IIRI facility uses the prime focus antenna due to its simplistic design and cost-effectiveness. Since IIRI is primarily designed for educational purposes, the effect of feed blockage on aperture efficiency is a minor concern. The primary goal of the IIRI antenna system is to demonstrate the fundamental principles of radio interferometry and provide hands-on training in instrumentation and signal processing. Therefore, while the feed structure introduces some loss in aperture efficiency, it is an acceptable trade-off for the simplicity and cost-effectiveness of the axial feed design. Thus, in the case of IIRI, the significant challenges were the feed design and the feed alignment for proper antenna illumination with minimum spillover. As the IIRI parabolic reflectors have an F/D ratio of ∼0.4 thus, to have a complete illumination, the VE4MA feed was selected having a bandwidth of 600 MHz from 1250 to 1850 MHz and a beamwidth of $\sim 79^{c}irc$. A VE4MA feed is a circular horn antenna with a kumar choke [236]. Figure J.8 shows the antenna's CAD design and Radiation pattern, whereas Figure J.9 shows the reflection characteristics of the antenna.

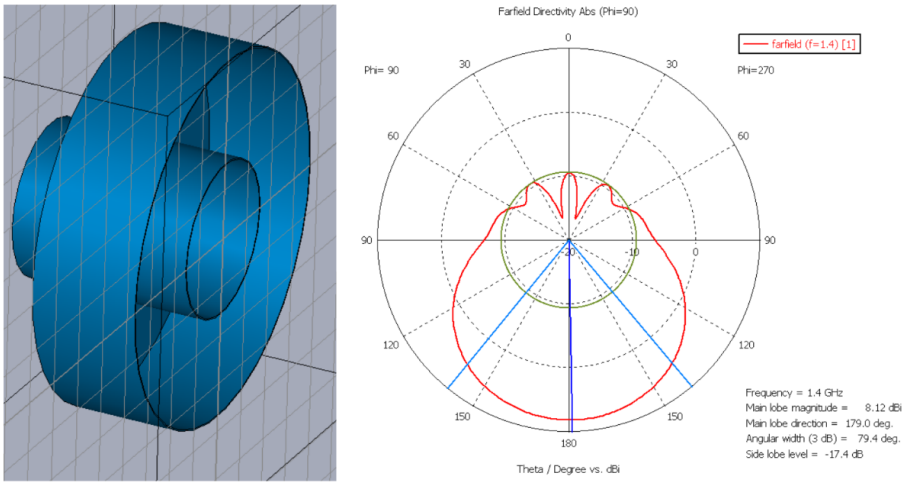

Figure J.8: The image on the right shows a CAD diagram of VE4MA feed and the image on the left shows the radiation pattern of the feed.

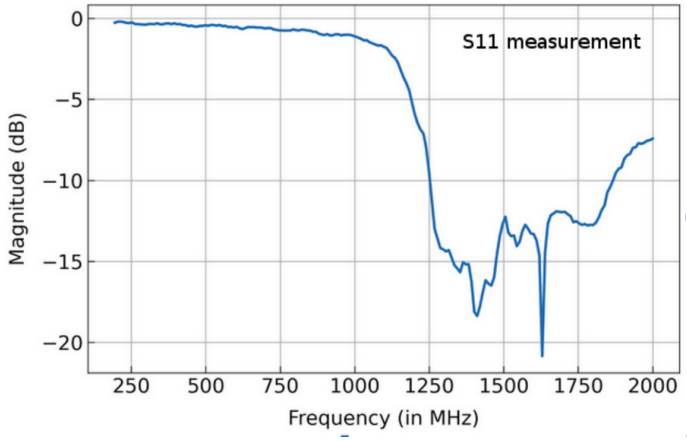

Figure J.9: The image illustrates the measured S11 characteristics of the VE4MA feed.

J.3.2 Front-End Electronics

Following the antenna, the next component in the receiver chain is the RF Front-End Electronics unit, as depicted in Figure J.5. This unit is critical in amplifying the received signal to a level suitable for long-distance transmission. The RF front end must be highly sensitive while introducing minimal noise to preserve signal integrity. Additionally, it should effectively suppress unwanted frequency bands. Thus, the Front-End unit should consist of Low Noise Amplifiers (LNAs) and Filters. LNAs are a type of amplifiers that have a very low noise Figure[3] (NF).

Figure J.6 presents a detailed block diagram of the complete receiver system, including the RF front-end components. The RF Front-End features a bandpass filter (BPF) centered at 1.42 GHz with a roll-off rate of -60 dB/decade, followed by a low-noise amplifier (LNA) with a noise figure (NF) of 0.75 dB and a gain of approximately 40 dB. This configuration is repeated with another

[3]A measure to quantify the noise contribution of any device and is defined as the ratio of the signal-to-noise power ratio at the input to the signal-to-noise power ratio at the output.

identical BPF and LNA in sequence, providing an overall gain of ∼79 dB. This configuration was designed to suppress the noise in the L band due to mobile communication signals.

J.3.3 Back-End Electronics

The Back-End Electronics block is another critical component of the radio receiver system. Its design is closely tied to the observation's operational frequency band and the digital receiver's capabilities. Since digital receivers often operate at lower frequencies than the observational band, a superheterodyne or heterodyne receiver is employed to downconvert the signal to a frequency compatible with the digital receiver's operational range[4].

In the detailed block diagram of the IIRI signal flow, illustrated in Figure J.6, the design of the Back-End Electronics is elaborated. The amplified signal from the front end is transmitted via coaxial cable and passed through an LNA to preserve the signal-to-noise ratio (SNR). It is then filtered through a band-pass filter, further amplified using an RF amplifier, and subsequently heterodyned with a single-tone frequency of 1200 MHz. The resulting intermediate frequency signal is passed through a low-pass filter (LPF) with a cutoff of 300 MHz and a roll-off rate of -40 dB/decade. Afterward, the signal undergoes another amplification stage using an LNA before being delivered to the digital receiver for processing.

J.3.4 Digital Back-End: X-Engine

A digital Back-End system is one of the most crucial blocks of the radio receiver. This block is responsible for converting an analog or real-time signal into a digital signal and its correlation with the signals from different antennae. In order to perform these tasks, the instrument needs to be sensitive and configurable to adjust the errors in the signal. As discussed in Section J.3, the ROACH2 Board is selected as a Digital Receiver for IIRI. It has built or attached two-channel ADCs with Vertex 6 FPGA, which can digitize and correlate signals within the ROACH2 board by programming the FPGA, making it a configurable Digital Signal Processing unit (DSP). At IIRI, FX correlator is implemented due to its computational efficiency, superiority in delay compensation, scalability, and configurability[5] [237–239]. This FX correlator has been implemented on ROACH2 using the Casper Toolflow.

Figure J.10 illustrates the block diagram of the DSP/X-Engine used in the system. The X-Engine's process begins by converting the intermediate frequency (IF) signal received from the RF Back-End or Superheterodyne receiver into a digital signal. This is accomplished using onboard ZDOKs with ADC 1x5000-8 DMUX1:1 modules. Each ADC generates eight parallel 8-bit samples per clock cycle, operating at a sampling frequency of 1200 MHz. By Nyquist's criterion, the maximum input frequency for the correlator is 600 MHz. The ADC outputs data in 2's complement format, while the clock fed to the FPGA operates at $1/8^{th}$ of the ADC clock frequency, derived from one of the onboard ADCs. Consequently, data is transferred to the FPGA every 6.67 ns (1/150 MHz). The ADC handles a maximum peak-to-peak analog input voltage of 500 mV (-2 dBm)[6].

[4]Heterodyning is the process of mixing two signals or frequencies to produce an intermediate frequency (IF) that is either higher or lower than the original observed frequency. This technique shifts the frequency of a received signal—either increased or decreased—by combining it with a single-tone reference frequency. Whether up or down, the instrument responsible for this frequency conversion is called a Superheterodyne Receiver or simply a Heterodyne Receiver [85].

[5]https://library.nrao.edu/public/memos/alma/memo342.pdf

[6]https://casper.berkeley.edu/wiki/ADC1x5000-8

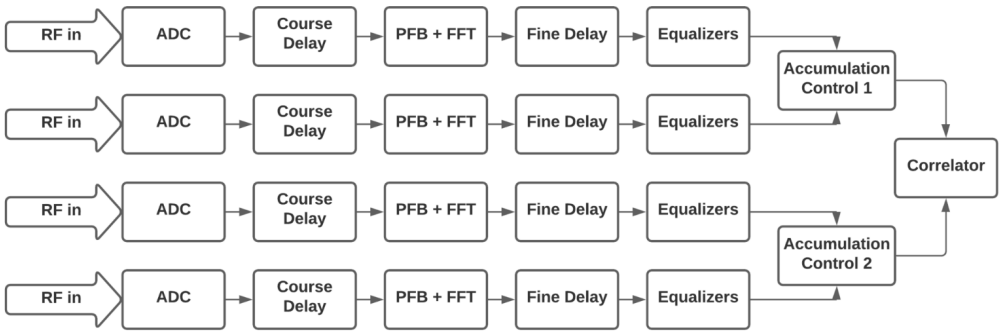

Figure J.10: Block diagram of X-Engine of IIRI - four element interferometer, implemented on the ROACH2.

Once digitized, the ADC samples are passed through coarse delay blocks, which add a specified number of clock cycle delays to synchronize signal paths before reaching the FFT blocks. This step is crucial for compensating path delays between inputs. The signal enters the Polyphase Filter Bank (PFB) and Fast Fourier Transform (FFT) blocks. The PFB applies a Hamming window function to minimize DFT leakage in the subsequent FFT operation. The FFT transforms the time-domain real samples into frequency-domain complex samples using a 2048-point FFT core from the Xilinx library. This setup achieves a frequency resolution of approximately 0.585 MHz, calculated as:

$$\text{Frequency Resolution} = \frac{\text{Bandwidth}}{\text{Number of Channels}} = \frac{600 \text{ MHz}}{1024} = 0.585 \text{ MHz}.$$

A Fine Delay block follows the FFT to perform phase and fringe corrections. However, this block is unused in the current design since phase calibration tests are yet to be conducted. Calibration is typically needed when fringes appear without proper tuning. Next, the Accumulation Control block integrates FFT samples over a specific time to limit the number of processed samples. In this design, the integration time is approximately 0.89 seconds, computed as:

$$\text{Integration Time} = \frac{1}{150 \text{ MHz}} \times 256 \times \text{Accumulation Length}$$

the accumulation length is a configurable software register set via Python, initialized at approximately 524,288. Finally, the multiplication and accumulation operations are executed using a direct-X (dir_x) or correlator block. This block multiplies the signals received from different antennas, producing the correlated power and phase for each frequency channel. The resulting data is then stored in the designated storage unit.

J.4 Initial Results

Figure J.11 provides an image of the antenna site, highlighting the six baselines formed between the four antennas (A1–A4). The yellow structure visible in the image serves as the control center, housing all the Back-End electronics.

Before implementing the four-element interferometer design, preliminary testing of the antennas was conducted to ensure proper feed alignment and verify the functionality of the RF front. The feed alignment was tested by pointing the antennas toward a radio source in drift scan mode. In this mode, as the radio source transits across the antenna's beam, the signal intensity peaks when the source aligns with the antenna's pointing direction, confirming correct feed alignment. Figures J.12 and J.13 display the results of this feed alignment experiment for antennas A1 and A4,

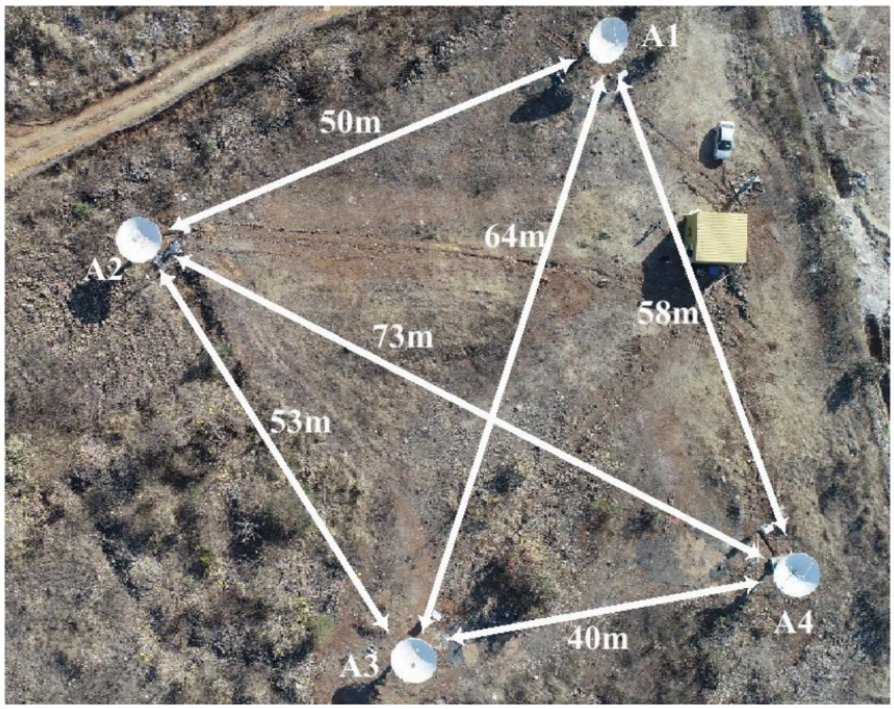

Figure J.11: A top view of IIRI displaying all the Baselines and dimensions.

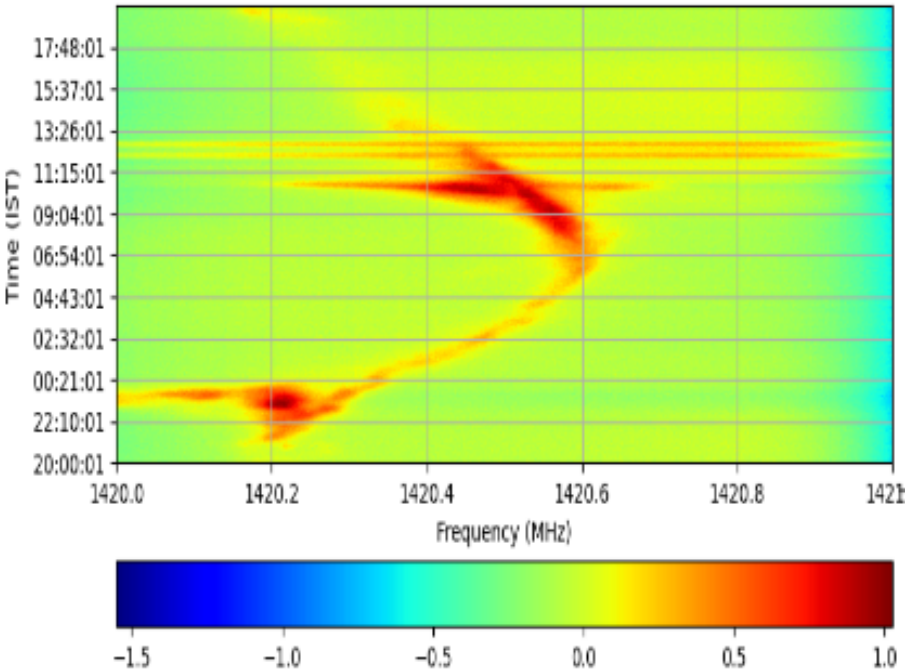

Figure J.12: Drift scan results of antenna A1 when pointed towards Milky way Galaxy center.

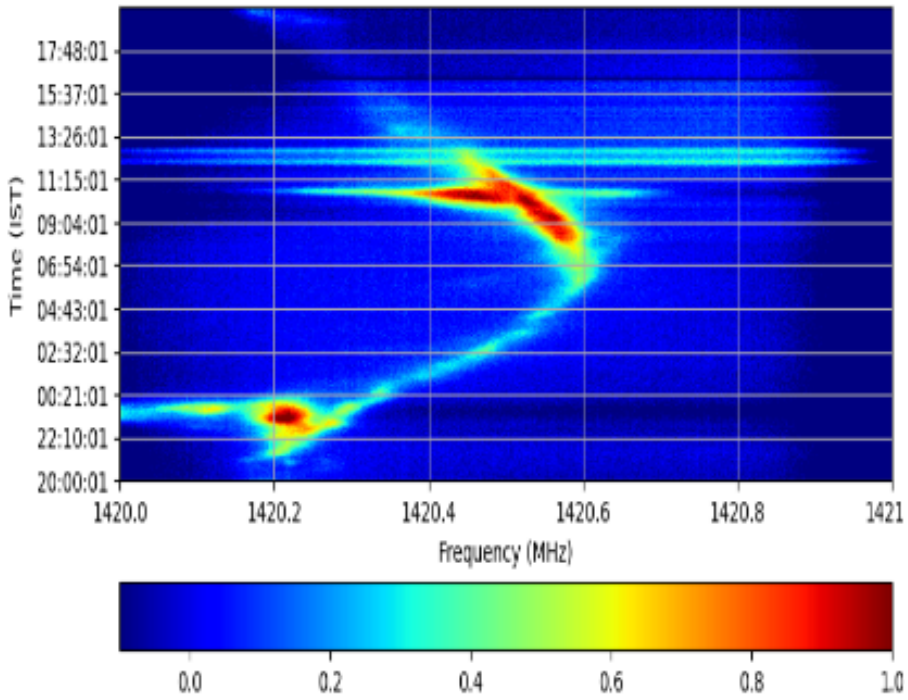

Figure J.13: Drift scan results of antenna A4 when pointed towards Milky way Galaxy center.

respectively. Similar tests were performed for the other antennas to ensure consistent performance across the array.

Once feed alignment corrections were completed, the interferometer design was implemented. Figure J.14 shows the drift scan results of the interferometer, revealing fringe-like power patterns characteristic of correlated signals from multiple antennas. Additionally, during the initial experiment, antenna A4 was undergoing maintenance. However, as shown in Figure J.13, antenna A4 was confirmed to function correctly during its testing phase.

J.5 Discussion

The development and deployment of the IIRI facility aim to educate young and aspiring astronomers on the importance of radio instrumentation and the complexities involved in its design. As shown in Figure J.14, the initial results indicate that the implemented interferometer is functioning as expected. The presence of fringes in the data confirms successful cross-correlation between antennas, a critical feature of interferometric observations. However, the cross-correlation involving antenna A1 exhibits a slanted interference pattern. This anomaly could be attributed to several factors, including frequency-dependent noise contributions from amplifiers, issues with ADC clock synchronization (as the ROACH system uses two dual-channel ADC boards that must be synchronized accurately), or minor misalignments in the feed. These results reveal the sensitivity of interferometric systems to slightest of the variations in its parameters. This phase provided valuable insights into subtle yet significant factors that can affect observations. However, the initial results show multiple challenges, such as calibration, synchronization issues, which must be addressed before it could be established as a fully functional platform for students' observational projects. These lessons will contribute to refining the system and enhancing its utility as a teaching tool.

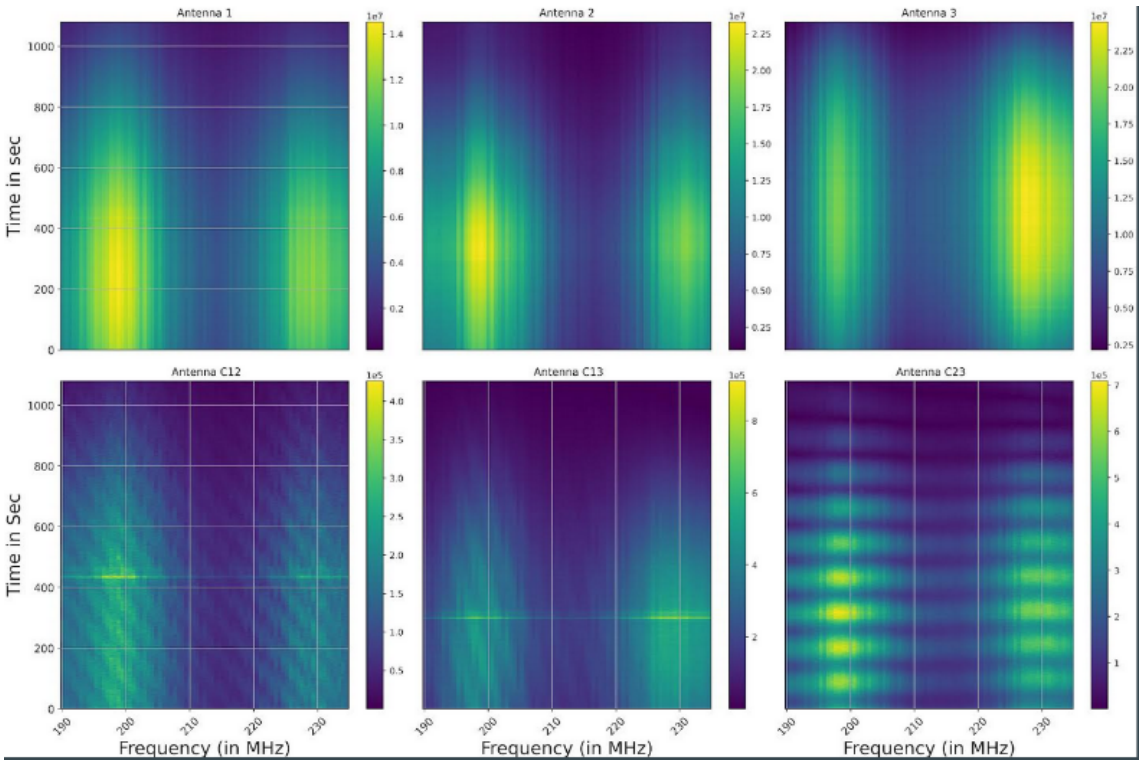

Figure J.14: Drift scan results of the three element interferometer pointed towards the Sun. As A4 is under maintenance. The top row illustrates autocorrelation (R_{xx}) and the bottom row illustrates cross-correlations (R_{xy}). The top left pannel is displays R_{xx} value of signal received by antenna A1, whereas the top middle pannel shows R_{xx} of A2, and the top right pannel shows R_{xx} of A3. The bottom left pannel is displays R_{xy} value of signal from A1 & A2, whereas the bottom middle pannel shows R_{xy} of A1 & A3, and the bottom right pannel shows R_{xy} of A2 & A3. The two bright spot is observed due to the band shape of the system.

Bibliography

[1] J. Fainberg, "Solar radio bursts at low frequencies," *Symposium - International Astronomical Union*, vol. 57, p. 183–200, 1974.

[2] B. Cecconi, P. Zarka, and W. S. Kurth, *SKR polarization and source localization with the Cassini/RPWS/HFR instrument: First results.* Verlag der Österreichischen Akademie der Wissenschaften, 2006.

[3] M. Marians, "Computed scintillation spectra for strong turbulence," *Radio Science*, vol. 10, pp. 115–119, Jan. 1975.

[4] T. K. Sarkar and O. Pereira, "Using the matrix pencil method to estimate the parameters of a sum of complex exponentials," *IEEE Antennas Propagation Mag.*, vol. 37, pp. 48–55, 1995.

[5] L. K. Daldorff, D. S. Turaga, O. Verscheure, and A. Biem, "Direction of arrival estimation using single tripole radio antenna," *ICASSP, IEEE International Conference on Acoustics, Speech and Signal Processing - Proceedings*, pp. 2149–2152, 2009.

[6] L. Chen, A. Aminaei, H. Falcke, and L. Gurvits, "Optimized estimation of the direction of arrival with single tripole antenna," *2010 Loughborough Antennas and Propagation Conference, LAPC 2010*, pp. 93–96, 2010.

[7] Y. Leblanc, G. A. Dulk, and J. L. Bougeret, "Tracing the electron density from the corona to 1 au," *Solar Physics*, vol. 183, pp. 165–180, 1998.

[8] W. T. L., R. K., and H. S., *Tools of Radio Astronomy.* Springer, 2013.

[9] J. du Preez and S. Sinha, *Reflector and Lens Antennas*, pp. 85–106. Cham: Springer International Publishing, 2016.

[10] P. Zarka, "Plasma interactions of exoplanets with their parent star and associated radio emissions," *Planetary Space Sci.*, vol. 55, pp. 598–617, 4 2007.

[11] M. J. Bentum, "Algorithms for direct radio detections of exoplanets in the neighbourhood of radiating host stars," *IEEE Aerospace Conference Proceedings*, vol. 2018-March, pp. 1–7, 6 2018.

[12] R. T. Rajan, A. J. Boonstra, M. Bentum, M. Klein-Wolt, F. Belien, M. Arts, N. Saks, and A. J. van der Veen, "Space-based aperture array for ultra-long wavelength radio astronomy," *Exp. Astro.*, vol. 41, pp. 271–306, 2 2016.

[13] M. J. Bentum, "The search for exoplanets using ultra-long wavelength radio astronomy," in *2017 IEEE Aerospace Conference*, pp. 1–7, IEEE, 3 2017.

[14] M. J. Bentum, M. K. Verma, R. T. Rajan, A. J. Boonstra, C. J. Verhoeven, E. K. Gill, A. J. van der Veen, H. Falcke, M. K. Wolt, B. Monna, S. Engelen, J. Rotteveel, and L. I. Gurvits, "A roadmap towards a space-based radio telescope for ultra-low frequency radio astronomy," *Adv. Space Res.*, vol. 65, pp. 856–867, 1 2020.

[15] S. K. Bisoi, P. Janardhan, M. Ingale, P. Subramanian, S. Ananthakrishnan, M. Tokumaru, and K. Fujiki, "A study of density modulation index in the inner heliospheric solar wind during solar cycle 23," *Astrophysical Journal*, vol. 795, 11 2014.

[16] M. Xiong, X. Feng, B. Li, J. He, W. Wang, Y. Gao, M. Zhang, L. Yang, Z. Huang, J. Cheng, C. Su, Y. Yan, and K. Ying, "Interplanetary scintillation observation and space weather modelling," *Frontiers in Astronomy and Space Sciences*, vol. 10, p. 1159166, 7 2023.

[17] K. W. Weiler, "The promise of long wavelength radio astronomy," *Geophysical Monograph Series*, vol. 119, pp. 243–255, 2000.

[18] A. Lecacheux, "Direction finding of a radiosource of unknown polarization with short electric anten- nas on a spacecraft," *Astro. Astrophys.*, vol. 70, p. 701, 1978.

[19] J. K. Alexander, L. W. Brown, T. A. Clark, R. G. Stone, and R. R. Weber, "The spectrum of the cosmic radio background between 0.4 and 6.5 mhz," *The Astrophysical Journal*, vol. 157, p. L163, 9 1969.

[20] J. K. Alexander, M. L. Kaiser, J. Novaco, F. Grena, and R. Weber, "Scientific instrumentation of the radio-astronomy-explorer-2 satellite," *Astronomy and Astrophysics, vol. 40, no. 4, May 1975, p. 365-371.*, vol. 40, pp. 365–371, 1975.

[21] L. W. Brown, "The galactic radio spectrum between 130 and 2600khz," *Astrophys. J.*, vol. 180, pp. 359–370, 3 1973.

[22] Y. Jia, Y. Zou, J. Ping, C. Xue, J. Yan, and Y. Ning, "The scientific objectives and payloads of chang'e- 4 mission," *Planetary and Space Science*, vol. 162, pp. 207–215, 2018.

[23] B. Cecconi, "Influence of an extended source on goniopolarimetry (or direction finding) with cassini and solar terrestrial relations observatory radio receivers," *Radio Sci.*, vol. 42, p. 2003, 2007.

[24] J. O. Burns, S. Bale, and R. F. Bradley, "Dark Cosmology: Investigating Dark Matter and Exotic Physics using the Redshifted 21-cm Global Signal with the Dark Ages Polarimeter Pathfinder (DAPPER)," in *American Astronomical Society Meeting Abstracts #234*, vol. 234 of *American Astronomical Society Meeting Abstracts*, p. 212.02, June 2019.

[25] R. Borade, G. N. George, and D. C. Gharpure, "Fpga based data acquisition and processing system for space electric and magnetic sensors (seams)," *AIP Conf. Proc.*, vol. 2335, p. 030005, 3 2021.

[26] R. Borade, D. Gharpure, and S. Anathakrishnan, "Design and implementation of data acquisition and analysis system for seaps," *In Computational Mathematics, Nanoelectronics, and Astrophysics: CMNA*, vol. 2018, pp. 64–72, 2018.

[27] B. Cecconi and P. Zarka, "Direction finding and antenna calibration through analytical inversion of radio measurements performed using a system of two or three electric dipole antennas on a three-axis stabilized spacecraft," *Radio Sci.*, vol. 40, p. 3003, 5 2005.

[28] W. A. Baan, "Suro-lc: A space-based ultra-long wavelength radio observatory," *Proceedings of Science*, vol. 2012-June, 2012.

[29] P. Janardhan, S. K. Bisoi, S. Ananthakrishnan, M. Tokumaru, K. Fujiki, L. Jose, and R. Sridharan, "A 20 year decline in solar photospheric magnetic fields: Inner-heliospheric signatures and possible implications," *Journal of Geophysical Research: Space Physics*, vol. 120, pp. 5306–5317, 7 2015.

[30] M. Tokumaru, K. Fujiki, and K. Iwai, "Interplanetary scintillation observations of solar-wind disturbances during cycles 23 and 24," *Solar Physics*, vol. 298, 2 2023.

[31] E. N. Parker, "Dynamics of the interplanetary gas and magnetic fields," *The Astrophysical Journal*, vol. 128, p. 664–676, 1958.

[32] M. Neugebauer and C. W. Snyder, "Solar wind observations from mariner 2 to mariner 10," *Solar Physics*, vol. 27, p. 181–212, 1972.

[33] N. Meyer-Vernet, *Basics of the Solar Wind*. Cambridge University Press, 2007.

[34] L. F. Burlaga, "Interplanetary magnetohydrodynamics," *Reviews of Geophysics*, vol. 22, p. 489–514, 1984.

[35] J. D. Richardson and L. F. Burlaga, "Voyager 2 observations of magnetic fields and solar wind properties in the outer heliosphere," *Journal of Geophysical Research: Space Physics*, vol. 118, p. 2783–2789, 2013.

[36] V. S. Team, "Voyager heliosphere data," 2005. NASA/JPL.

[37] F. N. J., R. N. E., B. S. D., and et al., "The parker solar probe: Revolutionizing our understanding of the sun," *Nature Astronomy*, vol. 4, p. 383–385, 2020.

[38] K. . Zonen, "Atmospheric science instruments," n.d. Accessed: 2024-12-09.

[39] M. Marians, "Computed scintillation spectra for strong turbulence," *Radio Science*, vol. 10, pp. 115–119, 1975.

[40] W. A. Coles, "Interplanetary scintillation," *Space Science Reviews*, vol. 21, pp. 411–425, 2 1978.

[41] P. K. Manoharan, S. Ananthakrishnan, P. K. Manoharan, and S. Ananthakrishnan, "Determination of solar-wind velocities using single-station measurements of interplanetary scintillation.," *MNRAS*, vol. 244, p. 691, 1990.

[42] P. K. Manoharan, S. Ananthakrishnan, M. Dryer, T. R. Detman, H. Leinbach, M. Kojima, T. Watanabe, and J. Kahn, "Solar wind velocity and normalized scintillation index from single-station ips observations," *Solar Physics*, vol. 156, pp. 377–393, 2 1995.

[43] P. Zarka, "Auroral radio emissions at the outer planets: Observations and theories," *Journal of Geophysical Research: Space Physics*, vol. 109, 2004.

[44] D. A. Gurnett, W. S. Kurth, and F. L. Scarf, "The cassini radio and plasma wave investigation," *Space Science Reviews*, vol. 114, pp. 395–463, 2005.

[45] W. S. Kurth, D. A. Gurnett, and F. L. Scarf, "Voyager 1 and 2 observations of jovian kilometric radiation," *Geophysical Research Letters*, vol. 8, pp. 659–662, 1981.

[46] L. Lamy, P. Zarka, B. Cecconi, *et al.*, "Saturn kilometric radiation: A comprehensive view after cassini," *Geophysical Research Letters*, vol. 45, pp. 9398–9406, 2018.

[47] J. O. Burns, R. J. MacDowall, T. J. W. Lazio, *et al.*, "Farside: A low radio frequency interferometric array on the farside of the moon," *The Astrophysical Journal*, vol. 907, p. 12, 2021.

[48] N. Barry, G. Bernardi, B. Greig, N. Kern, and F. Mertens, "Ska-low intensity mapping pathfinder updates: Deeper 21 cm power spectrum limits from improved analysis frameworks," *Journal of Astronomical Telescopes, Instruments, and Systems*, vol. 8, no. 1, p. 011007, 2022.

[49] M. F. Morales and J. S. B. Wyithe, "Reionization and cosmology with 21 cm fluctuations," *Annual Review of Astronomy and Astrophysics*, vol. 48, pp. 127–171, 2010.

[50] J. D. Bowman, A. E. Rogers, R. A. Monsalve, *et al.*, "An absorption profile centered at 78 megahertz in the sky-averaged spectrum," *Nature*, vol. 555, pp. 67–70, 2018.

[51] A. Liu and J. R. Shaw, "Implications for cosmology and dark matter physics from the global 21 cm signal detected by edges," *Physical Review D*, vol. 100, p. 023806, 2019.

[52] R. Beck, "Galactic and extragalactic magnetic fields," *Astrophysics and Space Science*, vol. 320, pp. 77–87, 2009.

[53] A. W. Strong, T. A. Porter, and I. V. Moskalenko, "Global cosmic-ray-related luminosity and energy budget of the milky way," *Astrophysical Journal Letters*, vol. 722, p. L58, 2010.

[54] R. Jansson and G. R. Farrar, "A new model of the galactic magnetic field," *Astrophysical Journal*, vol. 757, p. 14, 2012.

[55] R. B. Wayth, E. Lenc, M. Bell, *et al.*, "The murchison widefield array: Status and key science in 2015," *Publications of the Astronomical Society of Australia*, vol. 32, 2015.

[56] A. Fletcher and R. Beck, "Cosmic-ray propagation and the magnetic field of the milky way," *Annual Review of Astronomy and Astrophysics*, vol. 58, pp. 491–527, 2020.

[57] J. R. Pritchard and A. Loeb, "21 cm cosmology in the 21st century," *Reports on Progress in Physics*, vol. 75, p. 086901, 2012.

[58] C. Dickinson, R. D. Davies, and R. J. Davis, "Free–free absorption and emission at radio wavelengths," *Monthly Notices of the Royal Astronomical Society*, vol. 341, pp. 369–384, 2003.

[59] R. J. Reynolds, "Measurements of the diffuse ionized gas in the galaxy," *The Astrophysical Journal Letters*, vol. 372, pp. L17–L21, 1991.

[60] A. H. Bridle, "Low-frequency observations of free–free absorption in the galaxy," *Astronomy and Astrophysics*, vol. 4, pp. 436–443, 1970.

[61] X. H. Sun, W. Reich, A. Waelkens, and T. A. Enßlin, "The galactic warm ionized medium as observed by low-frequency radio surveys," *Astronomy & Astrophysics*, vol. 527, p. A74, 2011.

[62] D. R. Lorimer, M. Bailes, M. A. McLaughlin, *et al.*, "The discovery of the first fast radio burst," *Science*, vol. 318, pp. 777–780, 2007.

[63] J. Tarter, "The search for extraterrestrial intelligence (seti)," *Annual Review of Astronomy and Astrophysics*, vol. 39, pp. 511–548, 2001.

[64] J. Macquart, J. Prochaska, M. McQuinn, *et al.*, "A census of baryons in the universe from localized fast radio bursts," *Nature*, vol. 581, pp. 391–395, 2020.

[65] E. Petroff, J. W. Hessels, and D. R. Lorimer, "Fast radio bursts: A modern perspective," *Astronomy and Astrophysics Review*, vol. 27, p. 4, 2019.

[66] G. Hobbs, A. Archibald, *et al.*, "The international pulsar timing array project: Using pulsars as a gravitational wave detector," *Classical and Quantum Gravity*, vol. 27, p. 084013, 2010.

[67] J. Enriquez, A. P. Siemion, G. Foster, *et al.*, "The breakthrough listen search for intelligent life: 1.1–1.9 ghz observations of 692 nearby stars," *The Astrophysical Journal*, vol. 849, p. 104, 2017.

[68] R. Manning and G. A. Dulk, "Low-frequency observations of planetary and heliospheric phenomena," *Astronomy and Astrophysics*, vol. 372, no. 2, pp. 663–672, 2001.

[69] P. Zarka, M. Tagger, L. Denis, J. Girard, A. Konovalenko, M. Atemkeng, M. Arnaud, S. Azarian, M. Barsuglia, A. Bonafede, F. Boone, A. Bosma, R. Boyer, M. Branchesi, C. Briand, B. Cecconi, S. Celestin, D. Charrier, E. Chassande-Mottin, and V. Zakharenko, "Nenufar: Instrument description and science case," *ICATT*, pp. 1–6, 04 2015.

[70] H. A. Tanti, A. Datta, and S. Ananthakrishnan, "Snapshot averaged matrix pencil method (sam) for direction of arrival estimation," *Experimental Astronomy*, vol. 56, pp. 267–292, 8 2023.

[71] M. Bentum and A.-J. Boonstra, "The rfi situation for a space-based low-frequency radio astronomy instrument," in *2016 Radio Frequency Interference (RFI)*, pp. 1–6, IEEE, 10 2016.

[72] M. D. Desch and T. D. Carr, "Dekametric and Hectometric Observations of Jupiter from the RAE-1 Satellite," *The Astrophysical Journal Letters*, vol. 194, p. L57, Nov. 1974.

[73] J. P. Eastwood, M. S. Wheatland, H. S. Hudson, S. Krucker, S. D. Bale, M. Maksimovic, K. Goetz, and J.-L. Bougeret, "On the brightness and waiting-time distributions of a type iii radio storm observed by stereo/waves," *The Astrophysical Journal Letters*, vol. 708, p. L95, dec 2009.

[74] M. J. Bentum, A.-J. Boonstra, and W. Baan, "Space-based ultra-long wavelength radio astronomy — an overview of today's initiatives," in *2011 XXXth URSI General Assembly and Scientific Symposium*, pp. 1–4, IEEE, 8 2011.

[75] J. E. S. Bergman, R. J. Blott, A. B. Forbes, D. A. Humphreys, D. W. Robinson, and C. Stavrinidis, "First explorer – an innovative low-cost passive formation-flying system," *arXiv preprint arXiv:0911.0991*, 11 2009.

[76] W. T. Sullivan, *Classics in Radio Astronomy*. Springer-Verlag, 1982.

[77] G. Reber, "Cosmic static," *The Astrophysical Journal*, vol. 100, p. 279, 1944.

[78] A. R. Thompson, J. M. Moran, and G. W. Swenson, *Interferometry and Synthesis in Radio Astronomy*. Springer, 2017.

[79] M. Ryle and D. D. Vonberg, "Solar radiation on 175 mc.s.," *Nature*, vol. 158, p. 339, 1946.

[80] J. D. Kraus, *Radio Astronomy*. McGraw-Hill, 1986.

[81] J. J. Condon and S. M. Ransom, *Essential Radio Astronomy*. Princeton University Press, 2016.

[82] V. L. Ginzburg and S. I. Syrovatskii, "Cosmic Magnetobremsstrahlung (synchrotron Radiation)," *Annual Review of Astronomy and Astrophysics*, vol. 3, p. 297, Jan. 1965.

[83] H. C. Van de Hulst, "Radiogolven uit het wereldruim," *Nederlandse Tijdschrift voor Natuurkunde*, vol. 11, p. 210, 1945.

[84] S. Bandyopadhyay, P. Mcgarey, A. Goel, R. Rafizadeh, M. Delapierre, M. Arya, J. Lazio, P. Goldsmith, N. Chahat, A. Stoica, M. Quadrelli, I. Nesnas, K. Jenks, and G. Hallinan, "Conceptual design of the lunar crater radio telescope (lcrt) on the far side of the moon," in *2021 IEEE Aerospace Conference (50100)*, pp. 1–25, 2021.

[85] A. R. Thompson, J. M. Moran, and J. Swenson, George W., *Interferometry and Synthesis in Radio Astronomy, 2nd Edition*. John Wiley & Sons, Ltd, 2001.

[86] L. Collis Olivari, "Intensity mapping: A new approach to probe the large-scale structure of the universe," 2018. Accessed: 2024-12-10.

[87] A. R. Thompson, J. M. Moran, and G. W. Swenson, *Interferometry and Synthesis in Radio Astronomy*. Springer, 3rd ed., 2017.

[88] Balanis and C. A, *Antenna theory: analysis and design*. Wiley-Interscience, 4 ed., 2016.

[89] L. I. Gurvits, "Space vlbi: from first ideas to operational missions," *Adv. Space Res.*, vol. 65, pp. 868–876, 1 2020.

[90] J. Kasper, J. Lazio, A. Romero-Wolf, J. Lux, and T. Neilsen, "The sun radio interferometer space experiment (sunrise) mission concept," in *2019 IEEE Aerospace Conference*, pp. 1–11, 2019.

[91] T. J. W. Lazio, W. Brisken, K. Bouman, S. Doeleman, H. Falcke, S. Iguchi, Y. Y. Kovalev, C. J. Lonsdale, Z. Shen, A. Zensus, and A. J. Beasley, "Space vlbi 2020: Science and technology futures conference summary," *ArXiv*, 5 2020.

[92] E. L. Shkolnik, "On the verge of an astronomy cubesat revolution," *Nature Astronomy*, vol. 2, pp. 374–378, 5 2018.

[93] L. Chen, H. Falcke, J. Ping, and M. Klein Wolt, "Development of the Netherlands - China Low Frequency Explorer (NCLE)," in *42nd COSPAR Scientific Assembly*, vol. 42, pp. B3.1–26–18, July 2018.

[94] H. A. Tanti and A. Datta, "Validation of direction of arrival with orthogonal tri-dipole antenna for seams," *2021 IEEE Indian Conference on Antennas and Propagation, InCAP 2021*, pp. 312–315, 2021.

[95] T. Carozzi, R. Karlsson, and J. Bergman, "Parameters characterizing electromagnetic wave polarization," *Phys. Rev. E*, vol. 61, pp. 2024–2028, 2000.

[96] N. Yilmazer, J. Koh, and T. K. Sarkar, "Utilization of a unitary transform for efficient computation in the matrix pencil method to find the direction of arrival," *IEEE Trans. Antennas Propagation*, vol. 54, pp. 175–181, 2006.

[97] R. Roy, A. Paulraj, and T. Kailath, "Direction-of-arrival estimation by subspace rotation methods - esprit.," *ICASSP, IEEE International Conference on Acoustics, Speech and Signal Processing - Proceedings*, pp. 2495–2498, 1986.

[98] R. O. Schmidt, "Multiple emitter location and signal parameter estimation," *IEEE Trans. Antennas Propagation*, vol. 34, pp. 276–280, 1986.

[99] N. P. Waweru, D. Konditi, and P. K. Langat, "Performance analysis of music, root-music and esprit doa estimation algorithm," *World Academy of Science, Engineering and Technology, International Journal of Electrical, Computer, Energetic, Electronic and Communication Engineering*, vol. 8, pp. 209–216, 2014.

[100] A. Hewish, P. F. Scott, and D. Wills, "Interplanetary Scintillation of Small Diameter Radio Sources," *Nature*, vol. 203, pp. 1214–1217, Sept. 1964.

[101] L. T. Little and A. Hewish, "Interplanetary scintillation and its relation to the angular structure of radio sources," *Monthly Notices of the RAS*, vol. 134, p. 221, Jan. 1966.

[102] S. Ananthakrishnan, W. A. Coles, and J. J. Kaufman, "Microturbulence in Solar Wind Streams," *Journal of Geophysics Research*, vol. 85, pp. 6025–6030, Nov. 1980.

[103] P. Janardhan, V. Balasubramanian, S. Ananthakrishnan, M. Dryer, A. Bhatnagar, and P. S. McIntosh, "Travelling interplanetary disturbances detected using interplanetary scintillation at 327 mhz," *Solar Physics*, vol. 166, pp. 379–401, Jul 1996.

[104] P. Janardhan, S. K. Bisoi, S. Ananthakrishnan, M. Tokumaru, and K. Fujiki, "The prelude to the deep minimum between solar cycles 23 and 24: Interplanetary scintillation signatures in the inner heliosphere," *Geophysics Research Letters*, vol. 38, p. L20108, Oct. 2011.

[105] M. Kojima and T. Kakinuma, "Solar cycle dependence of global distribution of solar wind speed," *Space Science Reviews*, vol. 53, pp. 173–222, Aug. 1990.

[106] K. Asai, M. Kojima, M. Tokumaru, A. Yokobe, B. V. Jackson, P. L. Hick, and P. K. Manoharan, "Heliospheric tomography using interplanetary scintillation observations. III - Correlation between speed and electron density fluctuations in the solar wind," *Journal of Geophysics Research*, vol. 103, pp. 1991–+, Feb. 1998.

[107] P. Janardhan and S. K. Alurkar, "Angular source size measurements and interstellar scattering at 103 MHz using interplanetary scintillation.," *Astronomy and Astrophysics*, vol. 269, pp. 119–127, Mar. 1993.

[108] S. Ananthakrishnan, V. Balasubramanian, and P. Janardhan, "Latitudinal variation of solar wind velocity," *Space Science Reviews*, vol. 72, pp. 229–232, Apr 1995.

[109] P. Janardhan, S. K. Bisoi, S. Ananthakrishnan, M. Tokumaru, K. Fujiki, L. Jose, and R. Sridharan, "A 20 year decline in solar photospheric magnetic fields: Inner-heliospheric signatures and possible implications," *Journal of Geophysical Research (Space Physics)*, vol. 120, pp. 5306–5317, July 2015.

[110] S. K. Solanki, M. Schüssler, and M. Fligge, "Evolution of the Sun's large-scale magnetic field since the Maunder minimum," *Nature*, vol. 408, pp. 445–447, Nov. 2000.

[111] K. H. Schatten and W. D. Pesnell, "An early solar dynamo prediction: Cycle 23 is approximately cycle 22," *Geophysics Research Letters*, vol. 20, pp. 2275–2278, Oct. 1993.

[112] S. K. Bisoi, P. Janardhan, M. Ingale, P. Subramanian, S. Ananthakrishnan, M. Tokumaru, and K. Fujiki, "A Study of Density Modulation Index in the Inner Heliospheric Solar Wind during Solar Cycle 23," *The Astrophysical Journal*, vol. 795, p. 69, Nov. 2014.

[113] G. Swarup, V. K. Kapahi, N. V. G. Sarma, Gopal-Krishna, M. N. Joshi, and A. P. Rao, "Lunar Occultation Observations of 25 Radio Sources Made with the Ooty Radio Telescope: List 1," *The Astrophysical Journal Letters*, vol. 9, p. 53, Aug. 1971.

[114] U. Vijayanarasimha, S. Ananthakrishnan, and G. Swarup, "Interplanetary scintillation observations of 57 flat-spectrum sourcesat 327 MHz.," *Monthly Notices of the RAS*, vol. 212, pp. 601–608, Feb. 1985.

[115] S. Toledo-Redondo, M. Parrot, and A. Salinas, "Variation of the first cut-off frequency of the earth-ionosphere waveguide observed by demeter," *Journal of Geophysical Research: Space Physics*, vol. 117, 2012.

[116] W. S. Kurth, M. M. Baumback, and D. A. Gurnett, "Direction-finding measurements of auroral kilometric radiation," *J. Geophys. Res.*, vol. 80, p. 2764, 7 1975.

[117] J. W. Warwick, "Power spectrum of electrical discharges seen on earth and at saturn," *J. Geophys. Res.*, vol. 94, pp. 8757–8768, 1989.

[118] J. Xu, X. Xu, J. Wang, Y. Ye, Q. Chang, and Q. Xu, "The relaxation of reconnected open magnetic field lines in the earth's magnetosphere," *Astrophysical J.*, vol. 900, p. 52, 8 2020.

[119] T. L. Wilson, K. Rohlfs, and S. Hüttemeister, "Tools of radio astronomy," *Tools of radio astronomy*, 2013.

[120] H. O. Rucker, W. Macher, and S. Albrecht, "Experimental and Theoretical Investigations on the Cassini RPWS Antennas," in *Planetary Radio Emission IV*, pp. 327–337, Jan. 1997.

[121] A. Nehorai and E. Paldi, "Vector-sensor array processing for electromagnetic source localization," *IEEE Trans. Signal Process.*, vol. 42, pp. 376–398, 1994.

[122] A. Egido, M. Caparrini, G. Ruffini, S. Paloscia, E. Santi, L. Guerriero, N. Pierdicca, and N. Floury, "Global navigation satellite systems reflectometry as a remote sensing tool for agriculture," *Remote Sensing*, vol. 4, pp. 2356–2372, 8 2012.

[123] M. Dvorsky, M. T. A. Qaseer, and R. Zoughi, "Detection and orientation estimation of short cracks using circularly polarized microwave sar imaging," *IEEE Trans. Instrument. Meas.*, vol. 69, pp. 7252–7263, 9 2020.

[124] E. H. Nordholt and D. V. Will1Gen, "A new approach to active antenna design," *IEEE Trans. Antennas Propagation*, vol. 28, pp. 904–910, 1980.

[125] M. J. Bentum, A. J. Boonstra, W. Horlings, and P. van Vugt, "The radio environment for a space-based low-frequency radio astronomy instrument," in *2019 IEEE Aerospace Conference*, vol. 2019-March, pp. 1–7, IEEE, 3 2019.

[126] P. P. Kanjilal and S. Palit, "On multiple pattern extraction using singular value decomposition," *IEEE Trans. Signal Process.*, vol. 43, pp. 1536–1540, 1995.

[127] E. Gentilho, P. R. Scalassara, and T. Abrão, "Direction of arrival estimation methods: a performance complexity tradeoff perspective," *J. Signal Process. Syst.*, vol. 92, pp. 239–256, 2 2019.

[128] J. L. Walker and C. Hoeber, "Technical challenges of integration of space and terrestrial systems," *Handbook of Satellite Applications*, vol. 1, pp. 461–506, 1 2013.

[129] W. Tidd, J. W. Raymond, Y. Huang, and Y. Zhao, "A rf source localization and tracking system," in *2010 - MILCOM 2010 MILITARY COMMUNICATIONS CONFERENCE*, pp. 858–863, 2010.

[130] S. Jha and T. Durrani, "Direction of arrival estimation using artificial neural networks," *IEEE Transactions on Systems, Man, and Cybernetics*, vol. 21, pp. 1192–1201, 1991.

[131] Z.-M. Liu, C. Zhang, and P. S. Yu, "Direction-of-arrival estimation based on deep neural networks with robustness to array imperfections," *IEEE Transactions on Antennas and Propagation*, vol. 66, pp. 7315–7327, 12 2018.

[132] L. Wu, Z. M. Liu, and Z. T. Huang, "Deep convolution network for direction of arrival estimation with sparse prior," *IEEE Signal Processing Letters*, vol. 26, pp. 1688–1692, 11 2019.

[133] Y. Kase, T. Nishimura, T. Ohgane, Y. Ogawa, D. Kitayama, and Y. Kishiyama, "Fundamental trial on doa estimation with deep learning," *IEICE Transactions on Communications*, vol. E103B, pp. 1127–1135, 10 2020.

[134] F. Wang, X. Zhang, L. Liu, C. Chen, X. He, and Y. Zhou, "High-precision direction of arrival estimation based on lightgbm," *Circuits, Systems, and Signal Processing*, 2024.

[135] Y. Shkuratov, A. Konovalenko, V. Zakharenko, A. Stanislavsky, E. Bannikova, V. Kaydash, D. Stankevich, V. Korokhin, D. Vavriv, V. Galushko, S. Yerin, I. Bubnov, P. Tokarsky, O. Ulyanov, S. Stepkin, L. Lytvynenko, Y. Yatskiv, G. Videen, P. Zarka, and H. Rucker, "A twofold mission to the moon: Objectives and payloads," *Acta Astronautica*, vol. 154, pp. 214–226, 1 2019.

[136] A. Herique, B. Agnus, E. Asphaug, A. Barucci, P. Beck, J. Bellerose, J. Biele, L. Bonal, P. Bousquet, L. Bruzzone, C. Buck, I. Carnelli, A. Cheng, V. Ciarletti, M. Delbo, J. Du, X. Du, C. Eyraud, W. Fa, J. Gil Fernandez, O. Gassot, R. Granados-Alfaro, S. Green, B. Grieger, J. Grundmann, J. Grygorczuk, R. Hahnel, E. Heggy, T.-M. Ho, O. Karatekin, Y. Kasaba, T. Kobayashi, W. Kofman, C. Krause, A. Kumamoto, M. Küppers, M. Laabs, C. Lange, J. Lasue, A. Levasseur-Regourd, A. Mallet, P. Michel, S. Mottola, N. Murdoch, M. Mütze, J. Oberst, R. Orosei, D. Plettemeier, S. Rochat, R. RodriguezSuquet, Y. Rogez, P. Schaffer, C. Snodgrass, J.-C. Souyris, M. Tokarz, S. Ulamec, J.-E. Wahlund, and S. Zine, "Direct observations of asteroid interior and regolith structure: Science measurement requirements," *Advances in Space Research*, vol. 62, no. 8, pp. 2141–2162, 2018. Past, Present and Future of Small Body Science and Exploration.

[137] J. J. Condon and S. M. Ransom, *Essential Radio Astronomy*. Princeton University Press, 2016.

[138] A. R. Fogg, C. M. Jackman, J. E. Waters, X. Bonnin, L. Lamy, B. Cecconi, K. Issautier, and C. K. Louis, "Wind/waves observations of auroral kilometric radiation: Automated burst detection and terrestrial solar wind - magnetosphere coupling effects," *Journal of Geophysical Research: Space Physics*, vol. 127, no. 5, p. e2021JA030209, 2022. e2021JA030209 2021JA030209.

[139] V. de Paula, A. Segarra, D. Altadill, J. J. Curto, and E. Blanch, "Detection of solar flares from the analysis of signal-to-noise ratio recorded by digisonde at mid-latitudes," *Remote Sensing*, vol. 14, no. 8, 2022.

[140] P. Zarka, J. Bougeret, C. Briand, B. Cecconi, H. Falcke, J. Girard, J. GrieBmeier, S. Hess, M. KleinWolt, A. Konovalenko, L. Lamy, D. Mimoun, and A. Aminaei, "Planetary and exoplanetary low frequency radio observations from the moon," *Planetary and Space Science*, vol. 74, pp. 156–166, 12 2012.

[141] S. Agatonovic-Kustrin and R. Beresford, "Basic concepts of artificial neural network (ann) modeling and its application in pharmaceutical research," *Journal of pharmaceutical and biomedical analysis*, vol. 22, no. 5, pp. 717–727, 2000.

[142] S. J. Russell and P. Norvig, *Artificial intelligence: a modern approach*. Pearson, 2016.

[143] M. Choudhury, A. Datta, and S. Majumdar, "Extracting the 21-cm power spectrum and the reionization parameters from mock data sets using artificial neural networks," *Monthly Notices of the Royal Astronomical Society*, vol. 512, pp. 5010–5022, 03 2022.

[144] E. N. Parker, "Hydromagnetic Dynamo Models.," *The Astrophysical Journal*, vol. 122, pp. 293–+, Sept. 1955.

[145] E. N. Parker, "The Formation of Sunspots from the Solar Toroidal Field.," *The Astrophysical Journal*, vol. 121, pp. 491–+, Mar. 1955.

[146] M. Steenbeck and F. Krause, "On the Dynamo Theory of Stellar and Planetary Magnetic Fields. I. AC Dynamos of Solar Type," *Astronomische Nachrichten*, vol. 291, pp. 49–84, Jan. 1969.

[147] Y. Wang, N. R. Sheeley, Jr., and A. G. Nash, "A new solar cycle model including meridional circulation," *The Astrophysical Journal*, vol. 383, pp. 431–442, Dec. 1991.

[148] A. R. Choudhuri, M. Schussler, and M. Dikpati, "The solar dynamo with meridional circulation.," *Astronomy and Astrophysics*, vol. 303, pp. L29+, Nov. 1995.

[149] M. Dikpati and P. Charbonneau, "A Babcock-Leighton Flux Transport Dynamo with Solar-like Differential Rotation," *The Astrophysical Journal*, vol. 518, pp. 508–520, June 1999.

[150] P. Janardhan, S. K. Bisoi, and S. Gosain, "Solar Polar Fields During Cycles 21 - 23: Correlation with Meridional Flows," *Solar Physics*, vol. 267, pp. 267–277, Dec. 2010.

[151] S. K. Bisoi, P. Janardhan, D. Chakrabarty, S. Ananthakrishnan, and A. Divekar, "Changes in Quasi-periodic Variations of Solar Photospheric Fields: Precursor to the Deep Solar Minimum in Cycle 23?," *Solar Physics*, vol. 289, pp. 41–61, Jan. 2014.

[152] S. K. Bisoi, P. Janardhan, and S. Ananthakrishnan, "Another Mini Solar Maximum in the Offing: A Prediction for the Amplitude of Solar Cycle 25," *Journal of Geophysical Research (Space Physics)*, vol. 125, p. e27508, July 2020.

[153] L. Svalgaard and Y. Kamide, "Asymmetric Solar Polar Field Reversals," *The Astrophysical Journal*, vol. 763, p. 23, Jan. 2013.

[154] P. Janardhan, K. Fujiki, M. Ingale, S. K. Bisoi, and D. Rout, "Solar cycle 24: An unusual polar field reversal," *Astronomy and Astrophysics*, vol. 618, p. A148, Oct. 2018.

[155] G. J. D. Petrie, "Global solar photospheric and coronal magnetic field over activity cycles 21-25," *Journal of Space Weather and Space Climate*, vol. 14, p. 5, Feb. 2024.

[156] M. Ingale, P. Janardhan, and S. K. Bisoi, "Beyond the mini-solar maximum of solar cycle 24: Declining solar magnetic fields and the response of the terrestrial magnetosphere," *Journal of Geophysics Research Solar Physics*, vol. 124, pp. 6363–6883, Aug. 2019.

[157] A. Pramesh Rao, S. M. Bhandari, and S. Ananthakrishnan, "Observations of interplanetary scintillations at 327 MHz," *Australian Journal of Physics*, vol. 27, p. 105, Feb. 1974.

[158] S. Ananthakrishnan, S. M. Bhandari, and A. P. Rao, "Occultation of radio source pks 2025-15 by comet kohoutek (1973f)," *Astrophysics and Space Science*, vol. 37, pp. 275–282, Oct 1975.

[159] Y. Yamauchi, M. Tokumaru, M. Kojima, P. K. Manoharan, and R. Esser, "A study of density fluctuations in the solar wind acceleration region," *Journal of Geophysics Research*, vol. 103, p. 6571, Apr. 1998.

[160] R. A. Fallows, A. R. Breen, and G. D. Dorrian, "Developments in the use of EISCAT for interplanetary scintillation," *Annales Geophysicae*, vol. 26, pp. 2229–2236, Aug. 2008.

[161] W. Livingston, M. J. Penn, and L. Svalgaard, "Decreasing sunspot magnetic fields explain unique 10.7 cm radio flux," *The Astrophysical Journal Letters*, vol. 757, p. L8, aug 2012.

[162] Y.-M. Wang, E. Robbrecht, and N. R. Sheeley, Jr., "On the Weakening of the Polar Magnetic Fields during Solar Cycle 23," *The Astrophysical Journal*, vol. 707, pp. 1372–1386, Dec. 2009.

[163] E. W. Cliver and A. G. Ling, "The Floor in the Solar Wind Magnetic Field Revisited," *Solar Physics*, vol. 274, pp. 285–301, Dec. 2011.

[164] L. Svalgaard and E. W. Cliver, "A Floor in the Solar Wind Magnetic Field," *The Astrophysical Journall*, vol. 661, pp. L203–L206, June 2007.

[165] E. W. Cliver, S. M. White, and I. G. Richardson, "A Floor in the Sun's Photospheric Magnetic Field: Implications for an Independent Small-scale Dynamo," *The Astrophysical Journall*, vol. 961, p. L46, Feb. 2024.

[166] F. Clette, "Is the $F_{10.7cm}$ - Sunspot Number relation linear and stable?," *Journal of Space Weather and Space Climate*, vol. 11, p. 2, Jan. 2021.

[167] V. Sarp, A. Kilcik, V. Yurchyshyn, J. P. Rozelot, and A. Ozguc, "Prediction of solar cycle 25: a non-linear approach," *Monthly Notices of the RAS*, vol. 481, pp. 2981–2985, Dec. 2018.

[168] S. K. Bisoi and P. Janardhan, "A New Tool for Predicting the Solar Cycle: Correlation Between Flux Transport at the Equator and the Poles," *Solar Physics*, vol. 295, p. 79, June 2020.

[169] L. A. Upton and D. H. Hathaway, "Solar cycle precursors and the outlook for cycle 25," *Journal of Geophysical Research: Space Physics*, vol. 128, 10 2023.

[170] G. de Toma, "Evolution of Coronal Holes and Implications for High-Speed Solar Wind During the Minimum Between Cycles 23 and 24," *Solar Physics*, vol. 274, pp. 195–217, Dec. 2011.

[171] N. Gopalswamy, S. Yashiro, P. Mäkelä, G. Michalek, K. Shibasaki, and D. H. Hathaway, "Behavior of Solar Cycles 23 and 24 Revealed by Microwave Observations," *The Astrophysical Journall*, vol. 750, p. L42, May 2012.

[172] X. Sun, J. T. Hoeksema, Y. Liu, and J. Zhao, "On Polar Magnetic Field Reversal and Surface Flux Transport During Solar Cycle 24," *The Astrophysical Journal*, vol. 798, p. 114, Jan. 2015.

[173] N. Gopalswamy, S. Yashiro, and S. Akiyama, "Unusual Polar Conditions in Solar Cycle 24 and Their Implications for Cycle 25," *The Astrophysical Journall*, vol. 823, p. L15, May 2016.

[174] A. Mu noz-Jaramillo, N. R. Sheeley, J. Zhang, and E. E. DeLuca, "Calibrating 100 Years of Polar Faculae Measurements: Implications for the Evolution of the Heliospheric Magnetic Field," *The Astrophysical Journal*, vol. 753, p. 146, July 2012.

[175] P. K. Manoharan, "Three-dimensional Evolution of Solar Wind during Solar Cycles 22-24," *The Astrophysical Journal*, vol. 751, p. 128, June 2012.

[176] E. W. Cliver and K. Herbst, "Evolution of the Sunspot Number and Solar Wind B Time Series," *Space Science Reviews*, vol. 214, p. 56, Mar 2018.

[177] L. Svalgaard, E. W. Cliver, and Y. Kamide, "Sunspot cycle 24: Smallest cycle in 100 years?," *Geophysics Research Letters*, vol. 32, pp. 1104–+, Jan. 2005.

[178] C. Y. Tu and E. Marsch, "Mhd structures, waves and turbulence in the solar wind: Observations and theories," *SSRv*, vol. 73, p. 1, 7 1995.

[179] C.-Y. Tu and E. Marsch, "Mhd structures, waves and turbulence in the solar wind," *MHD Structures, Waves and Turbulence in the Solar Wind*, 1995.

[180] M. L. Goldstein, D. A. Roberts, and W. H. Matthaeus, "Magnetohydrodynamic turbulence in the solar wind," *ARAstronomy and Astrophysics*, vol. 33, p. 283, 1995.

[181] R. Bruno and V. Carbone, "The solar wind as a turbulence laboratory," *LRSP*, vol. 2, p. 4, 2005.

[182] E. Marsch, "Kinetic physics of the solar corona and solar wind," *LRSP*, vol. 3, p. 1, 2006.

[183] S. R. Spangler, "Plasma turbulence in the local bubble," *SSRv*, vol. 143, p. 277, 3 2009.

[184] P. A. Davidson, *An Introduction to Magnetohydrodynamics*. Cambridge Texts in Applied Mathematics, Cambridge University Press, 2001.

[185] J. N. Gordon, "The solar corona in active regions and the thermal origin of the slowly varying component of solar radio radiation.," *ApJ*, vol. 133, p. 983, 5 1961.

[186] W. L. L., "Heat flux and viscosity of protons in the collisionless solar wind," *ApJ*, vol. 453, p. 953, 11 1995.

[187] M. E. and T. C. Y., "Spectral and spatial evolution of compressible turbulence in the inner solar wind," *JGR*, vol. 95, p. 11945, 8 1990.

[188] B. Bavassano and R. Bruno, "Density fluctuations and turbulent mach numbers in the inner solar wind," *Journal of Geophysical Research: Space Physics*, vol. 100, pp. 9475–9480, 6 1995.

[189] J. P., B. V., A. S., *et al.*, "A numerical study of the pre-ejection, magnetically-sheared corona as a free boundary problem," *SoPh*, vol. 166, p. 379, 1996.

[190] A. I. Efimov, V. K. Rudash, M. K. Bird, P. Janardhan, J. Karl, M. Pätzold, P. Edenhofer, D. Plettemeier, and R. Wohlmuth, "Anisotropic structure of the solar wind in its region of acceleration," *AdSpR*, vol. 26, p. 785, 9 2000.

[191] S. R. Spangler, "The amplitude of magnetohydrodynamic turbulence in the inner solar wind," *The Astrophysical Journal*, vol. 576, pp. 997–1004, 9 2002.

[192] B. M. K., J. P., E. A. I., *et al.*, "Solar wind ten," 2003.

[193] M. Tokumaru, M. Kojima, and K. Fujiki, "Long-term evolution in the global distribution of solar wind speed and density fluctuations during 1997-2009," *JGRA*, vol. 117, p. 6108, 2012.

[194] S. R. Spangler, "Density fluctuations induced by nonlinear alfvén waves," *The Physics of Fluids*, vol. 30, pp. 1104–1109, 4 1987.

[195] W. H. Matthaeus and M. R. Brown, "Nearly incompressible magnetohydrodynamics at low mach number," *The Physics of Fluids*, vol. 31, pp. 3634–3644, 12 1988.

[196] B. J. Bayly, C. D. Levermore, and T. Passot, "Density variations in weakly compressible flows," *Physics of Fluids A*, vol. 4, pp. 945–954, 1992.

[197] S. R. Spangler and L. G. Spitler, "An empirical investigation of compressibility in magnetohydrodynamic turbulence," *Physics of Plasmas*, vol. 11, pp. 1969–1977, 5 2004.

[198] C. Y. Tu and E. Marsch, "On the nature of compressive fluctuations in the solar wind," *JGR*, vol. 99, p. 21481, 11 1994.

[199] B. Hnat, S. C. Chapman, and G. Rowlands, "Compressibility in solar wind plasma turbulence," *PhRvL*, vol. 94, p. 204502, 5 2005.

[200] D. Shaikh and G. P. Zank, "The turbulent density spectrum in the solar wind plasma," *MNRAS*, vol. 402, p. 362, 2010.

[201] V. Carbone, R. Marino, L. Sorriso-Valvo, A. Noullez, and R. Bruno, "Scaling laws of turbulence and heating of fast solar wind: The role of density fluctuations," *Physical Review Letters*, vol. 103, p. 061102, 8 2009.

[202] T. G. and M. R. J., "Effects of scattering on radio emission from the quiet sun at low frequencies," *ApJ*, vol. 676, p. 1338, 4 2008.

[203] P. Janardhan and S. K. Alurkar, "Angular source size measurements and interstellar scattering at 103 mhz using interplanetary scintillation.," *Astronomy and Astrophysics, Vol. 269, p. 119-127 (1993)*, vol. 269, p. 119, 3 1993.

[204] P. Subramanian and I. Cairns, "Constraints on coronal turbulence models from source sizes of noise storms at 327 mhz," *JGRA*, vol. 116, p. 3104, 2011.

[205] H. A. Reid and E. P. Kontar, "Solar wind density turbulence and solar flare electron transport from the sun to the earth," *ApJ*, vol. 721, p. 864, 9 2010.

[206] O. Alexandrova, C. H. K. Chen, L. Sorriso-Valvo, T. S. Horbury, and S. D. Bale, *Solar Wind Turbulence and the Role of Ion Instabilities*, pp. 25–63. Springer, Boston, MA, 2013.

[207] X. Zheng, M. M. Martinović, K. Liu, V. Pierrard, M. Liu, K. Klein, W. Ember, and J. B. Abraham, "Radial evolution of non-maxwellian solar wind electrons derived from quasi-thermal noise spectroscopy: Parker solar probe observation," *EGU24*, 3 2024.

[208] W. Liu, H.-Y. Jia, S.-M. Liu, W. Liu, H.-Y. Jia, and S.-M. Liu, "Radial evolution of the near-sun solar wind: Parker solar probe observations," *ApJL*, vol. 963, p. L36, 3 2024.

[209] D. A. Roberts and L. Ofman, "Hybrid simulation of solar-wind-like turbulence," *Solar Physics*, vol. 294, 11 2019.

[210] K. Iwai, R. A. Fallows, M. M. Bisi, D. Shiota, B. V. Jackson, M. Tokumaru, and K. Fujiki, "Magnetohydrodynamic simulation of coronal mass ejections using interplanetary scintillation data observed from radio sites isee and lofar," *Advances in Space Research*, vol. 72, pp. 5328–5340, 12 2023.

[211] S. Inoue, K. Hayashi, and T. Miyoshi, "An evolution and eruption of the coronal magnetic field through a data-driven mhd simulation," *The Astrophysical Journal*, vol. 946, p. 46, 3 2023.

[212] L. T. Little and A. Hezmsh, "Interplanetary scintillation and its relation to the angular structure of radio sources," *Monthly Notices of the Royal Astronomical Society*, vol. 134, pp. 221–237, 12 1966.

[213] P. Janardhan, S. K. Bisoi, S. Ananthakrishnan, M. Tokumaru, and K. Fujiki, "The prelude to the deep minimum between solar cycles 23 and 24: Interplanetary scintillation signatures in the inner heliosphere," *Geophysical Research Letters*, vol. 38, 10 2011.

[214] P. R. A., B. S. M., and A. S., "Observations of interplanetary scintillations at 327 mhz," *AuJPh*, vol. 27, p. 105, 1974.

[215] W. A. Coles and J. P. Filice, "Changes in the microturbulence spectrum of the solar wind during high-speed streams," *Journal of Geophysical Research: Space Physics*, vol. 90, pp. 5082–5088, 6 1985.

[216] Y. Yamauchi, M. Tokumaru, M. Kojima, P. K. Manoharan, and R. Esser, "A study of density fluctuations in the solar wind acceleration region," *Journal of Geophysical Research: Space Physics*, vol. 103, pp. 6571–6583, 4 1998.

[217] R. A. Fallows, A. R. Breen, and G. D. Dorrian, "Developments in the use of eiscat for interplanetary scintillation," *AnGeo*, vol. 26, p. 2229, 7 2008.

[218] A. W. Case, J. C. Kasper, P. S. Daigneau, D. Caldwell, M. Freeman, T. Gauron, B. A. Maruca, J. bookbinder, K. E. Korreck, J. W. Cirtain, M. E. Effinger, J. S. Halekas, D. E. Larson, A. J. Lazarus, M. L. Stevens, E. R. Taylor, and K. H. W. Jr., "Designing a sun-pointing faraday cup for solar probe plus," in *AIP Conference Proceedings*, vol. 1539, pp. 458–461, AIP Publishing, 6 2013.

[219] K. E. Korreck, J. C. Kasper, A. W. Case, P. Daigneau, J. A. bookbinder, D. Larson, J. S. Halekas, M. Stevens, M. Ludlam, and W. Marchant, "Solar wind electrons alphas and protons (sweap) science operations center initial design and implementation," *https://doi.org/10.1117/12.2057314*, vol. 9149, pp. 252–258, 8 2014.

[220] J. C. Kasper, R. Abiad, G. Austin, M. Balat-Pichelin, S. D. Bale, J. W. Belcher, P. Berg, H. Bergner, M. Berthomier, J. bookbinder, E. Brodu, D. Caldwell, A. W. Case, B. D. Chandran, P. Cheimets, J. W. Cirtain, S. R. Cranmer, D. W. Curtis, P. Daigneau, G. Dalton, B. Dasgupta, D. DeTomaso, M. Diaz-Aguado, B. Djordjevic, B. Donaskowski, M. Effinger, V. Florinski, N. Fox, M. Freeman, D. Gallagher, S. P. Gary, T. Gauron, R. Gates, M. Goldstein, L. Golub, D. A. Gordon, R. Gurnee, G. Guth, J. Halekas, K. Hatch, J. Heerikuisen, G. Ho, Q. Hu, G. Johnson, S. P. Jordan, K. E. Korreck, D. Larson, A. J. Lazarus, G. Li, R. Livi, M. Ludlam, M. Maksimovic, J. P. McFadden, W. Marchant, B. A. Maruca, D. J. McComas, L. Messina, T. Mercer, S. Park, A. M. Peddie, N. Pogorelov, M. J. Reinhart, J. D. Richardson, M. Robinson, I. Rosen, R. M. Skoug, A. Slagle, J. T. Steinberg, M. L. Stevens, A. Szabo, E. R. Taylor, C. Tiu, P. Turin, M. Velli, G. Webb, P. Whittlesey, K. Wright, S. T. Wu, and G. Zank, "Solar wind electrons alphas and protons (sweap) investigation: Design of the solar wind and coronal plasma instrument suite for solar probe plus," *Space Science Reviews*, vol. 204, pp. 131–186, 12 2016.

[221] M. Kojima and T. Kakinuma, "Solar cycle dependence of global distribution of solar wind speed," *SSRv*, vol. 53, p. 173, 8 1990.

[222] K. Asaj, Y. Ishida, M. K0jma, K. Maruyama, H. Misawa, and N. Yoshimi, "Multi-station system for solar wind observations using the interplanetary scintillation method," *J. Geomag. Geoelectr*, vol. 47, pp. 1107–1112, 1995.

[223] M. Tokumaru, M. Kojima, K. Fujiki, K. Maruyama, Y. Maruyama, H. Ito, and T. Iju, "A newly developed uhf radiotelescope for interplanetary scintillation observations: Solar wind imaging facility," *Radio Science*, vol. 46, 2011.

[224] S. Ananthakrishnan, W. A. Coles, and J. J. Kaufman, "Microturbulence in solar wind streams," *Journal of Geophysical Research: Space Physics*, vol. 85, pp. 6025–6030, 11 1980.

[225] L. T. Little and A. Hewish, "Radio source structure derived from interplanetary scintillation," *Monthly Notices of the Royal Astronomical Society*, vol. 138, pp. 393–406, 2 1968.

[226] E. N. Parker, "Dynamics of the interplanetary gas and magnetic fields.," *The Astrophysical Journal*, vol. 128, p. 664, 11 1958.

[227] M. J. Owens and R. J. Forsyth, "The heliospheric magnetic field," *Living Reviews in Solar Physics*, vol. 10, pp. 1–52, 11 2013.

[228] R. Woo, J. W. Armstrong, M. K. Bird, and M. Pätzold, "Variation of fractional electron density fluctuations inside 40 ro observed by ulysses ranging measurements," *GeoRL*, vol. 22, p. 329, 1995.

[229] I. N. da Silva, D. H. Spatti, R. A. Flauzino, L. H. B. Liboni, and S. F. dos Reis Alves, "Artificial neural networks: A practical course," *Artificial Neural Networks: A Practical Course*, pp. 1–307, 1 2016.

[230] M. Mohri, A. Rostamizadeh, and A. Talwalkar, *Foundations of Machine Learning*. The MIT Press, 2012.

[231] P. Flach, *References*, p. 367–382. Cambridge University Press, 2012.

[232] A. Tripathi, A. Datta, M. Choudhury, and S. Majumdar, "Extracting the Global 21-cm signal from Cosmic Dawn and Epoch of Reionization in the presence of Foreground and Ionosphere," *Monthly Notices of the Royal Astronomical Society*, vol. 528, pp. 1945–1964, 01 2024.

[233] T. L. Wilson, K. Rohlfs, and S. Hüttemeister, *Tools of Radio Astronomy*. Springer Berlin, Heidelberg, 5 ed., 2008.

[234] R. J. Blum, S. N. Andre, and J. O. Clark, "Rf parameter study in support of structures for orbiting radio telescopes (sort): Final report, 28 jan. - 28 oct. 1970," tech. rep., NASA, 1970. Accessed December 9, 2024.

[235] W. L. Stutzman and G. A. Thiele, *Antenna Theory and Design*. New York: John Wiley & Sons, 2nd ed., 1998. Provides a detailed explanation of the Cassegrain feed system and its applications in parabolic reflector antennas.

[236] P. Kumar, A. Biswas, and B. B. Karak, "Physical link of the polar field buildup with the waldmeier effect broadens the scope of early solar cycle prediction: Cycle 25 is likely to be slightly stronger than cycle 24," *Monthly Notices of the Royal Astronomical Society: Letters*, vol. 513, pp. L112–L116, 6 2022.

[237] Y. Chikada, M. Ishiguro, H. Hirabayashi, M. Morimoto, K. I. Morita, K. Miyazawa, K. Nagane, K. Murata, A. Tojo, S. Inoue, T. Kanzawa, and H. Iwashita, "A Digital FFT Spectro-Correlator for Radio Astronomy," in *Indirect Imaging. Measurement and Processing for Indirect Imaging* (J. A. Roberts, ed.), p. 387, Jan. 1984.

[238] C. Yoshihiro, "Correlators for interferometry - Today and tomorrow," in *IAU Colloq. 131: Radio Interferometry. Theory, Techniques, and Applications* (T. J. Cornwell and R. A. Perley, eds.), vol. 19 of *Astronomical Society of the Pacific Conference Series*, pp. 26–32, Jan. 1991.

[239] S. K. Okumura, Y. Chikada, and M. Momose, "Very large FX correlator system for enhanced ALMA," in *Radio Telescopes* (H. R. Butcher, ed.), vol. 4015, pp. 64 – 72, International Society for Optics and Photonics, SPIE, 2000.